

**UNDERSTANDING AND EVALUATION OF  
BADMINTON SHUTTLECOCKS THROUGH  
FLIGHT DYNAMICS AND EXPERIMENTAL  
APPROACH**

**LIN SHENGHUI CALVIN**

School of Mechanical and Aerospace Engineering

A thesis submitted to the Nanyang Technological University in partial  
fulfilment of the requirement for the degree of  
Doctor of Philosophy

2015



## **Acknowledgement**

First and foremost, I would like to thank Professor Chua Chee Kai and Associate Professor Yeo Joon Hock for supervising my research. I am especially thankful for their patience in guiding me through technical writing.

I would also like to extend my heartfelt gratitude to Associate Professor Leong Kah Fai for giving me the opportunity to pursue a degree under the ISR family.

I am grateful to ISR, especially Mr Pascal Joubert des Ouches and Mr Anthony Bert, for providing support to my work.

I would also like to express my sincere appreciation to Associate Professor Chen Chun-Hsien, Associate Professor Chan Weng Kong and Assistant Professor Wu Yanhua for their time in assessing my qualifying exam.

With special thanks to Mr Edwin Lam, Mr Leonard Lee, Mr Chia Yak Khoong, Mr Seow Tzer Fook, Associate Professor Ng Teng Yong and Assistant Professor Tiauw Hiong Yongki Go.

## Table of Contents

Acknowledgement	i
List of Tables	xi
List of Figures	xiii
List of Symbols	xxiii
List of Abbreviations	xxvi
Abstract	xxvii
1. INTRODUCTION	1
1.1 Background	1
1.2 Motivation	3
1.3 Objectives	6
1.4 Scope	7
1.5 Organisation of Thesis	8
2. LITERATURE REVIEW	10
2.1 Badminton Shuttlecock	10
2.2 Patents and Developments of Shuttlecocks	13
2.2.1 Patents Reinventing Badminton and the Shuttlecock	13
2.2.2 Patents Improving the Traditional Shuttlecocks	16
2.3 Flow along a shuttlecock	21
2.4 Aerodynamic Experiments on Shuttlecocks	27

2.5	Flight Experiments on Shuttlecocks	33
2.6	Spin Experiments on Shuttlecocks	38
2.7	Summary	41
3.	AERODYNAMICS of SHUTTLECOCKS	43
3.1	Model Geometry and ANSYS CFX Method	43
3.2	Flow Over a Perfect Gapless Conical Skirt	48
3.3	Effect of Gaps on Coefficient of Pressure and Drag	57
3.4	Reduction in Blunt Body Effect with Gap size	65
3.5	Discussion of Coefficient of Pressure with Gaps	69
3.6	Summary	74
4.	SHUTTLECOCK FLIGHT DYNAMICS	76
4.1	States of Flight	76
4.1.1	Unsteady Flight	77
4.1.2	Steady Flight	78
4.2	Flight Modelling	79
4.2.1	Multiple Reference Frame	79
4.2.2	Translation	81
4.2.2.1	Gravitational force	81
4.2.2.2	Lift and Drag	81
4.2.2.3	Magnus Force	84
4.2.2.4	Force Summation	85
4.2.3	Rotation	85
4.2.3.1	Pitch and Yaw Moment	86

4.2.3.2	Spin	87
4.2.3.3	Angular Damping Factor	90
4.2.3.4	Torque Summation	91
4.2.4	Equation of motion	91
4.3	Flight Phenomena	92
4.3.1	Turnover	92
4.3.1.1	Stability in Turnover	93
4.3.1.2	Modelling	98
4.3.1.3	Physical Parameters	99
4.3.2	Axial Spin	100
4.3.2.1	Theory	100
4.3.2.2	Preliminary Observations	101
4.3.3	Gyroscopic Precession	105
4.3.3.1	Theory	105
4.3.3.2	Primary and Secondary Precession	107
4.3.3.3	Implications	110
4.3.3.4	Experimental Observation	112
4.3.3.5	Modelling and Simulation	114
4.3.3.6	Reverse Gyroscopic Precession	121
4.4	Important Parameters	124
4.4.1	Unsteady Flight State	124
4.4.2	Steady Flight State	126
4.5	Summary	127
5.	SHUTTLECOCK TESTING: PHASE I (STATIC)	129
5.1	Overview of Testing	129
5.2	Introduction to Phase I	130
5.2.1	Physical Properties	131
5.2.1.1	Mass	131

5.2.1.2	Diameter and Chord	132
5.2.1.3	Moments of Inertia	135
5.2.2	Wind Tunnel Study	135
5.3	Experimental Method	137
5.3.1	Shuttlecock Specimens	137
5.3.2	Physical Properties	138
5.3.2.1	Mass	138
5.3.2.2	Diameter and Chord	138
5.3.2.3	Moments of Inertia	139
5.3.3	Wind Tunnel Study	141
5.4	Results and Discussion	144
5.4.1	Physical Properties	144
5.4.1.1	Mass	144
5.4.1.2	Diameter and Chord	146
5.4.1.3	Moments of Inertia	147
5.4.2	Wind Tunnel Study	150
5.4.2.1	Drag Parameter, <b><i>C<sub>dS</sub></i></b>	150
5.4.2.2	Axial Spin	151
5.4.2.3	Skirt Deformation	152
5.4.2.4	Drag per Unit Mass, <b><i>C<sub>dS/m</sub></i></b>	155
5.5	Summary of Phase I	158
6.	SHUTTLECOCK TESTING: PHASE II (FLIGHT)	159
6.1	Shuttlecock Launcher Development	159
6.1.1	Existing Problems	159
6.1.2	Motion Analysis of Racket Speed	160
6.1.3	Developed Launcher	161

6.1.4	Initial Trial	163
6.1.4.1	Experimental Method	163
6.1.4.2	Results and Discussion	164
6.1.4.3	Launch Condition	167
6.2	Overview of Phase II	169
6.2.1	Turnover	169
6.2.2	Flight Trajectory	169
6.3	Experimental Setup and Methodology	171
6.3.1	Turnover	171
6.3.1.1	Experimental Method	171
6.3.1.2	Response Modelling	173
6.3.2	Flight Trajectory	174
6.3.2.1	Shuttlecocks	174
6.3.2.2	Experimental Setup	175
6.3.2.3	Methodology	177
6.3.2.4	Experimental Error from High-Speed Capturing	178
6.4	Result and Discussion	180
6.4.1	Turnover	180
6.4.1.1	Parameter Identified from Experimental Data	180
6.4.1.2	Response Modelling	184
6.4.1.3	Realistic Damping Parameters	186
6.4.2	Flight Trajectory	187
6.4.2.1	Shuttlecock Launch Velocity and Range	187
6.4.2.2	Feather Shuttlecock Trajectories	189
6.4.2.3	Synthetic Shuttlecock Trajectories	193
6.4.2.4	Velocity Profile	197
6.4.2.5	Feather Shuttlecock Spin Rate	198
6.4.2.6	Synthetic Shuttlecock Spin Rate	201
6.4.2.7	Stall Velocities	205
6.4.2.8	Trajectory Similarities	206
6.5	Summary of Experimental Work	209

7.	SHUTTLECOCK TESTING: PHASE III (MECHANICAL)	211
7.1	Introduction	211
7.2	Shuttlecock Skirt Compression Tester (SSCT)	213
7.2.1	SSCT Components	213
7.2.2	SSCT Functioning	215
7.2.3	SSCT Preliminary Trial	217
7.3	Wear Induction Machines	219
7.3.1	Vane Wear Induction Device (VWID)	221
7.3.1.1	VWID Components	222
7.3.1.2	VWID Functioning	223
7.3.1.3	VWID Preliminary Trial	225
7.3.1.4	VWID Limitations	228
7.3.2	Smash Test Machine (STM)	229
7.3.2.1	STM Components	229
7.3.2.2	STM Functioning	230
7.3.2.3	STM Preliminary Trial	231
7.3.2.4	STM Limitations	234
7.4	Experimental Methods	236
7.4.1	Skirt Stiffness	236
7.4.2	Durability	237
7.4.2.1	Shuttlecock Preparation- VWID	237
7.4.2.2	Shuttlecock Preparation- STM	237
7.4.2.3	Flight Evaluation	238
7.5	Results and Discussion	240
7.5.1	Skirt Stiffness	240
7.5.2	VWID Prepared Specimen	245

7.5.3	STM Prepared Specimen	247
7.5.4	Flight Evaluation	252
7.5.4.1	Launch Conditions	252
7.5.4.2	Trajectory	253
7.5.4.3	Spin	256
7.6	Summary	260
8.	SHUTTLECOCK DEVELOPMENT PROCESS	261
8.1	Overview	261
8.2	Design Objectives	262
8.3	Conceptual Design	263
8.4	Preliminary Concept Exploration	264
8.5	Concept Selection	266
8.6	Concept Development- Design	267
8.6.1	Feasibility Analysis	268
8.6.2	Physical Properties Simulation	269
8.6.3	Flow Design	270
8.7	Concept Development- Testing	271
8.8	Advantages	272
8.9	Limitations	273
8.10	Summary	274
9.	CONCLUSION AND RECOMMENDATIONS FOR FUTURE WORK	275
9.1	Conclusion	275

9.1.1	Shuttlecock Evaluation Framework	276
9.1.2	Flight Modelling	278
9.1.3	Rapid Design iteration	278
9.2	Future Work	279
9.2.1	Improvement to Motion Capture	279
9.2.2	Perception studies	279
9.2.3	Spin Effect on Skirt Deformation	280
9.2.4	Racket-Shuttlecock Impact Mechanism	281
9.2.5	Extension to Shuttlecock Development Process	281
9.3	Publications	282
9.3.1	Journal Papers	282
9.3.2	Conference Papers	283
	REFERENCES	285
	Appendix A	301
	Translation	301
	Rotation	302
	Flight Path Frame	303
	Appendix B	304
	Experimental Setup	304
	Results	307
	Range and Velocity	312

Spin Rate	315
Shuttlecock Damage	319
Appendix C	322
Appendix D	324
Appendix E	325
Calibrating for Lens Radial Distortion	325
Applied Error (Planar)	334
Appendix F	337
Appendix G	338
Appendix H	345

## List of Tables

Table 1 Permissible dimensions for badminton shuttlecock based on BWF standards. .....	10
Table 2 Patents that reinvent badminton and the shuttlecock. ....	16
Table 3 Patents that improve on the current shuttlecocks. ....	21
Table 4 BWF standard for shuttlecock testing [38]. ....	36
Table 5 Gap size and area of gaps for the profiles. ....	44
Table 6 Grid independency study for optimum number of "volumes" required. ....	47
Table 7 Tabulated experimental and numerical drag coefficients for Profile A, Profile C, and Profile E, at 15 m/s, 30 m/s and 50 m/s. ....	63
Table 8 Contribution of pressure drag to the overall drag for Profile A to Profile F, at speed of 6 m/s, 15 m/s, 30 m/s and 50 m/s. ....	65
Table 9 Tabulated summary of the experimental result presented in Appendix B.	104
Table 10 Position coordinates of the cameras used. ....	114
Table 11 Initial guess of parameters in identification process. ....	118
Table 12 Values of the identified parameters, where $C_d$ and $C_\theta$ are of reasonable value, but $dC_{ld\alpha}$ and $dC_{md\alpha}$ do not make physical sense. ....	120
Table 13 Gyroscopic effect predicted motion and the observed output motion. ....	120
Table 14 Identified values for the aerodynamic parameters, showing good order of magnitude. ....	124
Table 15 Shuttlecocks used for the wind tunnel evaluation. ....	137
Table 16 Summary of the mass recorded for the shuttlecocks. ....	144
Table 17 Mean diameter and chord length of the shuttlecocks. ....	146
Table 18 Moments of inertia obtained for the shuttlecocks. ....	148

Table 19 Mass of the shuttlecock specimens. ....	156
Table 20 Recorded racket tip speed in a smash. ....	161
Table 21 Details of the camera positions and settings. ....	163
Table 22 Range and height of simulated trajectories with varying launch conditions. .....	168
Table 23 Shuttlecocks used in the turnover test. ....	173
Table 24 Types of shuttlecocks tested for referential and benchmarking. ....	175
Table 25 Camera position in the shuttlecock evaluation setup. ....	176
Table 26 Identified parameters for the turnover process of the shuttlecocks. ....	180
Table 27 Initial launch velocities and velocity ratios of the accepted runs. ....	188
Table 28 Stall velocities observed for all the tested shuttlecocks. ....	206
Table 29 Measurements of the skirt diameters when the shuttlecocks were new, after 5 smashes and after 10 smashes. Test was discontinued for the Ashaway after just 2 smashes because the skirt collapsed into an ellipsoid. ....	232
Table 30 Changes in the camera positions, where the new positions are bolded in the table. ....	239
Table 31 Smash speeds recorded for the tested shuttlecocks during the STM treatment. The boxes highlighted in red are smash attempts where part of the shuttlecock contacted the racket frame. ....	247
Table 32 The initial launch flight conditions of the shuttlecocks. ....	253
Table 33 The Pugh Matrix used for preliminary shuttlecock concept development. .....	267
Table 34 Sample virtual prototyping specification iteration table. ....	268

## List of Figures

Figure 1 Integration of existing experiments with novel test experiments to form the integrated shuttlecock test methodology. ....	5
Figure 2 A traditional feather shuttlecock [32]. ....	10
Figure 3 (L-R) Shuttlecock model fabricated by additive manufacturing, Mizuno NS-5 synthetic shuttlecock, regular synthetic shuttlecock and traditional feather shuttlecock. ....	11
Figure 4 Mizuno NS-5 artificial feather shuttlecock. ....	12
Figure 5 Profile difference between designs. On the left is a conventional cone and cork design, while on the right is the general design profile connecting the skirt and cork with a shaft. ....	14
Figure 6 Various types of Speedminton speeders compared against the feather shuttlecock. (L-R: Match speeder, night speeder, fun speeder, feather shuttlecock)	14
Figure 7 Feather shaft cross-sectional profile for different designs of replaceable feather shuttlecock. The design by Chen et al. [48] and Dai [49] follows closely to the traditional profile of a shuttlecock feather, while the design of Lee [50] employs a more circular shaft. ....	17
Figure 8 Li-Ning Phoenix replaceable feather shuttlecock. ....	17
Figure 9 Drag coefficients obtained by numerical and experimental method, as published in [70]. All data under the label of “present” are numerical results. All others are experimental results. ....	23
Figure 10 Change in drag coefficient with speed (Reynold's number) as tested for different soccer ball by Passmore et al. [72]. ....	24

Figure 11 Particle image velocimetry flow field vector obtained by Hasegawa et al. [31] showing the rotation and flow reversal in the near field wake of the skirt.....	27
Figure 12 Experimental result for synthetic shuttlecocks [30]. .....	30
Figure 13 Experimental result for feather shuttlecocks [30].....	31
Figure 14 Shrink ratio- skirt deformation as observed by Kitta et. al. The filled and open symbols denote shuttlecocks with and without gap, respectively [32]. .....	40
Figure 15 Dimensions of the cone geometry used in simulation and physical modelling. All dimensions in mm. ....	44
Figure 16 Thin-walled profile cones with and without gaps, manufactured with Objet printing. ....	45
Figure 17 Fluid domain and placement of profile model in ANSYS CFX.....	46
Figure 18 Calculated $Y^+$ for the applied mesh in profile A at flow speed of 6 m/s. ....	48
Figure 19 The Seed Studio 500 g load cell used for the wind tunnel experiment... ..	49
Figure 20 The experimental setup for wind tunnel measurement with the additive manufactured cone profile.....	49
Figure 21 Comparison of numerical and experimental drag coefficients. ....	50
Figure 22 Flow field velocity vector plot around Profile A, the gapless cone skirt. Freestream velocity is 6 m/s.....	51
Figure 23 Gapless cone of Profile A with the tubing attachment points for inner pressure measurement in the wind tunnel. ....	53
Figure 24 Outer surface pressure coefficient along the Profile A. Chord locations on plot are true to the superimposed cone model.....	54
Figure 25 Inner surface pressure coefficient along Profile A. Chord locations on plot are true to the superimposed cone model. ....	55

Figure 26 Coefficient of pressure for Profile A at 50m/s and 6 m/s. ....	56
Figure 27 Coefficient of pressure plot for Profile B to D at free stream velocity of 6 m/s and 50 m/s.....	58
Figure 28 Coefficient of pressure plot for Profile E and D at free stream velocity of 6 m/s and 50 m/s.....	59
Figure 29 Change in drag force with increasing gap size at free stream speed of 50 m/s. The larger % surface area reduction will refer to bigger gaps. ....	60
Figure 30 Drag coefficients for the different sized gap profiles. ....	62
Figure 31 Velocity plots of air bleeding through the gaps show increased air flow into the skirt as the gap size increases.....	66
Figure 32 Region of the flow wake that is compared in Figure 33.....	67
Figure 33 Velocity vector plot of wake behind the cone for Profile A to F. It is seen that intensity of the recirculating vortices reduces with larger gaps. Beyond the critical gap size, vortices are no longer present. ....	68
Figure 34 Coefficient of pressure plot with respect to chord length for Profile E. The symbols R1 to R3 refer to region 1 to 3, while the dotted lines refer to the locations along the chord for the cut planes. ....	69
Figure 35 Pressure plot of the plane at 28.3 mm, with the clip plane set at 29.2 mm. This is a segment from R2.....	70
Figure 36 Pressure plot on plane at 34.3 mm behind the cork, where the pressure peak occur. The clip plane is at 35.1 mm.....	71
Figure 37 Velocity vector plot around Profile E at 6 m/s. This plot shows the high speed stream that was deflected by the cork hitting on the stems of the skirt, causing the high pressure peak. ....	72

Figure 38 Pressure plot of the plane at 57.3 mm, near the end of the gaps. Clip plane was set to 57.5 mm. Increased pressure is seen around the skirt forming a ring of higher pressure region. ....	73
Figure 39 Pressure contour at plane 59.8 mm behind the cork, where the gaps end on the skirt. The termination of the gaps creates a high pressure region around the skirt. ....	74
Figure 40 Illustration of shuttlecock heading with respect to flight path in the unsteady state flight.....	77
Figure 41 Illustration of pre-stall and post-stall regime of steady flight state. ....	78
Figure 42 Reference frames and direction of axes as used in this report. ....	80
Figure 43 Shuttlecock flight with angle of attack and side slip will have an additional flight path axis.....	83
Figure 44 Axis system showing the angle of attack, $\alpha$ , between the flight path axis and body axis.....	83
Figure 45 Control volume of area and length as given. ....	88
Figure 46 Free body diagram of torque equilibrium. ....	89
Figure 47 Turnover behaviour of a badminton shuttlecock [64]. ....	93
Figure 48 Effect of C.G. location with respect to C.P. on stability.....	94
Figure 49 The unstable prototype which had a rearward C.G. ....	95
Figure 50 The unstable turnover process where the shuttlecock flips continuously. ....	95
Figure 51 A stable turnover where heading is corrected.....	95
Figure 52 Angular response of a stable feather shuttlecock (Li-Ning A+600) as compared with an unstable prototype.....	96
Figure 53 Experimental setup for the preliminary trial in capturing of spin rate....	102

Figure 54 The markings drawn on the shuttlecock for determining spin rate in post-experiment video processing. ....	102
Figure 55 Heading change of shuttlecock in free-fall, without spin (left) and with spin (right). ....	108
Figure 56 Distance travelled and heading change with time for the spinning and non-spinning shuttlecock. ....	110
Figure 57 Illustration of the camera setup for the experimental observation of the shuttlecock precession. ....	113
Figure 58 Simulated and experimental result for the trajectory beyond vertex. ....	119
Figure 59 Experimental and simulated flight behaviour using the equations in (59) and (60). ....	123
Figure 60 The developed badminton shuttlecock evaluation framework. ....	130
Figure 61 Different aggressiveness of fold features (flutes) along the shuttlecock skirt. The flutes on the model on the right are more aggressive. ....	133
Figure 62 Using the standard diameter for estimation, both models in this figure will have the same characteristic area. This is misleading. ....	134
Figure 63 The chord length of the shuttlecock refers to the height starting from the tip of the cork to the end of the skirt. ....	135
Figure 64 Modified Vernier caliper for chord length measurement. ....	139
Figure 65 Trifilar swing experiment for determining the $I_{xx}$ . ....	139
Figure 66 Bifilar swing setup for measurement of $I_{yy}$ and $I_{zz}$ . ....	140
Figure 67 Wind tunnel mounting set up for working with badminton shuttlecock. ....	141
Figure 68 The shuttlecock mounting fixture for free rotation. ....	142
Figure 69 The shrinkage ratio is the ratio of $D/D_i$ . ....	143

Figure 70 Plot of $C_dS$ with respect to the air speed for all six tested shuttlecocks.	150
Figure 71 Axial spin rates of the six tested shuttlecocks. ....	152
Figure 72 Plot of the shrinkage ratio and air speed.....	153
Figure 73 $C_dS/m$ plot for the tested shuttlecocks. ....	156
Figure 74 Motion tracking markers on the badminton racket. ....	160
Figure 75 Shuttlecock- string bed impact location that is defined as acceptable for this study. ....	164
Figure 76 Impact locations and launch velocities for Babolat Tournament (77) within the predefined box.....	165
Figure 77 Impact locations and launch velocities for Wilson Club (77) within the predefined box.....	165
Figure 78 Trajectories obtained for the 12 Babolat shuttlecocks.....	166
Figure 79 Trajectories obtained for the 12 Wilson feather shuttlecocks.....	166
Figure 80 Experimental setup for trajectory capture of the shuttlecocks.....	176
Figure 81 Experimental setup for trajectory capture showing the placement of the cameras and the trajectory.....	176
Figure 82 Turnover behaviour observed from one of the runs of the Li-Ning A600 shuttlecock.....	182
Figure 83 Turnover behaviour observed from one of the runs of the Yonex Mavis 350 shuttlecock.....	182
Figure 84 Angular response of runs presented in Figure 82 and Figure 83. ....	183
Figure 85 Experimental and simulated turnover responses of the A600. ....	184
Figure 86 Experimental and simulated turnover responses of Mavis 350. ....	185
Figure 87 Simulated responses using the averaged parameters from Table 24. ....	186

Figure 88 Experimental trajectories observed for the various shuttlecocks.....	190
Figure 89 Trajectories observed for the synthetic nylon shuttlecocks as compared to the reference feather shuttlecock (AS40 (2)). .....	194
Figure 90 Difference in trajectory height observed at camera 1. ....	195
Figure 91 Trajectory plot for the NS-5 artificial feather shuttle against the AS40 tournament-grade feather shuttlecocks.....	197
Figure 92 Comparison of velocity profile for the Li-Ning X800 (Green) and Yonex AS40 (2) shows negligible difference. ....	198
Figure 93 Spin rate profile for the Yonex AS40, Li-Ning Grandprix Gold, and Wilson Club feather shuttlecock. ....	200
Figure 94 Compiled spin-time data for the synthetic shuttlecocks. ....	202
Figure 95 Comparing the X800 (Green) and AS40 (2) spin-time profile showed significant differences between the feather and synthetic shuttlecocks. ....	203
Figure 96 Spin rates of the GP Gold feather shuttlecock and the X800 synthetic shuttlecock.....	204
Figure 97 Only translation was required to fit the post-stall trajectory of the Mavis 2000 to that of the AS40. ....	207
Figure 98 Components of the SSCT. ....	213
Figure 99 Calibrated load cell system chart. ....	215
Figure 100 Mechanical motion of the sliding platen on the SSCT. ....	216
Figure 101 Displacement-Compression force plot for the trial compression test...	217
Figure 102 Surface roughness from the grain of FDM process. ....	218
Figure 103 Displacement-force curves for the specimens tested with and without the acrylic plate on the platen.....	218

Figure 104 (L) Feather vane wear from usage. ....	220
Figure 105 (R) Feather shaft breakage from usage. ....	220
Figure 106 Top view of the VWID, showing the three servos and the shuttlecock being tested.....	223
Figure 107 The direction of motion for the compression platen.....	223
Figure 108 The spin direction of the shuttlecock with respect to the motion of the platen. ....	224
Figure 109 Feather vane wear after vane wear induction on Babolat Tour (Tournament-grade) and Carlton Club (Practice-grade). ....	226
Figure 110 Deformation of the skirt under smash impact from the racket. ....	229
Figure 111 The extended badminton racket for attaining the desired smash speed.	230
Figure 112 High-speed chronographs of the smash deformation process using the STM.....	231
Figure 113 Visual condition of the shuttlecock skirts before (New) and after the STM treatment (Damaged).....	233
Figure 114 Experimental set up for the post-wear performance evaluation of the shuttlecock specimens. ....	239
Figure 115 Compressive force-displacement plot of Babolat Tour (77). ....	240
Figure 116 Compressive force-displacement plot of Yonex AS40 (2). ....	240
Figure 117 Compressive force-displacement plot of Yonex AS40 (3). ....	241
Figure 118 Compressive force-displacement plot of Yonex Mavis 350.....	241
Figure 119 Compressive force-displacement plot of Li-Ning X800 (Blue). ....	241
Figure 120 Compressive force-displacement plot of Li-Ning X800 (Green). ....	242
Figure 121 Compressive force-displacement plot of Ashaway Practice.....	242

Figure 122 Compressive force-displacement plot of Carlton Club.....	242
Figure 123 Change in skirt stiffness with compressive displacement of the tournament-grade AS40 feather shuttlecock and the X800 synthetic shuttlecock..	244
Figure 124 Change in skirt stiffness with compressive displacement of the top-grade AS40 feather shuttlecock and the practice-grade feather shuttlecock.....	245
Figure 125 The feather vane condition of the shuttlecock specimens at each interval of the VWID treatment process.....	246
Figure 126 Diameter measurements for the Ashaway Practice feather shuttlecock. ....	249
Figure 127 Diameter measurements for the A62XD feather shuttlecock. ....	249
Figure 128 Diameter measurements for the Yonex AS40 feather shuttlecock. ....	249
Figure 129 Diameter measurements for the Yonex Mavis 350 synthetic shuttlecock. ....	250
Figure 130 Visual condition of the shuttlecock specimens before and after the smash attempts. ....	251
Figure 131 Feather vane condition of the Yonex AS40 (left) and Li-Ning A62XD (right) after 15 smashes. ....	252
Figure 132 Trajectories of the Babolat and Li-Ning Grandprix Gold shuttlecocks before and after the VWID treatment.....	254
Figure 133 Trajectories observed for the three feather shuttlecocks before and after STM.....	255
Figure 134 Trajectories observed for the Yonex Mavis 350 shuttlecock before and after STM. ....	255

Figure 135 Spin rate of the feather shuttlecocks before and after the VWID process. .....	257
Figure 136 Comparison of the spin rates of the feather shuttlecocks before and after the smash test. ....	258
Figure 137 Spin rate profiles of the Yonex Mavis 350 synthetic shuttlecock .....	259
Figure 138 Conceptualisation process model applied for shuttlecock development. .....	261
Figure 139 The developed shuttlecock development process model that involves design and testing. ....	262
Figure 140 Key considerations (qualitative) translated to target project specifications (quantitative). ....	263
Figure 141 Work process of preliminary concept exploration.....	265
Figure 143 Additive manufactured shuttlecock prototype in the wind tunnel for design validation [125].....	271

## List of Symbols

$[F]$	Force matrix
$[I]$	Inertia tensor
$[R]$	Transformation matrix
$A_{cv}$	Projected area of control volume
$C$	Chord length
$C_d$	Drag coefficient
$C_L$	Lift coefficient
$C_M$	Pitch moment coefficient
$C_{M_z}$	Yaw moment coefficient
$C_{mag}$	Magnus force coefficient
$C_p$	Coefficient of pressure
$C_Q$	Spin torque coefficient
$C_S$	Side force coefficient
$C_T$	Torque coefficient
$C_\theta$	Pitch damping coefficient
$c$	Damping factor
$D$	Drag
$d$	diameter
$F_{gravity}$	Gravitational force (earth frame)
$F_x$	Force in x axis (earth frame)
$F_y$	Force in y axis (earth frame)
$F_z$	Force in z axis (earth frame)
$G$	Gravitational acceleration
$H$	Gap height
$I_{xx}$	Moment of inertia about roll
$I_{yy}$	Moment of inertia about pitch
$I_{zz}$	Moment of inertia about yaw
$k$	Spring constant
$L$	Lift

$l$	Control volume length
$M$	Moment
$M_{racket}$	Moment from racket
$M_x$	Moment in $x$ axis
$M_y$	Moment in $y$ axis
$M_z$	Moment in $z$ axis
$m$	Mass
$P$	Pressure
$p$	Roll rate (body frame)
$\dot{p}$	Roll acceleration (body frame)
$Q$	Spin torque
$q$	Pitch rate (body frame)
$\dot{q}$	Pitch acceleration (body frame)
$Re$	Reynolds number
$r$	Yaw rate (body frame)
$\dot{r}$	Yaw acceleration (body frame)
$S$	Reference area
$SF$	Side force
$T$	Resistive spin torque
$t$	Time
$V$	Overall air speed
$v_t$	Terminal velocity
$v_t'$	Acceleration of terminal velocity
$v_{xi}$	Initial velocity in $x$
$v_{yi}$	Initial velocity in $y$
$v_\infty$	Free stream velocity
$X$	Gap width
$x$	$x$ direction displacement (earth frame)
$\dot{x}$	$x$ direction velocity (earth frame)
$\ddot{x}$	$x$ direction acceleration (earth frame)
$x_b$	$x$ direction displacement (body frame)

$\dot{x}_b$	x direction velocity (body frame)
$Y_+$	Y_plus
$y$	y direction displacement (earth frame)
$\dot{y}$	y direction velocity (earth frame)
$\ddot{y}$	y direction acceleration (earth frame)
$y_b$	y direction displacement (body frame)
$\dot{y}_b$	y direction velocity (body frame)
$z$	z direction displacement (earth frame)
$\dot{z}$	z direction velocity (earth frame)
$\ddot{z}$	z direction acceleration (earth frame)
$z_b$	z direction displacement (body frame)
$\dot{z}_b$	z direction velocity (body frame)
$\alpha$	Pitch angle of attack
$\beta$	Side slip angle
$\omega_n$	Natural frequency
$\emptyset$	Pitch angle (earth frame)
$\dot{\emptyset}$	Pitch angular velocity (earth frame)
$\rho$	Air density
$\psi$	Yaw angle (earth frame)
$\dot{\psi}$	Yaw angular velocity (earth frame)
$\theta$	Roll angle (earth frame)
$\dot{\theta}$	Roll angular velocity (earth frame)
$\zeta$	Damping ratio

## List of Abbreviations

Aft	Behind of
BWF	Badminton World Federation
C.G.	Centre of gravity
C.P.	Centre of pressure
CAD	Computer aided design
CFD	Computational fluid dynamics
CNT	Carbon nanotube
DOF	Degree of freedom
FIFA	Fédération Internationale de Football Association
FPS	Frames per second
K.E.	Kinetic energy
LES	Large eddy simulation
N.A.	Not available
RANS	Reynolds-averaged Navier-Stokes
Re	Reynolds number
URANS	Unsteady Rans
SBA	Singapore badminton association
SSCT	Shuttlecock skirt compression tester
SST	Shear stress transport
STM	Smash test machine
VWID	Vane wear induction device
Y <sub>plus</sub> (Y <sub>+</sub> )	Dimensionless wall distance

## **Abstract**

Traditionally, a badminton shuttlecock is made with waterfowl feathers which are susceptible to supply inconsistency. This makes the synthetic shuttlecock an attractive alternative to the feather shuttlecocks. Despite good availability, the synthetic shuttlecocks remain unpopular because of criticism in performance. Current understanding of differences between feather shuttlecocks and the synthetic ones is limited. The lack of thorough testing method also means that the differences cannot be evaluated comprehensively. These impede the progress in shuttlecock development. The objective of this research is to develop a badminton shuttlecock testing framework for investigating and understanding the flight performance.

The badminton shuttlecock was first investigated through numerical method that was validated with experimental results. Through study of cone models with openings (gaps) of various sizes, the high drag flight characteristic was explained through analysis of surface pressure and wake. The critical gap size—beyond which diminishes the blunt body effect and drag—shows that there is more than one design point for a performance target.

The flight motion of a shuttlecock was explained by derivation of a system of equations. The axial spin, turnover and spin-induced yaw are three important flight behaviours that were modelled along with experimental data. The properties that should be identified for effective comparison of shuttlecocks were also identified from the model. Consequently, a three phase shuttlecock evaluation framework was developed. This system of tests aims to investigate the differences between the shuttlecocks while providing a reference value of good performance.

In phase I, the static tests consisted of measurements of the physical properties and also wind tunnel experiment. Methods of measurement were developed and demonstrated. Misrepresentations in the usage of grain weight, characteristic area and drag coefficient as comparison tool were discussed. The wind tunnel experiment showed the tested synthetic shuttlecocks to have more drag per unit mass than the feather shuttlecocks. The one piece construction of the synthetic skirt also better resisted the skirt expansion at high flow-high spin conditions.

The second phase of the testing framework consisted of flight testing where a unique experimental rig was developed. The experimental data and modelling showed the tested feather shuttlecocks having superior turnover performance. It also demonstrated the insufficiency of previous approaches in comparing turnover. The flight trajectories of 14 shuttlecock types were compared. Regardless of grade, the feather shuttlecocks had the same trajectory. However, the higher drag of the synthetics resulted in shorter flight range. Despite similar linear velocity profiles among the shuttlecocks, the axial spin rates differed. Analysing the spin rates and stall velocities showed the tested synthetic shuttlecocks and feather shuttlecocks to have the same post-stall trajectories.

Finally, destructive testing was performed in Phase III to evaluate the durability of the shuttlecocks. A skirt compression machine, shuttlecock smash tester and feather vane wear machine were developed for testing. These original approaches to durability investigated the strength of the feather shaft and the degradation on the feather vane. Flight testing was subsequently conducted and the results differentiated the top tier feather shuttlecocks from the practise-grade ones.

The major contribution of this research is the development of a comprehensive shuttlecock testing framework to provide knowledge on shuttlecock performance. It also offers an evaluation platform for future shuttlecock development.

# **1. INTRODUCTION**

## **1.1 Background**

The racket sports market, which was stagnant for a decade, saw a boom in demand since 2008. According to Datamonitor [1-4], the racket sports equipment accounted for almost 14% of the whole Asia sports industry in 2011, doubling from data recorded for 2002-2007. This was largely fuelled by the success of Asian teams in the racket sports arena at the 2008 Beijing Olympics. Badminton, being one of the prominent racket sports of Asia, also saw unprecedented growth. Boom in the popularity of badminton in Asia has even become a topic for research, such as the work in [5-11].

However, the popularity of badminton also brings about an ever worsening problem- Scarcity of good quality feather for the manufacturing of badminton shuttlecock. Shortage of quality feather has been an issue for the past decade [12-16] and will continue to be an issue in the years to come. This is because the supply of feather is influenced by many external factors, such as water fowl diseases (especially seasonal bird flu), politically biased import-export restrictions and even the usage of growth hormones at poultry farms. This means that the development of a feather-replacing, synthetic shuttlecock is becoming ever more attractive for manufacturers.

Synthetic shuttlecocks have been around for ages. Carlton Sports, a UK based company has been developing synthetic shuttlecocks for more than half a century. In fact, Mr. W.C. Carlton himself filed a patent [17] on nylon synthetic shuttlecocks from as early as 1963. Through the years, there have been claims of synthetic

shuttlecocks taking over feathered ones in near future, but usage and sales of synthetic shuttlecocks remained lacklustre. In an article published in 1994 by Cooke and Mullins [18], manufacturers claimed that, “Within 18 months, a new generation of shuttlecocks with carbon fiber feathers could transform players’ attitudes”. Yet, almost 2 decades later, synthetic badminton shuttlecocks have not caught on, in both performance and popularity.

Most players have two main gripes over synthetic shuttlecocks. Firstly, synthetic shuttlecocks do not give the same tactile feedback to the players during the racket-shuttlecock contact. More importantly, there is significant difference in flight path between synthetic and feather shuttlecocks. Synthetic shuttlecocks are usually thought to fly further than a feather shuttlecock without the near vertical post-stall free-fall behaviour that is expected of a shuttlecock [19]. Alam et al. [20] attributed this phenomenon to the unique property observed only on feather shuttlecocks- low drag coefficient at low speed; high drag coefficient at high speed. However, there have also been contradicting reports of synthetics being slower (and fly less far) than a feather shuttlecock, such as the claim by famous shuttlecock engineer, Gordon Willis [21].

In an attempt to understand the fundamental differences between the feather shuttlecocks and the synthetics, comparative analysis on flight performance and parameters were carried out in various publications. Cooke [18, 22-27], who worked closely with the Carlton Sports in the 1990s, is one pioneer of such work. While her work presented significant shuttlecock knowledge that is still being cited today, the results obtained were for shuttlecocks from two decades ago. Since then, many

improvements have been made to the synthetic shuttlecocks, but their effects remain unknown. Moreover, advancements in technology have brought about new experimental tools that were not available at the time of her work. These include computational fluid dynamics (CFD), high resolution digital high-speed cameras, and improved wind tunnel instrumentation. Following the work of Cooke [18, 22-27], there have been many publications on shuttlecocks. These include the work by a research group at the Royal Melbourne Institute of Technology (RMIT) [19, 20, 28-30], very interesting flow analysis and visualisation by a group of Japanese researchers [31-33], Cohen et al. [34, 35] who worked on sports projectile, and also a group from the Singapore National Institute of Education (NIE) [36, 37] who studied the trajectory. However, most works were limited to simulations or wind tunnel testing with few significant findings beyond that of Cooke [18, 22-27]. Moreover, the scopes of the experiments in those literatures were not comprehensive because each was only focused on a small section of the shuttlecock. To fully evaluate the shuttlecock performance and provide knowledge that can benefit development of a feather replacing synthetic shuttlecock, a more thorough and comprehensive evaluation methodology is required.

## **1.2 Motivation**

As discussed, the literatures reviewed show that many of the work on shuttlecock experimentations are only focused on one or two particular part of the shuttlecock performance parameter. This means that it is impossible to fully evaluate and understand the badminton shuttlecock through these works, especially when different shuttlecocks were tested in each article. There remains a lot more work that can be done to contribute to the understanding of badminton shuttlecocks, in both

development and testing. To date, there exists no modern standard test methodology in the open literature for effective comparison of shuttlecocks. Original equipment manufacturers have their own test standards, but such are typically confidential. Through interaction with some sports brand, it was observed that testing done in the industry is very much perception based. Shuttlecock testing based on the Badminton World Federation (BWF) equipment approval scheme is also perception-driven, making it difficult for scientific comparison of shuttles. Moreover, the testing by BWF is also confidential.

The lack of a shuttlecock evaluation methodology suggests a real need to establish an integrated evaluation framework. It is thought that the knowledge that can be gained from comparing the various types of shuttlecocks will enhance understanding in this field. Moreover, a well-defined test methodology can ensure consistency in result and sensitivity to differences when evaluating a shuttlecock against the other shuttlecocks. The approach integrates applicable existing experimental work with non-existing but required test segments to form a novel and significant evaluation framework. This proposed approach is presented in Figure 1. This will aid future shuttlecock development, especially for synthetic shuttlecocks.

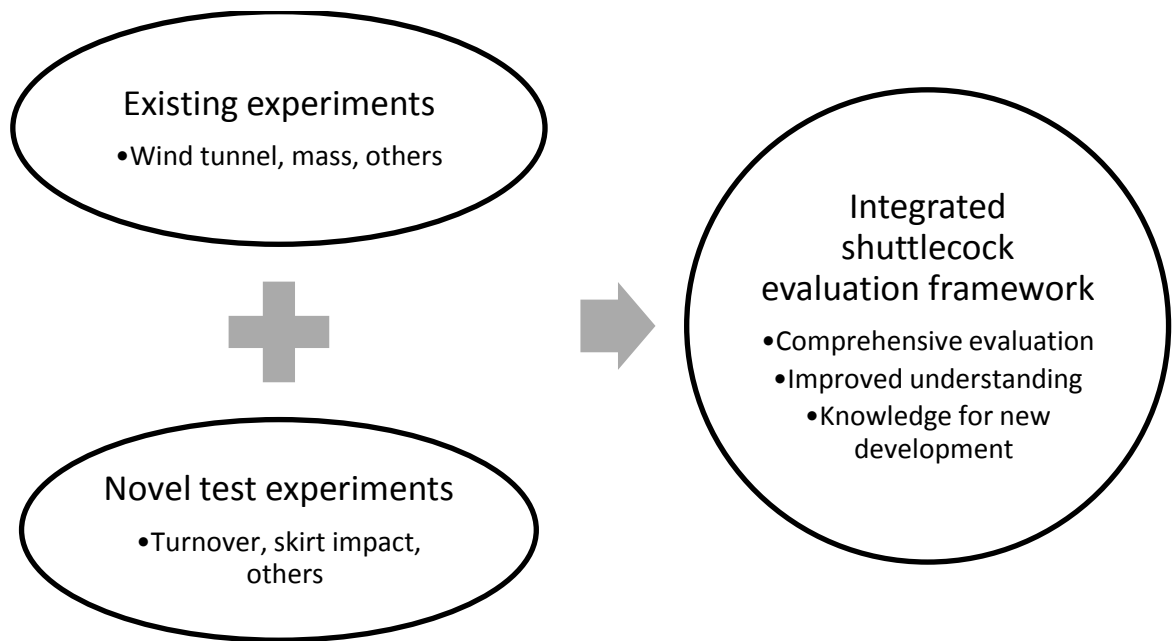


Figure 1 Integration of existing experiments with novel test experiments to form the integrated shuttlecock test methodology.

Unlike wind tunnel measurements and 2-dimensional flight trajectory simulations which have been well documented in literatures, transient flight performance (such as turnover and stability) and mechanical measurements are seldom discussed. By applying techniques made possible with technological advancement, performance variables that were previously difficult to study can be investigated. This includes in-situ spin observation, skirt stiffness and deformation, and turnover performance. New techniques will also be updated in some of the existing tests.

In addition to the advantage of serving as a consistent and comparable test for current and future shuttlecocks, this integrated evaluation framework will also help to recognise a reference baseline from tournament-grade shuttlecocks. This reference can then serve as target parameters for development of shuttlecocks.

Lastly, this need for extensive study in testing and development of shuttlecocks was also fuelled by the industry funded shuttlecock development projects at the Institute

for Sports Research. At the time of writing, the experimental work and the knowledge derived have benefited two projects- one with a world renowned sports brand and the other with the BWF.

### **1.3 Objectives**

The eventual objective is to derive an integrated shuttlecock evaluation framework to aid future shuttlecock developmental work. This framework will increase understanding of current shuttlecocks, identify a reference performance target desired for a good shuttlecock and provide a platform for evaluation of current and future shuttlecocks. More precisely, the objectives of this project are:

- (1) To develop an integrated evaluation framework for effective comparison of shuttlecock performance. The methodology will be built upon an array of critical measurements that includes mechanical and flight properties. Testing with practise-grade and tournament-grade shuttlecocks, their difference will be identified. The desired parameters of a good feather shuttlecock can then be collected.
- (2) To model the 3-dimensional, six degree of freedom flight (6 DOF) behaviour of the badminton shuttlecock. This will aid understanding and prediction of shuttlecock flight phenomena that cannot be accounted for by using the commonly available 2-dimensional models. In addition, the model will help to identify parameters that should be evaluated in experiments.
- (3) To provide a rapid design iteration framework for development of the next generation shuttlecock. This virtual prototyping process, which focuses on

design, will complement the integrated evaluation framework that focuses on physical testing.

#### **1.4 Scope**

The scope of this research is as follows:

- (1) To study the effect of gaps through flow simulation and experimental validation. The presence of the gaps on the shuttlecock skirt is the dominant drag inducing feature. Thus, the gaps should be studied for fundamental understanding of the most critical flight parameter: drag.
- (2) Modelling the badminton shuttlecock flight in a 6 DOF multiple frames of reference system of equation for better understanding of the flight performance.
- (3) To identify relevant existing test measurements.
- (4) To identify, plan and conduct test measurements that should be conducted but do not currently exist in literatures.
- (5) Integration of the existing test methods and the developed methodologies to form an integrated evaluation framework.
- (6) Investigate the differences between the current feather shuttlecocks and the synthetics, while determining a reference point from the feather shuttlecocks.
- (7) Establish a rapid design iteration process using virtual prototyping and rapid prototyping.

This research will cover experimental investigation of shuttlecock flight dynamics, focusing on quantifiable engineering parameters that produce the flight characteristic. Perception-based shuttlecock evaluation will not be covered. This is

because the focus of this thesis is on the measurable engineering parameters of the shuttlecock.

### **1.5 Organisation of Thesis**

This report consists of 9 chapters.

Chapter 1 introduces the background of research on badminton shuttlecock and the motivations for this research. The objectives and scope are then listed.

Chapter 2 reviews the literatures of previous research efforts on shuttlecocks. The chapter starts with definition of a badminton shuttlecock, followed by innovations and developments of the shuttlecock. Publications on the shuttlecock and their evaluation methods are then reviewed, focusing on the existing aerodynamics, flight and spin experiments. Possible areas of research are then identified.

Chapter 3 investigates the aerodynamics of a shuttlecock, focusing on the effect of the drag inducing gaps along the shuttlecock skirt. Flow simulation is conducted for a gapless cone, with the results validated against experimental data. This not only shows the correctness of the result, but also validates the numerical method. Numerical data is then obtained for various other cone and cork models with different gap sizes. Comparison of results shows the effect of the gaps on the pressure distribution and drag.

Chapter 4 develops the flight model of a shuttlecock in 3-dimensional space using multiple frames of reference. Through this model, the various behaviours and phenomena associated with a badminton shuttlecock can be explained using the fundamental performance variables. This means that the important physical

(mechanical) parameters and flight performance indicators can be identified. It helps to establish the specification of the integrated evaluation framework. The phenomena that are predicted by theory are also validated through experimental data. These include the axial-spin effect, the turnover and the precessional (gyroscopic) effect.

Chapters 5 to 7 cover the experimental work done in the formulation of the test methodology. The various experiments for collecting the important parameters that were identified in chapter 4 are combined in chapters 5 and 6 to form the evaluation framework. Durability is investigated in chapter 7, where degradation is measured with the same evaluation framework after the shuttlecocks have been worn out.

Chapter 8 describes a shuttlecock development framework which is a methodology to translate a set of design objectives into a design that is ready for production process development. The work applies additive manufacturing, virtual prototyping and simple decision tools to explore, select and develop a feasible conceptual design. In addition to reducing the time required for each iteration cycle, the application of computer simulation and additive manufacturing also increases the probability of obtaining a feasible design.

Finally, chapter 9 concludes this research with recommendations for future work. Publications derived from this dissertation are listed.

## 2. LITERATURE REVIEW

### 2.1 Badminton Shuttlecock

A badminton shuttlecock consists of two parts: a cork and the skirt. The cork is a hemispherical dome in front of a short cylinder and the skirt is a cone formed by waterfowl feathers or synthetic polymer. For approval by the Badminton World Federation (BWF), the shuttlecock skirt must be constructed by 16 feathers attached to a cork base [38]. The permissible weight is 4.74-5.50 g. The other permissible dimensions are presented in Table 1. The feather skirt can be replaced by a synthetic netting which does not deviate from the BWF published specifications.

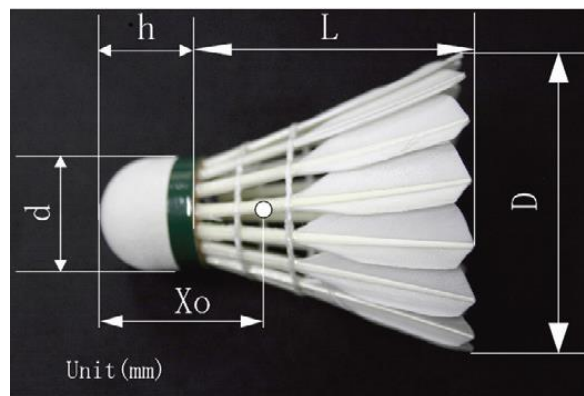


Figure 2 A traditional feather shuttlecock [32].

Table 1 Permissible dimensions for badminton shuttlecock based on BWF standards.

	D /mm	L/mm	d/mm
Permissible dimension	58-68	62-70	25-28

The large dimensional tolerance means that the shuttlecocks designed in accordance with the standard can have totally different flight characteristic [27]. For instance, assuming the same drag coefficient, climate and airflow rate, a 68 mm diameter shuttlecock will have 37% more drag than a 58 mm shuttlecock. Based on the listed

specification in Table 1, it means that these two different shuttlecocks, which have very different flight performance, are both approved for use. However, this does not happen in reality because players are accustomed to the shuttlecock flight behaviour, and thus, have expectation of the flight trajectory. This reference is often built upon the flight path observed on feather shuttlecocks. In the actual flight testing conducted by the BWF (which is confidential and not documented on the public domain), flight distance is a criterion for approval. Interestingly though, the test of trajectory variance, which is the trajectory deviation from top-grade tournament shuttlecocks, is not mandatory for approval.

There are various types of shuttlecocks available on the market, as presented in Figure 3. They range from traditional natural feather ones to sophisticated artificial feather synthetics. Figure 3 also shows an additive manufactured prototype. The loose specification in Table 1 is an invaluable tool in tailoring the performance of a synthetic shuttlecock design to suit the general market preference. For instance, a synthetic shuttle that is too heavy can maintain the same rate of deceleration as the feather shuttles by utilising a larger skirt diameter.



Figure 3 (L-R) Shuttlecock model fabricated by additive manufacturing, Mizuno NS-5 synthetic shuttlecock, regular synthetic shuttlecock and traditional feather shuttlecock.

It is important to note that only shuttlecocks for tournaments are expected to pass the approval scheme by BWF. Badminton shuttlecocks for recreational or practise purpose need not be certified. Therefore, non-tournament-grade shuttlecocks need not obey the specifications. In year 2009, Mizuno introduced the NS-300 shuttlecock which is constructed of artificial feathers in the same arrangement as the traditional feather ones. As opposed to a standard 16 feather shuttlecock, the NS-300 only has 15 feathers. This violates the requirement in the BWF shuttlecock approval scheme. However, it does not affect the usage or sales of the NS-300 because it was never intended to be for tournament purpose. Thus, it does not require approval. In 2011, the NS-5 (Figure 4), which is a revised version that also only has 15 feathers, was launched. Despite similarity in outlook with the natural feather shuttlecocks, their performance (and more importantly, sales and availability) of the NS-5 was lacklustre. The launch of these shuttlecocks started a trend of artificial feather shuttlecocks in the industry, as will be discussed in the next section on patents.



Figure 4 Mizuno NS-5 artificial feather shuttlecock.

## **2.2 Patents and Developments of Shuttlecocks**

Patents on shuttlecocks can be classified into two categories: improving the traditional shuttlecocks or reinventing the shuttlecock. Patents that involve improving the traditional shuttlecocks will focus on development in enhancing the feather shuttlecocks or the synthetics, while adhering to current standards. On the other hand, patents that reinvent the shuttlecock deviate significantly from the current standards, often focusing on the creation of a brand new game or making a game that is playable in conditions that are inappropriate for traditional badminton.

### **2.2.1 Patents Reinventing Badminton and the Shuttlecock**

As described, a traditional badminton shuttlecock takes the shape of a conical skirt behind a hemispherical dome (cork), where the two members are connected directly. A patent from 1948 separates the cork and skirt by adding a shaft between the two [39]. The general profile as compared to a conventional shuttlecock is given in Figure 5. While this design was not adopted in later production synthetic shuttles, it has been adopted in an outdoor shuttlecock design [40] which claims to have superior wind resistance over existing ones. Interestingly, Hart et al. [40] has decoupled the spin production from the drag producing element of the skirt. A short conical skirt behind the shaft produces the drag required, while a propeller enclosed within the short skirt produces the spin. This is very different from the traditional design where both the spin moment (for rifling of the shuttlecock) and the drag force are generated from the same skirt component. Based on the design diagrams, it is likely that such a shuttlecock will require a much heavier cork than a traditional shuttlecock to prevent a rearward centre of gravity which will manifest into instability during turnover.

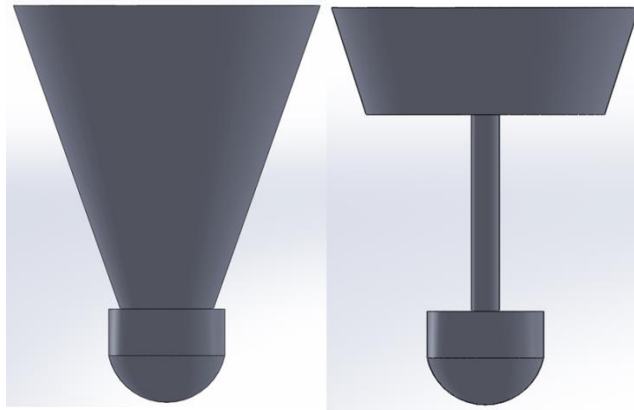


Figure 5 Profile difference between designs. On the left is a conventional cone and cork design, while on the right is the general design profile connecting the skirt and cork with a shaft.

There have also been other attempts at moving the game of badminton to the outdoor. The miniature shuttlecocks patented by Brandes [41, 42] was developed into the game of speedminton (Speed Badminton) [43]. These shuttlecocks, which are known as speeders, measure less than 60 mm in length and are much smaller than a standard shuttlecock. They take the shape of the usual nylon synthetic shuttlecocks and weigh between 7-9 g. A comparison of the various speeders with a feather shuttlecock is presented in Figure 6. To accommodate the increased impact force from the use of the heavier speedminton projectile, squash-like rackets are used in place of the standard badminton rackets.



Figure 6 Various types of Speedminton speeders compared against the feather shuttlecock. (L-R: Match speeder, night speeder, fun speeder, feather shuttlecock)

While the smaller dimensions and increased weight provided a higher weight-to-drag ratio for resisting the effect of environmental wind on flight path stability, it also increased the speed of the game tremendously. This caused it to lose the fundamental low weight-high drag characteristic of a badminton shuttlecock. In addition to outdoor play, the game of speedminton was also adapted for night play with the Night Speeder. This speeder features a translucent cork that accommodates a replaceable glow stick to aid visibility at night. The idea of a glow stick was also designed for regular shuttlecocks by Tsung [44].

Peterson [45] also proposed a non-conventional shuttlecock design. The proposed shuttlecock retains the conventional cork and cone profile, but with a modified cork and a much more aerodynamically porous skirt. To cater to the increased speed, a new set of rules and methods of play was also included. At present, this is not available as a commercial product.

The unique high drag property of a badminton shuttlecock skirt has also been used to slow down the play of balls. Ryu [46] proposed replacing the cork portion with a high density elastomer to allow for single player practise by playing the shuttlecock against a wall, which is very much like a slower game of squash. York [47] proposed attaching the skirt to a bigger ball, such as a baseball, to reduce the ball speed for training.

The patents discussed in this section were tabulated and are shown in Table 2.

Table 2 Patents that reinvent badminton and the shuttlecock.

New shape	USD148732	Umbrella shaped	[39]
	WO2013005044	Inverted Umbrella	[40]
New game	US20110034277	Speedminton speeder (60mm shuttlecock)	[41]
	US20060199683		[40]
	US6709353	Tennis-like badminton	[43]
	WO2013005044	Single player badminton	[44]
	WO2010021497	Speed reducer for balls	[45]
Night play	US20100255939		[42]

### 2.2.2 Patents Improving the Traditional Shuttlecocks

Traditional shuttlecocks can be divided into natural feather shuttlecocks and synthetic shuttlecocks. Most patents related to the natural feather shuttlecocks refer to methods of production, rather than shuttlecock designs. Since the only criticism of feather shuttlecocks is durability, most design improvements focus on improving the useable lifespan. The fundamental failure modes of feather shuttlecocks are wear on the feather vane and breakage of the feather shaft.

For feather shaft damage, a shuttlecock is usually ruined because of damage to one or two feathers, while the remaining feathers are still in playable state. To overcome this issue, different techniques of achieving a replaceable feather shuttlecock have been published by various inventors, including [48-50]. The principle behind these innovations is the same: a moulded plastic base that replaces the string and glue used to hold the feathers into a cone. Therefore, all designs consist of 3 components: the cork, the base holder and the feathers. Details in implementation are what separate the different designs. The designs by Lee [50] and Dai [49] both featured snap-in style insert that plugs the base into the cork. This is similar to the design often seen on synthetic shuttlecocks, such as those by Carlton. On the other hand, Chen et al.

[48] choose to use a threaded screw type connector for assembly of the holder and cork. In addition to using different feather shaft lengths in the base-feather interface, the different designs also applied different cross-sectional profiles (Figure 7) for the feather shafts to achieve the required interference fit. The design by Chen et al. [48] has been commercialised as the Li-Ning Phoenix 1000 shuttlecock and this is shown in Figure 8.

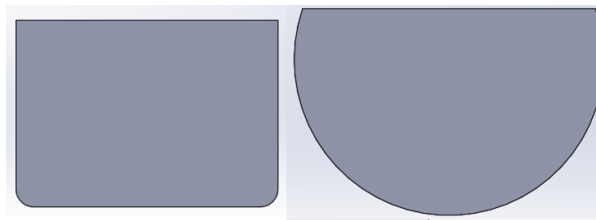


Figure 7 Feather shaft cross-sectional profile for different designs of replaceable feather shuttlecock. The design by Chen et al. [48] and Dai [49] follows closely to the traditional profile of a shuttlecock feather, while the design of Lee [50] employs a more circular shaft.



Figure 8 Li-Ning Phoenix replaceable feather shuttlecock.

Kim [51] attempted to improve the durability of feather shuttlecocks by reducing the number of feathers to between 10 and 14, and changing the angle between the feather and cork base. While this is against the BWF regulation [38] of a shuttlecock being required to have 16 feathers, such an invention can still fulfil the needs of

play outside of tournaments. In fact, the idea of reduced number of feathers was also seen in the early effort of commercialising artificial feather shuttlecocks. Mizuno sold the NS-5 synthetic with 15 artificial feathers. It is likely that reduction in number of feathers was due to weight constraint because of the heavier artificial feathers.

While the Mizuno NS-5 and NS-300 artificial feather shuttlecocks did not replace natural feather shuttlecocks at the badminton courts, it started a trend in development of synthetic shuttlecocks: Artificial feathers. A literature search of patents shows that the idea of an artificial feather shuttlecock is not new. In the 1980's, Larsen [52] had already developed composite feather of thermoplastic and carbon fiber for shuttlecock usage. Usage of polymer resin as artificial feather material has also been applied in [53-55]. In recent years, major sports product brands have also started filing for patents involving artificial feathers for shuttlecocks.

Babolat [56] invented an artificial hybrid feather comprising of a natural feather shaft and an artificial vane. This retains the benefits of the natural feather shafts without the poor durability of natural feather vanes. However, it does not solve the issue of feather supply and cost because natural feathers are still required for the supply of the shafts. Mizuno [57-61] and Yonex [62, 63] have also filed numerous patents on artificial feather shuttlecocks, suggesting the possibility of artificial feather shuttlecocks replacing synthetic nylon skirts in the near future. This is because it does not make sense for commercial firms to invest so much in research and development of artificial feather shuttlecocks if it is not going into production. In summary, these patents focus on three major components:

1. Profiles and materials for shaft strength.
2. Methods to assemble the shuttlecock, such as stringing of artificial feather and insertion into the base.
3. Flight performance and perception evaluation.

An interesting difference in approach between Mizuno and Yonex is in the fabrication of the artificial feather shaft component. Replicating the stiffness and lightness of natural feather shaft is a difficult but crucial step in the development of artificial feather. Mizuno approached the issue through the use of polymer and profile extrusion, as demonstrated in [58, 60]. The end product, as also seen in their NS-5 commercial shuttlecock, is a “+” shaped profile. This profile is identical to a typical feather shaft, where the width of the profile tapers away from the cork, into a smaller rectangular profile at the vane-shaft interface. To increase the skirt rigidity, a ring of string is threaded around each shaft. This binds the various feathers together, increasing skirt rigidity and reducing skirt deformation [64]. In contrast, Yonex emulated the low density natural feather shaft with a hard shell-foam core structure. In [63], the H-shaped, the circular and the rectangular cross-sectioned profiles were explored. Feasibility study of the hard shells fabricated from composite material reinforced with glass fiber and carbon nano tube (CNT) was also conducted [62]. It was proposed that reinforcement of 22.3% glass fiber and 0.2% CNT gave the preferred feel. Durability deteriorated with increase in the composition of CNT.

Similar to the artificial feather shuttlecock, composite material has also been applied in development of synthetic nylon skirt shuttlecock. As a solution to the common criticism of poor skirt stiffness on the typical synthetic shuttlecock, Li et al. [65]

proposed the addition of clay and elastomer to Nylon 11 which is commonly used in synthetic shuttlecocks. Application of elastomer to skirt material composition was also disclosed by Sato & Omori [66]. In addition to material improvement, many patents on the synthetic skirt shuttlecock attempted to improve skirt rigidity through design features on the skirt. For instance, Yonex [67] incorporated aerofoil shaped ribs to generate pressure difference between the inner and outer surface of the skirt. This pressure difference produces a resultant outward force on the skirt which stabilises the shuttlecock skirt profile. Willis [68, 69], who is a renowned shuttlecock designer, applied spars and ribs as stiffeners to strengthen the synthetic skirt. The invention in [68] proposes the skirt to be moulded in two separate pieces. This is against the convention of a one-piece moulding found in almost all synthetic skirt shuttles. Moulding in separate pieces allows for features that cannot be reproduced with the conventional methods. This innovation has inspired the Bird2 shuttlecock [21] which claims superior performance for a synthetic shuttlecock.

The patents on improving the current shuttlecocks were tabulated and are presented in Table 3. Based on these reviewed literatures, developmental effort to invent a synthetic shuttlecock which can replace the natural feather ones remains strong.

Table 3 Patents that improve on the current shuttlecocks.

Replaceable feather	WO2010075720	Different ways of implementing similar function	[46]
	WO2011020224		[47]
	WO2011046250		[48]
Reduced number of feather	WO2010008145		[49]
Synthetic feather	WO1986002570	Thermoplastic-carbon fiber feather	[50]
	CN2226477	Polymer feathers	[51]
	CN2790531		[52]
	CN101810929		[53]
Recent efforts in artificial feathers	WO2008099086	Artificial feather vane	[54]
	WO2012133520	Mizuno artificial shuttlecock	[55]
	WO2011021512		[56]
	WO2010029914		[57]
	WO2010038657		[58]
	WO2009088011		[59]
	WO2013027535	Yonex artificial shuttlecock	[60]
	WO2012011498		[61]
Nylon shuttlecocks	US8686082	Nylon-elastomer-clay material	[63]
	WO201000473	Nylon-elastomer material	[64]
Stiffening nylon skirt	WO2009069349	Aerofoil ribs	[65]
	WO2008038040	Spars and ribs	[66]
	WO96/31260		[67]

### 2.3 Flow along a shuttlecock

Despite their differences in construction and design, the feather shuttlecocks and the synthetic versions utilise the same principle in drag induction by having features along the conical skirt. In the most fundamental form, a shuttlecock can be represented by a cork and a perfect gapless cone. This approach has been taken by Cooke [22], Kitta et al. [31, 32], and Verma et al. [70]. Cooke [22] conducted experiments to investigate the flow around a solid cone with a cork, similar to the model in Figure 5. Comparing to the work of Calvert [71], in which flow study was conducted on a solid cone without a cork, it was determined that the cork upstream

of the model does not change the flow regime. Kitta et al. [31, 32] further investigated the flow around a gapless cone model.

Unlike Cooke [22] who worked with a solid cone, Kitta et al. [31, 32] was able to better represent the shuttlecock model by experimenting with a hollow cone. This thin-walled hollow cone was modelled by covering the gaps along a feather shuttlecock skirt to create a gapless shuttlecock. Compared to a normal shuttlecock with gaps, it was observed experimentally that drag was reduced when the gaps were covered. Flow visualisation showed that the gaps resulted in air bleeding through the skirt to create jets of air in the wake that reduced the air pressure on the skirt inner surface. This increases the pressure difference between the leeward and windward surface, thereby increasing the drag. Cooke [22, 26] made similar observations in flow visualisation of shuttlecocks. The air stream bleeding through the skirt was termed as "base bleed", while the stream coming out from the inner end on the leeward side was termed as "air jet". It was also noted that unlike a two-dimensional geometry, the drag acting on the three-dimensional axisymmetric shuttlecock increased with skirt porosity. This means that analysis of shuttlecock body, both experimentally and numerically, should always be done three dimensionally.

One of the earliest three-dimensional numerical simulations of the badminton shuttlecock was published by Frank et al. [24]. Using the Reynolds-averaged Navier-Stokes (RANS) method, a time-averaged approach for fluid flow, flow simulation was conducted on a synthetic shuttlecock. The use of RANS simplified the time-dependent turbulent flow around a shuttlecock into a time-independent fully developed flow case. While simulation seemed feasible, the study was inconclusive

because the fine details on the skirt could not be modelled effectively. Moving forward into more than a decade later, numerical comparison of the gapless cone, a feather shuttlecock and a synthetic shuttlecock was conducted by Verma et al. [70]. Similar observations were made as the experimental work that was discussed. The drag coefficient,  $C_d$ , of the gapless cone skirt was lower than the shuttlecock models. The dimensionless drag parameter,  $C_d$ , of a shuttlecock is given as:

$$D = 0.5\rho v_{\infty}^2 S C_d \quad (1)$$

where D is the drag force,  $\rho$  is the air density,  $v_{\infty}$  is the free-stream velocity and S is the frontal area of largest diameter of the shuttlecock. From the drag coefficients presented by Verma et al. [70] (Figure 9), it is seen that drag coefficients of the shuttlecocks are almost constant within the range of typical operating air speeds. The reasons for the slight variation will be discussed in section 2.4.

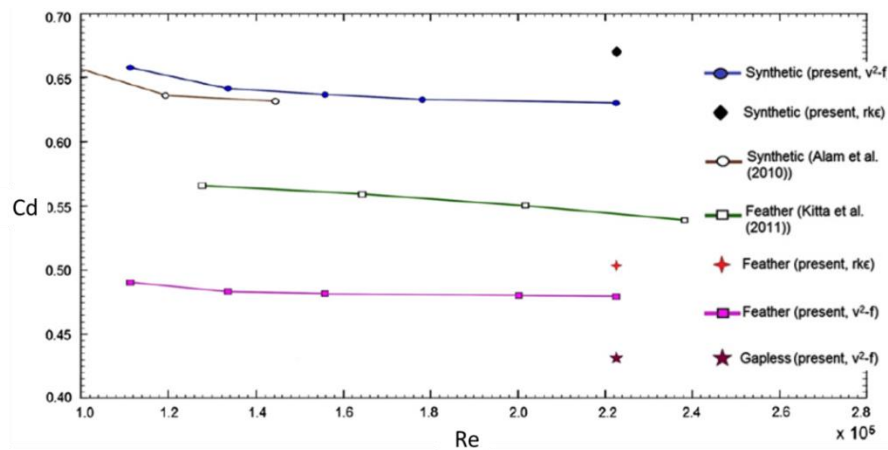


Figure 9 Drag coefficients obtained by numerical and experimental method, as published in [70]. All data under the label of “present” are numerical results. All others are experimental results.

This is an interesting aerodynamic property of the badminton shuttlecock which arises from the geometrical shape. In stark contrast, the drag coefficients of balls vary with air speed. Investigating the drag coefficient of Fédération Internationale de

Football Association (FIFA) approved soccer balls, Passmore et al. [72] observed large reduction in drag when the speed was increased, as shown in Figure 10. The unique characteristic of a constant drag coefficient of the shuttlecock suggests that flow around the shuttlecock stays in the subcritical flow regime throughout the operating speed. Technically, it may be possible to reduce the shuttlecock drag at high speed by using texture to induce transition into the critical or transcritical regime. However, this is not desired because a shuttlecock is supposed to be "draggy". Counter intuitively, drag coefficient of the shuttlecock operating within the subcritical flow regime is highly unaffected by the surface roughness. This is because the dominant drag component acting on the shuttlecock, as observed by Verma et al. [70], is pressure drag (base drag). Viscous drag component that was calculated numerically for the synthetic shuttlecock only accounted for less than 2% of the total drag. This means that the work on profile design of synthetic shuttlecock to achieve the desired pressure profile is critical for flight performance. The surface texture is probably of little relevance.

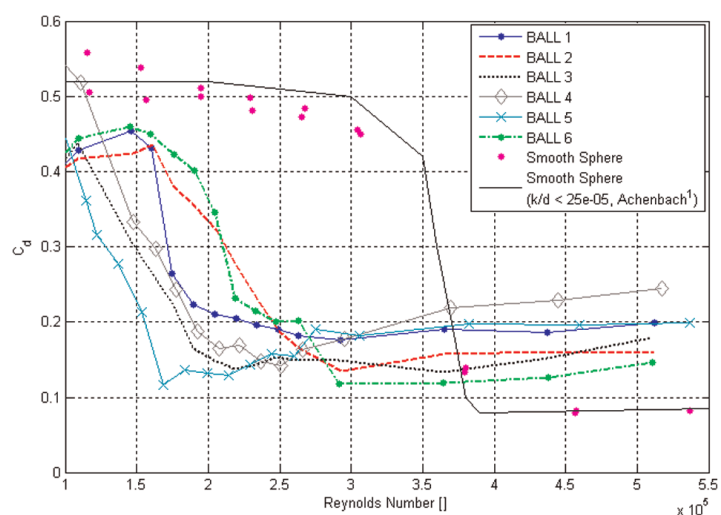


Figure 10 Change in drag coefficient with speed (Reynold's number) as tested for different soccer ball by Passmore et al. [72].

The major advantage of the numerical method is the ability to obtain insight on the local flow condition without the need for elaborate experimental setup. For instance, Verma et al. [70] was able to obtain various flow properties with simulation: drag estimation, pressure distribution on plane and surface, velocity field along the longitudinal direction, various velocity contours in different plane along the chord of the object, and vorticity. All these results were obtained from just one RANS simulation case, making numerical method highly efficient. Based on the simulation detail provided, the work done in [70] was well within the capability of a desktop computer of year 2013. This means that further extension of that work to study the actual effect of geometry is highly feasible, even without the availability of elaborate computational power.

In contrast, a high performance computer will be required for time dependent simulations such as an unsteady RANS (URANS) simulation or a large eddy simulation (LES) case. This is because of the grid cell count requirement of the time-dependent simulations. The URANS applies the RANS equations to a transient simulation case. The LES is a set of equations used for modelling turbulence condition.

Hart [73] compared RANS and URANS simulations for a synthetic shuttlecock model. It was determined that while RANS is incapable of resolving the time-dependent flow structure (which is to be expected because RANS itself is averaged), it is capable of estimating the time-averaged flow conditions that would otherwise have been predicted by URANS. Therefore, it is likely that RANS is sufficient for fundamental flow phenomenon investigation work, such as in this thesis. It is

interesting to note that the work by Hart [73] has evolved into an innovation [40] and is featured by ANSYS<sup>TM</sup> [74].

Flow study through numerical method should always be validated with experimental data. Advancement in additive manufacturing enables physical models to be built efficiently and accurately from the computer aided design (CAD) file [75]. This capacity means that the same model can be analysed in numerical method with the CAD file and then experimentally validated using the additive manufactured model which has little to no geometry variation. Terming the numerical design and simulation as virtual prototyping, and additive manufacturing as rapid prototyping, Chua et al. [76] compared their practicality and usage. The increase in availability of virtual prototyping and rapid prototyping means that they are increasingly being combined to aid designs and studies. Examples of applications include: irrigation technology [77], mechanical pump [78] and biomedical applications [79-82]. This is also a feasible approach in flow study of badminton shuttlecocks.

Based on the surveyed literatures, the effect of the presence of gaps on the flow is known. The gaps increase skirt porosity which will increase the base bleed that produces the air jets. This also changes the pressure profile and increases the drag. However, the actual effect of the size of the gaps on the flow is unclear. It is likely that there exists a gap size limit, where going beyond that size will produce too much of the skirt porosity and base bleed such that drag is reduced. Flow simulation work should be applied to investigate this occurrence.

In addition to the mentioned blunt body effects observed on the shuttlecock, the experimental flow visualisation efforts in [22, 26, 27, 31, 32] also demonstrated the

presence of counter-rotating vortices in the near field wake behind the skirt. This is especially prevalent for the gapless conical skirt. This rotational flow, as shown in Figure 11 [31], also results in flow reversal in the core region of the wake directly behind the skirt. It is a commonly described feature of blunt body flow, such as in [83-86]. The diminishing of this phenomenon for a shuttlecock with gaps signals the reduction in blunt body effect. Therefore, a study on effect of the gap size on the resultant blunt body effect is likely to be important in understanding the flow around a shuttlecock.

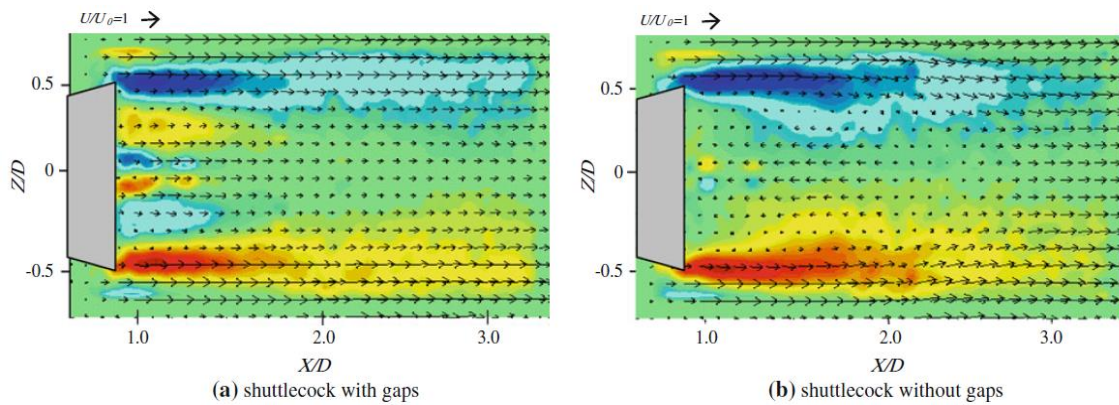


Figure 11 Particle image velocimetry flow field vector obtained by Hasegawa et al. [31] showing the rotation and flow reversal in the near field wake of the skirt.

## 2.4 Aerodynamic Experiments on Shuttlecocks

One of the earliest documented work on shuttlecocks was conducted by Peastrel et al. [87] in 1979. The terminal velocity of a shuttlecock that is under gravitational free-fall was studied. An electronic timer which was triggered by a micro switch using a mechanical-magnetic mechanism was used to time the flight. The free-fall velocity was observed to have a quadratic relation with the drag force acting against a shuttlecock. Despite a non-spherical shape, the established quadratic drag equation is obeyed by a shuttlecock for flow between Reynolds number ( $Re$ ) 1 to  $10^5$ . The

Reynolds number is a dimensionless quantity measuring the flow condition of fluid. The same Re value in different flow situations (viscosity, object size and density) should generally produce the same flow pattern. The parameters obtained for the same Re values are also comparable across different fluid type. Such was the rudimentary approach to shuttlecock aerodynamics of that time. McCreary [88] attempted to verify the result in 2005 using high-speed camera for motion analysis. However, the result was inconclusive due to a lack of data points for insufficient number of test air speeds. Moreover, McCreary only conducted experiment for a free-fall height of up to 1.88 m. This would not have given the shuttlecock sufficient time to reach the terminal velocity. Nonetheless, the work demonstrated that high-speed capturing, when properly conducted, is a feasible method for measuring shuttlecock velocity. Through experimental work with high speed capturing technique, Shibata et al. [89] verified the drag-velocity relation.

Chen et al. [90] also worked on verification of the relationship between drag force and velocity. Through curve fitting with experimental data, drag force was confirmed as being proportionate to the square of the velocity. It means that the generic drag equation that is used for most incompressible sub-sonic flow can also be applied to a shuttlecock.

Cooke [18, 23, 25-27] set the precedent for comparison work between the synthetic shuttlecocks and the feather shuttlecocks. Working with Carlton Sports, Cooke compared the wind tunnel measured drag coefficients of the feather and synthetic shuttlecocks [22, 23, 26, 27]. As the magnitude of force at low speed is relatively small for low Reynolds flow, force study was accomplished by free-fall drop in

water column. By adding various weights to the shuttlecock, the drop speed was controlled. Despite technological advancement, this is still a relevant issue for wind tunnel force study. The challenge is to have a sensor that is sensitive enough for low speed flow involving drag force as small as 0.05 N at 6.5 m/s airspeed, but yet still be capable of withstanding the weight of the experimental setup. This might partly account for the lack of data points for shuttlecocks at 5 to 10 m/s flow speed.

Cooke observed that the drag coefficient for the tested synthetic shuttlecock decreases at high Reynolds number. This is in contrast to the relatively constant drag coefficient for the feather shuttlecock. This was also observed by Alam et al. [20, 28-30] who experimented on more shuttlecock types. Two explanations were identified to account for the difference: skirt deformation and skirt porosity. Alam et al. [29, 30] had similar conclusion. According to Cooke [26], the skirt deformation for a synthetic shuttlecock was approximately 1mm reduction in diameter at 38m/s (Reynolds number 165,000). This deformation is due to the softer synthetic skirt as compared to the much stiffer stem on the feather skirt. On the other hand, the tested feather shuttlecocks had no observable deformation.

However, it should be noted that a frontal diameter reduction of 2mm will only decrease the drag coefficient by approximately 0.03. This means that the effect of skirt deformation on drag coefficient might not be as significant as what Cooke and Alam et al. have thought. Alam et al. have not published quantitative result on skirt deformation. At this point, it is vital to note that drag variation within different types of synthetic shuttlecocks can be large, as can be seen from Figure 12. The symbols S1 to S5 in Figure 12 refer to the different synthetic shuttlecocks that were tested.

The trend also showed the synthetic shuttlecocks having reduced drag coefficient at low speed ( $Re \sim 70000$ ). The measurements for the feather shuttlecocks that Alam et al. [30] obtained also showed the same drop in drag coefficient at the same speed, as shown in Figure 13. This is in contrast to results in the other publications, such as those in [23, 26, 32, 34, 91], where the drag coefficient at low speed did not show much variation from high speed. This is likely to the issue of load cell capacity used by Alam et al. [30], where error was  $\pm 0.1N$ . As the drag force acting on a generic shuttlecock at 15 m/s ( $Re \sim 70000$ ) is just 0.3 N, the error margin could have been larger than  $\pm 33\%$ . This again demonstrates the difficulty in instrumentation of shuttlecock experiment.

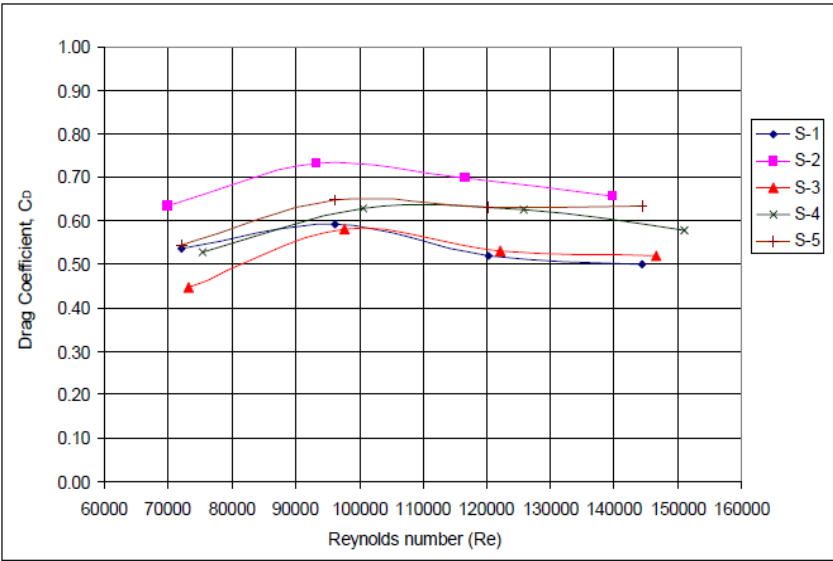


Figure 12 Experimental result for synthetic shuttlecocks [30].

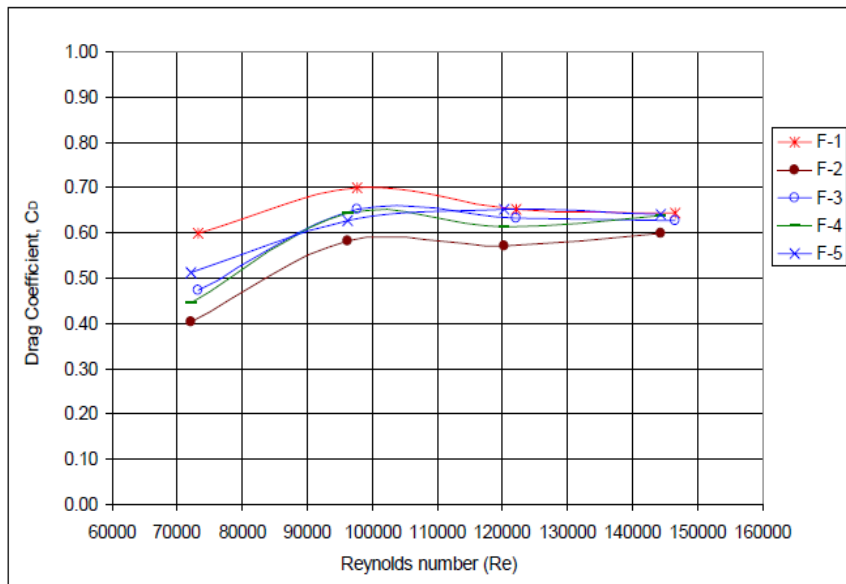


Figure 13 Experimental result for feather shuttlecocks [30].

The more commonly published drag coefficient- air speed relation of badminton shuttlecocks will follow the trend shown in Figure 9. In general, the drag coefficients of shuttlecocks, as surveyed in literatures, are between 0.5-0.7. The drag coefficients reviewed were all collected at zero incidence to the free-stream velocity. Although a shuttlecock usually flies with little to no angle of attack, it is still important to understand the effect of incidence angle on shuttlecock parameters.

Alam et al. collected measurements at an angle of attack of 15 degree, but only the data collected for zero angle of attack was published in [20]. Cooke presented results for lift, drag and pitching moment at different flight angle of attack in [26]. In the work by Foong and Tan [36, 37] that studied the trajectory difference between the feather shuttles and the synthetic shuttles, a performance indicator that is dependent on the aerodynamic parameters was discussed. Unlike previous works on flight trajectory, shuttlecock orientation angle with respect to the ground was also recorded. Orientation angle in that study would have been highly dependent on the

lift coefficient and pitching moment coefficient of the shuttlecock because there was only small deviation in the launch conditions for the feather shuttles and the synthetic ones. More recently, Chan and Rossmann [91] measured the aerodynamic drag and lift, and pitching moment of the badminton shuttlecock. The wind tunnel experiment was conducted at various angles of attack. Hasegawa et al. [31] also published experimental data of the drag, the lift and the pitching moment of a feather shuttlecock at various angles of attack. Measurements up to 24 degree angle of attack showed that linearity can be assumed for the lift coefficient and the pitching moment coefficient with respect to angle of attack. Zero moment and lift were observed when there was no angle of attack. This is to be expected because a shuttlecock is an axisymmetric body which has an averaged zero lift. This is the same as a flat plate or a cylinder. Change in the drag coefficient with the angle of attack was observed to be small.

From the wind tunnel measurement work that was reviewed, it is clear that the drag parameter is an important performance indicator of flight. Unlike the other flying objects, such as an airplane or a Frisbee, the lift force of shuttlecock is seldom studied. This is because a shuttlecock usually flies with little to no angle of attack. This means that the axisymmetric body of the shuttlecock does not experience much lift and moment. Nonetheless, the inclusion of the lift and the pitching moment is important for improved accuracy in the trajectory simulation. This is discussed in the next sub-section (2.5). The more important reason for the emphasis of drag analysis of a shuttlecock is that the drag force acting on the shuttlecock gives it the characteristic flight behaviour. In addition to shaping the flight trajectory, drag also slows down the shuttlecock at rates that are not experienced in other sports

projectile, thereby making the game interesting. A simple calculation with equation (1) suggests that drag acting on a shuttlecock flying at 30 m/s is 1.1 N. In the body acceleration rate, this is a 22 g ( $22 \times 9.81 \text{ m/s}^2$ ) deceleration! Thus, it is no surprise that the emphasis of shuttlecock aerodynamic performance is always on drag.

## **2.5 Flight Experiments on Shuttlecocks**

While the aerodynamic parameters that were discussed are important in understanding the flight of a shuttle, the key performance indicator of a shuttlecock is still the flight trajectory. Feather shuttlecocks have significantly different flight path when compared to synthetic versions. Since players are accustomed to that of a feather shuttle, the synthetic version is generally viewed as inferior and unpredictable. However, it is to be noted that the “ideal” shuttlecock flight trajectory derived from the feather shuttles is very different from an ideal projectile motion. These differences were studied by Foong and Tan [36]. According to Cohen et al. [35], a projectile that is launched slower than the terminal velocity produces a parabola curve. Increasing the launch speed beyond the terminal velocity will produce a trajectory that resembles the cannonball (Tartaglia) curve, in which the descent path of the projectile is of a much more vertical drop than the initial ascent.

Unlike most other sports balls, the high drag-to-weight ratio of a badminton shuttlecock results in a low terminal velocity. This means that the shuttlecock is launched above the terminal velocity in most types of flight, except in a net shot. Flight of a shuttlecock can be categorised into the four major modes- Net, serve, clear and smash. The launch velocity means that the net shot follows a parabola curve, while the other three modes will produce a Tartaglia flight curve.

In 1989, Cooke conducted trajectory study and simulation for badminton shuttlecock [23]. That was one of the earliest publications on the badminton shuttlecock trajectory which has set the basis for modern understanding of trajectory difference between the traditional feather shuttlecocks and the synthetics. In that research, a digital camera was used to observe the flight trajectory of a feather shuttlecock launched with a custom-developed compressed air launcher. The observed trajectory was then compared to the simulated trajectory. The simulated trajectory is the result of applying drag and lift values measured in the wind tunnel to the two-dimensional equation of motion for a shuttlecock [23].

The equation of motion [23] was given as:

$$m \frac{d^2x}{dt^2} + D \cos \theta + L \sin \theta = 0 \quad (2)$$

$$m \frac{d^2y}{dt^2} - L \cos \theta + D \sin \theta + g = 0 \quad (3)$$

The symbol  $m$  is the object mass,  $L$  and  $D$  are the aerodynamic lift and drag forces respectively,  $g$  is gravitational acceleration,  $\theta$  is the angle between the flight path and the horizon, and  $\frac{d^2x}{dt^2}$  and  $\frac{d^2y}{dt^2}$  are the acceleration in the horizontal and vertical direction. This 2 dimensional equation of motion is one of the most commonly used models for shuttlecock flight trajectory. However, in her Ph.D thesis [22], Cooke recommended that a third axis be included for future flight modelling of the shuttlecock. Such an axis will allow for a full 6 DOF trajectory modelling of a shuttlecock. At the time of writing, no such development was found in the open literature.

There are two approaches to trajectory simulation for shuttlecocks. The first approach utilises the physics-based differential equations of motion, such as the work in [22, 25, 91]. These are systems of equations built upon the summation of the forces and the moments on the shuttlecock. The second approach to trajectory simulation is the formulation of mathematical-based models with some aerodynamic parameters, such as drag coefficient or terminal velocity. This is the approach taken in [36] and [90]. An example, as presented by Chen et al. [90] is:

$$y = \frac{v_t^2}{g} \ln \left| \frac{\sin\left[\frac{v_t'}{v_{x_i}} \left(e^{\frac{gx}{v_t'^2}} - 1\right) + \tan^{-1}\left(\frac{v_t'}{v_{y_i}}\right)\right]}{\sin\left[\tan^{-1}\left(\frac{v_t'}{v_{y_i}}\right)\right]} \right| \quad (4)$$

The symbol  $y$  refers to height,  $v_t$  is the terminal velocity,  $v_t'$  is the first time derivative of terminal velocity, and  $v_{x_i}$  and  $v_{y_i}$  are the initial velocities. By applying various initial conditions to equation (4), typical trajectories of various badminton strokes were simulated. Personnic et al. [19] applied the same equation for trajectory simulation of both the feather shuttlecocks and the synthetic shuttlecocks. Simulation result showed feather shuttlecocks to have steeper fall towards the end of the flight. However, both studies lacked data from physical experiment to support the validity of the developed model.

The same phenomenon was observed in the simulation work done by Cooke [25] using her two-dimensional model, involving three degrees of freedom (pitch, ground distance and height). Unlike the work done by Personnic et al. [19] and Chen et al. [90], Cooke [25] substantiated her simulation results with physical measurements that verified the trajectory differences between synthetic and feather shuttles. While

deviations between physical and simulated trajectories were observed for the various shuttles that were tested, differences were small. Her simulated trajectories also showed lift force to be relatively insignificant in trajectory estimation. The largest difference in range among the model with and without lift force input was a mere 0.07 m for a range of 8.4 m.

Interestingly, the BWF [38] equipment approval scheme on the public domain does not have any specific regulation for shuttlecock trajectory. Instead, only test standard for shuttlecock speed rating were stated.

It states that:

Table 4 BWF standard for shuttlecock testing [38].

3.	<b>TESTING A SHUTTLE FOR SPEED</b>
3.1	To test a shuttle, use a full underhand stroke which makes contact with the shuttle over the back boundary line. The shuttle shall be hit at an upward angle and in a direction parallel to the side lines.
3.2	A shuttle of correct speed will land not less than 530 mm and not more than 990 mm short of the other back boundary line as in Diagram B.

The testing method can be seen as rather rudimentary because the stroke of a player will significantly affect the eventual range travelled by the shuttlecock. Chen et al. [90] recognized that too and called for a more objective and consistent method.

The shuttlecock speed and trajectory are extremely sensitive to local climatic conditions. The distance travelled for the same shot can vary by 1m or more from change in air density and temperature [92]. Such ambient difference can come about from seasonal weather changes, geographical location or even just climate control

within the court. Therefore, shuttlecocks are manufactured with speed rating to suit the local court climate. Speed ratings typically ranges from 75-79, where a 20-30 cm increase in distance will be observe for each corresponding speed rating increment [93, 94]. The speed rating number refers to the number of grains (437.5 grains=1 ounce, 1 grain ~ 0.0647 g) that will be equivalent to the weight of the shuttlecock. Therefore, a speed 76 shuttlecock will weigh approximately 4.9 g ( $76 \times 0.0647$  g). Variation of the speed rating (weight) of the shuttlecock helps the shuttlecock to have the same flight range in different air density. The speed 75-76 shuttlecocks are suitable for tropical climate of South East Asia where the air is less dense. On the other hand, the speed 78-79 shuttles are appropriate for play in the winter months of continental Europe because the heavier shuttlecocks have higher penetration power in the cold air which is much denser. To suit the local (Singapore) climate, the shuttles used for comparison purpose in this study, will consist of a majority of speed 76 and 77.

From the literatures reviewed, it is clear that three areas of work related to trajectory are lacking. Firstly, most of the works discussed were focused on trajectory simulation and measurement, but little has been done to account for the difference between the various types of shuttles. It is also unlikely for the drag coefficient to be the only factor of trajectory differences. Secondly, flight trajectories in publications are usually limited to the steady flight state. Little work has been done for the angular response of the shuttlecock during the unsteady flight state, which will be discussed in detail in chapter 4. Lastly, none of the trajectory studies has a detailed study on the velocity of the shuttlecock at various points of flight. Thus, it is unclear how much speed is lost or brought forward into each part of the flight trajectory. A

more established and consistent methodology to observe the flight path will be vital for both academic research work and international regulatory bodies of badminton sport.

## **2.6 Spin Experiments on Shuttlecocks**

Axial spin of the badminton shuttlecock stabilises the flight path and eliminates wobble. Wobble, as listed on the shuttlecock approval scheme data sheet of BWF [38], is an acceptable flight property of a badminton shuttlecock. The flight stability of the shuttlecock is divided into four grades- A (no wobble), B (little wobble), C (wobbling), and D (big wobbling). Any shuttlecock that is graded C or better can be accepted. However, the general acceptance of wobble does not imply that spin is unimportant because the axial spin of a shuttlecock will also determine the other flight performance.

To understand the effect spin of a shuttlecock, the axial spin rate to linear air speed relation should be studied. While various wind tunnel studies of the spin rate-air speed relation can be found in the open literature, such as in [22, 31-33, 91], no work has been done on actual spin measurement of a shuttlecock in flight. Spin measured in the wind tunnel can be termed as the steady state spin, which is a constant for each linear air speed. This is similar to a fixed pitch propeller. While this provides insight on the spin-velocity relation, it is unlikely to be representative of the actual condition experienced in flight. This is because time is likely to be required for the acceleration and deceleration of spin. Given that a shuttlecock experiences very large rate of change in the linear air speed during flight (due to the high drag), it is then unlikely for the shuttlecock to attain the steady state spin rate that was observed in

the wind tunnel. Interestingly, Cooke [22] observed insignificant time delay in the change of spin rate with air speed.

The closest work to understanding rate of change in axial spin rate was conducted by Cao et al. [95] and was published three years after this project started. The spin acceleration and deceleration of the shuttlecock was studied in the wind tunnel, with the spin deceleration being attributed to resistance moment. In that study, it was observed that a shuttlecock may take up to 0.8 s to reach steady spin rate from stationary, at a flow speed of 20.3 m/s. While the result is wind tunnel measured and not from actual flight, this supports the proposition that the spin of a shuttlecock is not immediate. Time is required for the spin acceleration and deceleration of the shuttlecocks. Thus, it is unlikely for a shuttlecock to attain the wind tunnel measured steady state spin rate immediately after leaving the racket at high linear speed with very low axial spin rate. It is seen that work needs to be done in flight measurement of spin rate.

Contrary to belief, axial spin of a shuttlecock does not influence the flight trajectory by changing the drag coefficient. A Japanese research group [31-33] measured the drag coefficient of the same shuttlecock with and without rotation. It was observed that drag coefficient increases significantly with the rotation rate when flow is faster than  $Re = 210,000$ . However, this increase was due to skirt expansion at high speed, where the centrifugal force from the fast spin rate pushed the feather vanes outwards. This means that the drag coefficient of a shuttlecock will not change from rotation if the spin is not sufficiently fast to cause skirt expansion. The steady state spin at  $Re = 210,000$  was 300 rad/s, a rate that is unlikely to be observed for a shuttlecock in

flight because of the delay in spin acceleration and the fast deceleration in linear speed.

As seen from their result (Figure 14), spin can also be used as a method to prevent skirt shrinkage at high flow speed because the centrifugal force counters the deformation. It was also concluded that the gaps along the skirt do not influence the spin rate.

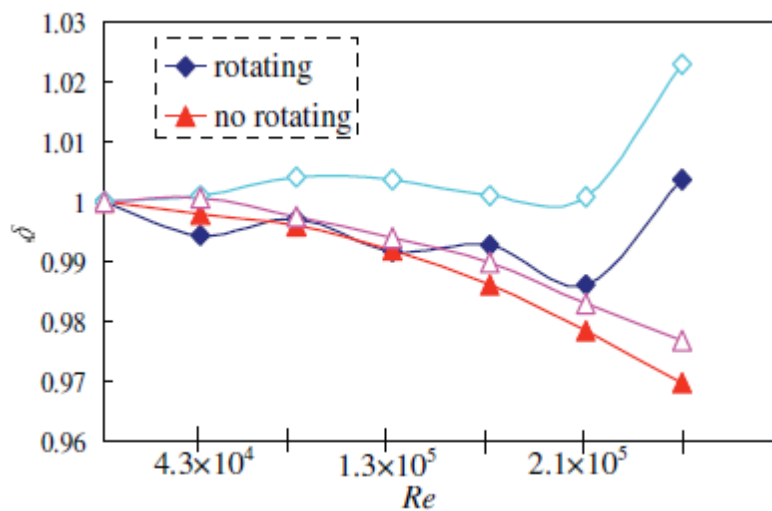


Figure 14 Shrink ratio- skirt deformation as observed by Kitta et. al. The filled and open symbols denote shuttlecocks with and without gap, respectively [32].

The second effect of the shuttlecock axial spin is the gyroscopic precession. Till date, [22] remains the only publication in the open literature to discuss about this phenomenon. The gyroscopic precession is a side way deviation that results from the yawing of the shuttlecock. This yawing, which occurs after the vertex of the flight trajectory, is induced from the coupling of heading (pitch) change and axial spin. For this effect to be significant, the rate of heading (pitch) change must be large, and the rate of axial spin must be significant. In essence, this is the same effect as the gyroscopic stabilisation of a spinning top.

A faster spinning (axial spin) shuttlecock results in more undesired side deviation in the trajectory. However, due to the coupling of the angular motion, as will be derived in chapter 4, the precessional yaw also induces a secondary angular response in the pitch axis which may affect the flight trajectory. Perhaps the reason for the lack of work in this area is because the shuttlecock axial spin is usually regulated by design to prevent excessive side way deviation from the induced yawing. This would reduce the induced angular response in the pitch direction. Nonetheless, it demonstrates the importance in understanding spin rate, especially at the vertex of the clear shot where the pitch change rate is large.

## **2.7 Summary**

The fundamental allowable shuttlecock dimensions that were reviewed show a large tolerance for altering dimensions to suit the desired performance. The patent review shows that development of synthetic shuttles has always been an on-going process. At the time of writing (2014), shuttlecock with artificial feathers are observed to be the trend in development. There have also been various attempts at reinventing the game of badminton and the shuttlecock used. Regardless of the outcome of these innovations or any future inventions, it is clear that an integrated shuttlecock evaluation framework is always applicable to review the product.

The literatures reviewed demonstrate the existing work on shuttlecock, while identifying some of the parameters and performance criteria that should be evaluated. Knowledge that are lacking in the existing literatures have also been identified. These include the understanding of the effect of gap sizes, the actual difference between the synthetic shuttlecocks and the feather shuttlecocks, and the

angular response in the axial spin and the pitch. It was also discovered that physical (mechanical) properties of the shuttlecock are seldom documented in literatures. Thus, an integrated shuttlecock evaluation framework which includes physical properties and flight performance is required.

### **3. AERODYNAMICS of SHUTTLECOCKS**

Contrary to intuition, the presence of openings (gaps) along the badminton shuttlecock skirt does not decrease the frontal drag [70]. Instead, the gaps increase pressure drag by inducing pressure difference between the inner and outer surface of the skirt. This implies that a badminton shuttlecock will experience more drag than a gapless cone of the same dimensions when it is under the same condition. In this chapter, the effect of the gaps on the cone model is evaluated. This work addresses the lack in understanding of how the gap size affects the shuttlecock design.

A perfect gapless cone behind a hemispherical dome was first evaluated using computational fluid dynamics (CFD). The numerical result was then validated with experimental result. This serves as the baseline reference. Cones with various gap sizes were then compared with the gapless cone. Salient features of the badminton shuttlecock skirt were then discussed. The reported findings in this chapter have been published in the Journal of Wind Engineering and Industrial Aerodynamics [96].

#### **3.1 Model Geometry and ANSYS CFX Method**

The reference gapless cone body, Profile A, comprises of a 0.5 mm thick conical skirt of 65mm in diameter and 60 mm in length. The skirt is attached to a solid cork (comprising of a cylinder and a hemisphere) of length 25 mm and diameter 26.4 mm. These dimensions were referenced from Verma et al. [70], and used in [96, 97]. Five cones with different gap sizes, labelled Profile B to Profile F, were also studied. Each profile has 16 triangular gaps, of X mm width and are evenly distributed

around the circumference of the cone. The profiles are illustrated in Figure 15. The gap sizes and the resultant surface area of the various profiles are given in Table 5.

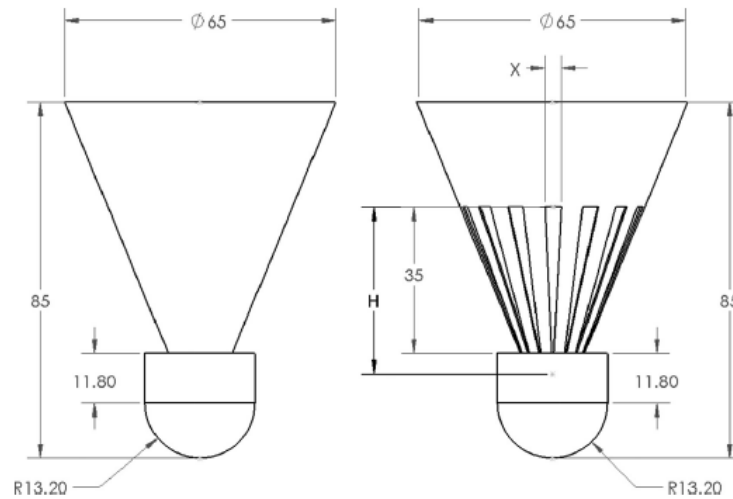


Figure 15 Dimensions of the cone geometry used in simulation and physical modelling. All dimensions in mm.

Table 5 Gap size and area of gaps for the profiles.

Profile	Gap Width (X/mm)	Gap Height (H/mm)	Cone Surface (area/mm <sup>2</sup> )	Surface of Gap (area/mm <sup>2</sup> )
A	-	-	8420	0
B	2	20	7865	555
C	2	40	7551	869
D	4	40	6910	1510
E	6	40	6268	2152
F	7.5	40	5784	2636

With the provided gap dimensions, the resultant skirt porosity was between 6.5% surface area in Profile B to 31.3% surface area in Profile F. Profiles B to F have the same thickness and external dimensions as the gapless Profile A. Therefore, it is unlikely for findings to be attributes of exterior dimensional difference. In addition to numerical analysis, Profile A, C and E were manufactured by an Objet<sup>TM</sup> Eden

350V printer using the FullCure 720 model material and the FullCure 705 support material. The manufactured models are shown in Figure 16. The selection of Profile A was because it serves as a reference case and can be validated against previous work on gapless cone and shuttlecock in [22, 31-33, 70]. Profile C and Profile E were selected based on their numerical drag values which are close to that of a typical speed 76 shuttlecock. Moreover, these two profiles give interesting finding in the numerical simulations. More will be discussed on these profiles in the subsequent sub-sections of this chapter. The wall thickness of the physical models was increased to 0.8 mm for reducing the possibility of shape deformation during high speed test in the wind tunnel.

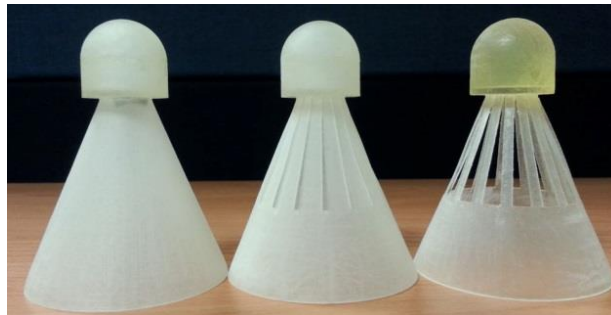


Figure 16 Thin-walled profile cones with and without gaps, manufactured with Objet printing.

Using the same predefined simulation workflow for all the six profiles, numerical analysis was conducted with the ANSYS<sup>TM</sup> suite. Each profile was enclosed by a cylinder of diameter 310 mm, with the model positioned 135 mm downstream from the inlet. Figure 17 shows a profile model within the cylindrical domain. The outlet of the flow-field (fluid domain) was placed 500 mm further downstream from the profile model. In the CFX<sup>TM</sup> CFD software, the inlet was set as a velocity inlet, while the outlet is a zero static pressure boundary. For wall boundaries, the cylindrical wall of the fluid domain is a free-slip wall, and the profile model is a

smooth no-slip wall. The exclusion of surface roughness is because the Objet<sup>TM</sup> manufactured models are expected to be smooth. Moreover, it is expected that the drag regime of a blunt body, such as the shuttlecock and the profile models, is predominantly pressure drag (base drag) that is unlikely to be affected by surface roughness.

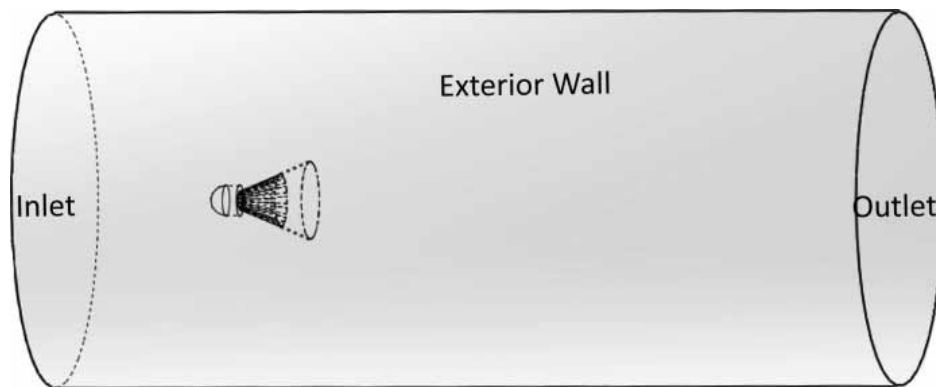


Figure 17 Fluid domain and placement of profile model in ANSYS CFX.

Unstructured mesh was generated in the fluid domain within the cylinder through ICEM<sup>TM</sup>. Analysis of grid independence for all six profiles was achieved by comparing the numerical drag forces at 50 m/s for the applied mesh and for a refined version of the applied mesh. It was observed that a grid size of between 3.5 million to 4.08 million volumes is sufficient for grid independency. Comparison of the applied mesh against the refined version shows drag force to be within +/- 5%. This result is similar to the grid requirement presented by Verma et al. [70] in the simulation of a gapless conical skirt. The numerical results of the grid independency study for this section is presented in Table 6. The trend arising from gap size variation will be discussed in detail in section 3.3 of this thesis.

Table 6 Grid independency study for optimum number of "volumes" required.

Profile	Applied mesh		Refined mesh		Difference %
	Number of volumes	Drag force/N	Number of volumes	Drag force/N	
A	3.50 mil	2.61	5.95 mil	2.63	-0.77
B	4.04 mil	3.08	6.02 mil	3.26	-5.84
C	4.02 mil	3.39	5.99 mil	3.56	-5.01
D	4.08 mil	4.04	5.83 mil	4.14	-2.48
E	3.99 mil	3.80	5.61 mil	3.72	2.11
F	3.86 mil	3.49	5.56 mil	3.31	5.16

Shear stress transport (SST), a K-Omega based turbulence model that is more accurate for near wall boundary layer, was selected for the simulation [98, 99]. SST model builds on the advantages of both the Wilcox and K-epsilon model to give increased accuracy in prediction of flow separation. The K-epsilon model applies the wall function approach regardless of the value of the dimensionless wall distance,  $Y^+$ . This is inappropriate for slower speed or fine grid simulation case where  $Y^+$  is small ( $< 11$ ) and the near wall cells are rightfully in the laminar sub-layer. The  $Y^+$  is important because it is an indicator of how well the mesh can resolve the boundary layer. It can be calculated with equation (5).

$$Y^+ = \frac{(Wall\ friction\ velocity)(distance\ to\ nearest\ wall)}{local\ kinematic\ viscosity} \quad (5)$$

Outside of the sub-layer, the log-law region remains accurate despite possible error from ignoring the sub-layer. The scalable wall function approach in CFX<sup>TM</sup> can compensate for this, but the recommended approach by ANSYS<sup>TM</sup> is still the SST model with automatic wall function. The automatic wall function approach reduces

the dependency on the wall mesh refinement ( $Y^+$ ) by using a blend of wall function and low Re approach. Nonetheless, the calculated  $Y^+$  for the applied mesh in Profile A has been plotted in Figure 18 for flow speed of 6 m/s. The small  $Y^+$  values show that the SST approach was probably appropriate and that the K-epsilon model may not be suitable for the applied mesh.

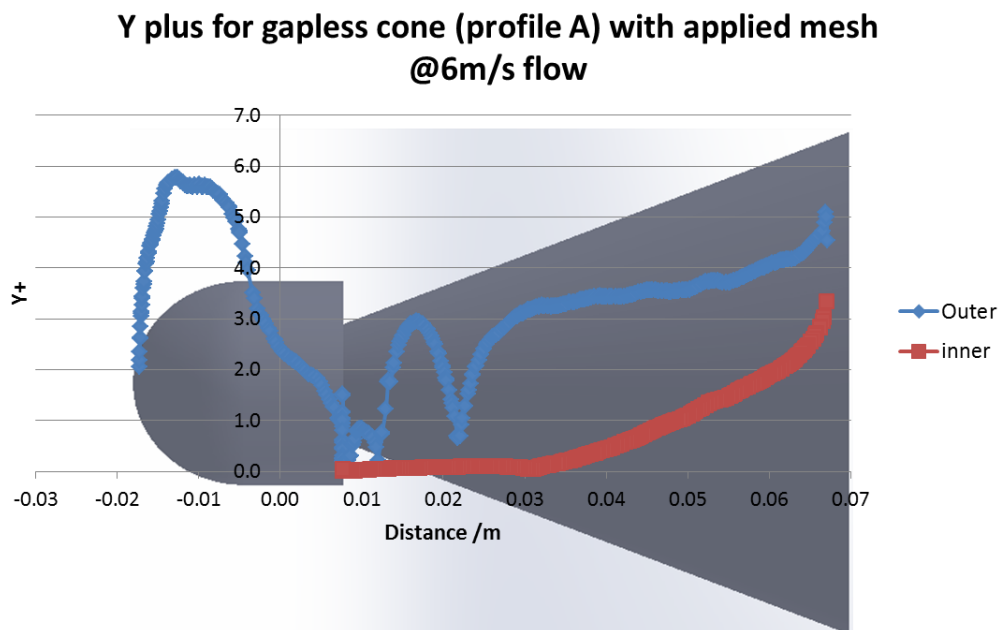


Figure 18 Calculated  $Y^+$  for the applied mesh in profile A at flow speed of 6 m/s.

### 3.2 Flow Over a Perfect Gapless Conical Skirt

Using the defined numerical method, the drag coefficient of Profile A was calculated at flow speeds of 6 m/s ( $Re \sim 2.7 \times 10^4$ ), 15 m/s ( $Re \sim 6.7 \times 10^4$ ), 30 m/s ( $Re \sim 1.3 \times 10^5$ ) and 50 m/s ( $Re \sim 2.2 \times 10^5$ ). The data at 6 m/s gives insight on the magnitude of drag near the terminal velocity, while the simulation cases at 15 m/s and at 30 m/s give good comparison with the results from literatures, such as in [22, 32, 70]. Drag coefficient from the higher speed 50 m/s test case provides comparison with previous work at higher Reynolds's number, such as [31, 32]. This also validates the

observation that the drag coefficient of the shuttlecock is near constant with respect to air speed.

The drag coefficient of Profile A was also determined experimentally by wind tunnel measurement of the physical model seen in Figure 16. Drag measurement was conducted in a closed-loop wind tunnel from STEM ISI ImpiantiS.p.A. This wind tunnel has a test section measuring 780 mm wide, 720 mm tall and 2000 mm in length. Force measurement was conducted by a calibrated load system using a Seed Studio 500 g load cell (SEN128A3B) which is shown in Figure 19. The experimental setup in the wind tunnel test section is shown in Figure 20.

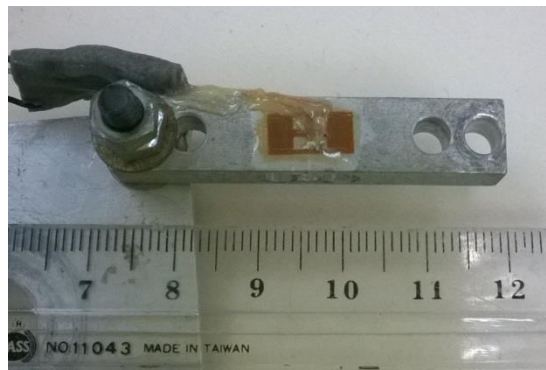


Figure 19 The Seed Studio 500 g load cell used for the wind tunnel experiment.

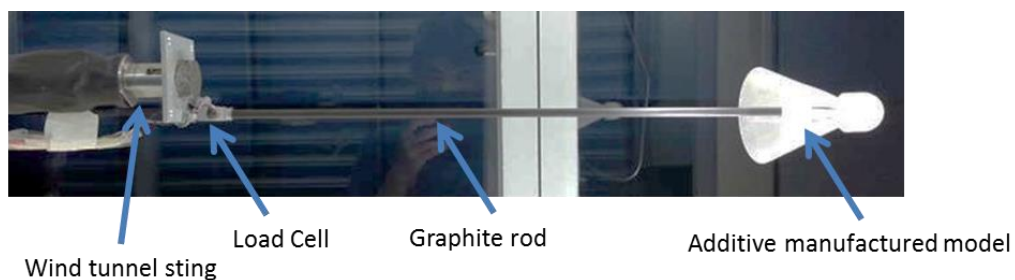


Figure 20 The experimental setup for wind tunnel measurement with the additive manufactured cone profile.

Experimental data was not collected for 6 m/s because it is expected that the corresponding drag force of  $< 5$  g, which is smaller than 1% of the rated load

capacity, will result in large error. The experimental and numerical drag coefficients were plotted and are shown in Figure 21. It was observed that drag coefficient of a conical body behind a hemisphere is almost constant with respect to air speed. This is true for the range of velocities that a shuttlecock is likely to encounter in use. Experimental and numerical drag coefficients showed less than 2% change as air speed increases. Variations between experimental and numerical drag coefficients range from 1.5% to 4.5%. This is a good agreement between experimental and numerical result.

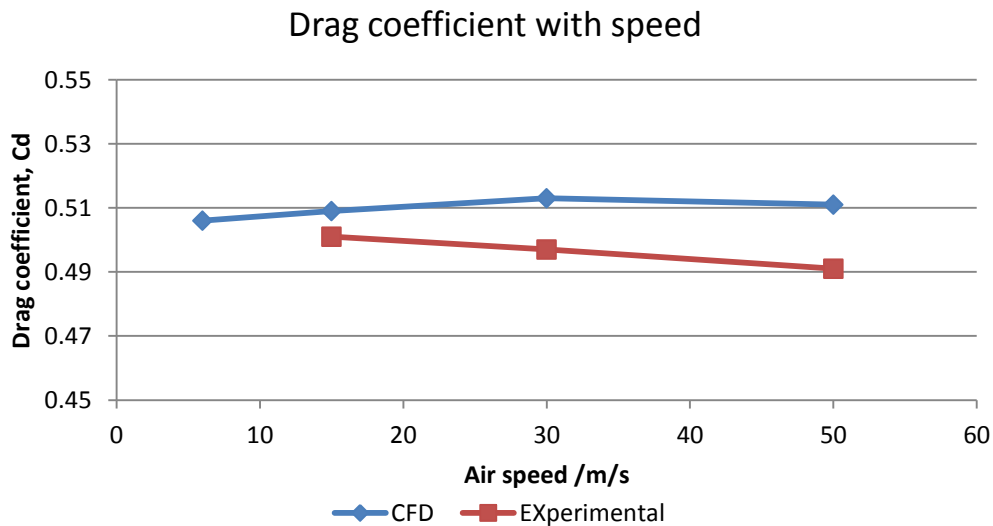


Figure 21 Comparison of numerical and experimental drag coefficients.

The flow vector around the gapless cone, Profile A, was also studied. Figure 22 shows the velocity vector in the flow field around the conical skirt in free stream velocity of 6 m/s. The most salient feature of the vector plot is the pair of counter rotating vortices in the wake region immediate of the skirt, extending in the upstream direction into the low pressure region of the cone inner surface. The presence of this pair of vortices produces an inward curling effect on the flow around the core region in the near field wake. This curling effect extends to a low magnitude reverse flow

(< 2 m/s) that pushes in towards the low pressure inner surface of the cone. At two chord length behind the conical skirt in the wake, the velocity in the core region is still around 2 m/s going in the free stream direction. This observed effect of wake vortices is similar to the wake observed behind a blunt body, such as a square cylinder [83]. Even with rounded edges, a blunt body may still exhibit such a wake behaviour [84]. In her experimental work in flow visualisation, Cooke [26] concluded the same for shuttlecock.

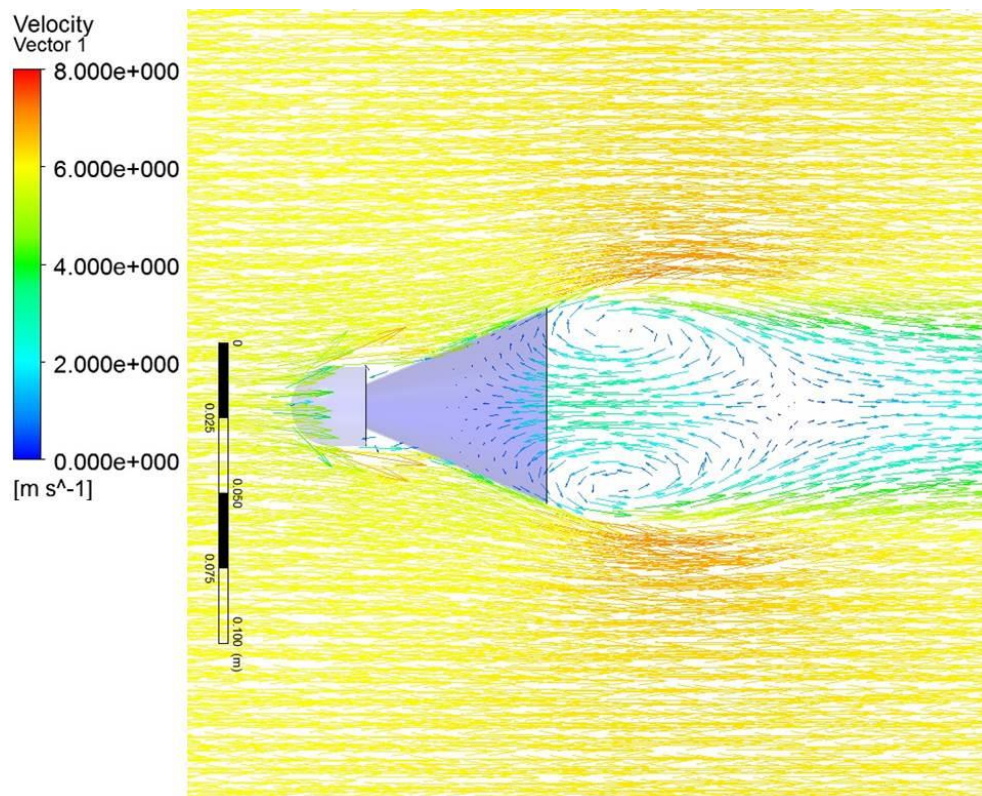


Figure 22 Flow field velocity vector plot around Profile A, the gapless cone skirt. Freestream velocity is 6 m/s.

The key essence from the above description is that Profile A, and possibly a shuttlecock, is under the influence of blunt body aerodynamics. The drag regime of an object in this shape will follow that of a blunt body, where the dominant component of drag comes from the pressure difference between inner (or leeward)

and outer (or windward) surface of the object. Indeed, the numerical result on Profile A shows that pressure drag (base drag) accounts for 94.3% of the drag force experienced at 6 m/s. The pressure drag contribution increases to 97.1% at 50 m/s. This agrees with finding from Verma et al. [70] where pressure drag component of the same cone was quantified as 98% of the total drag at 50 m/s. Since viscous drag has a low contribution, it should be noted that surface roughness is unlikely to significantly affect the flight performance of shuttlecocks. Shape profile is the dominant determinant for drag performance.

To investigate the pressure distribution along the chord of the skirt, pressure plots of Profile A with respect to chord length was obtained numerically. Comparison was made using the dimensionless pressure coefficient, which is defined as:

$$\text{pressure coefficient} = \frac{P}{0.5\rho V^2 S c} \quad (6)$$

The outer surface pressure coefficient was then validated against experimental result from Cooke [22]. As Cooke [22] worked with a solid cone, no pressure plot of the inner surface was published in her thesis. Therefore, the inner surface pressure coefficient of Profile A was also determined experimentally to validate the numerical result. This part of the work also aided in validating the numerical method that was applied to Profile A and the other profiles. The physical experimental model, as shown in Figure 23, was fabricated with the same additive manufacturing method that was described. Fittings which are flush with the inner surface of the cone (leeward side) extend outside the skirt for connection to the MPXV7002DP differential pressure sensor. The fittings were added at 30 mm to 80 mm aft of the tip

of the cork, at a 10 mm interval. All dimensions remained the same as the original Profile A model.

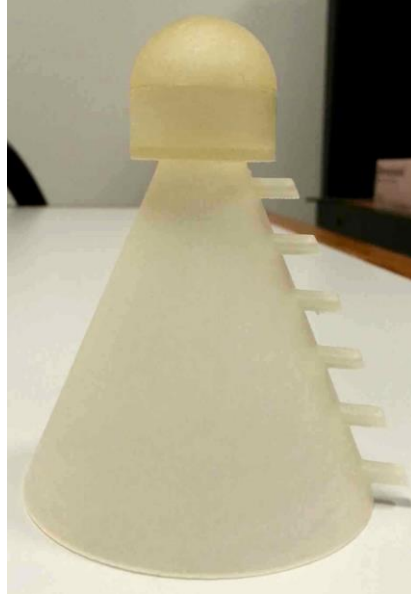


Figure 23 Gapless cone of Profile A with the tubing attachment points for inner pressure measurement in the wind tunnel.

The outer and inner surface pressure coefficients along Profile A are plotted in Figure 24 and Figure 25 respectively. Chord locations on the plots are with the origin at the tip of the cork. Numerical data of the outer pressure coefficient agrees well with the data from Cooke [22]. Deviation is seen at the intersection between the cone and cork, at the pressure peak between 30 mm to 40 mm chord length and also toward the end of the skirt at 80 mm chord length. The deviation at the cone and cork intersection is likely to be the effect of the geometry difference at this area, where the model used by Cooke [22] has a smoother transition from the cork to skirt at chord length of approximately 25 mm. This is further supported by the numerical result from Verma et al. [70] where the dip in pressure at around 30 mm chord was also observed. At chord length of 30 mm to 40 mm, it was observed that the pressure peak occurs earlier in the experimental data. This is likely because the experiment

was conducted on a cone of 81 mm in length in [22], while the numerical data was modelled after the 85 mm long cone used by Verma et al. [70]. The difference in experimental and numerical data at the end of the skirt may be the difference between the testing of a solid cone (experimental) and the simulation of a hollow thin-wall cone (numerical). The solid cone model will not have allowed the near field wake vortices to extend into the cone like on the hollow cone. Despite that, the experimental and numerical result for mid chord segment of interest show good agreement.

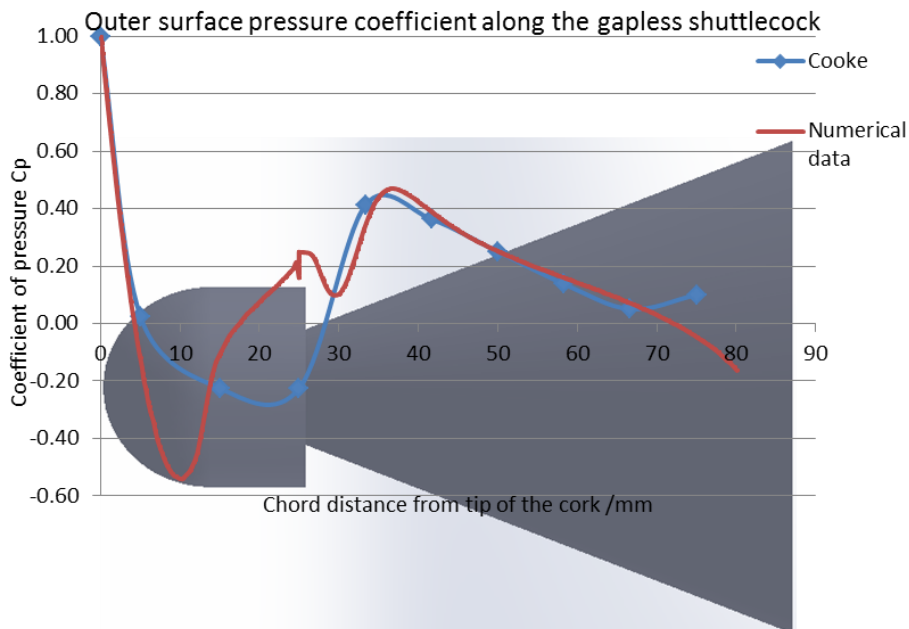


Figure 24 Outer surface pressure coefficient along the Profile A. Chord locations on plot are true to the superimposed cone model.

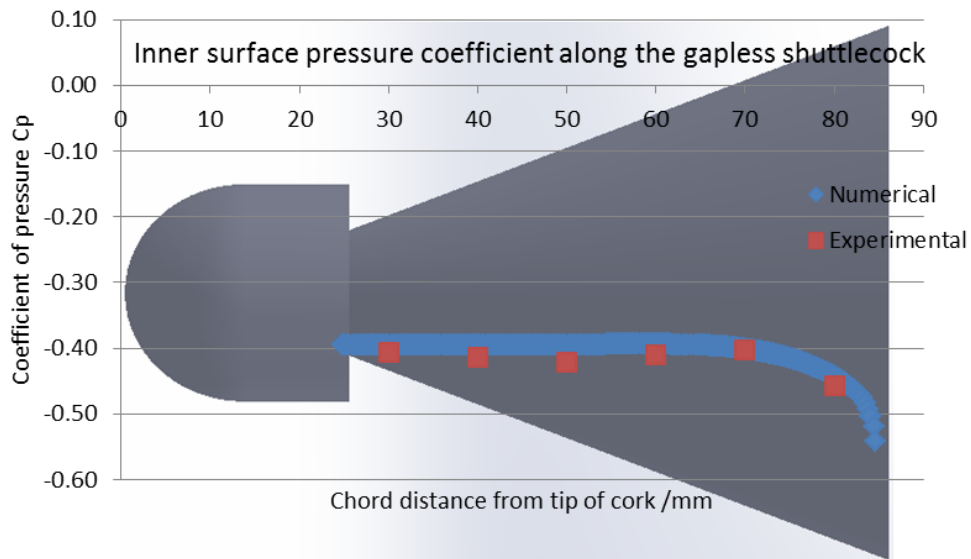


Figure 25 Inner surface pressure coefficient along Profile A. Chord locations on plot are true to the superimposed cone model.

Good agreement is observed in the comparative analysis between the numerical result and the experimental data for the inner surface pressure coefficient. This further reinforces the validity of the numerical work. In both sets of data, the inner surface coefficient of pressure is approximately -0.4 along the chord of the skirt. Closer to the trailing edge of the skirt, it was observed that pressure further decreases. This is possibly the effect of the wake vortices which extend into the cone, as seen in Figure 22. Negative pressure coefficient means suction pressure on the inner surface that pulls the shuttlecock to resist the motion, thereby increasing drag force. The resultant effect when combined with the positive pressure on the windward side (outer surface) produces the high pressure drag associated with a blunt body like Profile A. The plots of coefficient of pressure for inner and outer surface of the cone (Profile A) have been compiled in Figure 26 for free stream flow of 6 m/s and 50 m/s. The pressure coefficient for the segment of the cork has been removed to enhance the ease of reading. The curve that is dominantly positive is always the outer surface (windward) pressure coefficient, while the dominantly

negative curve is for the inner surface. The area between the two curves in each plot gives the resultant drag force. No difference was observed between the plot of coefficient of pressure for 6 m/s and 50 m/s. This supports the observation of a constant drag coefficient with respect to the tested speed because drag is a function of pressure. This also means that the flow regime does not change within the applied flow speed.

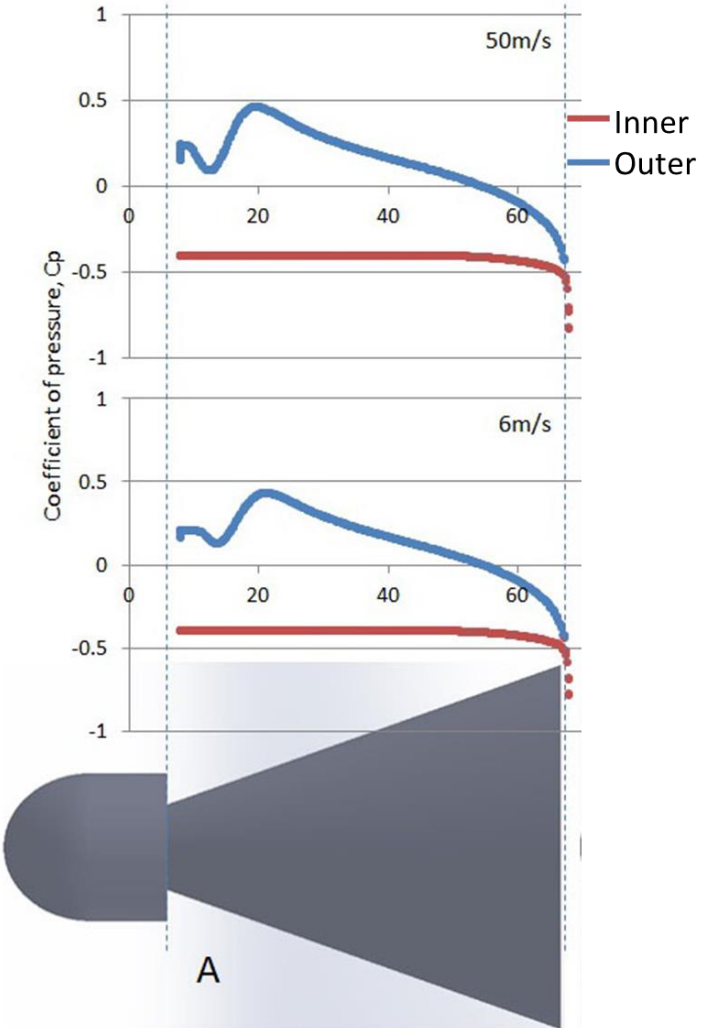


Figure 26 Coefficient of pressure for Profile A at 50m/s and 6 m/s.

### **3.3 Effect of Gaps on Coefficient of Pressure and Drag**

Pressure coefficient plots that are similar to Figure 26 were also obtained numerically for the other profiles. Figure 27 and Figure 28 are the plots for Profile B to Profile F. Comparing the pressure profiles, it was seen that this area increases with increasing gap sizes (from Profile A to Profile D), peak at Profile D, then decrease with Profile E and F. The drag force and the drag coefficient increase as gap size increases from Profile B to Profile D.

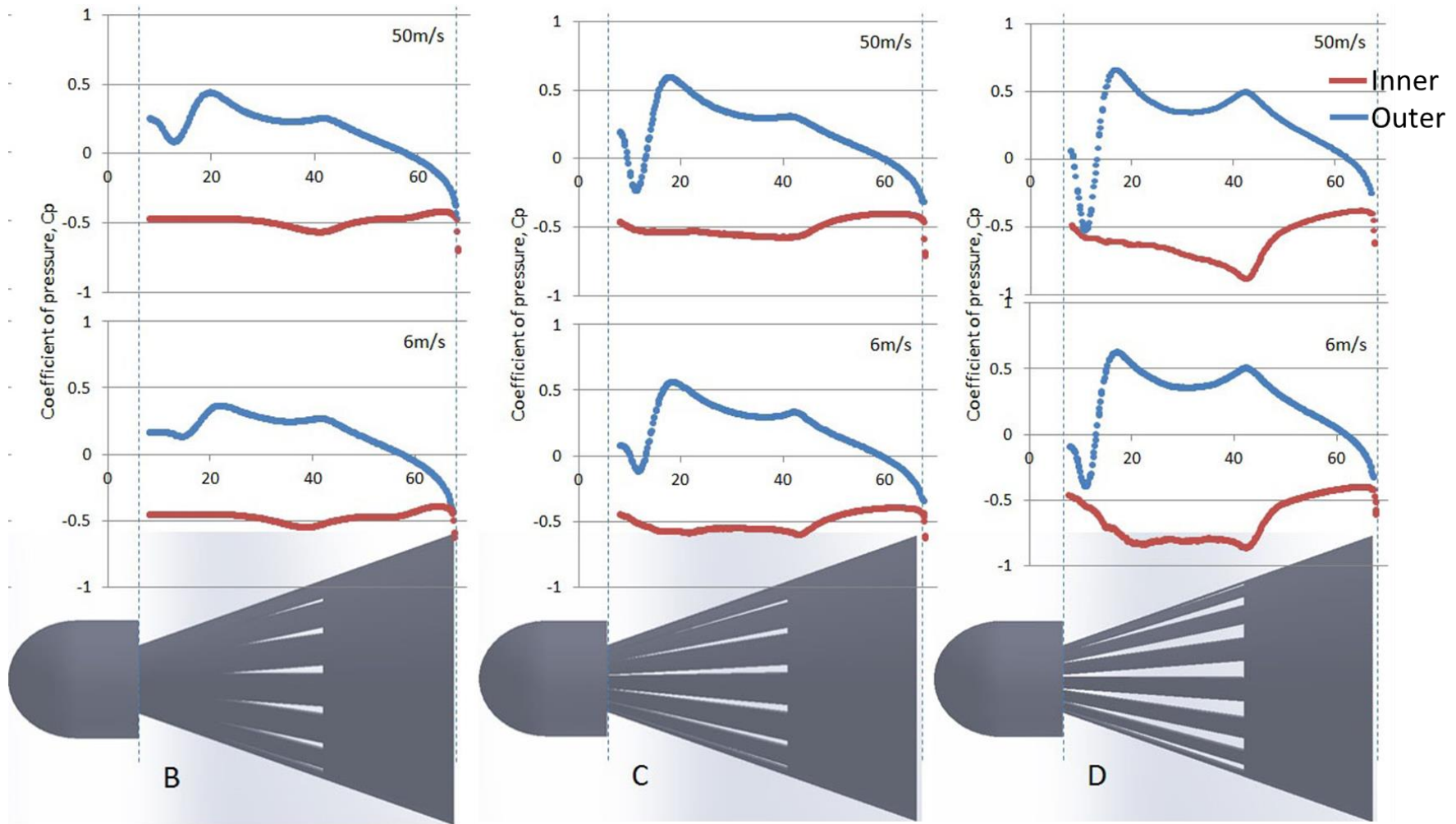


Figure 27 Coefficient of pressure plot for Profile B to D at free stream velocity of 6 m/s and 50 m/s.

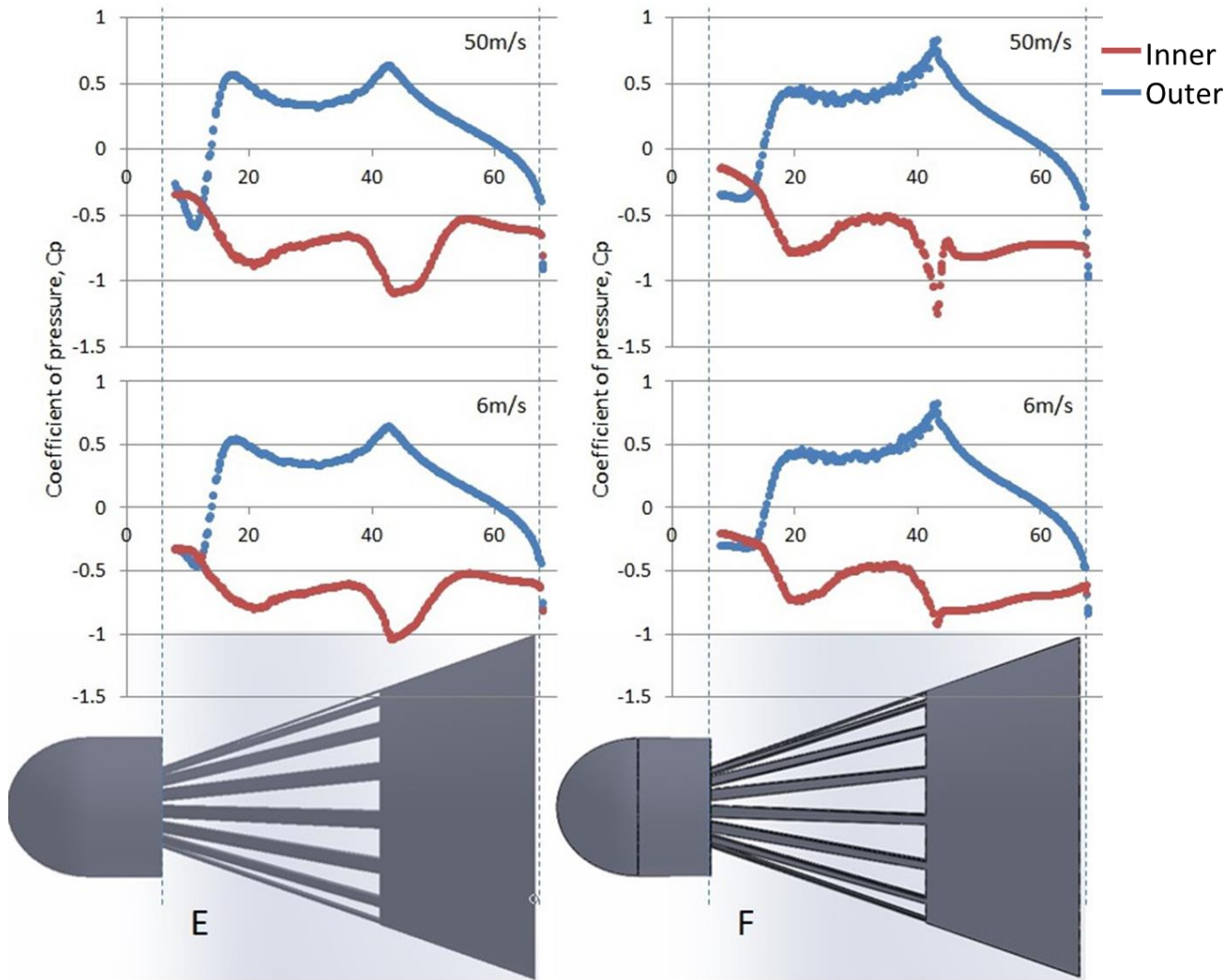


Figure 28 Coefficient of pressure plot for Profile E and D at free stream velocity of 6 m/s and 50 m/s.

As gap size further increases, as in Profile E and Profile F, drag force decreases. This is observed when comparing the numerical drag forces of the profiles at 50 m/s, as presented in Figure 29. If the gap size where drag force is peaked is termed as the critical gap size, then it can be said that a gap size above it will reduce the aerodynamic drag. Similarly, a gap size smaller than the critical gap size is also drag reducing. From Figure 29, it is observed that a gap size of 17.93% surface area reduction (Profile D) is the critical gap size. This means that the gap sizes larger than or smaller than the gap in Profile D will reduce the drag force.

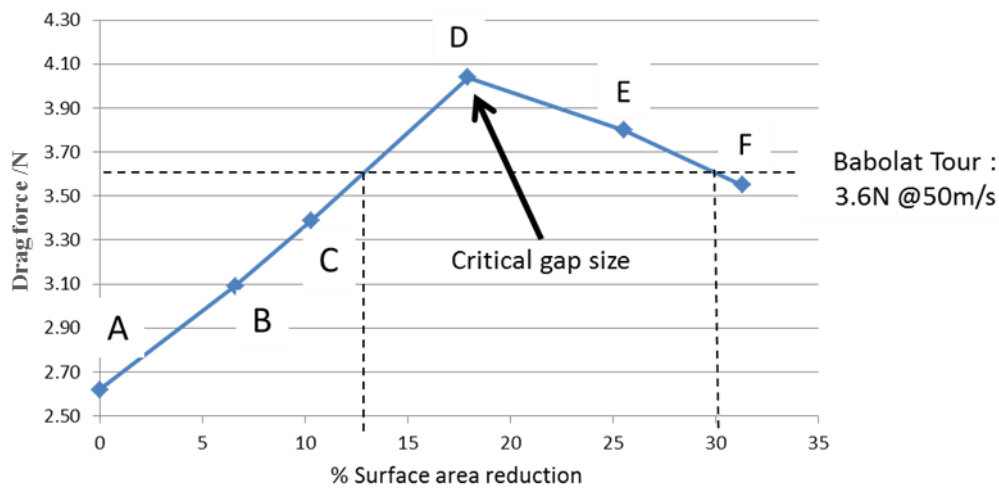


Figure 29 Change in drag force with increasing gap size at free stream speed of 50 m/s. The larger % surface area reduction will refer to bigger gaps.

The critical gap size is a very interesting property for the shuttlecock design. If such a characteristic curve is built during the shuttlecock skirt pattern design phase, then it can be seen that for the same drag requirement, there can be two design points that will fulfil it. For instance, the wind tunnel measured drag (section 5.4.2) of a Babolat Tour feather shuttlecock is 3.6 N at 50 m/s. If this flight characteristic is to be replicated on the present cone design, then the characteristic curve in Figure 29 can be applied. Through Figure 29, it can be seen that a surface area reduction of either

13% or 30% will provide a geometry that has the desired drag characteristic. Realistically, the larger gap size will be preferred because it reduces mass, decreases the moment of inertia and shifts the centre of gravity forward. These are desired properties of a better shuttlecock. However, such characteristic curves are design specific and a different one is required for a different design. The presented characteristic curve is for the same conical skirt with 15 triangular gaps that extends 35 mm up the skirt.

Increasing the number of velocity points for calculating the numerical drag coefficients of each profile gave information on velocity dependency of the drag coefficient. The drag coefficients for Profile A to Profile F at flow speed of 6 m/s, 15 m/s, 30 m/s and 50 m/s were plotted and they are presented in Figure 30. With the exception of Profile F, changes in drag coefficient with respect to the simulated air speed was less than 2% for all models. This result supports the proposition of the shuttlecock remaining in sub-critical flow regime throughout the typical operating flow speed seen in this study. Numerical drag coefficients for Profile F, which is the cone with the largest gaps, showed a variation of approximately 4% across the range of air speeds. This difference is more likely to be from the reduced blunt body effect of the larger gaps than numerical error. This is because the same simulation methodology was used for all the profiles. Thus, error from numerical method would have affected all the profiles and not just profile F.

Velocity independent drag coefficient was also proposed and observed in experimental data of literatures [20, 26, 31, 32, 91]. In those literatures it was proposed that variation in drag coefficient with air speed is the function and effect of

skirt deformation. For a non-spinning shuttlecock tested at high speed flow in the wind tunnel, skirt deformation (shrinkage) will occur. On the other hand, testing at high speed with the shuttlecock allowed to spin freely will induce skirt expansion because of the large outward centrifugal force acting on the feathers of the spinning shuttlecock. This increases the drag coefficient. In theory, the skirt deformation (and change in cross-sectional area) would have been taken into account by varying the area during the calculation of the drag coefficient. However, realistically, the common practice is to assume a constant diameter of the shuttlecock, measured without deformation. This causes the velocity dependency of drag coefficient, which is more likely to be a function of the cross-sectional area. The phenomenon was observed in the wind tunnel experiment of the shuttlecocks and will be presented in the chapter 5 of this thesis.

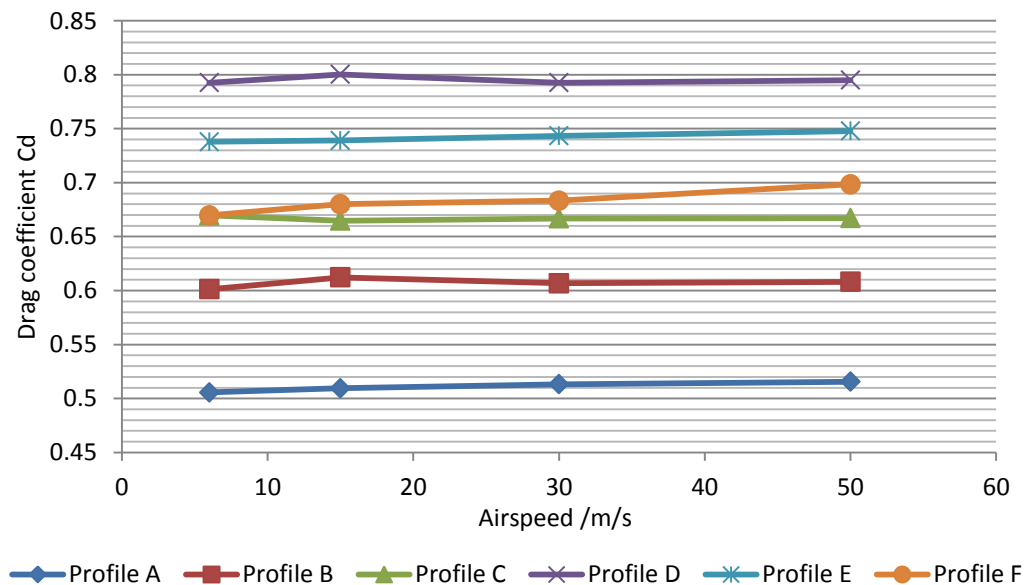


Figure 30 Drag coefficients for the different sized gap profiles.

Numerical drag coefficients for Profile A, C, and E were also validated against the experimental data and they are tabulated in Table 7. Profile A shows 3.1% difference

between experimental and numerical result, while Profile E has a 5.3% variation. These are good agreements between simulation and wind tunnel result. While the 8.5% difference observed between numerical and experimental drag for Profile C is higher than Profile A and Profile E, the result is still acceptable for such work. The differences can be attributed to numerical error, less than perfect geometrical reproduction for the physical model, and wind tunnel force balance tolerance.

Table 7 Tabulated experimental and numerical drag coefficients for Profile A, Profile C, and Profile E, at 15 m/s, 30 m/s and 50 m/s.

Profile	Airspeed (m/s)	CFD (numerical)	Wind tunnel (experimental)
A	15	0.509	0.501
	30	0.513	0.497
	50	0.514	0.491
C	15	0.665	0.612
	30	0.667	0.611
	50	0.667	0.606
E	15	0.739	0.658
	30	0.743	0.714
	50	0.734	0.728

Based on the coefficient of pressure plots in Figure 26, Figure 27 and Figure 28, the drag distribution (contribution) along the chord length of the skirt can also be deduced. Across the plots, it is seen that there is little change in coefficient of pressure in the region directly behind the cork (chord distance < 20 mm in pressure plots). As gap size was increased, only minor increase in magnitude of both the inner and outer pressure was observed in this region. Moving to the middle of the skirt (chord distance 20-40 mm on the plot), it was observed that both the inner and outer

surface pressure increased with magnitude as gap size was increased. In other words, the pressure difference between inner and outer surface at this region is increasing greatly with the increase in gap size. However, this is unlikely to be the reason for the large increase in aerodynamic drag with larger gaps. This is because having larger gaps reduces the surface area on the skirt that pressure can act on. Therefore, drag effect from increased pressure difference at this area will diminish with reduced surface area along this segment of the skirt.

Increased pressure difference was also observed at the end section of the cone directly behind the trailing edge of the gaps. This region corresponds to a chord length of 40-65 mm on the plots shown in Figure 26 to Figure 28. Physical geometry of this segment remains unchanged through the profiles. Therefore, unlike the middle segment of the skirt where gap size changes the resultant surface area, the surface area at this part of the skirt remains constant. Any change in inner or outer surface pressure at this segment will translate to change in the drag force. Comparing coefficient of pressure on the outer surface, it is seen that gaps increase the resultant pressure for chord length under 60 mm. Beyond that, there is no observable change in windward surface pressure. For Profile E and Profile F where the gaps are larger than the critical gap size, the magnitude of the negative inner pressure is also elevated at the end section. This pressure change at the end section of the cone is likely to be the reason for Profile E and Profile F to experience more drag than Profile A, Profile B and Profile C. This will also mean that a larger percentage of the total drag force is contributed by the end section when the gaps are large. It can then be inferred that the centre of pressure on Profile E and Profile F is likely to be more rearward and thus, they may be more stable in the turnover phase of the shuttlecock.

Detailed explanation of the change in coefficient of pressure will be given in subsequent section of this chapter.

### 3.4 Reduction in Blunt Body Effect with Gap size

From the characteristic curve in Figure 29, it can be deduced that gaps beyond the critical gap size reduce the drag force because of increased bleeding through the skirt that reduces the blunt body effect. Despite that, pressure drag remains the dominant drag, accounting for more than 90% of the observed drag. As seen in Table 8, the increase in gap size does not reduce the significance of the pressure drag in the overall drag. In fact, it was observed that drag forces for Profile E and Profile F comprise of larger fraction of pressure drag than the critical gap sized Profile D.

Table 8 Contribution of pressure drag to the overall drag for Profile A to Profile F, at speed of 6 m/s, 15 m/s, 30 m/s and 50 m/s.

Pressure drag as percentage of overall drag force at each simulation flow velocity				
	6 m/s	15 m/s	30 m/s	50 m/s
Profile A	94.3%	95.8%	96.7%	97.1%
Profile B	94.3%	96.2%	97.0%	97.7%
Profile C	93.5%	95.6%	96.7%	97.2%
Profile D	93.8%	96.0%	96.9%	97.4%
Profile E	94.1%	96.4%	97.4%	97.8%
Profile F	94.7%	96.8%	97.7%	98.1%

While the dominance of pressure drag does not decrease with larger gaps, the reduced blunt body effect from the gaps is evident in the flow-field study. Comparing the velocity plots of Profile A to Profile F in Figure 31, the increase in skirt porosity can be observed from the increase in air bleeding through the conical

skirt. The air bleeding through forms jets (lines) of air streams which are likely to induce the lower inner pressure that was observed in Figure 27 and Figure 28. This was also suggested in [32]. Cooke [27] made similar observation of air bleeding through the skirt in her experimental work, calling the stream of air as air jets. Further study of Profile D to F demonstrates a sudden growth of this flow stream going through the skirt when gap size is increased beyond the critical gap size. The low velocity zone in the near-field wake within the core region is also eliminated with the increased bleed through. This is likely to be the effect of the flow, which is coming out from the inner side of the cone, diluting the intensity of the recirculation vortices. In other words, the gaps increase skirt porosity and decrease the blunt body effect.

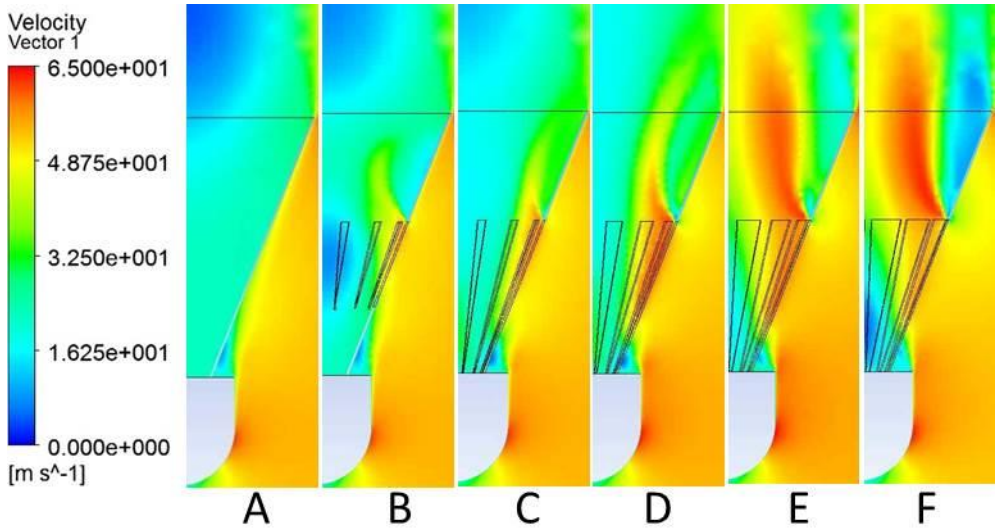


Figure 31 Velocity plots of air bleeding through the gaps show increased air flow into the skirt as the gap size increases.

To further analyse the result, flow field velocity vectors were plotted for the near wake region that is immediate of the skirt. This region is outlined in Figure 32. For visual comparison, the near wake vector plots of the six cone profiles were plotted

and are shown in Figure 33. Just like the gapless cone Profile A, the planar wake vector plot of Profile B and C in Figure 33 retains the pair of counter-rotating recirculating vortices. Despite the differing amount of flow going through the gaps and out of the cone, the wake vector plot for these three profiles are similar. With the introduction of the gaps, intensity of circulation is slightly decreased and the locations of the vortices propagate further away from the cone. Unlike Profile B and Profile C, wake vortices observed for the critical gap sized Profile D are much weaker. Beyond the critical gap size, circulation vortices are absent in the vector plot. The diminution and elimination of the circulating vortices is likely to be an effect of the increase in skirt porosity that increases the flow going through the inner surface of the skirt. This means that larger gaps increase skirt porosity and through-skirt flow, thereby reducing the blunt body effect.

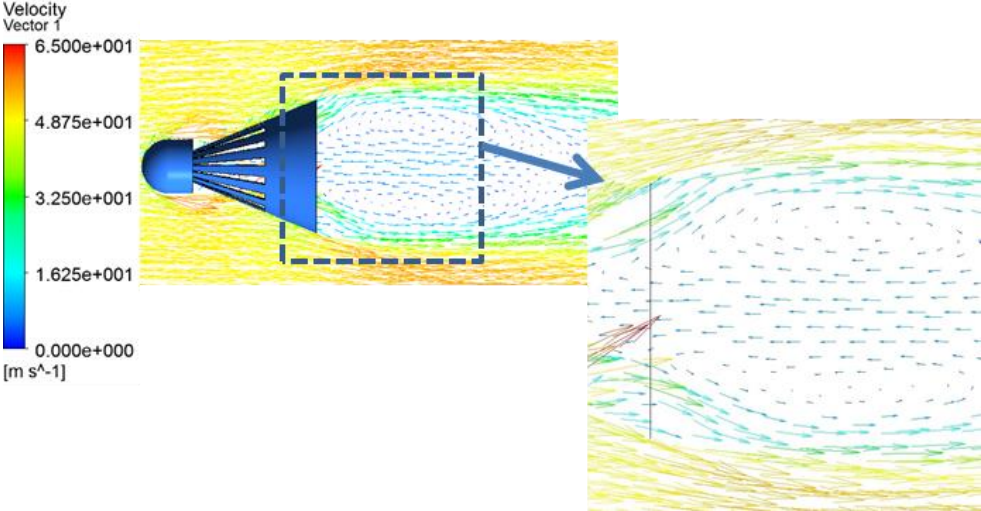


Figure 32 Region of the flow wake that is compared in Figure 33.

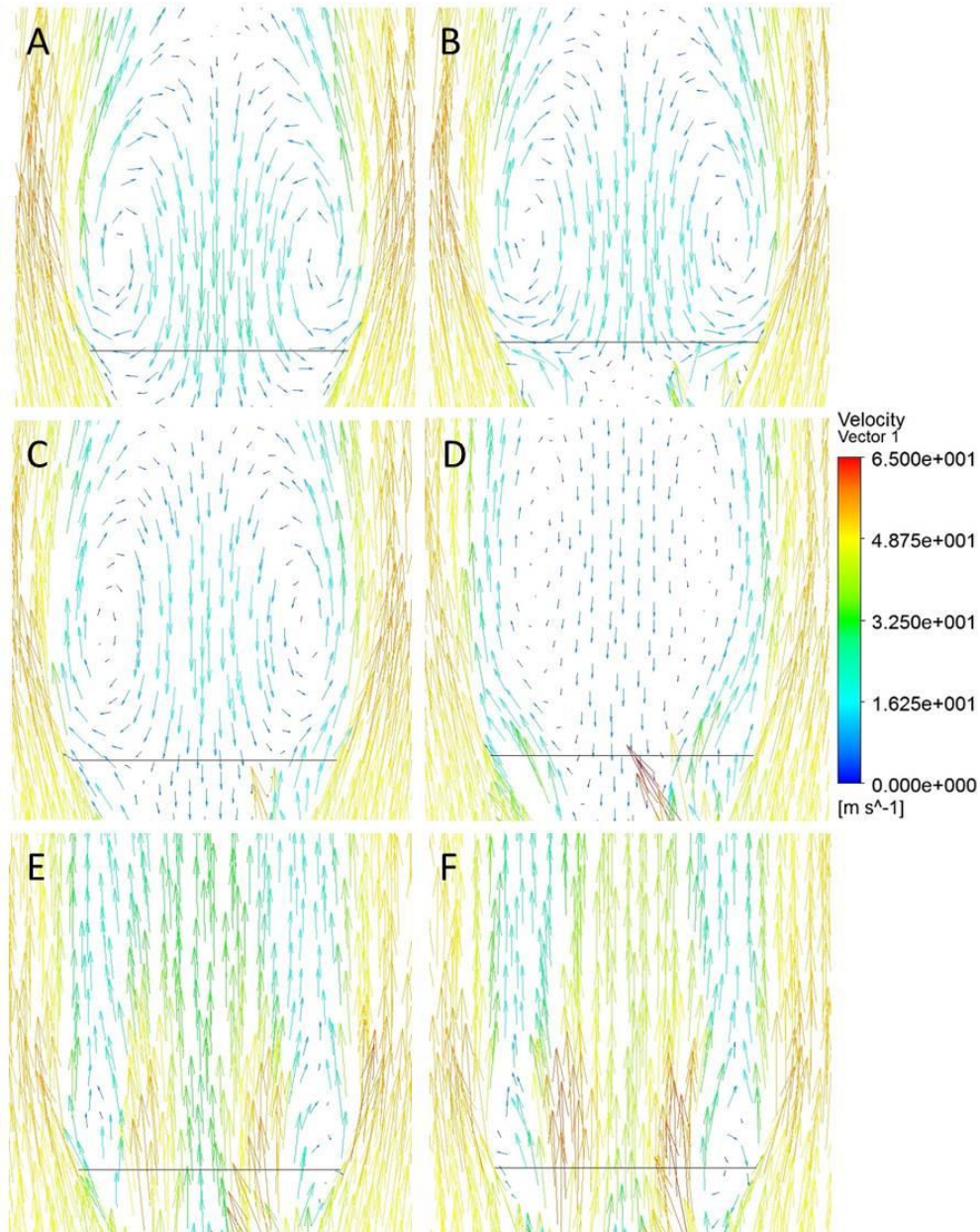


Figure 33 Velocity vector plot of wake behind the cone for Profile A to F. It is seen that intensity of the recirculating vortices reduces with larger gaps. Beyond the critical gap size, vortices are no longer present.

Flow deflection on the outer surface of all profiles remains similar regardless of the size of the gaps. This suggests that the gaps, which are located further upstream, do not affect the flow condition on the outer (windward) surface near the end of the cone. This is supported by Figure 27 and Figure 28, where little variation is seen for the outer surface pressure beyond 60 mm chord length. The observation is in contrast

to [32] which suggested that bleeding of air into the skirt will reduce outer surface flow.

### 3.5 Discussion of Coefficient of Pressure with Gaps

The change in coefficient of pressure with gaps can be described by splitting the pressure distribution into three distinct regions. These three regions are marked as R1, R2 and R3 in Figure 34. The dashed-dotted lines that cut across the model are locations of the cut planes which will be used to explain the phenomenon. These segments were taken at their chord distance because they correspond to the locations of the pressure peaks and the pressure dips.

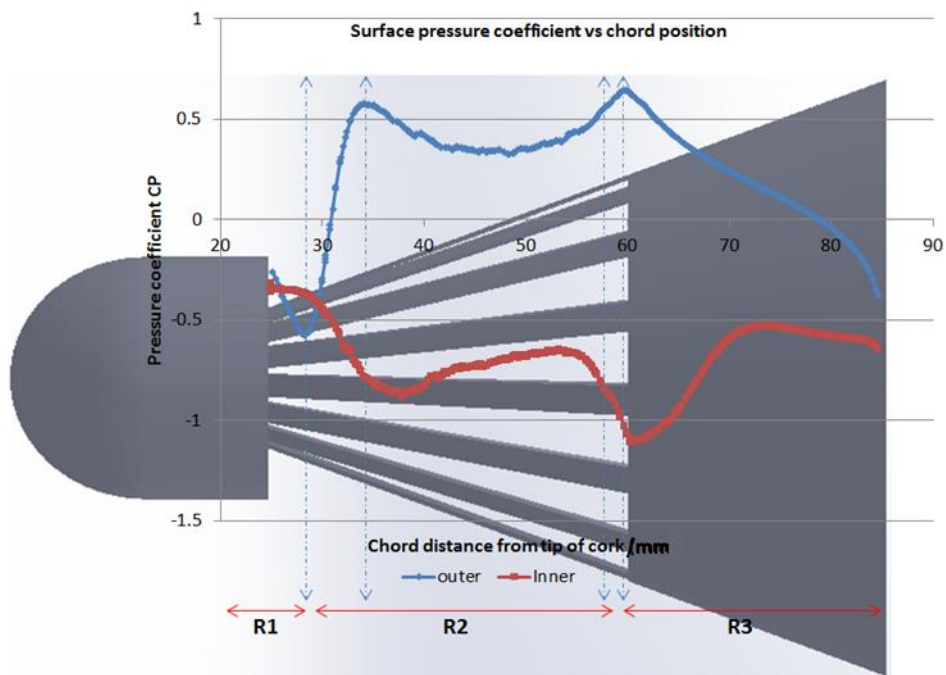


Figure 34 Coefficient of pressure plot with respect to chord length for Profile E. The symbols R1 to R3 refer to region 1 to 3, while the dotted lines refer to the locations along the chord for the cut planes.

The first region, R1, that occurs behind the tip of the cork exhibits low pressure on the outer surface. This phenomenon is the same as the low pressure that is usually observed for leeward back wall of blunt bodies in flow, such as in [86] and [100]. In

the case of a badminton shuttlecock, it is likely that the cork upstream acts as the bluff body. A pressure plot of the plane at 28.3 mm is presented in Figure 35, with a clip plane of the shuttlecock set at 29.2 mm. In the pressure plot of the plane, it is observed that low pressure is only experienced in the area sheltered by the cork, supporting the proposition of the cork being the blunt body here. Going outward in the axial direction of this plane, pressure increases rapidly. Since pressure difference between the inner and outer surface is small here, drag is unlikely to be produced from this area. It is possible that this pressure drop may not be observed if the skirt is flush with the cork at the intersection where chord distance is 25 mm in Figure 34.

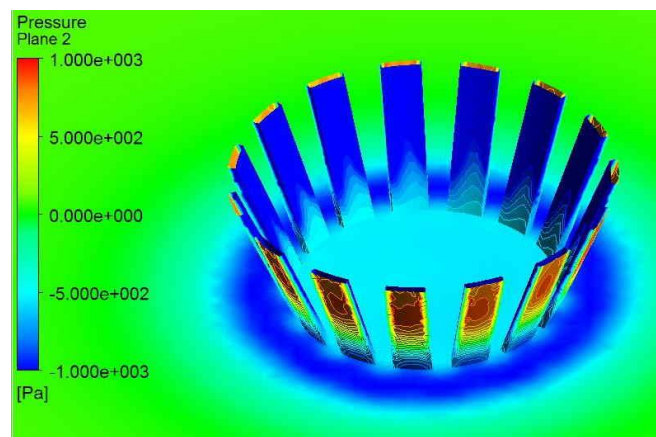


Figure 35 Pressure plot of the plane at 28.3 mm, with the clip plane set at 29.2 mm. This is a segment from R2.

Beyond the low pressure depression in R1, magnitude of the pressure on both the inner and outer surfaces increase rapidly in R2, peaking at 34 mm chord distance in Figure 34. The pressure contour plot in Figure 36 shows the pressure along the plane at 34.3 mm. The reason for this pressure spike on the outer surface is a high speed flow stream hitting on the stems (shafts) between the gaps. This stream is the flow that was deflected by the cork. In the upstream region at the hemispherical end of the cork, air is slowed down and deflected to skirt around the cork. This means that the

deflected air flow will effectively join the free stream that is flowing pass the cylindrical part of the cork, increasing the flow speed around the cork and producing a high speed stream that exceeds the speed of the free stream velocity. Therefore, a high pressure peak is created when this stream is blocked by the stems between the gaps. The velocity vector plot in Figure 37 shows this stream of air. While the magnitude of this peak is dependent on the presence of gaps, this pressure peak will be present regardless of the gaps because it originates from the increased flow deflected by the cork.

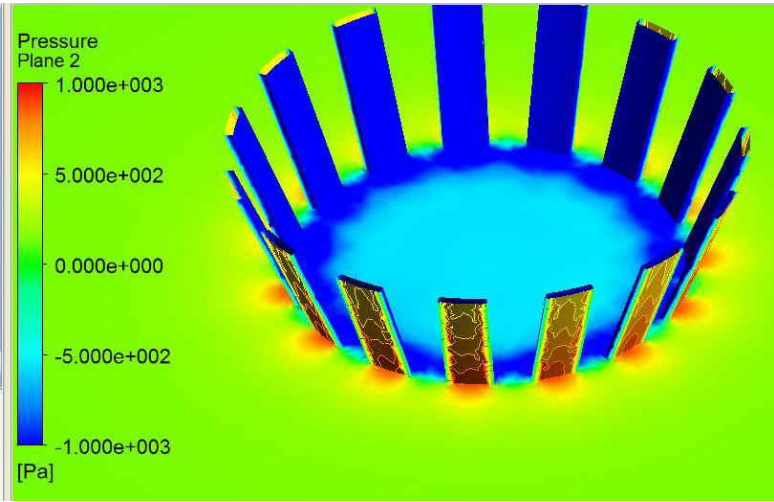


Figure 36 Pressure plot on plane at 34.3 mm behind the cork, where the pressure peak occur. The clip plane is at 35.1 mm.

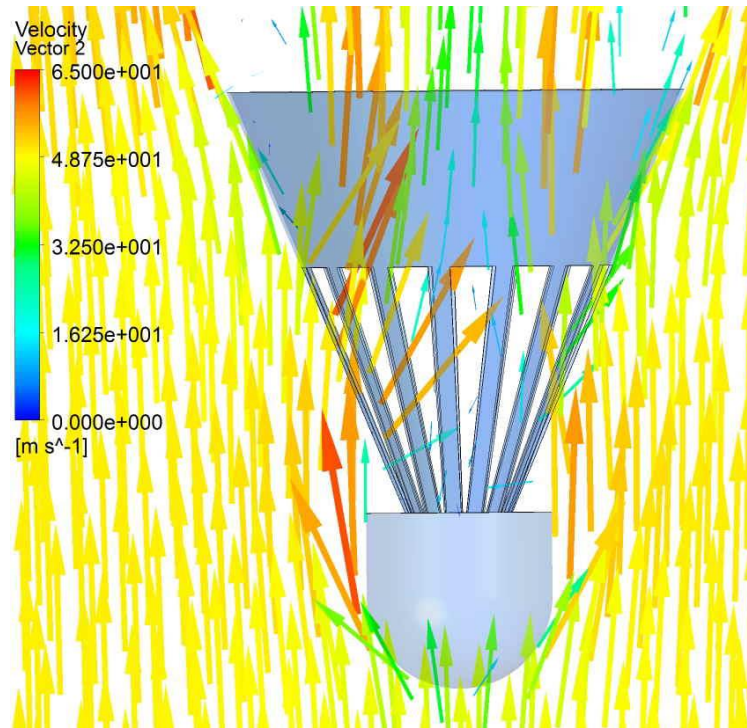


Figure 37 Velocity vector plot around Profile E at 6 m/s. This plot shows the high speed stream that was deflected by the cork hitting on the stems of the skirt, causing the high pressure peak.

Between R2 and R3, differential pressure between the inner and outer surface remains high across the stems. A second pressure peak is observed at R3 (60 mm) of Figure 34, where the gaps on the skirt terminate. This is likely to be the effect of the flow being blocked by the end of the gaps, where the flow is split to either go along the contour on the outer surface or through the inside of the cone. In other words, the end of the gaps on the skirt against the flow will represent an angled plate in a free stream. Therefore, the pressure peak can be viewed as a stagnation point caused by the blockage. Pressure contour of the plane at 57.3 mm and 59.8 mm behind the tip of the cork are given in Figure 38 and Figure 39. The plane at 57.3 mm is near the end of the gaps, while the plane at 59.8 mm is at the end of the gaps. In Figure 38, it can be seen that a ring of higher pressure region is forming around the skirt. Moving to the end of the gaps in Figure 39, the pressure contour shows the termination of

gaps producing a ring of high pressure region on the outer surface and a low pressure region in the inner surface. This large pressure difference contributes to the pressure drag acting on the skirt. Unlike the first pressure peak on the skirt, this second pressure peak is not only affected by the size of the gaps, but is also dependent on the presence of gaps. This is because there will be no stagnation or splitting of the air at 60 mm when gaps are not present. Therefore, this pressure peak is not seen on the gapless Profile A. In the design of the shuttlecock, the location of this pressure peak (and thus, the location of the centre of pressure) can be adjusted by changing the end points of the gaps.

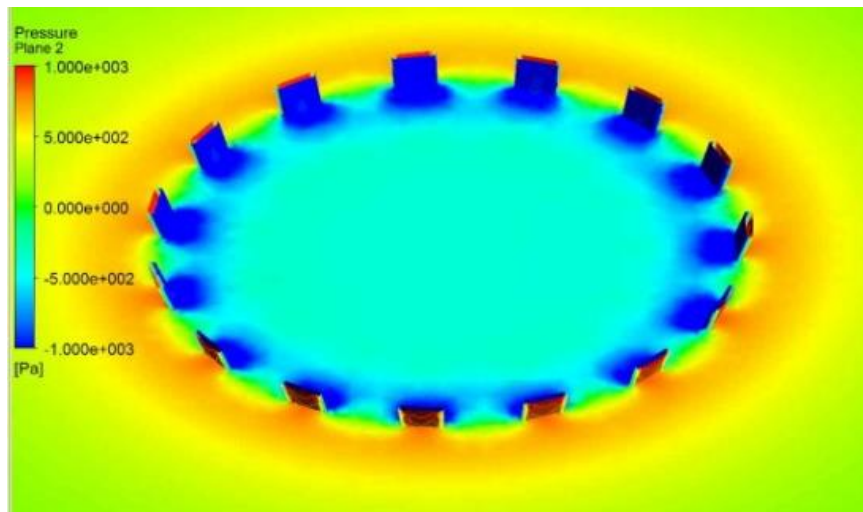


Figure 38 Pressure plot of the plane at 57.3 mm, near the end of the gaps. Clip plane was set to 57.5 mm. Increased pressure is seen around the skirt forming a ring of higher pressure region.

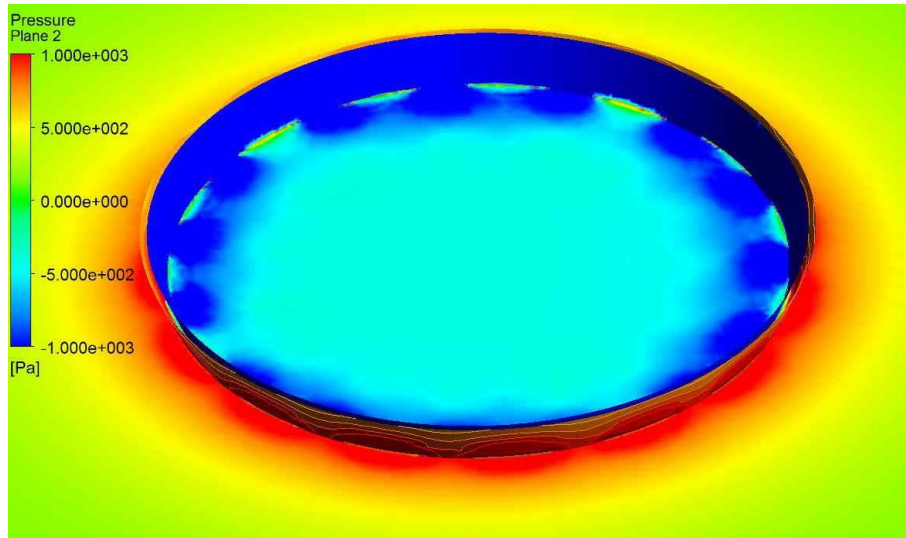


Figure 39 Pressure contour at plane 59.8 mm behind the cork, where the gaps end on the skirt. The termination of the gaps creates a high pressure region around the skirt.

### 3.6 Summary

Flow around a gapless cone and cork model was investigated through numerical method. Good agreement was obtained between the experimental and numerical result for drag and pressure distribution. This validated the result and the simulation method. Five other cones with various gap sizes (Profile B to Profile F, Table 5) were then analysed. The results presented include aerodynamic drag, pressure plane plots, flow field vector plots and pressure distribution.

It was observed that while drag was increased by the presence of gaps, there exists a critical gap size beyond which drag will decrease. The characteristic drag curve that was shown is useful in obtaining design points when replicating the drag characteristic of a shuttlecock. Through the flow field vector plot, it was discovered that blunt body effect diminishes with increased gap size. This is because the increase in base bleed dilutes the wake structure that was observed on a gapless cone. This means that a shuttlecock, which has always been categorised

aerodynamically as a blunt body, may not necessarily have the same wake structure as a perfect gapless blunt body cone.

The coefficient of pressure plots in Figure 26, Figure 27 and Figure 28 also gave new knowledge on the trend on aerodynamic drag with respect to gap size. The presence of a critical gap size means there may be two possible dimensions of the same design that can fit a design specification point. The pressure contour plot on the cut planes also demonstrated that the pressure peaks at the upstream region of the skirt are unavoidable, while the pressure peak located closer to the end of the skirt can be engineered by varying the gaps. This chapter has also established a simulation template for the rapid development framework that will be detailed in chapter 8.

## **4. SHUTTLECOCK FLIGHT DYNAMICS**

This chapter focuses on the flight dynamics of the badminton shuttlecock. A system of six degree of freedom (DOF) equation will be derived specifically for the badminton shuttlecock flight. This system is based on previous literatures, phenomenon of shuttlecock flight and understanding from the current work.

### **4.1 States of Flight**

Flight of a shuttlecock can be described by two distinct states. There is no specific naming for the stages or the regime of flight. Conventionally, they are termed as unsteady and steady flight state in badminton literatures. The unsteady state flight involves flight from contact with racket to the turnover process, till before reaching stabilized flight [23]. Stabilized flight in this context refers to a shuttlecock with heading that is aligned to the flight path. Flight transits into the steady state upon this stage. The unsteady flight state and the transition to steady flight state were illustrated and this is shown in Figure 40. As mentioned in the literature review, most works on shuttlecocks were focused on steady flight state focusing on trajectory and wind tunnel simulation. This is likely because the unsteady flight state is a fast occurring process that is much less dominant than the steady flight state. Moreover, the rapid transitional behaviour means that the unsteady flight state is difficult to be observed without good technology.

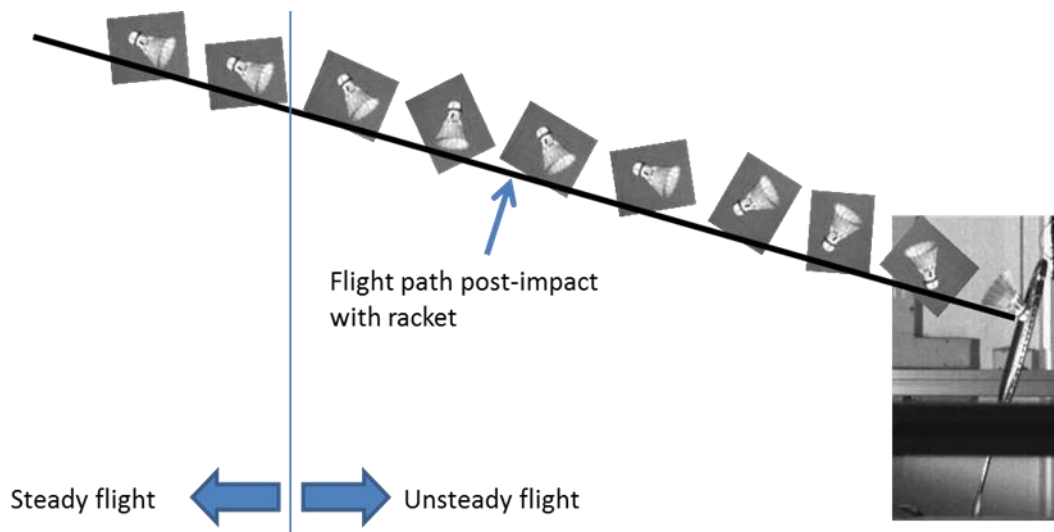


Figure 40 Illustration of shuttlecock heading with respect to flight path in the unsteady state flight.

#### 4.1.1 Unsteady Flight

The unsteady state flight is a fast occurring transitional stage. Upon impact with the racket, the shuttlecock deforms and bounces off the racket string bed. After the bounce off, the shuttlecock shape is restored. This process is the impact deformation of the skirt and may occur even if the skirt does not contact the racket on initial impact.

After returning to shape, the shuttlecock takes a 180 degree rotation to align to the flight path. However, it overshoots and goes beyond the flight-stable neutral heading, demonstrating an underdamped response. Being an absolute stable object, restoring moment steers the shuttlecock back into a heading with little to no angle of attack. This process of large heading change is termed as the turnover. Details of the investigation of turnover phenomenon will be discussed in section 4.3.1 of this report.

### 4.1.2 Steady Flight

Following the completion of turnover, the shuttlecock transits into the steady flight state, where the angle of attack (with respect to flight path) remains relatively small throughout the flight. Unlike the steady state flight condition that is use for describing aircraft flight, flight condition is constantly varying throughout the steady flight state of a shuttlecock. The shuttlecock continues to gain height and distance, while losing speed. Beyond the vertex of the flight trajectory, stall occurs and the shuttlecock trades height for speed. This behaviour was illustrated and it is shown in Figure 41. Stall of the shuttlecock refers to the instance when the shuttlecock starts to lose trajectory height. The segment of flight before stall is termed the pre-stall region, while the segment of flight after stall is termed as the post-stall region. A near vertical drop is desired for the post-stall region. Since the unsteady flight state is a short transient phase, bulk of the flight is spent in the steady state.

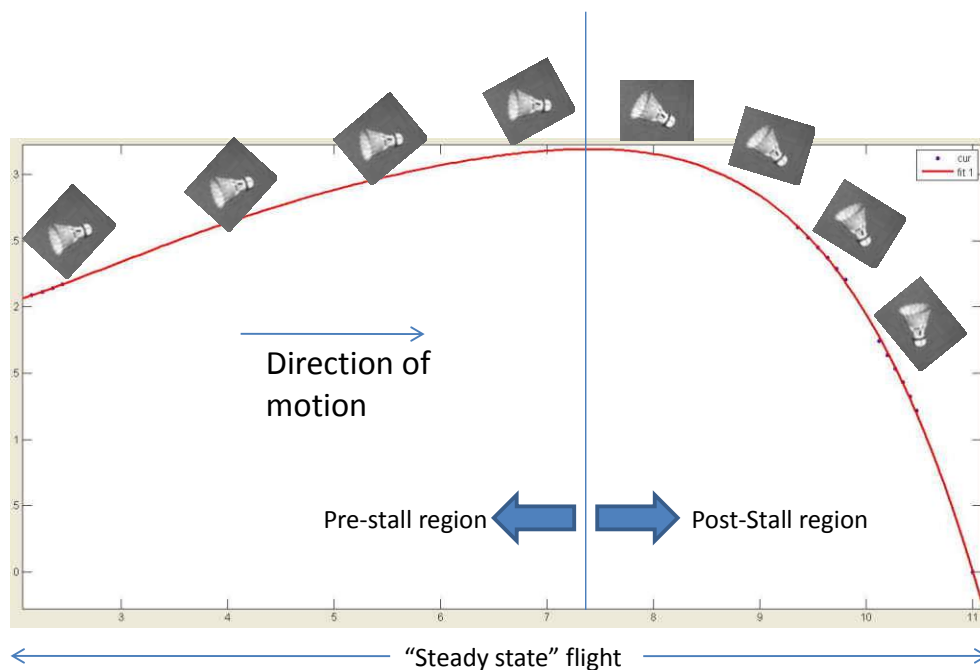


Figure 41 Illustration of pre-stall and post-stall regime of steady flight state.

## 4.2 Flight Modelling

### 4.2.1 Multiple Reference Frame

Similar to an object flying in space, the motion of a shuttlecock can be modelled by using multiple frames of reference, as illustrated in Figure 42. There are six DOF, from which, 12 states can be derived to describe its dynamic behaviour. Using a body-fixed reference frame within an earth-fixed reference frame, the 12 states in the body frame can be described by,

$$\text{States in body axis} = [x_b \ \dot{x}_b \ y_b \ \dot{y}_b \ z_b \ \dot{z}_b \ p \ \dot{p} \ q \ \dot{q} \ r \ \dot{r}] \quad (7)$$

where  $x_b, y_b$  and  $z_b$  are the position coordinates in the body frame. The symbols  $p, q$  and  $r$ , are the respective angular rate in the roll, pitch and yaw direction. The symbols  $\dot{x}_b, \dot{y}_b, \dot{z}_b, \dot{p}, \dot{q}$  and  $\dot{r}$  refer to the first time derivatives of  $x_b, y_b, z_b, p, q$  and  $r$  respectively. In the earth-fixed reference frame, the states of the shuttlecock are given by:

$$\text{States in earth – fixed frame} = [x \ \dot{x} \ y \ \dot{y} \ z \ \dot{z} \ \theta \ \dot{\theta} \ \phi \ \dot{\phi} \ \psi \ \dot{\psi}] \quad (8)$$

The Euler angles (Roll:  $\theta$ ; Pitch:  $\phi$ ; Yaw:  $\psi$ ) and the first time derivatives ( $\dot{\theta}, \dot{\phi}, \dot{\psi}$ ) give the attitude. Translation is represented by the position coordinates in the earth frame ( $x, y, z$ ) and the velocities ( $\dot{x}, \dot{y}, \dot{z}$ ).

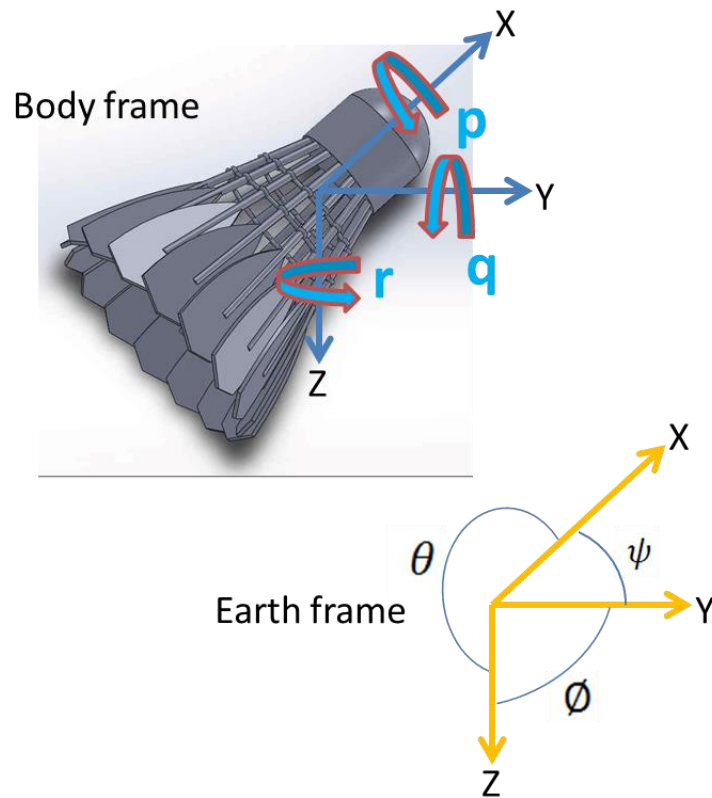


Figure 42 Reference frames and direction of axes as used in this report.

As shown in Appendix A [101], translational motion in the body frame can be mapped into the earth-fixed frame by,

$$\begin{bmatrix} \dot{x} \\ \dot{y} \\ \dot{z} \end{bmatrix}_{body} = [R] \begin{bmatrix} \dot{x} \\ \dot{y} \\ \dot{z} \end{bmatrix}_{earth} \quad (9)$$

where  $[R]$  is the derived transformation matrix. Angular motion can be mapped between coordinate frames by,

$$\begin{bmatrix} p \\ q \\ r \end{bmatrix} = \begin{bmatrix} 1 & 0 & -\sin\theta \\ 0 & \cos\phi & \sin\phi\cos\theta \\ 0 & -\sin\phi & \cos\phi\cos\theta \end{bmatrix} \begin{bmatrix} \dot{\phi} \\ \dot{\theta} \\ \dot{\psi} \end{bmatrix} \quad (10)$$

## 4.2.2 Translation

As given by Newton's law of motion, translation of a body in the earth-fixed frame is:

$$[F]_{earth} = \begin{bmatrix} m\ddot{x} \\ m\ddot{y} \\ m\ddot{z} \end{bmatrix}_{earth} = \begin{bmatrix} F_x \\ F_y \\ F_z \end{bmatrix} \quad (11)$$

where  $\ddot{x}$ ,  $\ddot{y}$  and  $\ddot{z}$  are the second time derivatives (acceleration) in the  $x$ ,  $y$  and  $z$  axis;  $F_x$ ,  $F_y$ ,  $F_z$  are the forces acting in the  $x$ ,  $y$  and  $z$  axis.

### 4.2.2.1 Gravitational force

Since gravity acts in the Z-direction of the earth frame, the gravitational acceleration can be expressed as,

$$[F_{gravity}]_{earth} = \begin{bmatrix} 0 \\ 0 \\ mg \end{bmatrix} \quad (12)$$

### 4.2.2.2 Lift and Drag

The most prominent body forces acting on a shuttlecock in flight are the aerodynamic forces, namely, lift (L) and drag (D). SF is the sideward force which is perpendicular to the drag and lift vector. S, the area, is an arbitrary area and is usually taken as the largest circular cross-section area of the skirt.

$$[F_{Aero}]_{Flight\ path} = \begin{bmatrix} D \\ SF \\ L \end{bmatrix} = \begin{bmatrix} 0.5\rho V^2 SC_d \\ 0.5\rho V^2 SC_s \\ 0.5\rho V^2 SC_L \end{bmatrix} \quad (13)$$

$C_d$  is the drag coefficient,  $C_s$  is the side force coefficient and  $C_L$  is the lift coefficient.

Airspeed is given by V which is,

$$V = \sqrt{\dot{x}_b^2 + \dot{y}_b^2 + \dot{z}_b^2} \quad (14)$$

In the treatment of lift and side force for air foils and aircrafts, the force is always assumed to have a linear relation with respect to the angle of attack,  $\alpha$ , or side slip angle,  $\beta$ . Equation (13) can then be expressed as:

$$[F_{Aero}]_{Flight\ path} = \begin{bmatrix} D \\ SF \\ L \end{bmatrix} = \begin{bmatrix} 0.5\rho V^2 S C_d \\ 0.5\rho V^2 S \frac{dC_s}{d\beta} \beta \\ 0.5\rho V^2 S \frac{dC_L}{d\alpha} \alpha \end{bmatrix} \quad (15)$$

Aerodynamic forces act in the direction of the flight path, rather than the body or earth reference frame. Two transformations are required to analyse the motion from an observer's point of view (earth-fixed frame). A first transformation converts value from flight path frame into the body frame. This is followed by the second transformation from the body frame into the earth-fixed reference frame. Therefore, a third reference frame termed as the flight path fixed frame is introduced, as seen in Figure 43 and Figure 44. The derivation of the transformation matrix is also provided in Appendix A.

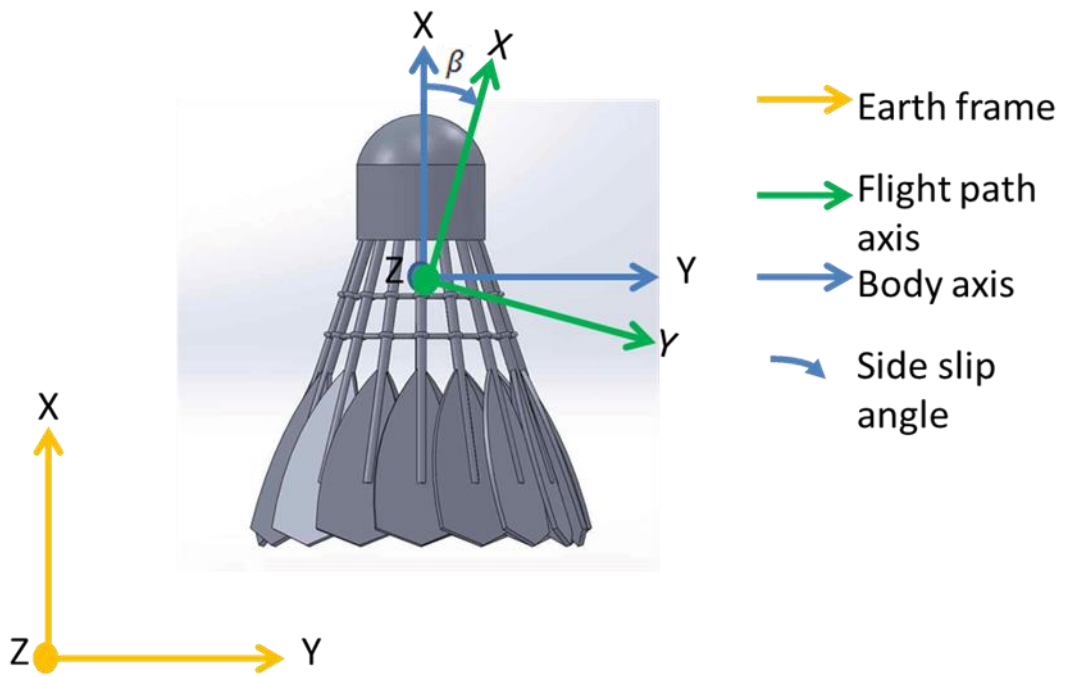


Figure 43 Shuttlecock flight with angle of attack and side slip will have an additional flight path axis.

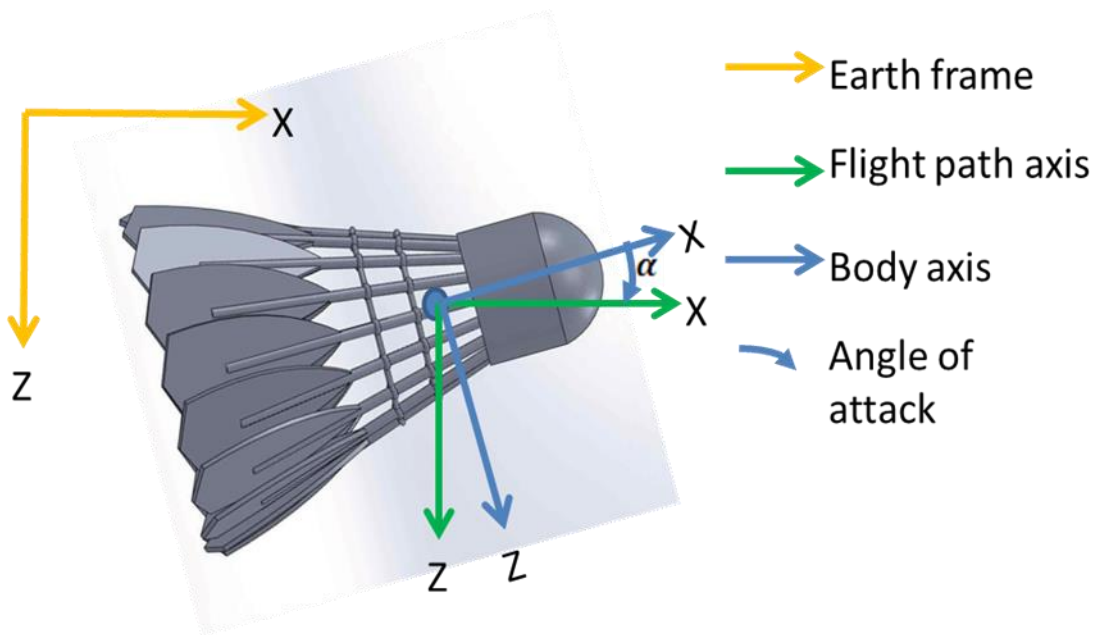


Figure 44 Axis system showing the angle of attack,  $\alpha$ , between the flight path axis and body axis.

A second transformation matrix is required. From equations (15) and (82), it can be shown that the resultant aerodynamic forces presented in the earth-fixed reference frame is,

$$[F_{Aero}]_{earth} = \begin{bmatrix} F_x \\ F_y \\ F_z \end{bmatrix}_{Aero-earth} = [R]^T [R_{FP}]^T \begin{bmatrix} D \\ SF \\ L \end{bmatrix} \quad (16)$$

#### 4.2.2.3 Magnus Force

For an object that is travelling (translating) with spin, a side force may be observed. A shuttlecock with angular velocity in the x-axis and linear velocity in the z-axis will experience a resultant force in the y-axis due to the asymmetrical flow field. This is the Magnus effect. It is observed in the flight of many ball types, such as soccer ball [102] and baseball [103]. From the formulation observed in [104, 105], Magnus effect can be expressed as,

$$[F_m] = 0.5\rho V^2 S C_{mag} \left( \begin{bmatrix} p \\ q \\ r \end{bmatrix} \times [\hat{V}] \right) \quad (17)$$

where  $C_{mag}$  is a dimensionless Magnus force coefficient.

Since the spin of a shuttlecock is usually only in the x-axis, equation (17) can be expressed as,

$$\begin{aligned} [F_m] &= 0.5\rho V S C_{mag} \left( \begin{bmatrix} p \\ 0 \\ 0 \end{bmatrix} \times \begin{bmatrix} \dot{x} \\ \dot{y} \\ \dot{z} \end{bmatrix}_{body} \right) \\ &= 0.5\rho V S C_{mag} \begin{bmatrix} 0 \\ p\dot{z} \\ p\dot{y} \end{bmatrix} \end{aligned} \quad (18)$$

Through force analysis, Cooke [22] observed the Magnus force on a shuttlecock to be negligible. It was also ignored in all past works on shuttlecock motion. As such, the Magnus effect is included here purely for completeness.

#### 4.2.2.4 Force Summation

Combining (11) with the derived force matrix in (12), (16), and (74), the resultant equation of motion for translational motion is given as,

$$\begin{bmatrix} m\ddot{x} \\ m\ddot{y} \\ m\ddot{z} \end{bmatrix}_{earth} = \begin{bmatrix} 0 \\ 0 \\ mg \end{bmatrix} + [R]^T [R_{FP}]^T \begin{bmatrix} D \\ SF \\ L \end{bmatrix} + [R]^T [F_m] \quad (19)$$

#### 4.2.3 Rotation

According to McGhee et al. [106], the equation of motion for a rigid body with 3 DOF in angular motion can be given by equation (22). Such is the Newton-Euler formula. This set of equation can be used to describe the angular motion of an object in space, which in this instance is a shuttlecock.

$$[\sum M] = \begin{bmatrix} \sum M_x \\ \sum M_y \\ \sum M_z \end{bmatrix} = [I] \begin{bmatrix} \dot{p} \\ \dot{q} \\ \dot{r} \end{bmatrix} + \begin{bmatrix} p \\ q \\ r \end{bmatrix} \times [I] \begin{bmatrix} p \\ q \\ r \end{bmatrix} \quad (20)$$

The inertia tensor,  $[I]$  is the generic inertia matrix,

$$[I] = \begin{bmatrix} I_{xx} & -I_{xy} & -I_{xz} \\ -I_{xy} & I_{yy} & -I_{yz} \\ -I_{xz} & -I_{yz} & I_{zz} \end{bmatrix} \quad (21)$$

$M_x$ ,  $M_y$  and  $M_z$  are the moments about the x, y and z-axis;  $I_{xx}$ ,  $I_{yy}$  and  $I_{zz}$  are the moments of inertia about the x, y and z-axis.

$$\begin{aligned} \left[ \sum M \right] = & \begin{bmatrix} I_{xx}\dot{p} - I_{xy}\dot{q} - I_{xz}\dot{r} - (I_{yy} - I_{zz})qr \\ -I_{xy}\dot{p} + I_{yy}\dot{q} - I_{yz}\dot{r} - (I_{zz} - I_{xx})pr \\ -I_{xz}\dot{p} - I_{yz}\dot{q} + I_{zz}\dot{r} - (I_{xx} - I_{yy})pq \end{bmatrix} + \\ & \begin{bmatrix} -I_{xz}pq - I_{yz}qq + I_{xy}pr + I_{yz}rr \\ -I_{xz}pp - I_{yz}pq + I_{xy}qr + I_{xz}rr \\ -I_{xy}pp - I_{yz}rp + I_{xy}qq + I_{xz}rp \end{bmatrix} \end{aligned} \quad (22)$$

Since a badminton shuttlecock can be assumed as an axisymmetric body, equations (21) and (22) can be simplified to:

$$[I] = \begin{bmatrix} I_{xx} & 0 & 0 \\ 0 & I_{yy} & 0 \\ 0 & 0 & I_{zz} \end{bmatrix} \quad (23)$$

$$\left[ \sum M \right] = \begin{bmatrix} I_{xx}\dot{p} - (I_{yy} - I_{zz})qr \\ I_{yy}\dot{q} - (I_{zz} - I_{xx})pr \\ I_{zz}\dot{r} - (I_{xx} - I_{yy})pq \end{bmatrix} \quad (24)$$

#### 4.2.3.1 Pitch and Yaw Moment

Forces acting on a body at points away from the centre of gravity, produce resultant torques. Since the major body forces acting on a shuttlecock in flight are the aerodynamic forces, the significant moments about the shuttlecock body are the corresponding aerodynamic moments. According to Bertin and Cummings [107], the aerodynamic moment for any air foil is given as,

$$M = 0.5\rho V^2 S C C_M \quad (25)$$

where C is the chord length and  $C_M$  refers to the moment of coefficient. Similar to S, C is an arbitrary term to fulfil the dimensionless property of  $C_M$ . By convention, C refers to the chord length, which can be taken as the overall length for a badminton shuttlecock. The approach of using the shuttlecock length as chord length was also applied in [26].

For a body in flight, such as a shuttlecock, change in moment with angle of attack is given as,

$$M = 0.5\rho V^2 SC \frac{dC_M}{d\alpha} \alpha \quad (26)$$

where  $\frac{dC_M}{d\alpha}$  is the first derivative of the coefficient of moment with respect to the angle of attack [101]. This linearity was experimentally determined in [22, 26, 31].

The aerodynamic pitching moment is then expressed as:

$$M_{aero} = \begin{bmatrix} M_x \\ M_y \\ M_z \end{bmatrix}_{Aero} = \begin{bmatrix} 0 \\ 0.5\rho V^2 SC \frac{dC_M}{d\alpha} \alpha \\ 0.5\rho V^2 SC \frac{dC_{M_z}}{d\beta} \beta \end{bmatrix} \quad (27)$$

where y-axis rotation is pitching moment, and z-axis rotation is yawing moment.

#### 4.2.3.2 Spin

Axial spin is generated by the aerodynamic moment in the x-axis. This is due to a moment (torque) being generated by air going around the profile of the shuttlecock skirt. Treating the shuttlecock as a wind milling propeller that is converting linear kinetic energy into rotational kinetic energy, the derivation in [108] can then be modified to represent this resultant driving torque (moment). Taking a control volume of projected area,  $A_{cv}$ , and length,  $L$ , for a shuttlecock travelling at air velocity,  $V$ , as seen in Figure 45, the kinetic energy, K.E., available is given as:

$$K.E. = 0.5\rho A_{cv} l V^2 \quad (28)$$

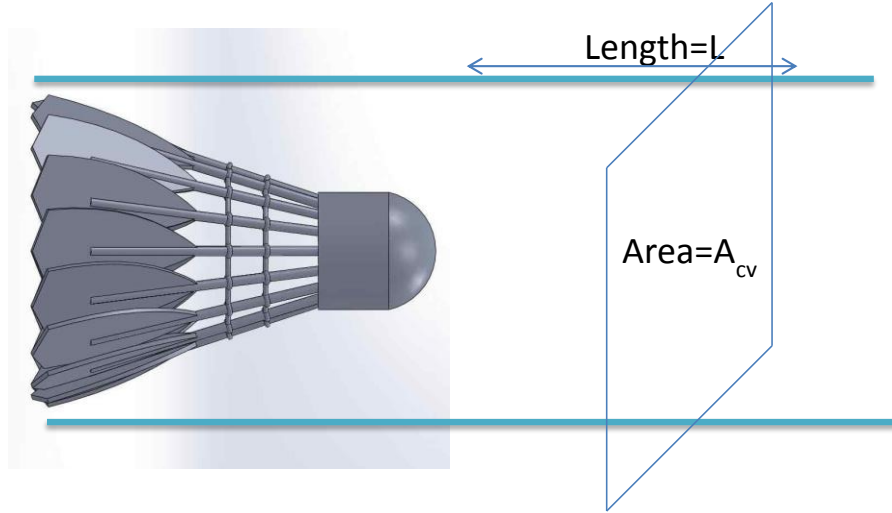


Figure 45 Control volume of area and length as given.

Therefore the power available in that control volume of air is:

$$\frac{d K. E.}{dt} = 0.5\rho A_{cv}V^2 \frac{d l}{dt} = 0.5\rho A_{cv}V^3 \quad (29)$$

Since torque is a function of power and spin rate, the potential driving torque, T, that can be extracted from the volume of air over the shuttlecock is:

$$T = \frac{0.5\rho A_{cv}V^3}{spin\ rate} \quad (30)$$

Equation (30) is the theoretical maximum driving torque when all the linear kinetic energy of the airflow is converted to rotational energy. Since the wake in the shuttlecock flow field is not a state of zero kinetic energy, a correction factor, which will be termed as the torque coefficient,  $C_T$ , is added to represent the incomplete extraction of kinetic energy.

$$T = \frac{0.5\rho A_{cv}V^3 C_T}{spin\ rate} \quad (31)$$

Assuming that only the spin generated by flow in the x-axis is significant, equation (31) can then be expressed for a shuttlecock as:

$$M_T = \begin{bmatrix} T \\ 0 \\ 0 \end{bmatrix} = \begin{bmatrix} 0.5\rho AC_T \frac{\dot{x}^3}{p} \\ 0 \\ 0 \end{bmatrix} \quad (32)$$

Equation (32) is the driving torque that spins a shuttlecock. However, for an object spinning in a viscous medium (such as air), there must exist a resistive torque that is attempting to slow down the object. This is a drag (counter torque) in the rotation. Taking the shuttlecock as a propeller, the torque required to spin the shuttlecock can be given by:

$$Q = \rho d^5 p^2 C_Q \quad (33)$$

where  $C_Q$  is a dimensionless torque coefficient [109]. The resultant torque effect of the driving torque,  $T$ , and the resistive torque,  $Q$ , on the spin rate,  $p$ , is illustrated in Figure 46.

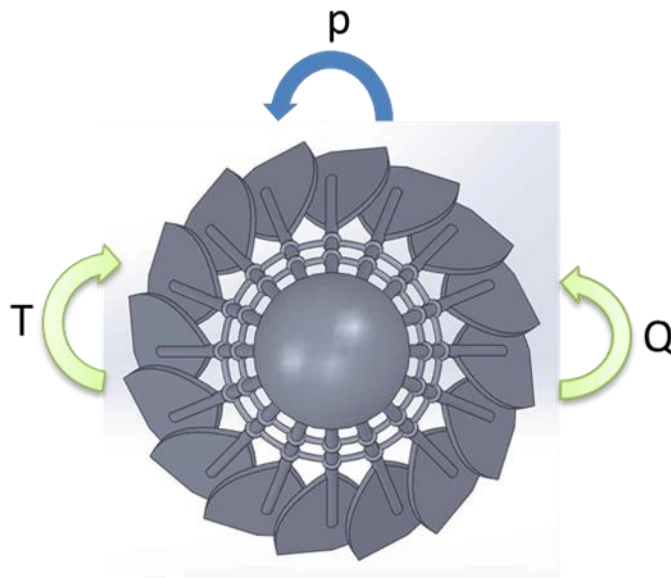


Figure 46 Free body diagram of torque equilibrium.

The resultant moment involving spin can thus be expressed by:

$$M_{spin} = \begin{bmatrix} Q - T \\ 0 \\ 0 \end{bmatrix} = \begin{bmatrix} \rho d^5 p^2 C_Q - 0.5 \rho A C_T \frac{\dot{x}^3}{p} \\ 0 \\ 0 \end{bmatrix} \quad (34)$$

where  $M_{spin}$  presents the resultant spin moment.

#### 4.2.3.3 Angular Damping Factor

In the thesis by Cooke [22], the angular response of the badminton shuttlecock pitching motion was thought to be a damped harmonic oscillation. This was thus represented by:

$$I_{yy} \ddot{\theta} + c \dot{\theta} + \left| \frac{dM}{d\alpha} \right| \alpha = 0 \quad (35)$$

where the damping factor,  $c$ , was added to model the dissipation of angular rate. This is an underdamped response that is similar to the underdamped mass-spring-damper setup. This was only assumed for steady flight because that thesis [22] was not focusing on the unsteady turnover process. Through experimental work on the turnover process, it was observed that this can also be used to model the unsteady flight state, as will be discussed in section 4.3.1. Therefore,  $c$  should also be included in the equation of motion. The axisymmetric property of the shuttlecock also means that  $c$  can be applied to model the yaw behaviour. The presentation of angular motion,  $\dot{\theta}$ , in the damping torque must also be converted to the body rates because Cooke [22] worked with a 2-dimensional system which does not apply multiple frames of reference. Therefore, the damping moments,  $M_{damping}$ , is:

$$M_{damping} = \begin{bmatrix} 0 \\ cq \\ cr \end{bmatrix} \quad (36)$$

The physical meaning of this term is similar to the resistive torque,  $Q$ , of the axial spin. This can be visualised by imaging a shuttlecock that is rotating (flipping) in the pitch direction. While the shuttlecock is rotating, two moments are being produced to restore the pitch heading. The first is the aerodynamic moment from the angle of attack, which was given in (27). The second moment is the resistance to rotation, where the faster a shuttlecock is rotating (flipping), the stronger this resistive moment is. This is  $M_{damping}$  which was not considered in [22].

#### 4.2.3.4 Torque Summation

Combining (24), (27), (34) and (36), the moments acting on the badminton shuttlecock are:

$$\begin{aligned} \left[ \sum M \right] &= M_{aero} + M_{spin} + M_{damping} \\ \left[ \sum M \right] &= \begin{bmatrix} \rho d^5 p^2 C_Q - 0.5 \rho A_{cv} C_T \frac{\dot{x}^3}{p} \\ -0.5 \rho V^2 S C \left| \frac{dC_M}{d\alpha} \right| \alpha - cq \\ -0.5 \rho V^2 S C \left| \frac{dC_{M_z}}{d\beta} \right| \beta - cr \end{bmatrix} = \begin{bmatrix} I_{xx} \dot{p} - (I_{yy} - I_{zz}) qr \\ I_{yy} \dot{q} - (I_{zz} - I_{xx}) pr \\ I_{zz} \dot{r} - (I_{xx} - I_{yy}) pq \end{bmatrix} \end{aligned} \quad (37)$$

#### 4.2.4 Equation of motion

From (19) and (37), the overall equation of motion is:

$$\begin{bmatrix} \dot{x}_{earth} \\ \dot{y}_{earth} \\ \dot{z}_{earth} \\ \dot{p} \\ \dot{q} \\ \dot{r} \end{bmatrix} = \begin{bmatrix} \begin{bmatrix} 0 \\ 0 \\ g \end{bmatrix} + [R]^T [R_{FP}]^T \begin{bmatrix} \left(\frac{D}{m}\right) \\ \left(\frac{SF}{m}\right) \\ \left(\frac{L}{m}\right) \end{bmatrix} + [R]^T \left[\frac{F_m}{m}\right] \\ \left(\rho d^5 p^2 C_Q - 0.5 \rho A_{CV} C_T \frac{\dot{x}^3}{p} + (I_{yy} - I_{zz})qr\right) / I_{xx} \\ \left(-0.5 \rho V^2 SC \left|\frac{dC_M}{d\alpha}\right| \alpha - cq + (I_{zz} - I_{xx})pr\right) / I_{yy} \\ \left(-0.5 \rho V^2 SC \left|\frac{dC_{M_z}}{d\beta}\right| \beta - cr + (I_{xx} - I_{yy})pq\right) / I_{zz} \end{bmatrix} \quad (38)$$

The translational behaviour is described by rates in the earth-fixed frame, while angular motion is described by rates of the body-fixed frame. This is because for a observer on the ground, such as a high speed camera in the earth-fixed frame, processing for earth-fixed rates in translation and body rates in angular is a more practical approach.

### 4.3 Flight Phenomena

The following are flight phenomena of the shuttlecock that are seldom covered in literatures, including turnover, axial spin behaviour and spin-induced side drift. The exploration work on turnover has been published in [64].

#### 4.3.1 Turnover

Turnover of the shuttlecock occurs in the unsteady flight state. This allows the shuttlecock to align itself to the flight path. The typical behaviour during turnover is illustrated in Figure 47. The motion was observed to be an underdamped oscillation.

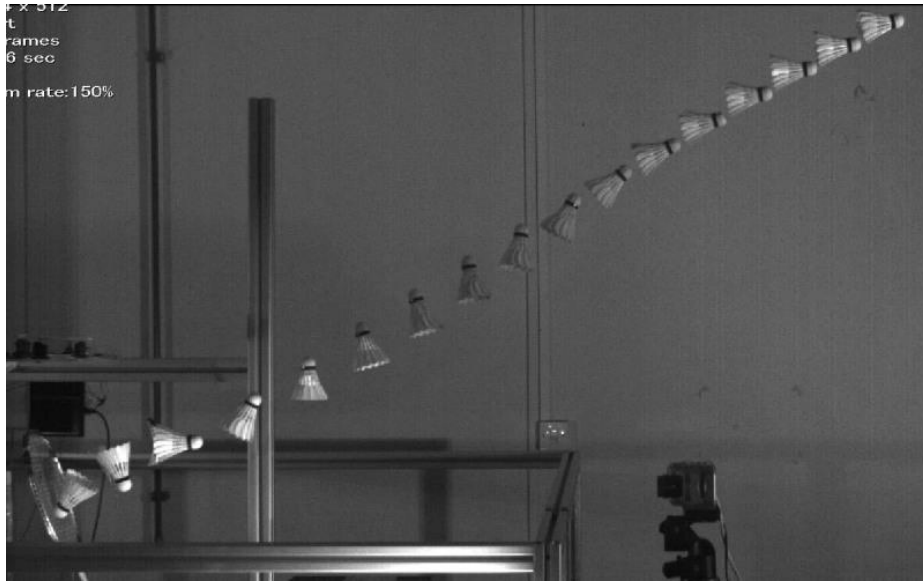


Figure 47 Turnover behaviour of a badminton shuttlecock [64].

#### ***4.3.1.1 Stability in Turnover***

The stability of the turnover response of a shuttlecock is determined by four dominant factors - Position of the centre of gravity (C.G.), position of the centre of pressure (C.P.), moment of inertia, and presence of aerodynamic forces. Figure 48 shows the effect of these variables. Just like a flying object, when C.P. is on the trailing end of C.G., the shuttlecock is dynamically stable. This is because the resultant aerodynamic forces that can be assumed to act through the C.P. produce a resultant moment about the C.G. that corrects and reduces the flight angle of attack. Consequently, stability of the shuttlecock is also dependent on the magnitude and direction of the aerodynamic forces acting at C.P., where a higher force produces a larger restoring moment, and thus, increased stability. In the extreme case of instability, where the C.P. is ahead of the C.G., the aerodynamic moment will increase the intensity of the flipping motion, instead of correcting it.

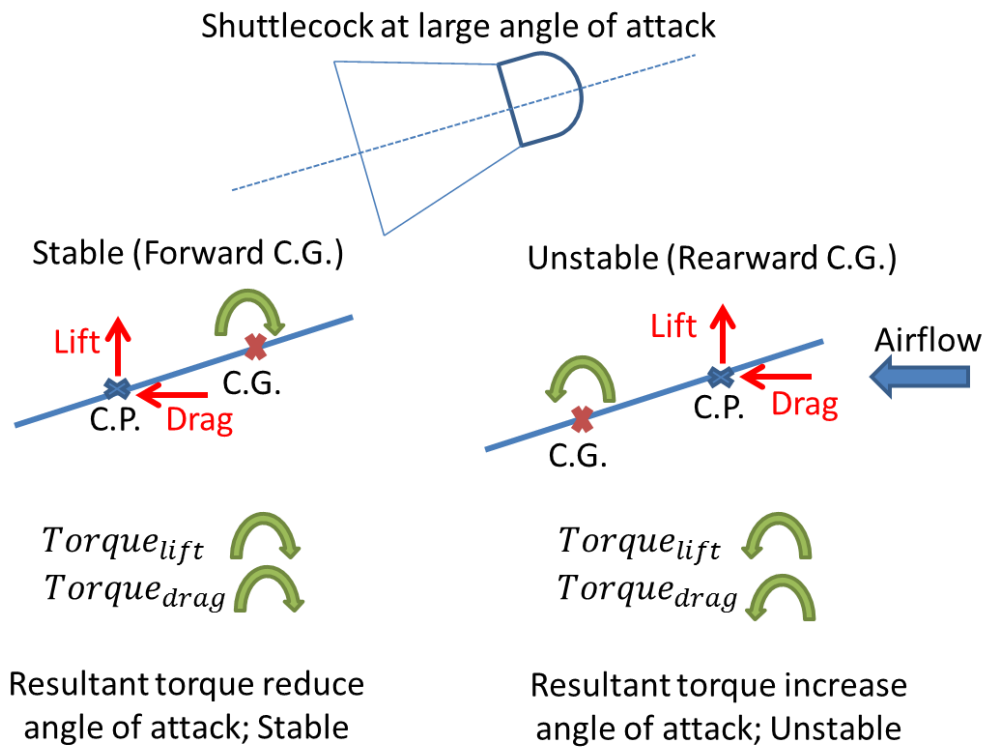


Figure 48 Effect of C.G. location with respect to C.P. on stability.

While it is unlikely for commercially available shuttlecocks to exhibit instability in turnover, prototype (Figure 49) studied in the lab did demonstrate the expected behaviour of an unstable turnover. The chronophotograph processed from the high-speed video of the unstable turnover behaviour is presented in Figure 50. For comparison, the same time-based image of a stable turnover is presented in Figure 51. These results were obtained by using a high-speed camera to film the turnover behaviour of shuttlecocks launched by an in-house fabricated racket-based shuttlecock launcher. The full description of the methodology applied for analysis of the shuttlecock turnover will be presented in chapter 6.4.1 together with the experimental work and result.

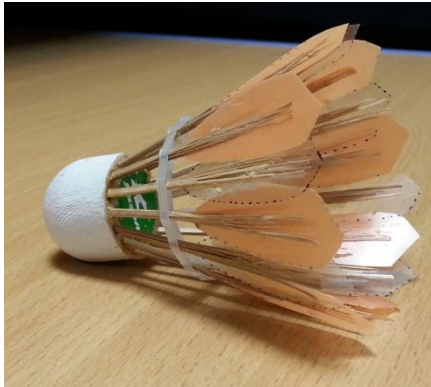


Figure 49 The unstable prototype which had a rearward C.G.



Figure 50 The unstable turnover process where the shuttlecock flips continuously.



Figure 51 A stable turnover where heading is corrected.

From the high-speed videos, the angles of attack with respect to time for a stable turnover were plotted against that of an unstable turnover and this plot is shown in Figure 52. Angle of attack refers to the angle between the shuttlecock heading and the flight path angle. Unlike the feather shuttlecock which demonstrated a damped oscillatory behaviour, the unstable shuttlecock continues to flip with no sign of alignment to the flight path.

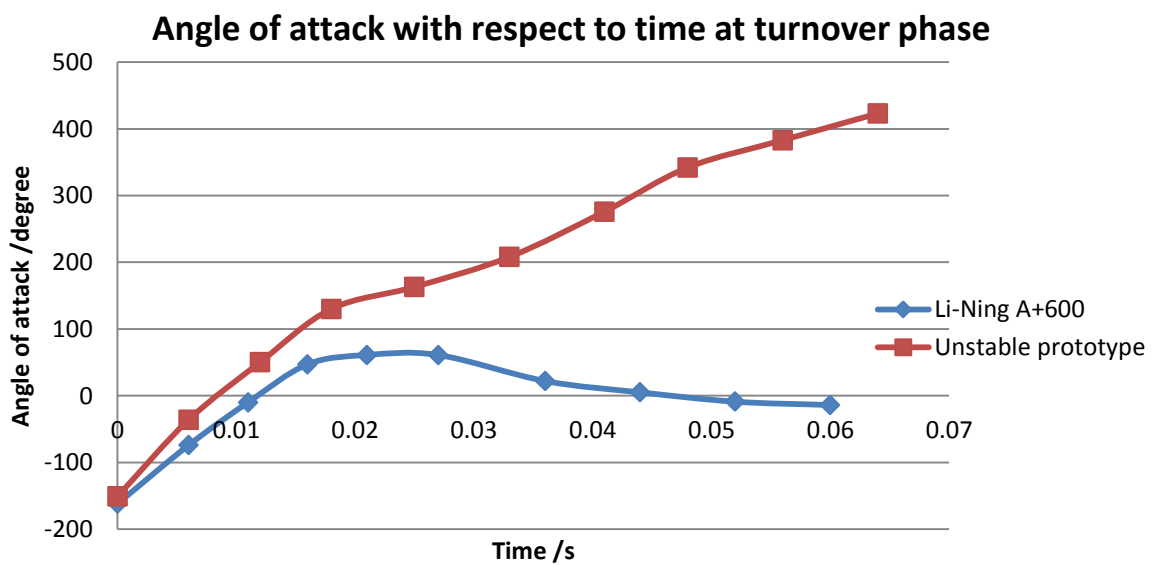


Figure 52 Angular response of a stable feather shuttlecock (Li-Ning A+600) as compared with an unstable prototype.

Through experimental result, it was observed that a stable shuttlecock has an angular response that is similar to that of a damped harmonic motion of a mass-spring-damper setup. This means, the angular response will go through the following phases in the below given order:

1. An excitation input that perturbs the system away from the neutral position, where neutral refers to the heading of zero angle of attack. In this case, this input was given by the badminton racket on the shuttlecock. This

perturbation away from neutral can be seen as the initial large negative angle of attack (time = 0 s) in Figure 52.

2. "Spring and damper"-like system attempts to restore the system back to the neutral position. For the badminton shuttlecock, the restoring moment is given by the aerodynamic (pitching) moment acting on it. In Figure 52, this refers to the flight segment at time  $< 0.01$  s, when the stable shuttlecock is attempting to reduce the large initial negative angle of attack.
3. Being an under-damped system, the badminton shuttlecock overshoots in the correction. This over compensation can be seen during  $0.015$  s  $<$  time  $<$   $0.03$  s in Figure 52, where the shuttlecock now has a large angle of attack but in the opposite direction.
4. The overshoot generates restoring moment to return the shuttlecock from a large positive angle of attack to neutral. This moment is in the opposite direction to that of the initial restoring moment described for time  $< 0.01$  s.
5. Due to the damped behaviour, the overshoot gets smaller with the oscillation and the shuttlecock eventually aligns to the flight path.
6. An important assumption for the above-described behaviour is the generation of sufficient restoring moment. If the self-restoring moment is insufficient to stabilize the shuttlecock, the flipping of the shuttlecock will go beyond one full revolution from neutral, as seen from the result of the unstable prototype in Figure 52.

The result of the experimental work comparing the turnover of feather and synthetic shuttlecocks will be presented in chapter 6.

### 4.3.1.2 Modelling

Equation (35) can be adapted to the body fixed axis as:

$$I_{yy}\dot{q} + cq + \left| \frac{dM}{d\alpha} \right| \alpha = 0 \quad (39)$$

Since the rate of change in angle of attack,  $\dot{\alpha}$ , is similar to the body pitch change rate,  $\dot{\theta}$ ,

$$\dot{\alpha} = \dot{\theta} \quad (40)$$

$$\ddot{\alpha} = \ddot{\theta} \quad (41)$$

which means that (39) can be given as:

$$I_{yy}\ddot{\alpha} + c\dot{\alpha} + \left| \frac{dM}{d\alpha} \right| \alpha = 0 \quad (42)$$

Including the external moment induced by the racket upon impact,  $M_{racket}(t)$  in time domain, then taking Laplace transformation,

$$I_{yy}S^2\alpha + cS\alpha + \left| \frac{dM}{d\alpha} \right| \alpha = M_{racket}(S) \quad (43)$$

a relationship that is similar to the generic expression for an externally excited mass-spring-damper system (44) is obtained. The racket excitation,  $M_{racket}(S)$ , is the short duration impulse-like interaction between shuttlecock and racket.

$$mS^2X + cSX + kX = F(S) \quad (44)$$

The symbol  $c$  is the damping constant,  $k$  is the spring constant,  $m$  is the mass of the load and  $F(S)$  is the excitation force in the Laplace domain. Similarity between (43) and (44) means that angular response of all shuttlecocks can be quantified by identifying the constants for the generic 2<sup>nd</sup> order transfer function of a spring mass damper system that is given as:

$$G(s) = \frac{k_p}{1 + 2\zeta\omega_n s + (\omega_n s)^2} \quad (45)$$

where  $\zeta$  is the damping ratio and  $\omega_n$  is the natural frequency. The advantage of such an approach is that it allows direct comparison between shuttlecocks without the need of other physical constants that could possibly introduce error. Theoretically, the highest  $\zeta$  and lowest  $\omega_n$  are desired for the best shuttlecock stability. Practically, there exists a certain range for the parameters, where performance is acceptable. This will be identified in section 6 through the application of Matlab system identification toolbox to the experimental data.

#### 4.3.1.3 Physical Parameters

Equation (43) can be rearranged as:

$$\frac{M_{racket}(s)}{\frac{I_{yy}}{\left|\frac{dM}{d\alpha}\right|} s^2 + \frac{c}{\left|\frac{dM}{d\alpha}\right|} s + 1} = \left|\frac{dM}{d\alpha}\right| \alpha \quad (46)$$

Comparing (46) to (45), it can be shown that  $\left|\frac{dM}{d\alpha}\right|$  and  $c$  can be expressed as:

$$\left|\frac{dM}{d\alpha}\right| = \frac{I_{yy}}{(\omega_n)^2} \quad (47)$$

$$c = 2 \left|\frac{dM}{d\alpha}\right| \zeta \omega_n = 2 \frac{I_{yy}}{\omega_n} \zeta \quad (48)$$

These are the physical parameters of (38) that determine the angular behaviour, when expressed in the obtained  $\zeta$  and  $\omega_n$ .

## 4.3.2 Axial Spin

### 4.3.2.1 Theory

In Figure 46, when both T and Q are in equilibrium, axial spin rate is a constant. This is the spin rate that is usually presented in previous works on shuttlecock spin. From (34), when,

$$T = Q$$
$$\rho d^5 p^2 C_Q = 0.5 \rho A C_T \frac{\dot{x}^3}{p}$$

and if it is a constant,

$$B = \frac{\rho d^5 C_Q}{0.5 \rho A C_T}$$

then a linear relationship between spin rate and air speed is:

$$p = \frac{\dot{x}}{\sqrt[3]{B}} \quad (49)$$

As mentioned in the literature review, work on spin of shuttlecock has been limited. At current, there is no derivation or empirical relation for spin and air speed in the open literature. The proposed linearity in (49) is under the assumption that  $C_Q$  and  $C_T$  are independent of the Reynold's number. Spin rate plot from the wind tunnel in [31, 32, 34] does support the linearity between axial spin and air speed. However, some of the shuttlecocks in those studies did not retain linearity at high air speed. This will be discussed in the wind tunnel experimentation in section 5.4.2. Linearity was not observed for the result in [22], but this is likely to be the mounting method applied for the shuttlecock that was restricting free motion.

It was mentioned in [22] that the time required to accelerate a shuttlecock to steady state airspeed is insignificant. However, preliminary work on actual spin rate that was measured in flight proves otherwise. This means, the spin rate of a shuttlecock in flight at a certain air speed can be very different from the spin rate of the shuttlecock in the wind tunnel at the same air speed. The experimental work and observations show that in-situ spin measurement of a shuttlecock is important.

#### ***4.3.2.2 Preliminary Observations***

In a preliminary study on measurements of the in-flight spin rates, work was conducted for six tubes of feather shuttlecocks. Three high-speed cameras were placed along the flight path, parallel to the X-Z plane of flight. The experimental set up is illustrated in Figure 53. Not shown in Figure 53 is the compressed gas launcher that was used for launch consistency. The first camera was placed 2.3m after the launcher to measure the initial flight condition after launch. Camera 2 and Camera 3 were placed much further down the flight path before and after the vertex of the clear shot trajectory. This was to observe the spin rate variation in flight with respect to air speed and position. Due to the resolution limitation of these cameras, each camera could only capture a small segment of the flight. With the acquisition of better high speed cameras, this issue has been resolved in subsequent studies. The captured video data were then processed manually for the velocities and spin rates. Velocities were obtained through digitising the videos using the physical shuttlecock length as a reference to determine the screen to physical length scale. Markings were made on the shuttlecock for identification of spin rate. By counting the changes of markings with time, the spin rates were determined. An example of the markings captured in video is presented in Figure 54.

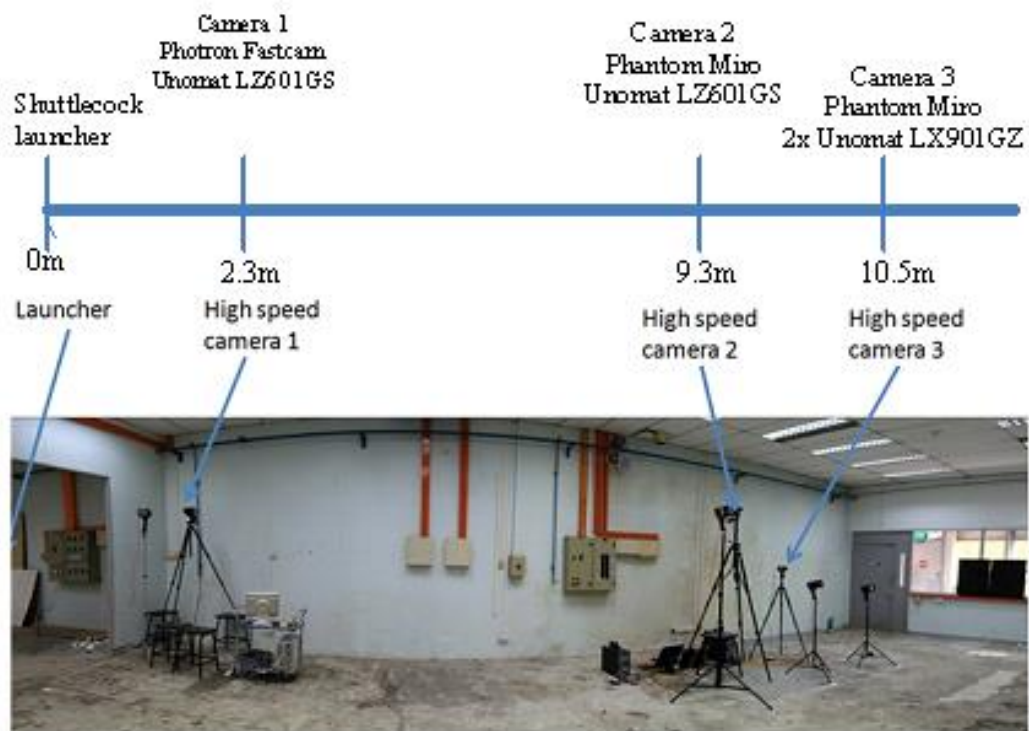


Figure 53 Experimental setup for the preliminary trial in capturing of spin rate.



Figure 54 The markings drawn on the shuttlecock for determining spin rate in post-experiment video processing.

As this was an initial investigation, only observations that are important to the development of this thesis will be discussed in this section. The result was summarised and is presented in Table 9. The detail of the methodology and the result is given in Appendix B. While the initial purpose of this study was to understand the magnitude of axial spin with respect to air speed, the result showed significant findings. The most significant finding of this work is that axial spin of a shuttlecock

does not occur instantly. Instead, a shuttlecock takes time to accelerate or decelerate in spin rate. This supports the proposed effect of delay in spin reaction that was discussed in section 2.6 of this thesis. Despite the relatively consistent air speed at camera 1, the shuttlecocks showed large variation in spin rate. However variation in spin rate was much less significant at position of camera 2 and camera 3. This supports the proposition that change in axial spin rate does not occur instantaneously.

Table 9 Tabulated summary of the experimental result presented in Appendix B.

			Yonex AS5		Ashaway Official		Li-Ning A+90 (76)		Li-Ning A+90 (77)		Yonex AS10	Li-Ning GrandPrix (76)
			Run 1	Run 2	Run 1	Run 2	Run 1	Run 2	Run 1	Run 2	Run 1	Run 1
Cam1	Airspeed /m/s	Mean	26.80	26.57	27.52	27.82	27.09	27.10	27.72	28.08	27.24	27.16
		Variance	2.24	2.44	2.91	0.96	0.31	2.61	1.08	1.27	2.84	0.89
	Spin rate /rad/s	Mean	86.50	64.75	91.28	107.58	100.21	67.11	64.57	76.08	27.65	50.20
		Variance	847.20	2048.00	684.23	2170.05	888.39	2711.74	2242.68	1659.12	1085.44	1648.94
Cam2	Airspeed /m/s	Mean	5.29	5.33	5.30	5.32	5.32	5.10	5.73	5.36	5.26	5.12
		Variance	0.07	0.07	0.06	0.02	0.02	0.08	0.05	0.02	0.03	0.02
	Spin rate /rad/s	Mean	51.92	52.12	53.08	55.42	45.22	43.07	45.66	46.32	39.50	44.82
		Variance	12.81	39.41	127.94	74.28	80.49	23.25	37.89	29.50	79.37	31.55
Cam3	Airspeed /m/s	Mean	5.50	5.06	5.29	5.12	5.24	5.14	5.20	5.29	5.11	5.25
		Variance	0.19	0.00	0.05	0.02	0.08	0.01	0.03	0.02	0.02	0.22
	Spin rate /rad/s	Mean	40.34	40.42	44.46	46.04	37.37	35.34	43.52	39.27	38.33	34.35
		Variance	17.37	63.05	42.80	32.71	32.05	25.91	83.04	37.31	83.15	219.94
	Distance travelled /m	Mean	10.96	10.65	10.50	10.46	10.93	10.70	11.05	10.83	10.80	10.79

Airspeeds processed from camera 2 and camera 3 were observed to be similar. This means that there is little change in air speed around and after the vertex of the trajectory. The average airspeed for each type of shuttlecock ranged from 5.06 m/s to 5.73 m/s. This agrees with the 5 m/s that was estimated in [22]. Despite similarity in linear speed, the average spin rates of the shuttlecocks were higher at camera 2 than at camera 3 for all tested tubes of shuttles. The average spin rate of all the tested shuttlecocks was 47.7 rad/s measured at camera 2, reducing to 39.9 rad/s when measured at camera 3. This is likely to be the effect of spin deceleration lagging behind the change in linear velocity.

It was noted that the shuttlecocks were easily damaged by the compressed air shuttlecock launcher. Moreover, the launcher was unable to test synthetic shuttlecocks or turnover performance. Therefore, a new launcher was developed. This will be discussed in Chapter 5.

### **4.3.3 Gyroscopic Precession**

#### ***4.3.3.1 Theory***

Gyroscopic precession of a shuttlecock was first discussed in the open literature in [22], where spin of a shuttlecock was compared to that of a top in precession. Since then, this has never been discussed in the open literature. In [22], the approach to modelling of gyroscopic effect was through the addition of a secondary set of equations. In this secondary set of equations, a first equation estimates the gyroscopic yawing, and then a second equation calculates the gyroscopic drift from the yaw angle. The gyroscopic drift is the effect of the side force produced by the angle of attack from gyroscopic yawing. The secondary set of equation was

independent of the main equation of motion for calculating the 2-D flight path. This is because the flight was modelled as 2-D with a separate 3<sup>rd</sup> dimension added to account for gyroscopic drift. Moreover, the main equation of motion was computed through time-step iteration, while the secondary equations were not. The intensity of drift was calculated as a constant. It was then recommended as a concluding remark that these two sets of equations should be combined in future work. It was also suggested that the gyroscopic effect should be computed through time-step iteration where the intensity of the angular effect can be varied in each iteration.

In the equation of motion that was presented in (38), the gyroscopic yawing effect has been accounted for through the application of the Newton-Euler formulation, as highlighted in (50). The subsequent gyroscopic drift effect is also integrated through the side force and lift force calculation. This means, it is unnecessary to further modify the equation of motion that was presented in (38).

$$\begin{bmatrix} \ddot{x}_{earth} \\ \ddot{y}_{earth} \\ \ddot{z}_{earth} \\ \dot{p} \\ \dot{q} \\ \dot{r} \end{bmatrix} = \begin{bmatrix} 0 \\ 0 \\ 0 \\ ((I_{yy} - I_{zz})qr)/I_{xx} \\ ((I_{zz} - I_{xx})pr)/I_{yy} \\ ((I_{xx} - I_{yy})pq)/I_{zz} \end{bmatrix} \quad (50)$$

Cooke [22] explained the gyroscopic precession as primary precession (the yaw) and secondary precession (the subsequent pitch). The primary and secondary precession is a part of the shuttlecock flight that is often confusing because its effect is subtle and not easily noticeable outside of theory. Cooke [22] gave an approximation of the precessional drift as 0.12 m. This means a side way drift of 0.12 m for a shuttlecock clear shot with 9 m range. The subtleness of this effect is easily unnoticed to the novice players.

From the moment components in (50), the gyroscopic angular effect on the shuttlecock in an axis is a product of the interaction between the angular rates in the other two axes. For instance, in the y-axis (pitch), the resultant angular moment from gyroscopic precession will be determined by the spin rate (x-axis) and yaw rate (z-axis). In the absence of axial spin, there will be no moment induced. Similarly, gyroscopic moment will be limited when rate of change in pitch is small. Since the rate of pitch change is small for most part of the flight, gyroscopic precession effect of a shuttlecock is limited to the post-stall flight regime. This is because the stall drops the nose down, creating large angular rate in pitch. This, as referenced from Figure 41, is mostly in the post-stall region. The magnitude of the moment is also dependent on the difference in moment of inertia between the axes. For instance, because a shuttlecock is considered as an axisymmetric body, the moment of inertia in the yaw and pitch axes are the same ( $I_{yy} = I_{zz}$ ). Therefore, no amount of pitch and yaw interaction can induce moment in the axial spin direction.

#### ***4.3.3.2 Primary and Secondary Precession***

The primary precession of a shuttlecock occurs when there is angular velocity in the pitch axis (y-axis) and spin axis (x-axis). This induces a yawing moment which turns the shuttlecock to produce an angle of attack in yaw axis. The turning of the shuttlecock by the yawing moment also means the presence of a yaw angular rate. Coupling of the yaw angular rate with axial spin creates a moment (and motion) in the pitch axis. This is the secondary precession, which has the same effect as the classical gyroscope example of a suspended spinning bicycle wheel which seemingly resists gravity.

To aid visualisation of the gyroscopic effect acting on a shuttlecock, a chronophotography shot of a shuttlecock in free-fall, with and without axial spin, is presented in Figure 55.

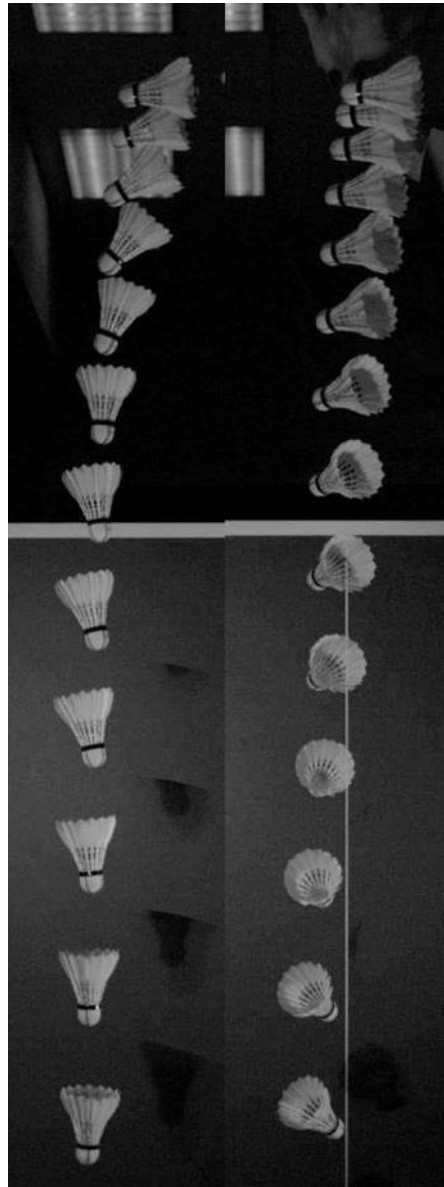


Figure 55 Heading change of shuttlecock in free-fall, without spin (left) and with spin (right).

Figure 55 was obtained through stitching of high-speed camera (Vision Research Miro 120s) shots at 0.02 s interval apart. Two launches were conducted on the same shuttlecock. The result on the left is for the first launch, where the shuttlecock was

released into a free-fall from rest without spin. This was achieved by holding a feather tip by two fingers and then releasing it. The shots on the right are for the same shuttlecock released from rest, but with spin induced manually on the shuttlecock. This was done by holding the cork part of the shuttle between two palms and then sliding the two palms in opposite directions prior to dropping the shuttlecock. The palm motion is similar to the action of inducing spin on a classic hand propeller toy (bamboo-copter).

The chronophotograph in Figure 55 shows that the heading of the shuttlecock that is not spinning will align to the flight path within 0.3 s upon release. On the other hand, the shuttlecock that is spinning maintains a large angle of attack with respect to the flight path. There is a moment holding the nose of the shuttlecock up, resisting the shuttlecock from pitching toward the ground. This is the secondary precession effect. The chronophotograph also shows the primary precession where the shuttlecock is yawing (rotating along the gravitational axis). This primary precession is unlikely to be an effect of the release method because the shuttlecock has almost no yaw upon the first 0.2 s of release. Yaw rate increased along the free-fall. The image was then processed for numerical data of the distance dropped and the shuttlecock heading with respect to time. This is shown in Figure 56, where 0 degree is parallel the horizon and 90 degree being aligned to the direction of gravity.

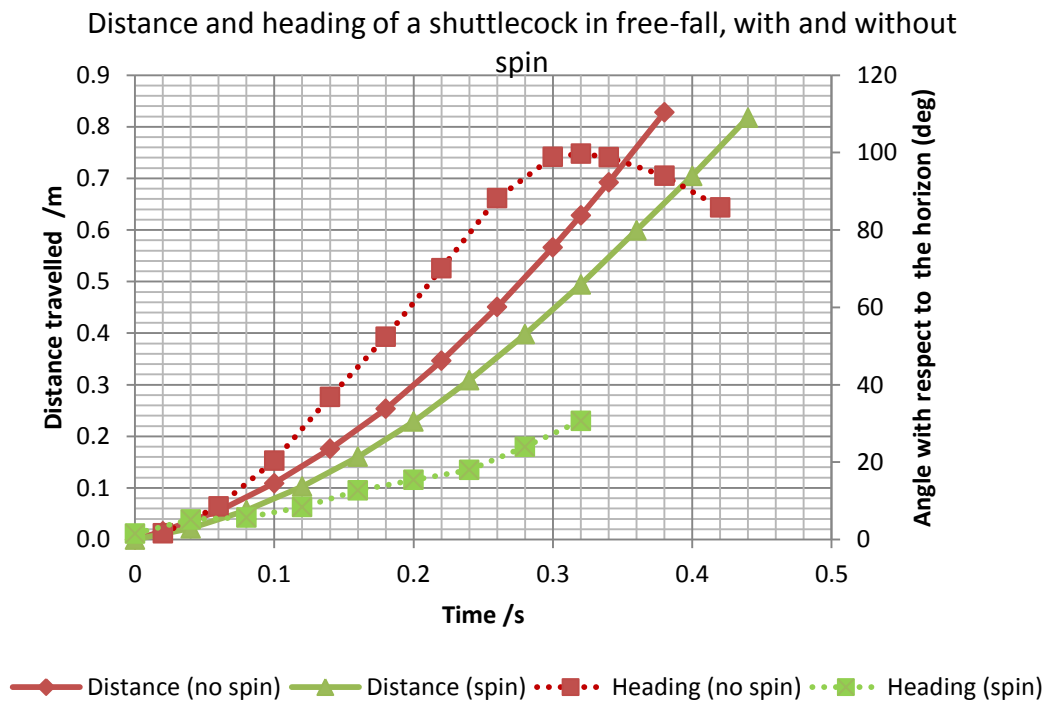


Figure 56 Distance travelled and heading change with time for the spinning and non-spinning shuttlecock.

The angular response of the non-spinning shuttlecock in Figure 56 shows the underdamped turnover behaviour that was discussed in section 4.3.1. It was also seen that the spinning shuttlecock has a slower drop velocity than the non-spinning shuttlecock. This is likely due to the spinning shuttlecock having larger angles of attack (due to secondary precession) which induced more drag acting against the motion. This increase in drag is unlikely to be observed in actual flight because the angle of attack in steady flight state is small. However, it is likely that secondary precession will affect the post-stall behaviour and possibly aid in producing the desired near vertical drop in the post-stall region.

#### 4.3.3.3 Implications

Theoretically, a more pronounced secondary precession effect can enhance the drop performance of the shuttlecock. Based on the observed phenomenon, the secondary

precession is likely to hold the nose of the shuttlecock up, inducing positive angle of attack. This will in turn induce additional lift and delay the onset of stall. Therefore, the flight velocity at stall may be lower than a shuttlecock that is not spinning and has no precession effect. The resultant impact on trajectory is a steeper drop.

This is in contrast to what was proposed by Cooke, who may not have explained the full phenomenon. According to Cooke, the gyroscopic precession causes a primary yaw effect. When this yaw is being corrected, the motion of returning to zero yaw produces the secondary pitching effect that causes a shuttlecock to nose down. Based on the observed delay in nose drop with the spinning shuttlecock in Figure 55, it is likely that the sudden nose drop is not just the secondary effect as proposed. It is a combination of delayed stall from initial yaw and gyroscopic angular effect from subsequent yaw correction.

However, the effect of primary precession should not be ignored. Similar to lift force being induced by secondary precession, the presence of primary precession means the generation of side force. The existence of side force will then translate into undesired sideways trajectory deviation. Since a stronger secondary precession is the consequence of larger primary precession, then a more vertical drop from secondary precession will also exhibit larger side-way. This means that the precessional effect, where the primary and secondary precession are interdependent, must be limited to prevent undesired flight deviation. Therefore, rather than exploring and enhancing the effect of gyroscopic precession of the shuttlecock, the focus should be on replicating the precessional effect of feather shuttles in the development of synthetics.

The complexity and subtleness of the gyroscopic effect makes it difficult to be observed accurately. Moreover, the observation of the symptoms (side drift) does not explain nor signal the requirement for replicating the effect. However, through equation (50), it can be seen that gyroscopic yaw and pitch are controlled by the following source parameters:

1. Axial spin rate ( $p$ ) of the shuttlecock
2. Moments of inertia ( $I_{xx}$ ,  $I_{yy}$ ,  $I_{zz}$ )
3. Difference between moment of inertia ( $I_{xx} - I_{yy}$ )
4. Pitch rate ( $q$ )
5. Yaw rate ( $r$ )

When the above parameters are matched, gyroscopic precession can be replicated. Through the described behaviour of gyroscopic precession, it can be seen that yaw rate and pitch rate are uncontrollable because they are by-products of primary precession from change in pitch and velocity vector. The physical properties that can be studied are the axial spin rate and the moments of inertia. The axial spin refers to the in-flight spin rate and this is different from the wind tunnel steady state spin rate. This supports the importance of in-flight spin measurement.

#### ***4.3.3.4 Experimental Observation***

The identification of the source parameters  $I_{xx}$ ,  $I_{yy}$ ,  $I_{zz}$  and  $p$  is used as the approach to gyroscopic effect in the shuttlecock evaluation framework. For understanding of the phenomenon, the actual in-flight gyroscopic effect will be studied in this sub-section. Four high-speed cameras at 500 frames per second (fps) were used to observe the shuttlecock (Babolat Tour 77, BWF approved) flight

around the vertex of the clear shot. The experimental setup of the cameras is illustrated in Figure 57. The position coordinates of the cameras are shown in Table 10, which is using the same coordinate system as Figure 40. The first camera, Cam 0, is placed up ahead of the flight where the shuttlecock has completed the turnover process and has reached stable flight. In this region, heading change is limited as the shuttlecock is gaining height. The purpose of Cam 0 is to observe for the initial flight deviation which may have occurred when the launch of the shuttlecock (by the launcher) is less than perfect. Cam 1 and Cam 2 are placed before and after the vertex of the trajectory, where gyroscopic effect will be the most prominent. Cam 0, Cam 1 and Cam 2 are aligned parallel to the X-Y plane. Cam 3 is aligned parallel to the X-Z plane and used to identify the pitch angle and spin rate. The variables collected from each camera are also tabulated in Table 10. Cam 1, Cam 2 and Cam 3 were frame synchronised, thereby allowing the data of various axes to be tabulated together to form a set of the 3-D 6 DOF flight data.

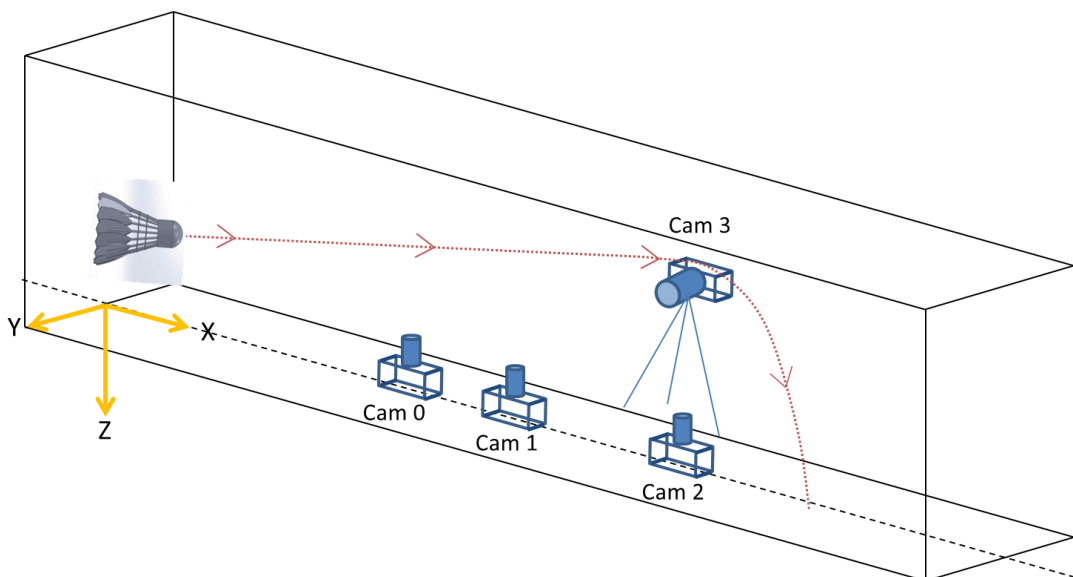


Figure 57 Illustration of the camera setup for the experimental observation of the shuttlecock precession.

Table 10 Position coordinates of the cameras used.

		Camera Coordinates			Time Synchronised	Variables Collected
		X /m	Y /m	Z /m		
Cam 0	Photron PCI 1024	3.75	0	-	No	X Coordinate, Y Coordinate
Cam 1	Phantom Miro 120s	5.75	0	-	Yes	X Coordinate, Y Coordinate, Yaw angle
Cam 2	Phantom Miro 120s	7.5	0	-	Yes	X Coordinate, Y Coordinate, Yaw angle
Cam 3	Phantom Miro 120s	7	-	- 2.92	Yes	X Coordinate, Z Coordinate, Pitch angle, Spin rate

The captured high-speed videos were then digitised through tracker. The variables that were collected from each camera are listed in Table 10. These variables were then tabulated through the synchronised time stamp and were used for parameter identification and trajectory simulation in Matlab. The experimental data are presented together with the simulated data in section 4.3.3.5. Accuracy of the angular data was estimated as  $\pm 0.5^\circ$ . This is considerably large when taking into account that yaw angle magnitude was in the order of 1. Thus, a smooth filter (Matlab “smooth” function) was applied to the yaw array prior to identification.

#### ***4.3.3.5 Modelling and Simulation***

The flight of the shuttlecock with gyroscopic precession can be modelled by (38) with some modifications. Instead of a 3-D, 6 DOF, 12 states equation of motion, the spin rate and spin acceleration were removed because these are input variables that are unlikely to be affected by gyroscopic effect. This is because the axisymmetric

shuttlecock has the same  $I_{zz}$  and  $I_{yy}$  value which results in no gyroscopic effect on the spin axis. Therefore, the 10 states of simulation are:

$$\begin{aligned}
 x_1 &= x \\
 x_2 &= \dot{x} \\
 x_3 &= y \\
 x_4 &= \dot{y} \\
 x_5 &= z \\
 x_6 &= \dot{z} \\
 x_7 &= \int q \, dt \\
 x_8 &= q \\
 x_9 &= \int r \, dt \\
 x_{10} &= r
 \end{aligned} \tag{51}$$

With axisymmetry, the roll angle becomes insignificant, therefore simplification of the transformation matrix ( $[R]^T$ ) becomes

$$[R]^T = \begin{bmatrix} \cos\psi\cos\theta & -\sin\psi & \cos\psi\sin\theta \\ \sin\psi\cos\theta & \cos\psi & \sin\psi\sin\theta \\ -\sin\theta & 0 & \cos\theta \end{bmatrix} \tag{52}$$

Assumption of small angles of attack in pitch and yaw also means transformation from flight path frame to the body frame is given as,

$$[R_{FP}] = 1 \tag{53}$$

which means that the first time derivative of (51) is

$$\begin{bmatrix} \dot{x}_1 \\ \dot{x}_2 \\ \dot{x}_3 \\ \dot{x}_4 \\ \dot{x}_5 \\ \dot{x}_6 \\ \dot{x}_7 \\ \dot{x}_8 \\ \dot{x}_9 \\ \dot{x}_{10} \end{bmatrix} = \begin{bmatrix} x_2 \\ \frac{1}{m}(D \cos \psi \cos \theta - SF \sin \psi + L \cos \psi \sin \theta) \\ x_4 \\ \frac{1}{m}(D \sin \psi \cos \theta + SF \cos \psi + L \sin \psi \sin \theta) \\ x_6 \\ g + \frac{1}{m}(-D \sin \theta + L \cos \theta) \\ x_8 \\ \left(-0.5\rho V^2 SC \left| \frac{dC_M}{d\alpha} \right| \alpha - c x_8 + (I_{zz} - I_{xx})x_{10}p\right) / I_{yy} \\ x_{10} \\ \left(-0.5\rho V^2 SC \left| \frac{dC_{M_z}}{d\beta} \right| \beta - c x_{10} + (I_{xx} - I_{yy})x_8 p\right) / I_{zz} \end{bmatrix} \quad (54)$$

where,

$$\theta = \tan^{-1} \left( \frac{-x_6}{x_2} \right) \quad (55)$$

$$\psi = \sin^{-1} \left( \frac{x_4}{V} \right) \quad (56)$$

$$V = \sqrt{x_2^2 + x_4^2 + x_6^2} \quad (57)$$

$$\psi = \sin^{-1} \left( \frac{x_4}{V} \right) \quad (58)$$

$$\alpha = x_7 - \theta \quad (59)$$

$$\beta = x_9 - \psi \quad (60)$$

and  $p$  being a time dependent function that varies with each time step.

The flight data around and beyond the vertex of the trajectory is used for system identification and then simulation with the non-linear greybox approach in Matlab. This is because the flight segment after the vertex is where the shuttlecock stalls and makes large pitch changes. Therefore, precessional effect should be the most significant here. The five input flight states are:  $[x, y, z, (\theta + \alpha), (\varphi + \beta)]$ . Axial spin rate was fed in as a time-dependent constant. In system identification, the parameters can be categorised into fixed parameters and identified parameters. Fixed

parameters are measured inputs which are fixed in the identification process, such as mass ( $m$ ), moment of inertia ( $I_{zz}$ ), and air density ( $\rho$ ). These fixed parameters maintain the physical meaning of the system. Identified parameters use the values identified from literatures as a first guess. These parameters are usually difficult to be determined accurately using experimental method.

This approach of system identification assumes all the parameters are constant throughout the simulated segment of flight. Although literatures [22, 25, 91] have shown that the parameters, such as the damping factor ( $c$ ), fluctuate with Reynold's number, the assumption remains valid. It is because air speed has little change beyond the vertex of the trajectory.

The initial input (first estimates) and identified values of the parameters are tabulated in Table 11. Various assumptions were applied. Firstly, the shuttlecock being an axisymmetric body was assumed to have zero lift when angle of attack is 0. It also means that pitching moment coefficient is the same as the yawing moment coefficient. Also, the increase in drag induced from lift was assumed to be zero. This is because the lift coefficient of a shuttlecock is small (due to small angle of attack), so the induced drag which is a function of the lift will be negligible as compared to the normal drag (base drag).

Table 11 Initial guess of parameters in identification process.

Parameters	Initial input (First estimate)	Fixed parameter	Unit
Mass (m)	5.05	Yes	g
Area (S)	0.003463	Yes	m <sup>2</sup>
Air density ( $\rho$ )	1.225	Yes	Kg/m <sup>3</sup>
Gravitational acceleration (g)	9.81	Yes	m/s <sup>2</sup>
Moment of inertia (I)	2.9 x10 <sup>-6</sup>	Yes	Kgm <sup>2</sup>
Drag coefficient (Cd)	0.58	No	-
Induced lift coefficient ( $\frac{dCl}{d\alpha}$ )	0.57	No	/rad
Pitch moment coefficient ( $\frac{dCm}{d\alpha}$ )	0.344	No	/rad
Pitch damping coefficient ( $C_\theta$ )	1 x10 <sup>-5</sup>	No	Kgm <sup>2</sup> /s

Figure 58 shows the experimental and simulated behaviour of the five states, where  $x_1$  to  $x_9$  follow their respective representations in (51). Good agreement between the experimental data and simulation was observed for the x-axis, z-axis, and the pitch angle. However, the simulated result was unable to replicate the yaw angle and side drift (y-axis) that was observed in the experimental work. The simulated drift was much larger than the experimental data, while the simulated yaw angle was less than the experimental data.

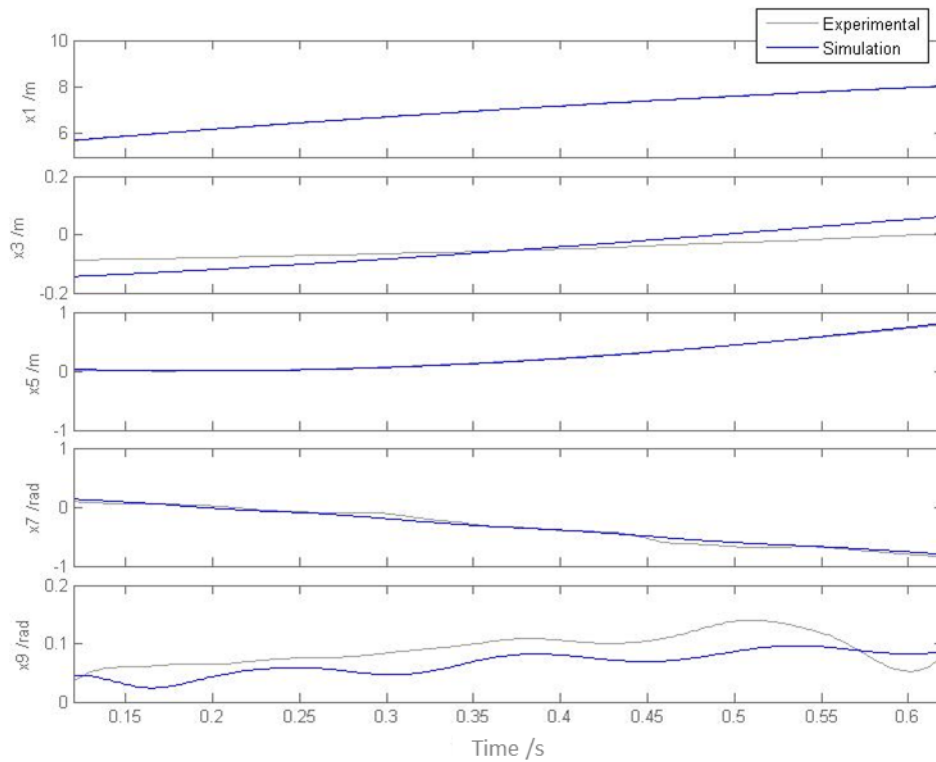


Figure 58 Simulated and experimental result for the trajectory beyond vertex.

Analysis of the identified parameters in Table 12 shows that only  $C_d$  and  $C_\theta$  are of reasonable values. Based on the prior literatures and physical meaning of the parameters, it is likely that the identified values of  $\frac{dC_l}{d\alpha}$  and  $\frac{dC_m}{d\alpha}$  are incorrect. This is because  $\frac{dC_l}{d\alpha}$  shows a negative lift coefficient which does not agree with positive lift from a conical body. Nonetheless, the ability of  $x$ ,  $z$  and pitch to retain good agreement despite the incorrect lift and pitch moment coefficients shows the dominance of drag in the shuttlecock trajectory.

Table 12 Values of the identified parameters, where  $C_d$  and  $C_\theta$  are of reasonable value, but  $\frac{dCl}{d\alpha}$  and  $\frac{dCm}{d\alpha}$  do not make physical sense.

Parameters	Initial input (First estimate)	Identified value
Drag coefficient ( $C_d$ )	0.58	0.565
Induced lift coefficient ( $\frac{dCl}{d\alpha}$ )	0.57 /rad	-5.13/rad
Pitch moment coefficient ( $\frac{dCm}{d\alpha}$ )	0.344 /rad	2.15/rad
Pitch damping coefficient ( $C_\theta$ )	1 x10-5	5.77 x10-5

In depth study of the equation of motion in (54) explains the phenomenon of poor identification results. The direction of gyroscopic precession, as predicted by (54), is opposite to what is expected in reality (as observed through flight and Figure 55). Using the post vertex flight condition as input and (50) as the proposed gyroscopic effect, the resultant directions of angular motions are as shown in Table 13.

Table 13 Gyroscopic effect predicted motion and the observed output motion.

	Input (observed experimental data)			Gyroscopic Output (theory)	Output (observed)
	Spin	Pitch or Yaw	Moment of inertia term	Yaw or Pitch	Yaw or Pitch
Suspended bicycle wheel	$p < 0$	$q < 0$	$(I_{xx}-I_{yy}) > 0$	$\dot{r} > 0$	$\dot{r} > 0$
	$p < 0$	$r > 0$	$(I_{zz}-I_{xx}) < 0$	$\dot{q} > 0$	$\dot{q} > 0$
Shuttlecock	$p < 0$	$q < 0$	$(I_{xx}-I_{yy}) < 0$	$\dot{r} < 0$	$\dot{r} > 0$
	$p < 0$	$r > 0$	$(I_{zz}-I_{xx}) > 0$	$\dot{q} < 0$	$\dot{q} > 0$
Shuttlecock with reversed gyroscopic	$p < 0$	$q < 0$	$(I_{xx}-I_{yy}) < 0$	$\dot{r} > 0$	$\dot{r} > 0$
	$p < 0$	$r > 0$	$(I_{zz}-I_{xx}) > 0$	$\dot{q} > 0$	$\dot{q} > 0$

Taking the classical suspended bicycle wheel as an example, the formulation in (50) is capable of accurately predicting the direction of the resultant gyroscopic precession. However, when the same equation is applied to the standard shuttlecock, the change in sign of the moment of inertia terms results in the gyroscopic equation predicting a reverse direction of precession from the bicycle wheel. This effect is commonly referred to as the retrograde precession in textbooks. However, it is completely opposite to what was observed on the actual badminton shuttlecock flight and would have caused the negative lift coefficient observed in Table 12.

#### 4.3.3.6 Reverse Gyroscopic Precession

In the experimental work on shuttlecock and also in Figure 55, it was observed that under the natural axial spin ( $p < 0$ ) with a negative pitch rate from the shuttlecock going nose down ( $q < 0$ ), the resultant motion is a yaw motion, where  $\dot{r} > 0$ . Consequently, the yawing motion produces the secondary gyroscopic effect of  $\dot{q} > 0$ . The proposed equation of motion estimates the response of  $\dot{r}$  and  $\dot{q}$  to be  $< 0$ , which is in the reverse direction. This means, the actual gyroscopic precession that is observed in flight is in the reverse of the predicted precession. This may be the reason for the large negative lift coefficient that was shown in Table 12.

Modifying (50) and thus, (54), the equations can be represented as:

$$\begin{bmatrix} \ddot{x}_{earth} \\ \ddot{y}_{earth} \\ \ddot{z}_{earth} \\ \dot{p} \\ \dot{q} \\ \dot{r} \end{bmatrix} = \begin{bmatrix} 0 \\ 0 \\ 0 \\ ((I_{yy} - I_{zz})qr)/I_{xx} \\ ((I_{xx} - I_{zz})pr)/I_{yy} \\ ((I_{yy} - I_{xx})pq)/I_{zz} \end{bmatrix} \quad (61)$$

$$\begin{bmatrix} \dot{x}_1 \\ \dot{x}_2 \\ \dot{x}_3 \\ \dot{x}_4 \\ \dot{x}_5 \\ \dot{x}_6 \\ \dot{x}_7 \\ \dot{x}_8 \\ \dot{x}_9 \\ \dot{x}_{10} \end{bmatrix} = \begin{bmatrix} x_2 \\ \frac{1}{m}(D \cos \psi \cos \theta - SF \sin \psi + L \cos \psi \sin \theta) \\ x_4 \\ \frac{1}{m}(D \sin \psi \cos \theta + SF \cos \psi + L \sin \psi \sin \theta) \\ x_6 \\ g + \frac{1}{m}(-D \sin \theta + L \cos \theta) \\ x_8 \\ \left(-0.5\rho V^2 SC \left| \frac{dC_M}{d\alpha} \right| \alpha - c x_8 + (I_{xx} - I_{zz})x_{10}p\right) / I_{yy} \\ x_{10} \\ \left(-0.5\rho V^2 SC \left| \frac{dC_{M_z}}{d\beta} \right| \beta - c x_{10} + (I_{yy} - I_{xx})x_8 p\right) / I_{zz} \end{bmatrix} \quad (62)$$

Through identification and simulation with (64) and (65), the results in Figure 59 were obtained. The simulation and experimental data showed good agreement with an average of 95% fit for the translational behaviour. For the angular motion, curve fit of 86% was obtained for pitch. Fit of the yaw axis is poor, but the general angular behaviour between the experimental and simulated results is agreeable. This poor fit is likely to be due to error in the raw yaw angular data.

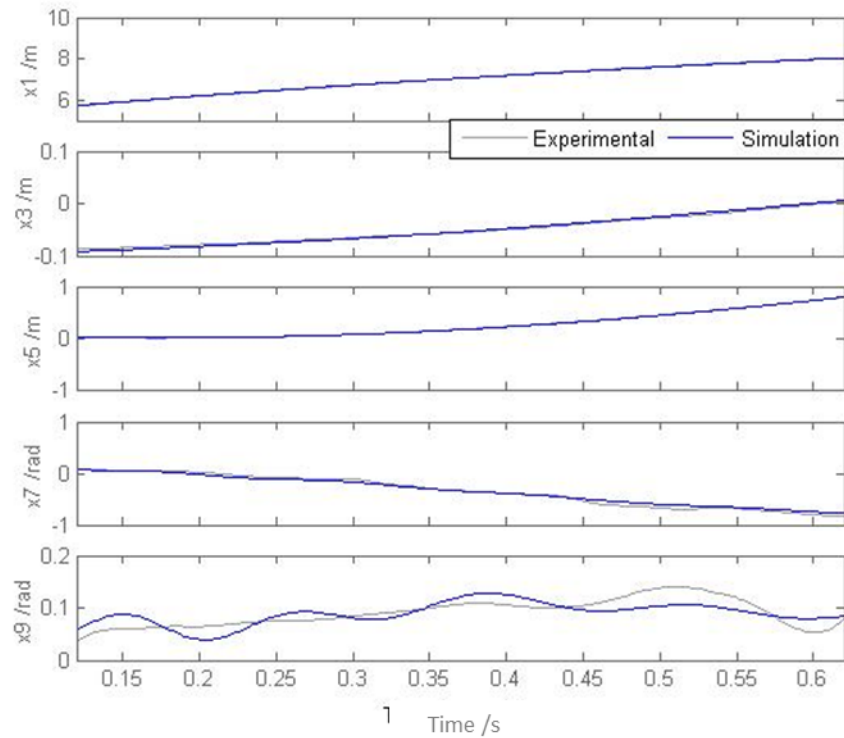


Figure 59 Experimental and simulated flight behaviour using the equations in (61) and (62).

The identified parameters as tabulated in Table 14 are of the same order of magnitude as experimental values in literatures. This means that the behaviour of the system in Figure 59 is not just in agreement with the experimental values, but the underlying parameters are physically sound and realistic. This is in contrast to Table 12, where the identified values of lift and pitch moment coefficients were unrealistic.

Table 14 Identified values for the aerodynamic parameters, showing good order of magnitude.

Parameters	Initial input (First estimate)	Identified value
Drag coefficient ( $C_d$ )	0.58	0.583
Induced lift coefficient ( $\frac{dCl}{d\alpha}$ )	0.57 /rad	1.05/rad
Pitch moment coefficient ( $\frac{dCm}{d\alpha}$ )	0.344 /rad	0.663/rad
Pitch damping coefficient ( $C_\theta$ )	$1 \times 10^{-5}$	$8.173 \times 10^{-6}$

Through the analysis, it was observed that gyroscopic precession is unlikely to have large impact on the 2-D x-z flight behaviour. However, it is important to study the spin of shuttlecocks because excessive axial spin in the post-vertex flight segment can lead to excessive sideways drift. This is not a desirable shuttlecock performance characteristic.

#### 4.4 Important Parameters

The important flight parameters that should be observed for a shuttlecock are discussed in this section.

##### 4.4.1 Unsteady Flight State

Mechanical parameters of the shuttlecock that affect flight performance can be identified from (38). For the unsteady flight state, it is seen that angular response is the performance indicator. Good angular performance can be classified as:

- Minimal time to stabilise the heading at turnover.
- Minimal overshoot in angular response at turnover.

The parameters to attain good angular performance are:

- **Moments of inertia in pitch**,  $I_{yy}$ , and yaw,  $I_{zz}$ , where smaller moment of inertia reduces the torque required for correction of heading.
- **Pitching moment coefficient**,  $C_M$ , where a larger pitching moment coefficient produces more torque for faster correction of heading.
- **Damping factor**,  $c$ , where increasing the damping factor reduces the overshoot during the turnover.

The shuttlecock moments of inertia can be easily determined through the bifilar and trifilar pendulum. The pitching moment coefficient and damping factor are much more difficult to be determined directly with accuracy. Cooke [22] measured the damping factor by oscillating the shuttlecock that was undergoing a free-fall in a vertical water column. It was concluded that the method was prone to large magnitude of error. Moreover, the damping factor, which was observed to increase with translational speed, was only measured at drop speed that was under 4 m/s. This makes the damping factor inapplicable to the turnover process which occurs at a much higher speed. Cooke [22] proposed the adaptation of measurement technique used for bomb models by oscillating the pitch angle of a suspended shuttlecock in the wind tunnel. This was not implemented in this study because it is highly possible that any fixture used for holding the light-weight shuttlecock (~ 5 g) will change the mass property and dynamics significantly. Moreover, the small pitching moment associated with the shuttlecock will be significantly influenced by the presence of minute amount of friction in the oscillating mechanism.

Therefore, the above approach was not applied in this study. Instead, in-flight measurement of the actual turnover behaviour was used for determining both  $C_M$  and

c. The availability of a programmable racket based shuttlecock launcher and the high-speed cameras, which were already used for flight trajectory studies, means that the turnover process can be easily investigated without additional cost. The major advantage of this approach over the previous methods is the ability to get repeated measurements of the turnover behaviour without introducing unnecessary changes to the shuttlecock dynamics. This is because the shuttlecock is tested in actual flight without any additional modification or fixture. The experimental work and the analysis on turnover will be discussed in detail in chapter 5.

#### **4.4.2 Steady Flight State**

The performance indicator of the steady flight state is the flight trajectory. Unlike in the unsteady flight state, the pitch rate and the yaw rate are much lower in the steady flight state. This means that the focus of evaluation should be different. In the understanding and evaluation of flight performance, the trajectory in the steady flight state can be separated into the low speed flight ( $< 7$  m/s) and high speed flight segment ( $> 7$  m/s).

In the early stage of flight, upon the transition into the steady flight state from the unsteady state, the badminton shuttlecock will travel with high speed. During this segment of high speed flight, the translational velocity is higher than the terminal velocity of the shuttlecock. This applies to a shuttlecock regardless if the shot was a clear, smash or serve. In the treatment of this flight segment, angular motion in pitch and yaw is limited and can be assumed to be negligible, therefore the important parameters are:

- **Drag force** (drag coefficient), where a higher drag force increases translational deceleration rate of the shuttlecock.
- **Mass**, where a heavier shuttlecock is able to carry more kinetic energy at the same velocity, thereby increasing the overall speed.

The above does not mean that the other parameters are unimportant to the shuttlecock trajectory. This is because the low speed flight segment, which occurs after the shuttlecock has slowed down to a speed that is less than the terminal velocity, gives the characteristic trajectory of the badminton shuttlecock. This part of the flight only happens in the clear and serve shots because a smash shot does not slow down this much while a properly executed net shot is mostly in the unsteady flight state. Gyroscopic effect, if present, is most prevalent in this part of the flight. This means that the parameters are similar to those of the gyroscopic precession process, as discussed in section 4.3.3.3.

#### **4.5 Summary**

In this chapter, the flight behaviour of the badminton shuttlecock was studied and modelled. The flight of a badminton shuttlecock was categorised in both the unsteady flight state and the steady flight state.

The various phenomena of the badminton flight were explained in detail through modelling and experimental observation. Since the previous significant work on badminton shuttlecock experimentation in 1992 [22], high-speed capturing technology has improved greatly. This has aided the study of flight phenomena that were difficult to be observed and analysed in the past.

Through the models developed, axial spin, turnover and spin-induced precessional drift were explained. The developed 6 DOF equation of motion was also applied and modified with validation from experimental data.

Concluding the chapter, the parameters and flight behaviour that should be studied in experiments were identified and discussed.

## **5. SHUTTLECOCK TESTING: PHASE I (STATIC)**

This chapter describes the experimental testing of shuttlecocks. An overview of the three phases of experiments that were conducted is first given. The first phase of the testing, Phase I, which covered the static testing is then discussed in detail in the chapter. An introduction to all the Phase I experiments are presented and these are followed by the description of the experimental methods and then the discussion on the obtained results.

### **5.1 Overview of Testing**

From the parameters identified in section 4.4, a three phase evaluation framework was developed and this was summarised and is presented in Figure 60. In Phase I (chapter 5), static testing was conducted to evaluate the physical properties of the shuttlecocks. Wind tunnel evaluation of spin and drag was also included. These tests in the first phase were for insight on flight performance and were not required for actual flight performance evaluation. In Phase II (chapter 6), techniques to evaluate and compare flight performance were developed. This phase of applied testing not only evaluated the steady flight state, but also the turnover performance in the unsteady flight state. Following the flight performance evaluation, the mechanical strength and durability of the skirt were tested in Phase III (chapter 7).

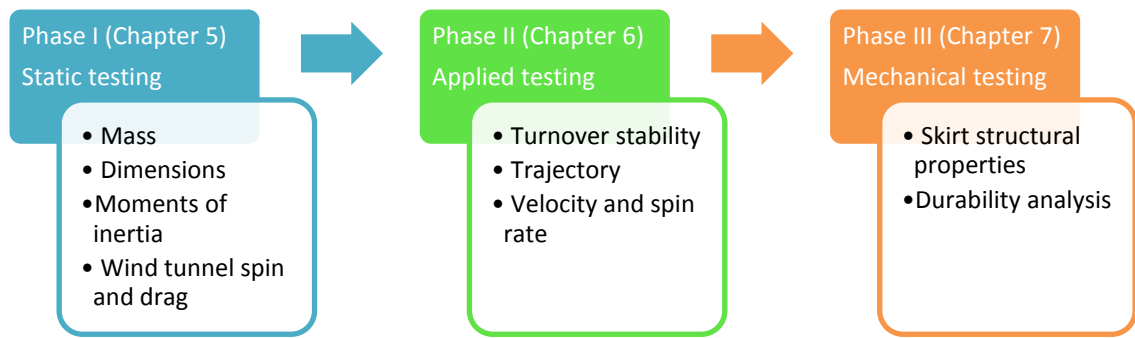


Figure 60 The developed badminton shuttlecock evaluation framework.

Physical properties of the shuttlecocks are influenced by environmental condition and storage. For instance, mass of a shuttlecock can change with humidity. The diameter of the shuttlecock has also been proven to be affected by the storage container (the tube) [22]. For effective comparison, all physical measurements should be evaluated at the same condition. All the work in this study, including the flight performance evaluation, were evaluated in air conditioned laboratory where room temperature was  $23^{\circ}\text{C} \pm 2^{\circ}\text{C}$ , and relative humidity was 60-65%.

## 5.2 Introduction to Phase I

Phase I of the shuttlecock testing consists of static measurements to evaluate the physical properties of the shuttlecocks. These properties determine the flight performance of the shuttlecocks. The physical properties are:

- Mass
- Skirt diameter and chord length
- Moments of inertia

In addition to the physical properties, the fundamental aerodynamic performance of the shuttlecocks is also evaluated in the wind tunnel. The parameters studied in the wind tunnel are:

- Drag behaviour
- Axial spin rate
- Skirt deformation.

The rationales behind the choice of measuring these parameters are discussed in the following sub-sections.

## **5.2.1 Physical Properties**

### ***5.2.1.1 Mass***

The mass of a shuttlecock is important because it determines the flight speed and range. It is seldom discussed for the shuttlecocks because it is often perceived as too fundamental and rudimentary to be worth any effort to be included in research. However, the mass is undeniably the basis to understanding a shuttlecock. As discussed in section 2.5, badminton shuttlecocks are speed rated in grains. In theory, all speed 76 shuttlecocks should weigh as much (or as little) as 76 grains. However, there are numerous parameters in production that prevent perfect control of the weight, such as the feather density and the amount of glue applied. Thus, weight variation is always present. Moreover, the design and material applied for some synthetic shuttlecocks also prevent strict adhesion to the defined weight.

### *5.2.1.2 Diameter and Chord*

Since the tolerance of the shuttlecock diameter is large [38], the measurement of shuttlecock diameter is purely for reference to the current shuttles. Therefore sophisticated measurements, such as those for other sports balls, are not required. The parameter to be measured, as quoted from the BWF approval scheme, states that:

“The tips of the feathers shall lie on a circle with a diameter from 58 mm to 68 mm.”

This means that the diameter of a shuttlecock measured by the BWF is the minimum diameter of an imaginary circle that will completely surround the widest segment of the conical skirt. In the surveyed literatures, this is also the diameter that was used to calculate the characteristic area for derivation of the drag coefficient. This is only an accurate representation of the real shuttlecock characteristic area when the flared flutes along the skirt are small. The flutes refer to the peaks and grooves that are formed by the folds along the circumference of the skirt and these are usually positioned at the near-wake side of the skirt. The flutes along the shuttlecock are illustrated in Figure 61, in which the model on the right can be seen to have sharper folds along the edge than the model on the left. Therefore, the flutes on the model in the right side of Figure 61 are more aggressive. Since the flutes function as propeller blades, they induce spin torque,  $T$ , and counter torque,  $Q$ , on the shuttlecock. Increasing the aggressiveness of the flutes is likely to increase  $T$  and  $Q$ .

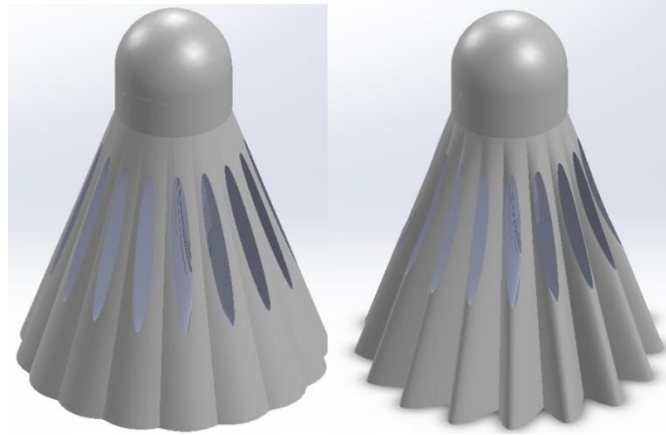


Figure 61 Different aggressiveness of fold features (flutes) along the shuttlecock skirt. The flutes on the model on the right are more aggressive.

When the flutes are aggressive and the edges are sharp, the characteristic area that is estimated through the standard diameter is likely to be an over-estimate of the actual area. This is demonstrated in Figure 62, which is the top view of the shuttlecock models that were presented in Figure 61. In Figure 62, it can be seen that the current evaluation method will estimate the same characteristic area for both of the models. This is equivalent to the area that is given by the blue outlined circle. However, the actual area of the model that has the more aggressive flutes will be much smaller than the estimated characteristic area. Therefore, the drag coefficient that is calculated with the over-estimated characteristic area will be lower than actual. Thus, comparison of the drag coefficients between different models, as done in the literatures surveyed, is likely to be biased.

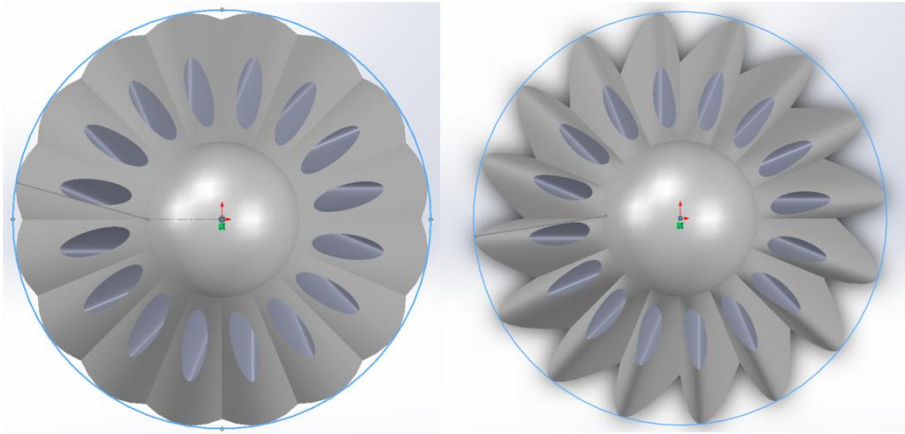


Figure 62 Using the standard diameter for estimation, both models in this figure will have the same characteristic area. This is misleading.

Chord length,  $C$ , of the shuttlecock refers to the height of the shuttlecock. Restriction of height, as given by BWF [38], is:

“The feathers shall be measured from the tip to the top of the base (cork) and in each shuttle shall be of the same length. This length can be between 62 mm and 70 mm....The base shall be 25 mm to 28 mm in diameter and rounded on the bottom.”

For the purpose of flight mechanics discussion,  $C$  in this thesis will refer to the overall length of the shuttlecock from the tip of the nose to the end of the skirt, as shown in Figure 63. Theoretically, an increase in  $C$  gives a longer moment arm for stabilising the shuttlecock heading. However,  $C$  of the shuttlecock seldom deviates much from a standard feather shuttlecock. This is because a longer  $C$  put the mass of the skirt further away from the cork, thereby shifting the centre of gravity backward. The length measurements in this section are purely for information on  $C$  of existing shuttlecocks.

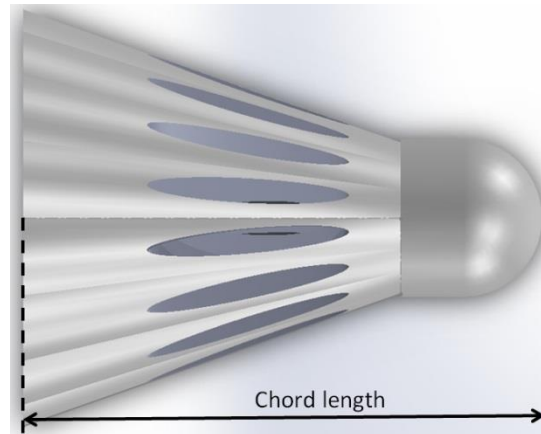


Figure 63 The chord length of the shuttlecock refers to the height starting from the tip of the cork to the end of the skirt.

### **5.2.1.3 Moments of Inertia**

Similar to the mass and dimensions of the shuttlecock, the moments of inertia is seldom studied in the literature. This is because it is a fundamental measurement that is of no scientific impact. However, the importance of the moment of inertia should not be ignored because it is the base determinant of all angular behaviour. From the equations of motion in section 4.2, it can be seen that the moment of inertia is a critical parameter of shuttlecock performance. The  $I_{xx}$  affects the axial spin behaviour, while the  $I_{yy}$  and  $I_{zz}$  determines the turnover angular response. The difference between  $I_{xx}$  and  $I_{yy}$  (or  $I_{zz}$ ) will also change the parameters of the spin-induced yaw. Therefore, in order to get the same angular performance, the moments of inertia of a synthetic shuttlecock should not deviate from that of the feather shuttlecock.

### **5.2.2 Wind Tunnel Study**

Wind tunnel study was conducted to measure the drag and the steady state spin rate.

The aim of the experiment is to investigate:

- Drag to mass ratio, for predicting the shuttlecock speed and flight range.
- Steady state spin rate, for comparison with the subsequent flight measured spin rate.
- Skirt deformation, for explanation of the drag and spin behaviour.

### 5.3 Experimental Method

In this section, the experimental methods applied for the Phase I of the shuttlecock testing are introduced. They are described in the following order:

- Shuttlecock specimens
- Experimental methods for obtaining the physical properties
- Experimental method for wind tunnel study

#### 5.3.1 Shuttlecock Specimens

The shuttlecock specimens used for this phase of the testing were tabulated and are presented in Table 15. Of the six types of shuttlecocks that were tested, three were BWF approved tournament-grade feather shuttlecocks. The results obtained from testing of the feather shuttlecocks represent the properties of the current top-tier feather shuttlecocks. The other three tested shuttlecocks were current production synthetic shuttlecocks that were readily available on the market. These represent the performance of the current synthetics. The specimens also consisted of two pairs of shuttlecocks of the same model but rated at different grain speed. These are the Yonex Aerosensa 40s and the Li-Ning X800s.

Table 15 Shuttlecocks used for the wind tunnel evaluation.

		Grain speed	BWF approved
Feather Shuttlecock	Babolat Tour	77	Yes
	Yonex Aerosensa 40	2(76-77)	Yes
	Yonex Aerosensa 40	3(77-78)	Yes
Synthetic shuttlecock	Yonex Mavis 350	Blue (77-78)	-
	Li Ning X800	Green (75-76)	-
	Li Ning X800	Blue (77-78)	-

The feather shuttlecocks came in tubes of 12, while the synthetic shuttlecocks were sold in tubes of 6. Although the full tube of each shuttlecock type was evaluated for the mass measurement, only one sample of each shuttlecock type was tested for the remaining experiments. These samples that were selected are the sample with the median flight distance of each tube. This was determined through flight distance test with a badminton shuttlecock launcher. These specimens were also used for the subsequent flight trajectory testing that will be described in chapter 6.

### **5.3.2 Physical Properties**

#### ***5.3.2.1 Mass***

The mass of the shuttlecocks were measured with a Precisa 262SMA-FR scale that is accurate to 0.0001 g. All the shuttlecocks in each tube were measured. The mean, the standard deviations and the ranges of the mass variation were evaluated.

#### ***5.3.2.2 Diameter and Chord***

A Vernier caliper is sufficient for the measurement of chord and diameter. With the end of the skirt resting vertically on a flat and level surface, the horizontal distance between two opposing feathers was measured. Opposing refers to a pair of feathers 180° apart. For a synthetic, the distance was taken as the horizontal distance between the most protruding segments of each fold along two opposing folds. The mean of five readings taken at random locations along the circumference gave the diameter.

To measure C, modification was made to the standard digital Vernier caliper. A flat steel plate was added to the measurement jaw of the calliper, parallel to the jaw. This addition provided a larger gripping surface for the vane end of the skirt, as

demonstrated in Figure 64. The caliper was zeroed with the fixture plate. Chord length,  $C$ , was measured as the distance from the tip of the cork to the tip of the skirt.

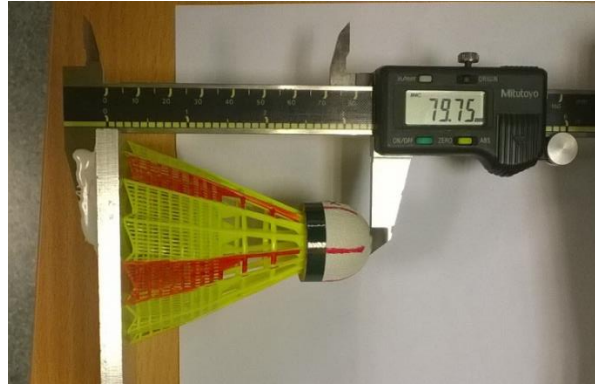


Figure 64 Modified Vernier caliper for chord length measurement.

### 5.3.2.3 Moments of Inertia

From [22], the  $I_{xx}$  of a badminton shuttlecock can be determined through a trifilar swing experiment which is illustrated in Figure 65. Hanging the shuttlecock by lightweight strings that were assumed to be massless, the shuttlecock was put into small amplitude oscillation symbolised by the arrows in Figure 65.

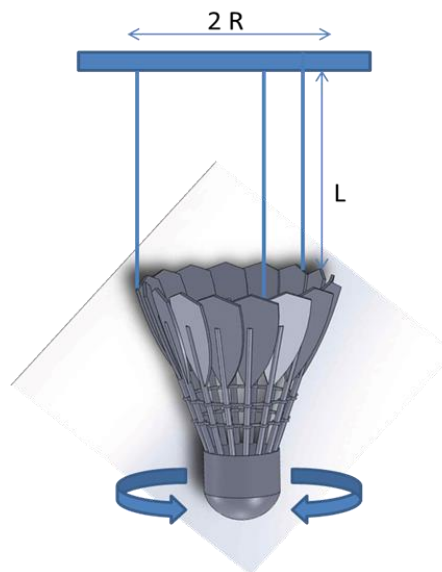


Figure 65 Trifilar swing experiment for determining the  $I_{xx}$ .

The moment of inertia was then calculated with the period of oscillation,  $T$ , using the formula shown in (63).

$$I = \frac{mgR^2T^2}{(2\pi)^2L^3} \quad (63)$$

The symbol  $R$  is the perpendicular distance between the C.G. and the string, while  $L$  is the length of the string. For the trifilar swing experiment,  $L$  was kept between 0.59 m to 0.6 m and  $R$  was at 0.033 m. The period,  $T$  was identified through the measurements of 15 oscillations, which gave a total time of more than 10s. Due to the relatively large variance, five readings were taken for each shuttlecock.

The  $I_{yy}$  and  $I_{zz}$  can also be obtained through similar method, with modification of the string to a bifilar setup, as illustrated in Figure 66. In the bifilar swing setup,  $L$  was between 0.43 m to 0.46 m, while  $R$  was kept to 0.028 m. The variation in  $L$  was due to the difficulty in maintaining the same  $L$  for every test shuttlecock. Moreover, it was unnecessary for  $L$  to be a constant across all the experimental runs because the difference would be accounted for in the calculation of the moments of inertia.

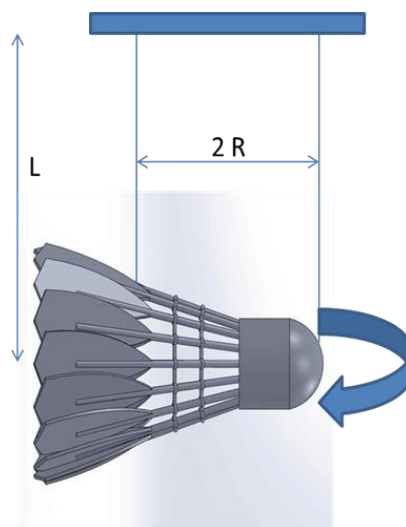


Figure 66 Bifilar swing setup for measurement of  $I_{yy}$  and  $I_{zz}$ .

### 5.3.3 Wind Tunnel Study

The six shuttlecocks were tested in a closed-loop wind tunnel commissioned by STEM ISI Impianti S.P.A. The wind tunnel has a test section measuring 780 mm (width) by 720 mm (height) by 2000 mm (length) and is suitable for flow speed of 6 m/s to 65 m/s. The wind tunnel fixture set up for holding the shuttlecock is presented in Figure 67. It consisted of a shuttlecock attachment piece, a ball bearing and a 6mm carbon rod. The shuttlecock was mounted to the attachment piece by automotive tape, thereby eliminating the need to apply destructive mounting methods such as gluing or drilling on the shuttlecock. The ball bearing that was attached between the attachment piece and the carbon rod allowed the shuttlecock to spin independently of the carbon rod. The various parts are illustrated in Figure 68. The length of the carbon rod was approximately 6 times the length of a shuttlecock, preventing the various components (wind tunnel sting, mounting plate, and load cell) in the wake from disturbing the flow field around the shuttlecock.

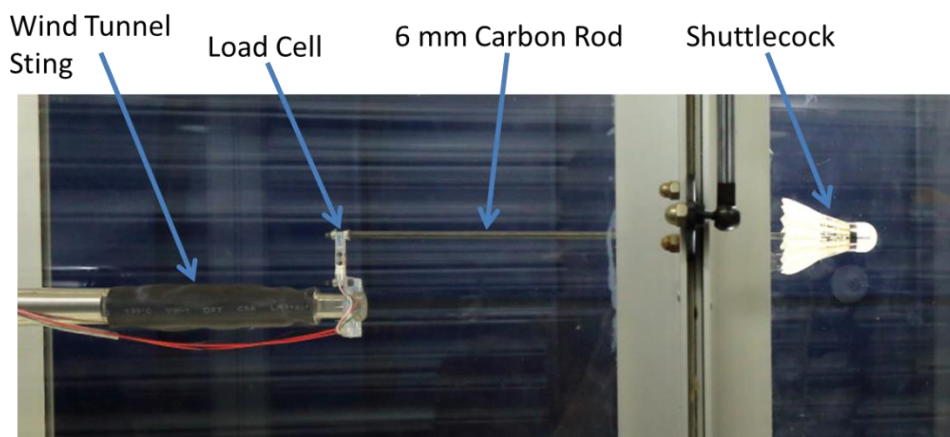


Figure 67 Wind tunnel mounting set up for working with badminton shuttlecock.

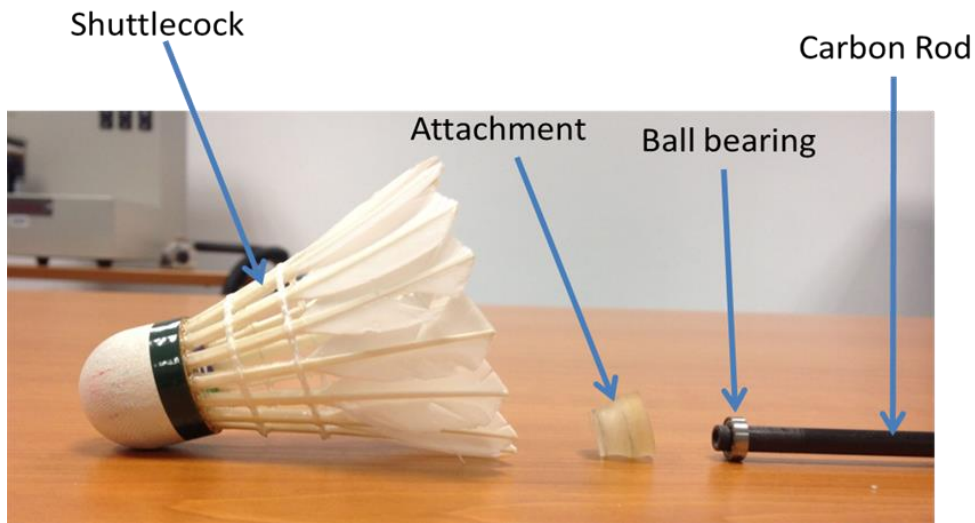


Figure 68 The shuttlecock mounting fixture for free rotation.

Force measurement was via a Seed Studio single axis 500 g load cell connected to a Vishay P-3500 strain indicator with gage factor at 0.300. Drag force on the entire fixture without the shuttlecock was measured and approximated as  $0.0136V^2$ . Drag force measurements were collected for air speed of 10 m/s to 50 m/s, in increment of 5 m/s.

Since the drag coefficients for shuttlecocks is likely to be insufficient for effective comparison between shuttlecocks, it was proposed that  $C_d S$  from (1) be used as the comparison parameter.

$$C_d S = D / 0.5 \rho v_{\infty}^2 \quad (64)$$

The symbol  $S$  in  $C_d S$  refers to the actual characteristic area.

The corresponding spin rates at each air speed were obtained by analysing high speed videos taken by the Phantom Miro 120s at 2000 fps. While spin should not affect the resultant drag [31, 32], the wind tunnel spin measurements provided comparison to flight captured spin rate.

With the shuttlecock aligned parallel to the flow direction and the camera, the skirt diameter at each flow condition was also obtained from the high-speed videos. Using the measured diameter, the skirt deformation was calculated. The deformation will be presented as shrinkage ratio [31, 32]. The shrinkage ratio is the ratio between the deformed shuttlecock diameter and the initial shuttlecock diameter. It is illustrated in Figure 69, where the shrinkage ratio is  $D/D_i$ . Therefore, a positive shrinkage ratio means that there is skirt expansion, while a negative shrinkage ratio means that the skirt has reduced in diameter.

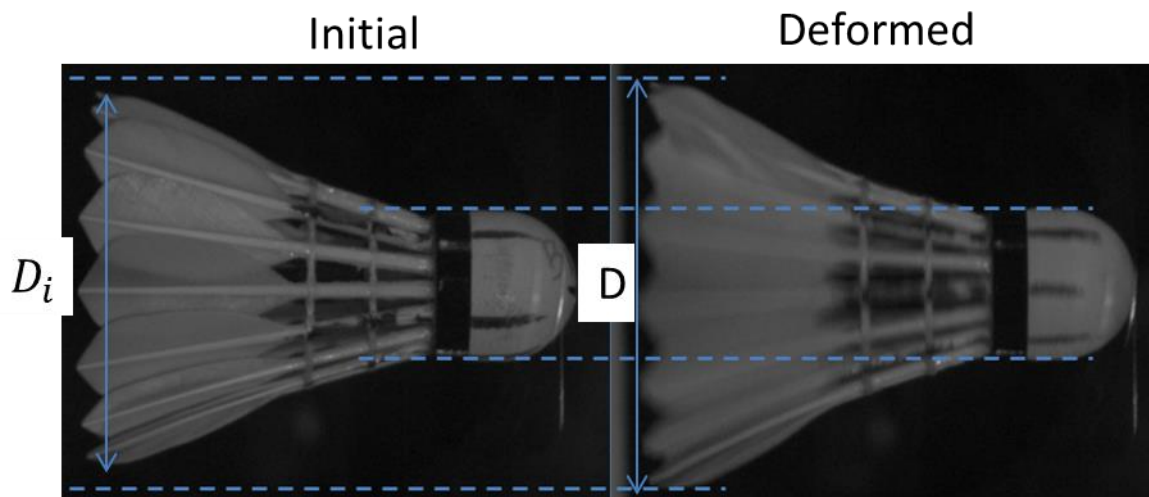


Figure 69 The shrinkage ratio is the ratio of  $D/D_i$ .

## 5.4 Results and Discussion

### 5.4.1 Physical Properties

#### 5.4.1.1 Mass

The results of each of the individual shuttlecocks are presented in Appendix C. The mean values are summarised in Table 16.

Table 16 Summary of the mass recorded for the shuttlecocks.

	Feather shuttlecocks			Synthetic shuttlecocks		
	Yonex AS40 (BWF)	Yonex AS40 (BWF)	Babolat Tour (BWF)	Yonex Mavis 350	Li-Ning X800	Li-Ning X800
Speed rating	2 (76)	3 (77)	77	Blue (76)	Blue (77-78)	Green (75-76)
Average mass /g	5.272	5.282	5.031	5.164	5.433	5.273
S.D. /g	0.105	0.050	0.126	0.040	0.020	0.023
Min mass /g	5.055	5.215	4.786	5.125	5.409	5.238
Max mass /g	5.378	5.395	5.203	5.219	5.454	5.293

Through these experimental results, it was observed that mass variation is unavoidable in badminton shuttlecocks. This is especially true in feather shuttlecocks. Even as a BWF approved tournament-grade shuttlecock, the mass of the samples within the same tube ranged from 4.786 g to 5.203 g. This is a variation of 0.417 g (8%) which is equivalent to a difference of more than 5 grain weight.

It was also observed that the synthetic shuttlecocks were generally heavier than the feather shuttlecock of the same speed rating. This is likely to be result of substituting

the light weight feather skirt with a much denser nylon skirt material. However, this does not imply that the same speed rated, but heavier synthetic shuttlecocks will fly further and faster than the lighter feather shuttlecocks. This is because the grain weight is only as an indicator to the “speed rating”. The actual parameter that is assessed is the flight range. Resolving to the fundamental parameters, this flight range is actually the drag-to-weight ratio. This means that a heavier shuttlecock can retain the same flight speed and range as a lighter one, so long as the drag-to-weight ratio is maintained. For instance, the drag can be increased by increasing the diameter of the skirt or changing the skirt pattern design (gaps, chapter 3).

Therefore, the traditional approach of using the grain weight as the absolute indicator of speed rating is likely to be flawed with the current shuttlecocks. A better measure of speed rating is the drag-to-weight ratio which is essentially the determinant of the range that is commonly used as a gauge in applied situation. The drag and range will be discussed in detail in section 5.4.2 and section 6.4.2.

From discussion with industry partners, it was said that speed ratings of shuttlecocks are determined through a speed rating sorting process where the shuttlecocks with the same flight range are grouped under the same speed. This means that a light-weight shuttlecock with slightly less drag than the average may be grouped together with a much heavier shuttlecock that has slightly more drag (or larger diameter) than the average. Moreover, the variability in the standard production process makes it difficult to manufacture the shuttlecocks to the desired grain speed. This creates a situation where a batch may not contain sufficient number of shuttlecocks of the correct grain speed. In such event, there is a possibility of manufacturers mixing in a

few shuttlecocks of slightly different grain speed into the tube of 12. This implies that a standard tube of shuttlecocks may not only contain shuttlecocks of different mass, but also of different speed ratings. Therefore, flight performance evaluation should always be conducted by using the shuttlecock of the median flight range from a tube. Such is also the approach in this thesis.

The mass measurement showed that all the shuttlecocks weighed more than their speed equivalent grain weight. This implies that a slight increase in shuttlecock weight is unlikely to influence play feel. This property of a shuttlecock being allowed to weigh more than the rated grain speed should be exploited in the substitution of feather with much denser synthetic materials.

#### *5.4.1.2 Diameter and Chord*

The chords and mean diameters of the shuttlecocks are shown in Table 17. The mean diameters of all the tested shuttlecocks were within 1 mm. The chord lengths showed much larger variation where the tested synthetics were less than 80 mm, while the feather shuttles were over 85 mm.

Table 17 Mean diameter and chord length of the shuttlecocks.

		Mean diameter /mm	Chord, C /mm
Feather	Babolat Tour (77)	65.31	85.12
	Yonex AS40 (3)	66.03	85.38
	Yonex AS40 (2)	65.85	85.53
Synthetic	Li-Ning X800 (Green)	65.66	79.84
	Li-Ning X800 (Blue)	65.77	79.03
	Yonex Maxis 350 (Blue)	65.79	79.79

Although a large dimensional tolerance is allowed for badminton shuttlecocks, the values in Table 17 show that current shuttlecocks have approximately the same dimensions. This is likely to be due to the performance requirement, where the proven recipe for dimensions is adhered to by the manufacturers. In the design of a badminton shuttlecock, the dimensions are used for the purpose of weight distribution and flight performance. Weight distribution refers to the resultant moment arm in aerodynamic moment and the moments of inertia. A common technique to varying the drag of a shuttlecock design is through adjustment of the skirt cone angle. The adjustment of cone angle allows for change in diameter without altering the chord length. Thus, changes in weight and moment of inertia can be kept to the minimum.

#### ***5.4.1.3 Moments of Inertia***

The moments of inertia that were recorded for the shuttlecocks are presented in Table 18. The differences between  $I_{yy}$  and  $I_{xx}$  were also given. Due to the variability that is often associated with results from such experiment, the standard deviations (Std. Dev.) were also included.

Table 18 Moments of inertia obtained for the shuttlecocks.

		$I_{xx} / \text{kgm}^2$		$I_{yy}, I_{zz} / \text{kgm}^2$		$I_{yy} - I_{xx} / \text{kgm}^2$
		Mean	Std. Dev.	Mean	Std. Dev.	
Feather	Babolat Tour (77)	1.19E-06	1.69E-08	2.96E-06	5.66E-08	1.77E-06
	Yonex AS40 (2)	1.39E-06	1.37E-08	3.32E-06	6.64E-08	1.93E-06
	Yonex AS40 (3)	1.4E-06	2.81E-08	3.11E-06	6.8E-08	1.72E-06
Synthetic	Li-Ning X800 (Green)	1.25E-06	2.56E-08	2.73E-06	2.19E-08	1.48E-06
	Li-Ning X800 (Blue)	1.34E-06	1.66E-08	2.67E-06	1.26E-08	1.33E-06
	Yonex Mavis 350	1.28E-06	3.12E-08	2.7E-06	2.93E-08	1.42E-06

The Std. Dev. obtained for the results were small with respect to the readings. This means that variability between readings is relatively small. Therefore, the treatment of using the means of five reading samples is sufficient. Comparing the  $I_{xx}$ , it was seen that both the AS40 had larger values than the other shuttlecocks. The  $I_{xx}$  of the Babolat Tour at  $1.19\text{E-}06 \text{ kgm}^2$  was 15% lower than the AS40. However, the in-flight observed axial spin behaviour of the Babolat shuttlecock appeared to be similar to the AS40 (section 6.4.2.5). The measurements for the synthetic shuttles were between that of the AS40 and the Babolat Tour. Despite that, the in-flight captured spin behaviour of the synthetics showed significant variation from the reference feather shuttlecocks. This suggests difference in the spin moment generation.

Interestingly, the  $I_{yy}$  and  $I_{zz}$  of the synthetics were lower than the feather shuttlecocks. Comparing the Mavis 350 to the AS40 (3), it was seen the  $I_{yy}$  of the Mavis 350 was 23% lower. The lower value of  $I_{yy}$  measured for the synthetic shuttlecocks suggests that they have better angular stability than the feather shuttlecocks. However, the experimental observation of turnover performance has shown that the angular stability of the synthetic shuttlecocks are worse [64]. This phenomenon is likely due to the weight distribution, the length of the skirt and the porosity of the synthetic skirt. The higher porosity, as observed by Cooke [22], and the shorter chord length of the synthetic skirt means there is less mass hanging from the vane portion of the skirt, thereby reducing the  $I_{yy}$ . However, the increased porosity would also have reduced the amount of air resistance and lowered the aerodynamic forces acting on the shuttlecock. Consequently, the aerodynamic moment of stabilisation, which is a function of the aerodynamic forces, is reduced [34]. The outcome is a degradation of the turnover stability.

The measurements suggest that the current synthetics are on par with the feather shuttlecocks. It is unlikely that performance improvement can be attained through modifications to the existing mass distribution on the synthetics. Further design improvements should come from modification of the skirt features to improve aerodynamic performance. These obtained values also provided a guideline to the moment of inertia that shuttlecock designs should have. Through the term  $I_{yy} - I_{xx}$ , the general spin-induced heading change can be estimated. Due to the smaller  $I_{yy} - I_{xx}$  on the synthetics, it is likely that more axial spin will be required for the synthetics to achieve the same secondary precession effect as the good feather

shuttlecocks. This supports the stall trajectory profile and axial spin behaviour observed in section 6.4.2.

## 5.4.2 Wind Tunnel Study

### 5.4.2.1 Drag Parameter, $C_d S$

The  $C_d S$  measured for the six shuttlecocks were plotted and are shown in Figure 70. Similar to the other results in this report, the parameters were plotted with respect to air speed instead of the commonly used Reynold's number. This is because the Reynold's number is dependent on the characteristic area and is likely to be a less accurate representation than air speed when skirt deformation is considered.

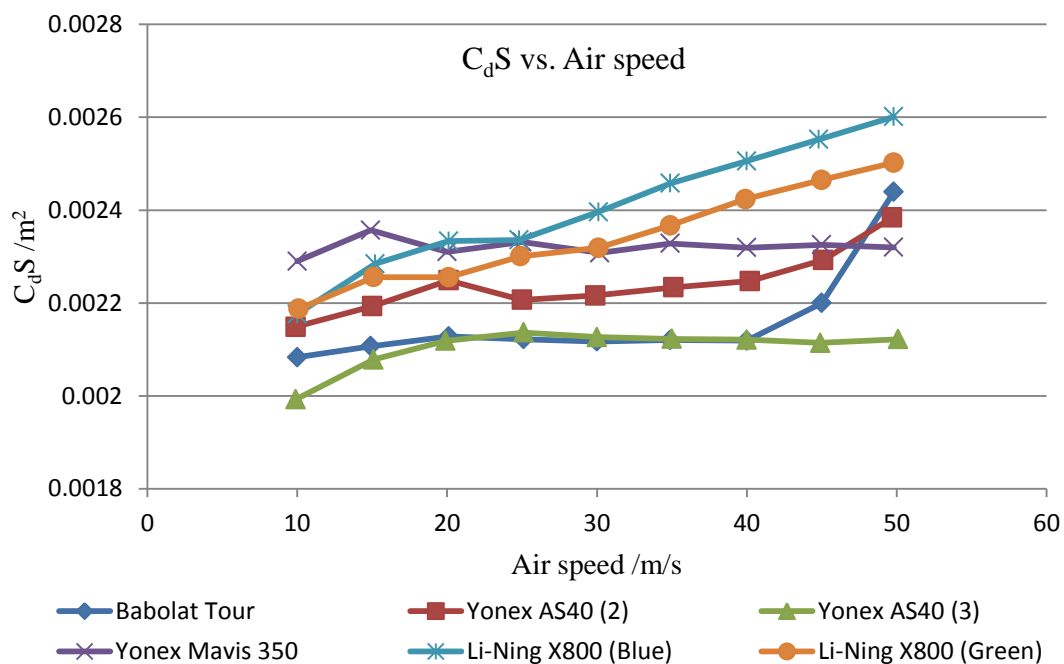


Figure 70 Plot of  $C_d S$  with respect to the air speed for all six tested shuttlecocks.

In general,  $C_d S$  of feather shuttlecocks were observed to be almost independent of the flow speed (and thus, Reynold's number), especially when the flow speed was slow. At high speed flow,  $C_d S$  of the feather shuttlecocks increased significantly. This was the most significant for the Babolat Tour and it is likely to be the effect of

skirt expansion from centrifugal force produced by the axial spin of the shuttlecock. Such a proposition was also suggested in [31, 32]. In contrast, the  $C_d S$  of the slower spinning Yonex AS40 (3) did not increase with air speed.

For the synthetic shuttlecocks, the  $C_d S$  recorded for the Yonex Mavis 350 suggests that the  $C_d S$  is air speed independent, even at high flow speed. In contrast, the  $C_d S$  recorded for both the Li-Ning synthetics increased with higher air speed. Since both the tested Li-Ning X800s exhibited the same drag behaviour, this is likely to be a characteristic of the shuttlecocks.

It was observed that the synthetic shuttlecocks have higher  $C_d S$  than the feather ones, making them more “draggy” than the feather ones. This is contradictory to popular belief that synthetics do not have sufficient drag.

#### ***5.4.2.2 Axial Spin***

The wind tunnel measured axial spin rates of the shuttlecocks were plotted and are presented in Figure 71. In general, the spin rates showed good linearity with air speed, supporting the theoretical model proposed in (49). For the Yonex AS40 (2) and the Babolat Tour, the spin rates increased exponentially when air speed exceeded 40 m/s. This is likely to be because of the spin-induced skirt expansion that was observed on these two shuttlecocks. Since the spin rate of the Yonex AS40 (3) was only about half that of the other feather shuttles, it is likely that there was no spin-induced deformation. This may account for the spin rate-air speed linearity that continues beyond air speed of 40 m/s for the AS40 (3).

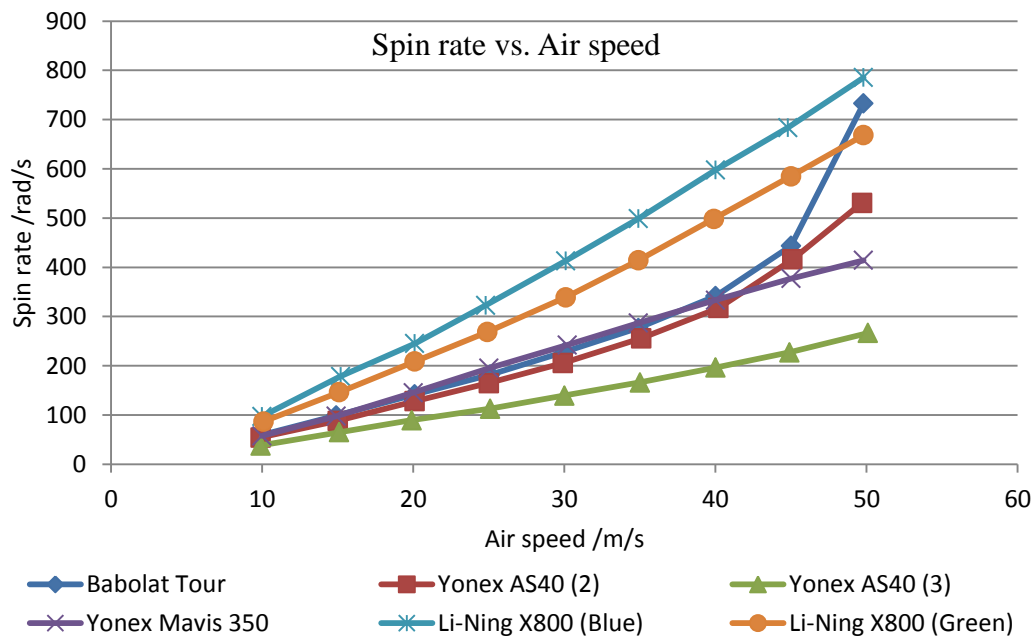


Figure 71 Axial spin rates of the six tested shuttlecocks.

As for the synthetic shuttles, although the X800s had similar spin rates as the Yonex AS40 (2) and the Babolat Tour, the loss in spin-air speed linearity were much less significant. Despite the large change in  $C_d S$  for the X800s, the spin rates were less affected. Large variation in spin rate was observed across the different shuttles, but these were wind tunnel steady state spin rate which are unlikely to be observed in actual flight. The actual in-flight spin rates will be studied in the experiment in Phase II of the testing.

#### 5.4.2.3 Skirt Deformation

The shrinkage ratios were plotted and are shown in Figure 72. At a flow speed of 50 m/s, skirt deformation of more than 3% was observed for the Babolat Tour, the Yonex AS40 (2), and both the Li-Ning X800 shuttlecocks. These shuttles also had higher spin rates. The data reinforces the idea that comparison of  $C_d$  is flawed because the change in area from deformation is not accounted for. With a 3% change

in diameter, the resultant change in area and drag will be 9%. This means that the  $C_d$  calculated from a fixed characteristic area, as traditionally done, will show a 9% increase at high speed simply because of unaccounted surface area change. Therefore, the  $C_d S$ , which can be obtained as easily as the  $C_d$ , is a more accurate alternative.

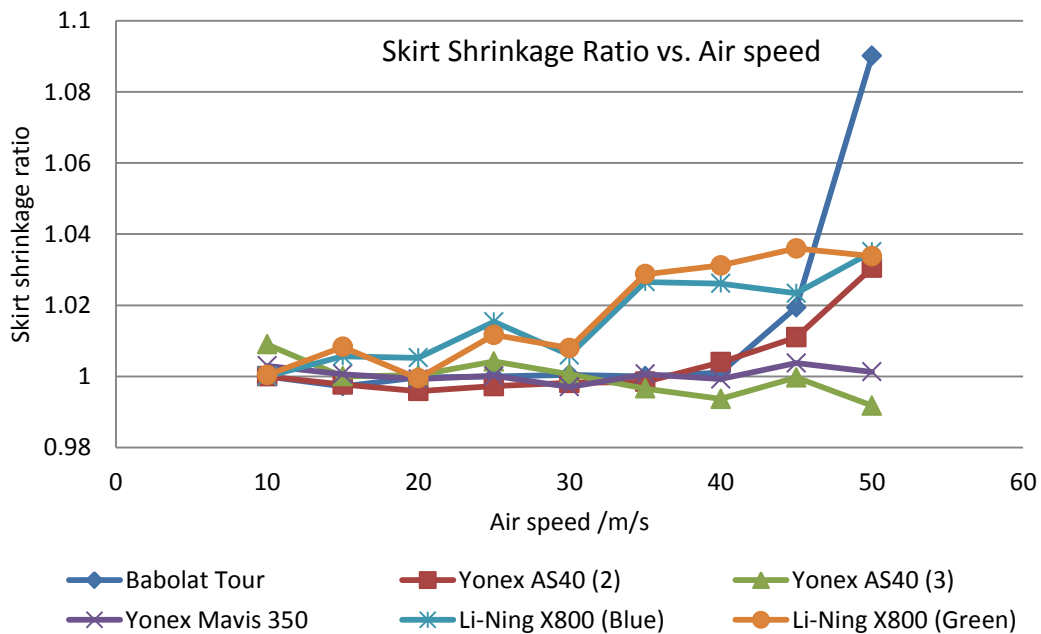


Figure 72 Plot of the shrinkage ratio and air speed.

The 66 mm shuttlecock captured through the high speed camera could be magnified into an image of 235 mm without significant pixilation. The magnification meant that a 1% change in shuttlecock diameter (0.66 mm) will appear as a 2.35 mm change on the image. This is a change that can be easily detected by analysis on the tracker software. Comparing the measurement resolution to the observed shrinkage ratio, it is unlikely that the skirt expansion observed for the Babolat Tour, the Yonex AS40 (2), and both the Li-Ning X800 shuttlecocks were experimental errors.

The Babolat Tour has the largest skirt expansion of 9% at 50 m/s flow. This coincides with the exponential increase in spin and  $C_d S$ , suggesting that the opening of the skirt is the cause. Since the skirt expansion only occurred at high speed flow, it is likely that spin is the reason for the expansion, as also proposed in [31, 32]. However, the in-flight spin rates that were measured in section 4.3.2 suggest that the shuttlecocks have much lower spin rates in actual flight than in the wind tunnel. Thus, it is unlikely for the spin-induced deformation to occur in actual use. This is a point that is not discussed in the literatures and it will be validated in the flight testing in Phase II (chapter 6).

Despite having the highest spin rate, the Li-Ning X800 synthetics did not experience more skirt expansion than the other shuttlecocks. Since the X800s have lower skirt stiffness than the feather shuttlecocks, the superior resistance to expansion is unlikely to be due to skirt stiffness. The skirt stiffness of the synthetic nylon skirt shuttles will be studied in chapter 7. Instead, this is possibly the effect of skirt construction where the one piece integral skirt design of the synthetic constraints the expansion. On the other hand, the unconstrained feathers on the feather shuttlecocks will mean the skirt has much more freedom in expansion. Deformation was also observed to be near negligible on the slower spinning shuttles (Yonex AS40 (3) and Yonex Mavis 350).

Interestingly, none of the tested shuttlecocks exhibited significant reduction in skirt diameter. This is in contrast to the result that was obtained by Cooke [22] where the skirt deformation was reported to be 1-5 mm in diameter at  $Re=1650,000$  ( $\sim 36$  m/s). There are two possible explanations. Firstly, the shuttlecocks that were tested by

Cooke [22] were from two decades ago and were likely to be less sophisticated in stiffness and strength. More likely, the deformation was due to the much lower steady state spin rate that was obtained in [22]. A possible cause may be the energy lost from the spin bearing mechanism. The observation points to the importance of spin, whereby the spin generates centrifugal force to resist drag deteriorating skirt shrinkage.

#### **5.4.2.4 Drag per Unit Mass, $C_d S/m$**

The wind tunnel evaluation demonstrated the linked behaviour of axial spin, drag and skirt deformation. This suggests that sufficient spin should be designed in a new shuttlecock to resist deformation and maintain drag characteristic. The usage of  $C_d S$  gave good comparison of drag characteristics between the shuttlecocks. However,  $C_d S$  is unable to fully explain the actual flight behaviour. This is because a heavier shuttlecock will naturally fly faster and further than a lighter shuttlecock with the same  $C_d S$ . It is proposed that the drag coefficient area per mass,  $\frac{C_d S}{m}$ , be used as the definitive parameter when designing shuttlecocks. It will be the equivalent of the original intention of the grain weight speed rating, which has a distorted meaning today. This parameter takes into account of the mass of the shuttlecock which can vary significantly in the modern designs. The mass of the shuttlecock specimens that were used for the wind tunnel testing are shown in Table 19. Using the wind tunnel result and the mass of the shuttlecocks, the  $\frac{C_d S}{m}$  at various speeds were plotted and are shown in Figure 73.

Table 19 Mass of the shuttlecock specimens.

		Mass /g
Feather Shuttlecock	Babolat Tour	5.04
	Yonex Aerosena 40	5.36
	Yonex Aerosena 40	5.24
Synthetic shuttlecock	Yonex Mavis 350	5.13
	Li Ning X800	5.45
	Li Ning X800	5.27

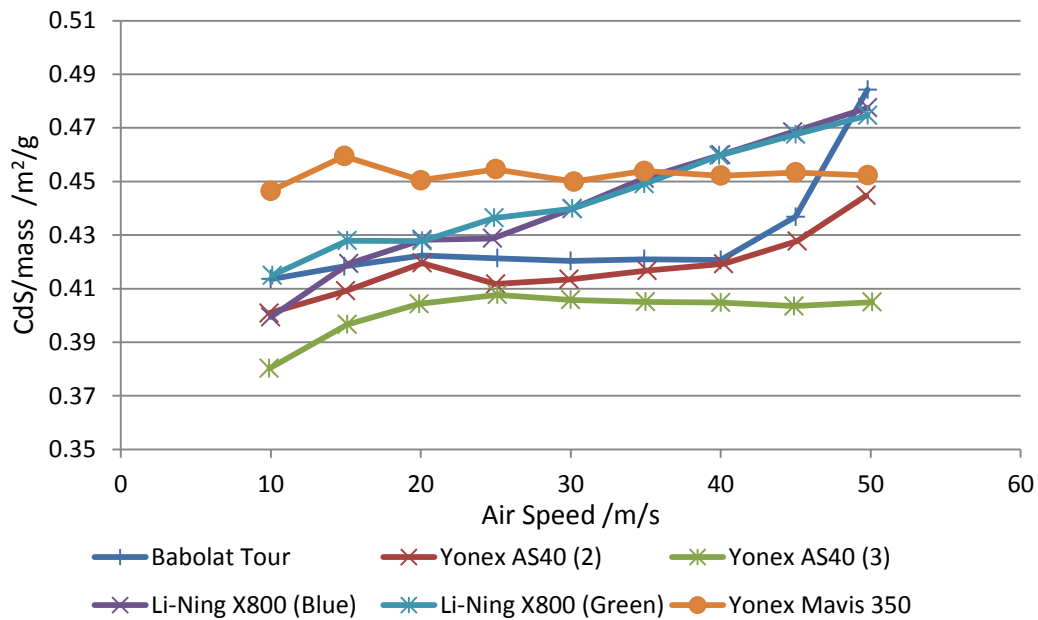


Figure 73  $C_dS/m$  plot for the tested shuttlecocks.

Figure 73 shows that the  $\frac{C_dS}{m}$  observed for the synthetic shuttlecocks were higher than the feather shuttlecocks. This suggests that the synthetics have less range and less speed than the feather shuttlecocks. The observation is contrary to the common perception of synthetics having more range and it should be validated in the flight testing.

Taking the average of the AS40 (2) and Babolat Tour shuttles, it was observed that a  $\frac{C_d S}{m}$  value of 0.42 m<sup>2</sup>/kg is required for a speed 77 shuttlecock. Therefore, an ideal reference value of  $\frac{C_d S}{m}$  can be approximated as 0.42 m<sup>2</sup>/kg. Comparing the  $C_d S$  results (Figure 70) of the two X800 shuttlecocks suggests that the “Blue” speed rated version is slower because of the larger measured  $C_d S$ . However, the  $\frac{C_d S}{m}$  plot gave a very different conclusion. The  $\frac{C_d S}{m}$  values suggested that both the X800 shuttlecocks have similar performance at speed above 30 m/s. Below 30 m/s, the X800 (Blue) was slightly faster than the Green speed rated one. Such a contrasting result is the effect of the mass, where the heavier mass of the X800 (Blue) offsets the increased drag. The above will be checked in the flight testing in chapter 6.

## 5.5 Summary of Phase I

In the static testing in Phase I, the physical properties were evaluated using the detailed experimental methods. Sample results were also presented. Controversies, such as those in the weight or the characteristic area, were discussed. Through the investigation, it was observed that the tested shuttlecocks had similar dimensions and mass properties.

Wind tunnel studies were also conducted for understanding of drag, spin rate and skirt shrinkage. The usage of  $\frac{CdS}{m}$  was proposed as the alternative to the grain weight speed indicator. This was because speed rating based on grain weight was no longer relevant to the modern shuttlecocks. The results from the wind tunnel analysis and the mass properties study showed that the synthetic shuttlecocks were actually superior to the feather shuttlecocks. The synthetic shuttlecocks had more drag per unit mass (better deceleration), less skirt expansion (more consistent drag performance), and lower moments of inertia (less rotational inertia).

## **6. SHUTTLECOCK TESTING: PHASE II (FLIGHT)**

This chapter describes the Phase II of the shuttlecock testing. In this phase, the significant flight processes which were discussed in chapter 4 are investigated and analysed. The experimental study includes both the turnover process (unsteady flight phase) and the flight trajectory (steady flight phase). In order to evaluate the flight performance, a badminton shuttlecock launcher had to be developed. Therefore, this chapter will first describe the development process of the launcher and the initial trial that was conducted. An introduction to the Phase II of flight testing is then presented. This is followed by the methodology of Phase II and then the results and discussion.

### **6.1 Shuttlecock Launcher Development**

#### **6.1.1 Existing Problems**

As seen in Appendix B, the compressed gas shuttlecock launcher was capable of launching the badminton shuttlecock at high speed. However, there were several limitations and these were:

- Shuttlecock damage - Feather shuttlecocks showed high rate of wear and tear on the feather strands even on the first launch. Moreover, the feather shaft was prone to breakage with the compressed air launcher.
- Testing of synthetic shuttlecocks - The compressed air launcher was unable to launch the synthetic shuttles.
- Turnover observation - Shuttlecocks were shot out flying nose first on a compressed air launcher. This means that there was no turnover process involved.

Therefore, a new launcher based on a rotating badminton racket was required for the subsequent experimental work.

### 6.1.2 Motion Analysis of Racket Speed

Motion tracking was conducted for observation of the racket head speed to serve as a guide for developing the launcher. A Vicon™ MX tracking system was used. Markers were placed on the racket as seen in Figure 74. The absolute head velocity in a smash was recorded. Absolute velocity refers to all motion induced upon the racket through arm movement and body movement.



Figure 74 Motion tracking markers on the badminton racket.

Two sets of 5 smashes were captured with two badminton amateurs. Tracking data showed random points of 0 position change. This was likely to be speed-induced data dropout of the tracking system because the racket is a near rigid object that has a continuous motion in the stroke. Therefore, those data were filtered. The processed results are presented in Table 20. Values generally agreed with the past works that were done for motion capture of badminton racket smash stroke, as seen in [110, 111].

Table 20 Recorded racket tip speed in a smash.

	1st	2nd	3rd	4th	5th
Player A	43.7	39.2	49.8	N.A.	40.1
Player B	38.3	34.5	37.6	35.9	43.5

Literatures have shown that top players are capable of using the elastic deflection of badminton racket to achieve a higher tip speed [112-114]. While it might be critical for racket dynamics, this experiment was only for observing an estimate to develop a launcher. Therefore, error from racket deflection was not significant for the purpose of the work. Moreover, the speed of the launcher is adjustable. Since the smash shot is the fastest badminton stroke, it was identified that a racket tip speed of less than 40 m/s would already be sufficient for the launcher.

### 6.1.3 Developed Launcher

Figure D1 of Appendix D shows the various functional components of the racket-based launcher. A Babolat alloy racket was spun by the geared down brushless motor, where the racket speed was controlled by an electronic speed controller. CAD model of the drivetrain group is shown in Figure D2 of Appendix D. The shuttlecock release mechanism consisted of three mini servos. Both the speed controller and release mechanism were controlled by an Arduino open source board. Triggering was via a flex resistor attached to the aluminium profile frame. The Arduino prototyping board and flex sensor are presented in Figure D3. Resistance of the flex sensor was changed whenever the racket passes through the sensor. This allowed feedback of the racket position and thus enabled the shuttlecock to be released consistently with respect to the racket position.

The whole procedure is described as follows:

- Powering on initializes the Arduino board to start the pre-programmed sequence. A zero-spin signal is sent to the motor speed controller.
- After a delay of 5 s, a second signal containing the desired motor speed is sent to the speed controller.
- A waiting time of 28 s is given for the motor, and thus, the racket, to accelerate up to speed.
- After the 28 s, Arduino awaits the trigger signal from the flex sensor before it releases the shuttlecock.
- Upon reaching the pre-determined position, the racket comes into contact with the flex sensor and in the process changes the resistance of the sensor. This sends a trigger signal to the Arduino.
- Another time delay is applied before the shuttlecock release mechanism is operated. This delay varies from 30 ms to 110 ms and can be adjusted to allow the different shuttles to always impact on the same point of the racket.
- Following the second delay, Arduino commands the opening of the drop mechanism and the shuttlecock is released into the path of the rotating racket.
- Launch is completed when the shuttlecock is hit by the racket.

The flight mode used for shuttlecock testing was a high-speed clear shot. The major advantage of a clear shot is the comprehensiveness in flight testing, where flight performance at both high-speed and low-speed were evaluated.

## 6.1.4 Initial Trial

### 6.1.4.1 Experimental Method

The consistency of the launcher was evaluated through trial experimental runs with two tubes of shuttlecocks- one tube of 12 Wilson Club (77) and another tube of 12 Babolat Tournament (77). Four high-speed cameras were used for the experiment. Three Phantom Miro 120s were setup along the flight path to capture the trajectory and angular behaviour. The positions of the cameras are as given in Table 21.

Table 21 Details of the camera positions and settings.

	Camera 0	Camera 1	Camera 2	Camera 3
Distance from launcher /m	1.5	2.14	5.01	8.03
Height of camera /m	1.1	1.85	2.82	2.11
Camera type	Photron EX1024	Phantom Miro 120s	Phantom Miro 120s	Phantom Miro 120s
Lens focal length /mm	35	24	24	28
Shutter speed /s	1/10000	1/5000	1/5000	1/2000
Frame rate /fps	1000	500	500	500

In a racket sweet spot study [115], it was observed that impact 2.5 cm away from the sweet spot will reduce the impact force from 28.80 kg to 22.45 kg on a racket testing machine. To prevent bias from launch variation, the impact locations on the racket string bed were recorded with a fourth camera (Camera 0). This camera was positioned directly in front of the rotating launcher racket. Ideally all the shuttlecocks should be launched through impact on the exact same point on the racket. However, this was infeasible with the developed launcher. Therefore in this

study, only launches within three string height (outlined in the white box in Figure 75) were accepted.

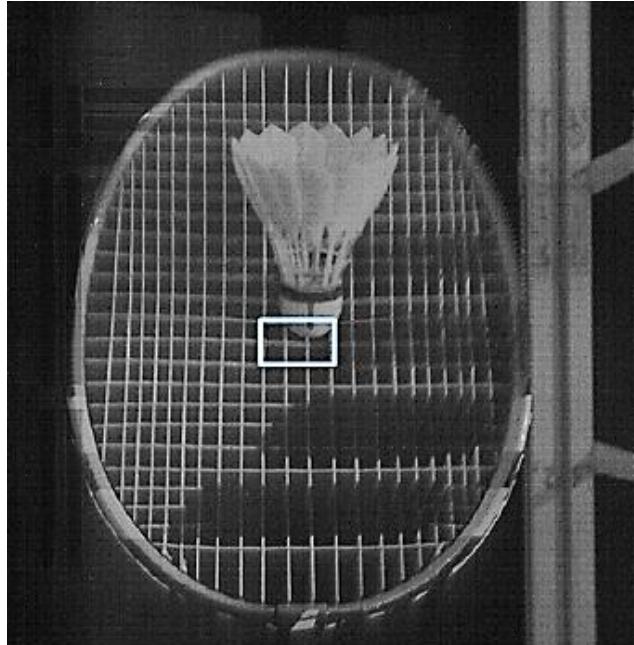


Figure 75 Shuttlecock- string bed impact location that is defined as acceptable for this study.

The shuttlecocks from each tube were labelled from 1 to 12. A launch was accepted if it fell within the box, otherwise the experiment was repeated for that shuttlecock. In general the launcher was relatively consistent. Only four out of the twelve Babolat shuttlecock required a second launch and all launches were acceptable in the second attempt. The recorded videos were then processed for the initial launch velocities and the flight trajectories.

#### ***6.1.4.2 Results and Discussion***

The recorded impact locations and the corresponding initial velocities for all the Babolat Tournament (77) and Wilson Club (77) are given in Figure 76 and Figure 77. The symbols used follow the coordinate system that was applied in chapter 4, where  $\dot{x}$  refers to the forward velocity component and  $\dot{z}$  symbolises the velocity

component in the direction of gravity. The initial shuttlecock velocities showed that the impact location criterion was appropriate.

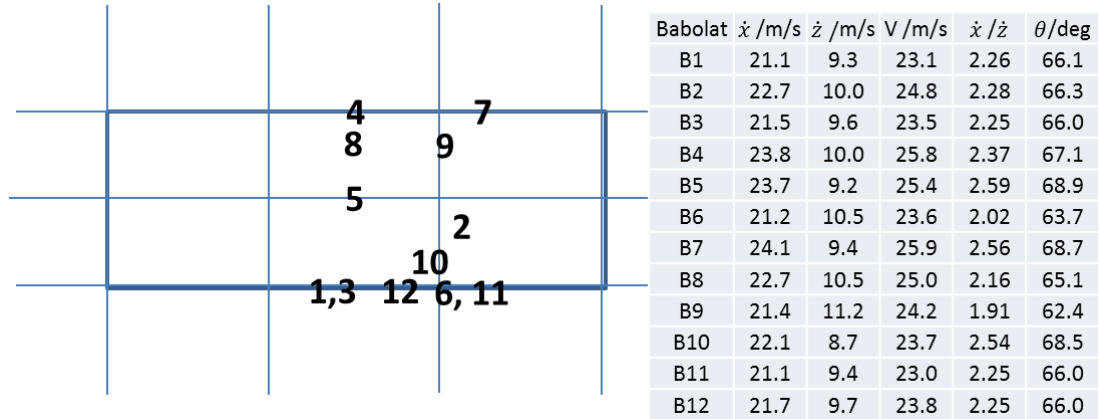


Figure 76 Impact locations and launch velocities for Babolat Tournament (77) within the predefined box.

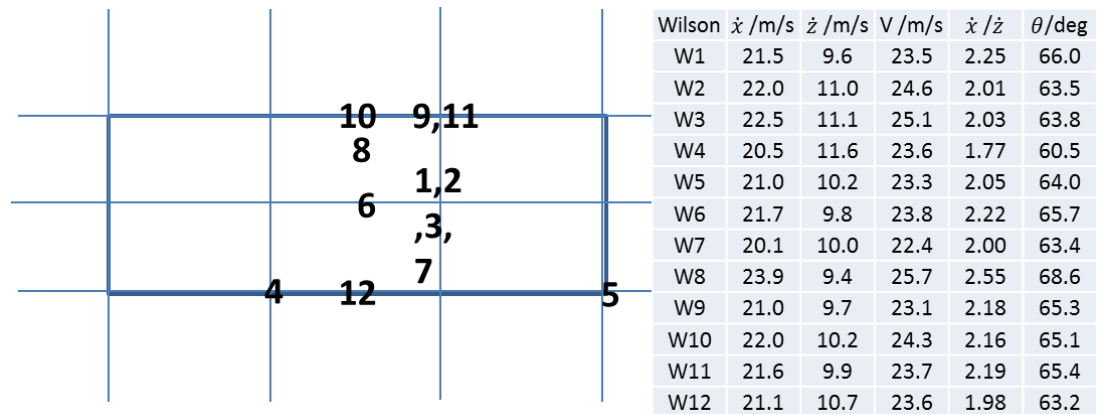


Figure 77 Impact locations and launch velocities for Wilson Club (77) within the predefined box.

The trajectories of the shuttlecocks were obtained through video analysis using Tracker. They are shown in Figure 78 and Figure 79, where each data marker symbolises one reading. The gaps between the clusters are the “blind spots” that were not captured by the cameras. This is an experimental setup limitation and can be eliminated with additional cameras. However, it is unlikely to be to be an issue for trajectory estimation because a shuttlecock has a smooth continuous motion.

Therefore, the blind spots can be easily extrapolated by trend line fitting when required. Moreover, differences between the trajectories could already be seen with the obtained raw data points.

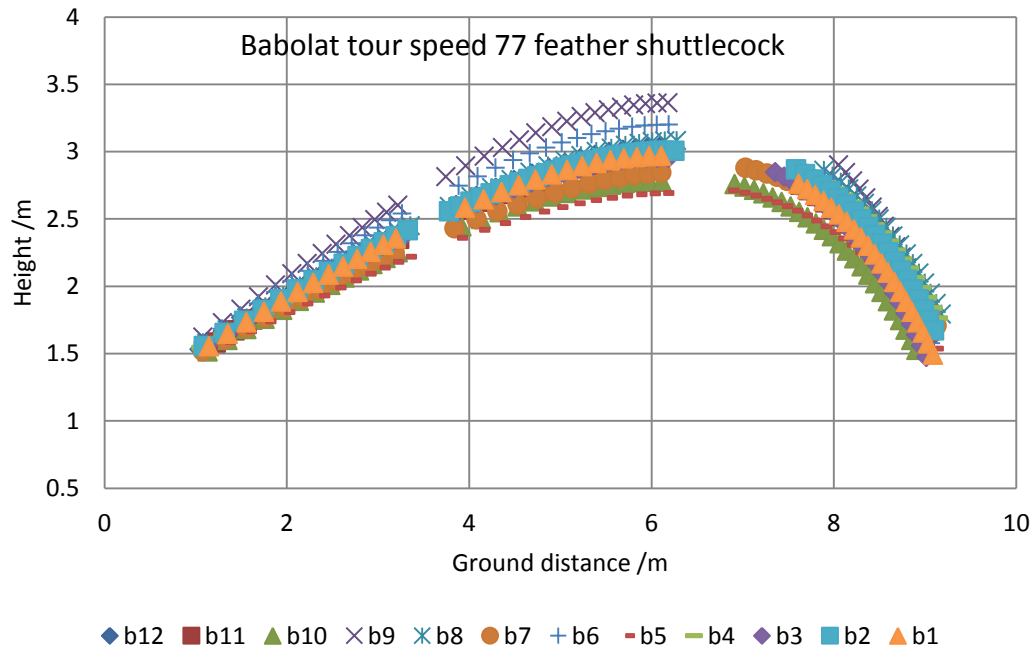


Figure 78 Trajectories obtained for the 12 Babolat shuttlecocks.

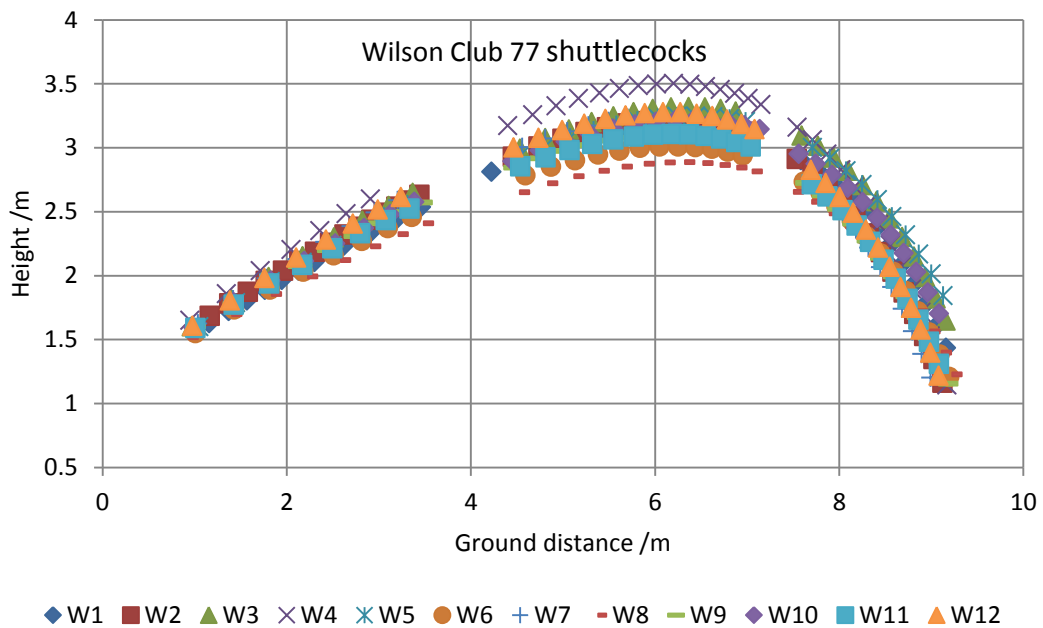


Figure 79 Trajectories obtained for the 12 Wilson feather shuttlecocks.

A large variation was observed between the 12 trajectories that were obtained from each tube of shuttlecocks. While variations between shuttlecocks may have resulted in slight trajectory differences, it is unlikely to result in such a range of trajectories. This was even more unlikely when taking into account that the Babolat shuttlecocks were BWF approved tournament-grade product. Further analysis of the results showed that the trajectories were heavily biased by the velocity ratio ( $\dot{x}/\dot{z}$ ). For instance, run W4 which had a small  $\dot{x}/\dot{z}$  (1.77) had a high flight path, while run W8 with 2.55  $\dot{x}/\dot{z}$  ratio had a very low flight path.

This trial study on the shuttlecocks showed that:

- Launch condition was critical for effective comparison of badminton shuttlecocks. The launch velocity ratio ( $\dot{x}/\dot{z}$ ) was as critical as the absolute launch velocity.
- Framing of the shuttlecock trajectory could be improved by relocating the second camera to also capture the vertex of the trajectory. This was demonstrated in the result in Figure 79.
- Testing of every individual shuttlecock was time consuming and would be infeasible when comparing various shuttlecock types. Testing of the median shuttlecock in each tube should be conducted in subsequent studies. Median shuttlecock refers to the shuttlecock within a tube that has the median flight range.

#### ***6.1.4.3 Launch Condition***

The results have shown that the launch condition determines the resultant trajectory of the shuttlecocks. To prevent bias in comparison, a launch condition of acceptance

must be defined. Recognising that it is impossible to ensure the exact same launch condition in every shot, trajectory simulation with (2) and (3) determined that a launch angle of  $65.5 \pm 0.5 \text{ deg}$  and initial velocity of  $24 \pm 0.5 \text{ m/s}$  would produce trajectories of acceptable deviations. This gave a  $\dot{x}/\dot{z}$  ratio of  $2.20 \pm 0.05$ . From Table 22, it can be seen that a change in launch velocity ratio,  $\dot{x}/\dot{z}$ , of  $2.20 \pm 0.05$  resulted in a height difference of  $\pm 0.04 \text{ m}$  with no change in range. On the other hand, changing the velocity in the defined range of  $24 \pm 0.5 \text{ m/s}$  gave a corresponding change of  $0.08 \text{ m}$  in range and  $0.03 \text{ m}$  in vertex height. This was less than 1% of the actual trajectory range and height. Therefore, the difference is probably negligible. The simulated trajectories are shown in Appendix F.

Table 22 Range and height of simulated trajectories with varying launch conditions.

Case	$\dot{x} / \text{m/s}$	$\dot{z} / \text{m/s}$	$\dot{x}/\dot{z}$	V /m/s	Angle /deg	Height /m	Range /m
Constant velocity and Varying $\dot{x}/\dot{z}$	21.76	10.12	2.15	24.00	65.06	3.14	9.31
	21.85	9.93	2.20	24.00	65.56	3.18	9.31
	21.93	9.74	2.25	24.00	66.04	3.22	9.31
Constant $\dot{x}/\dot{z}$ and Varying velocity	21.39	9.72	2.20	23.50	65.56	3.15	9.23
	21.85	9.93	2.20	24.00	65.56	3.18	9.31
	22.30	10.14	2.20	24.50	65.56	3.21	9.39

## **6.2 Overview of Phase II**

### **6.2.1 Turnover**

The turnover process was described and modelled in 4.3.1. This is the flight phase which enables a shuttlecock to flip over and fly nose-first. Traditionally [22, 34], this behaviour was quantitatively compared using “time to complete turnover”. Such a treatment is unlikely to be fair because the heading of a shuttlecock is always changing, making the determination of completion difficult. Moreover, the transient response of the angular stability was also not taken into account.

The turnover was studied in Phase II of the testing by experimental and simulation approach. Through identification of flight parameters from experimental data, the flight test provided a platform for comparison of angular stability. The experimental results were also published in [64]. Although the response time for  $t > 0.065$  s was not captured, it was modelled through the identified parameters using the derived model in 4.3.1.2. This gave insight on the subsequent oscillation amplitude.

### **6.2.2 Flight Trajectory**

In the previous works that attempted to compare flight trajectory, the flight paths were simulated from measured variable that were applied to a system with fixed initial flight condition [19, 25, 90]. This means that the trajectories were not measured and may have been prone to error from simulation. Moreover, sample sizes were usually too small to effectively gather a reference baseline trajectory of shuttlecock flight.

In this part of the study, various types and grades of feather and synthetic shuttlecocks were compared. The main objectives of this part of the experimental work were:

- To determine a reference flight trajectory and parameters from testing of the tournament-grade shuttlecocks.
- To identify the differences in flight performance between the various types of shuttlecocks.

Flight trajectories, linear air speeds, and the corresponding in-flight spin rates of various shuttlecocks were investigated using a shuttlecock launcher and three high resolution high-speed cameras. The clear shot was selected as the flight mode of comparison. This was because the clear shot is a good representation of shuttlecock performance. At the launch of a clear shot, the shuttlecock was launched at relatively high speed, almost equivalent to a smash shot. Therefore, the deceleration in the early segment of a clear shot would also represent the drag performance and give insights on how a shuttlecock will decelerate in a smash shot. As the flight progressed, the shuttlecock slowed down tremendously before transiting into a slow speed flight, stalling and then pitching towards the ground. This segment of flight is similar to the flight condition of the net shot and serve shot. The process of stall and quality of drop will also determine the perceived quality of the flight behaviour. This is because a good feather shuttlecock is traditionally thought to have a near vertical drop, while a synthetic shuttlecock does not. However, this is just players' opinion and thus far, there has been no extensive work to fairly compare the different shuttlecocks fairly.

## 6.3 Experimental Setup and Methodology

### 6.3.1 Turnover

#### 6.3.1.1 *Experimental Method*

The experimental setup for observation of the turnover behaviour consisted of a high speed camera and the racket based shuttlecock launcher. The detailed steps are as follows:

- The median performing shuttlecock of the tube was tested. Median performing refers to the shuttlecock within a tube with the median flight range. This is a common practice that should be enforced to prevent the result from being biased by the use of an outlier shuttlecock.
- The high-speed camera, which was shooting at 1000 fps, was aligned to the flight path. The distance between the camera and the launcher produced a captured frame of more than 1.5 m wide. This provided sufficient framing width to capture the main angular behaviour in turnover.
- Using the launcher, the shuttlecock was launched at speed of 22-24 m/s. Since the racket only rotated in the pitch axis, the excitation input to the shuttlecock and thus, the angular behaviour, was only in the pitch axis. Compared to the analysis of angular performance in both the pitch and yaw direction, this approach greatly simplified the analysis and increased the accuracy.
- Each shuttlecock was tested for 8 launches (runs) to give 8 sets of videos per shuttlecock.

- The videos were then analysed using Tracker™ for the pitch angular position with respect to time at a sampling interval of 0.005 s.
- Flight path angles were then subtracted from the angular positions to obtain the angle of attacks for each run. This was required to prevent additional error from slight variation in flight path angle from run to run. Flight path angle was assumed to be constant within each run.
- $\omega_n$  and  $\zeta$  were identified from data of each of the eight runs of each shuttlecock using the Matlab System Identification with a P2U (two poles, under-damped) structure.
- The runs with the six median  $\omega_n$  were then selected from the eight runs. Subsequently, four median runs were then selected from the remaining six, based on the value of  $\zeta$ .
- Average of the four median  $\omega_n$  and  $\zeta$  were used for analysis. The usage of the median runs reduced the possible error from unavoidable variation in launch conditions.

The above experimental methodology can also be applied for testing the shuttlecock with a different initial launch condition. However, the launch condition (especially speed and type of shot) must be consistent for fair comparison between the shuttlecocks. In this study, the launch condition was kept at the specified condition for every specimen.

Six shuttlecocks were tested. These consisted of feather and synthetic shuttlecocks and they are listed in Table 23.

Table 23 Shuttlecocks used in the turnover test.

	Type
Li-Ning Grandprix	Practise Feather
Li-Ning A+600	BWF Approved
Kason	Practise Feather
Mizuno NS-5	Synthetic
Max 550	Synthetic
Yonex Mavis 350	Synthetic

### 6.3.1.2 Response Modelling

The experimental results of the Li-Ning Grandprix, the Yonex Mavis 350 and the Mizuno NS-5 shuttlecocks were used for response modelling. The  $\omega_n$  and  $\zeta$  identified from the experimental data were used as input for building an underdamped 2<sup>nd</sup> order transfer function for each of the shuttlecocks. Using the “impulse” function in Matlab, the impulse responses were simulated. The proportional gain of each transfer function was then adjusted such that the simulated response and the experimental response had the same amplitude in the peak of the first oscillation. This step was necessary due to the difference in treatment of impulse input in identification and simulation. However, the proportionate constant is only a scale factor to the amplitude and does not affect the comparison of the resultant responses between shuttlecocks.

The modelling approach was validated through comparison with experimental data. The angular responses of one of the runs for the Li-Ning A+600 and for the Mavis 350 were first simulated. This was accomplished by building response transfer function using the  $\omega_n$  and the  $\zeta$  that were identified for those individual runs. The

$\omega_n$  and the  $\zeta$  from an individual experimental run were chosen over the four runs averaged values because there was no real experimental angular data available for the averaged parameters. This also means that it was impossible to validate simulated average response because the run average was not a real physical experimental run. The simulated angular responses were then plotted and compared with the experimental data from that run. Upon verification of the response modelling approach, the averaged responses of each of the three shuttlecocks were then simulated and compared.

## **6.3.2 Flight Trajectory**

### ***6.3.2.1 Shuttlecocks***

Table 24 lists the 14 types of shuttlecocks that were tested. They consisted of nine types of feather shuttlecocks and five types of synthetic shuttlecocks. The mixture of shuttlecock grades enabled the investigation of the effect of feather quality on shuttlecock flight. Moreover, the tournament shuttlecocks set the reference trajectory that can be benchmarked against the lower quality feather shuttlecocks and the other synthetics. The “Tournament-grade” shuttlecocks refer to shuttlecocks that were approved for official tournament usage by the BWF. To suit the lab condition, the shuttlecocks that were tested were all within speed rating 76 to 78. As different manufacturers have different representations of grain speed, the values given in parentheses are the original manufacturer ratings. Similar to the testing of turnover, only one sample was tested for each type of shuttlecock.

Table 24 Types of shuttlecocks tested for referential and benchmarking.

Feather	Equivalent Grain speed	Type
Li-Ning A62 XD	77	Practice
Li-NingGrandprix gold	78	Medium
Li-NingGrandprix gold	76	Medium
Ashaway Practise	77	Practice
Babolat Tournament	77	Tournament
Wilson Club	77	Practise
YonexAerosensa 40	76-77 (2)	Tournament
YonexAerosensa 40	77-78 (3)	Tournament
YonexAerosensa 2	77-78 (3)	Medium
<b>Synthetic</b>		
Yonex Mavis 350	77 (Blue)	Synthetic Nylon
Yonex Mavis 2000	77 (Blue)	Synthetic Nylon
Li-Ning X800	75-76 (Green)	Synthetic Nylon
Li-Ning X800	77-78 (Blue)	Synthetic Nylon
Mizuno NS-5	78 (4)	Artificial feather

### ***6.3.2.2 Experimental Setup***

The experimental setup that was described in 6.1.4.1 was applied to the work in this section. The positions of camera 2 and camera 3 were shifted for better framing of the trajectories. The updated camera positions are shown in Table 25. Figure 80 shows the experimental rig for flight evaluation. A 3-D figure is also shown in Figure 81 for easier visualisation of the setup.

Table 25 Camera position in the shuttlecock evaluation setup.

	Camera 0	Camera 1	Camera 2	Camera 3
Distance from launcher /m	1.5	2.14	5.84	8.37
Height of camera /m	1.1	1.85	2.82	1.97
Camera type	Photron EX1024	Phantom Miro 120s	Phantom Miro 120s	Phantom Miro 120s
Lens focal length /mm	35	24	24	28
Shutter speed /s	1/10000	1/5000	1/5000	1/2000
Frame rate	1000 fps	500 fps	500 fps	500 fps



Figure 80 Experimental setup for trajectory capture of the shuttlecocks.

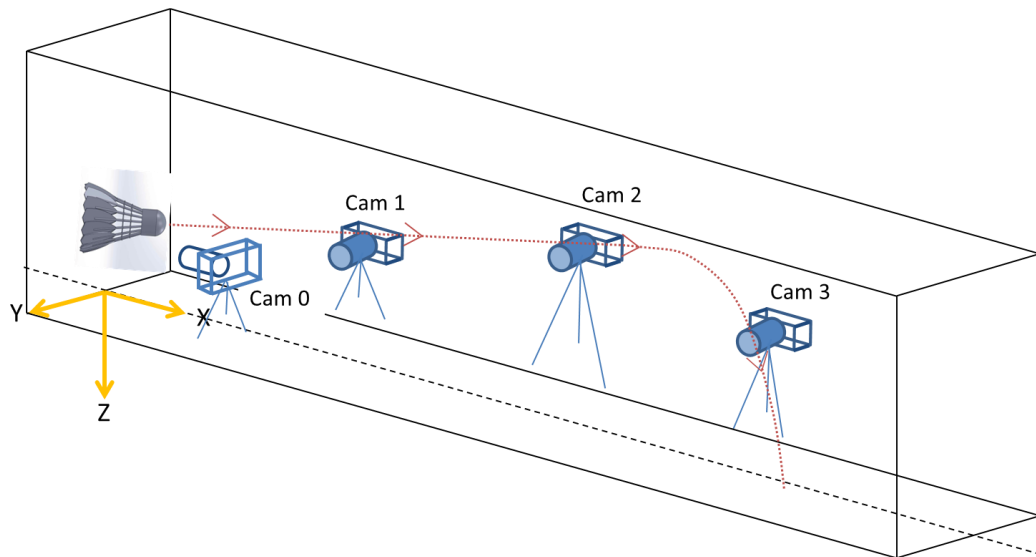


Figure 81 Experimental setup for trajectory capture showing the placement of the cameras and the trajectory.

### 6.3.2.3 Methodology

The test methodology that was applied for testing of the shuttlecocks is as follows:

- Launching of shuttlecock

The shuttlecock was launched with the same launcher settings that were used in the initial trial described in 6.1.4.1. The target launch speed and launch angle were determined in section 6.1.4.3 as  $24 \pm 0.5 \text{ m/s}$  and  $65.5 \pm 0.5 \text{ deg}$  respectively. The shuttlecock drop point on the launcher and the time delay had to be adjusted for the various shuttlecocks to attain the desired launch condition. This was especially so for the synthetic shuttlecocks which required the drop point to be pushed back for the same launch angle. No change in launcher racket speed was required for this experiment.

- Capturing

The high speed cameras were triggered upon the launch of the shuttlecock. Using a rate of 500 fps, each of the cameras had recording duration of more than 3 s. The actual flight duration of each shuttlecock was less than 1.5 s. The flight range of the shuttlecock was also recorded by using the measurements scales (grid lines) that were set up on the floor. There was 0.1 m spacing between the lines.

- Checking of launch condition

Upon the completion of flight recording, the data from camera 1 was processed using Tracker, which is a motion analysis tool. The initial flight speed and flight angle of the shuttlecock were reviewed. If the initial flight conditions met the launch criteria that were specified, the launch was accepted. Otherwise, the experiment was repeated for the shuttlecock. Repeated launch

was possible because the developed launcher did not degrade the shuttlecock with each launch.

- Data processing

Using tracker, the following parameters were obtained from the high speed videos:

- Initial flight velocity and angle
- Flight trajectory
- Flight velocity
- Axial spin rate
- Stall velocity

#### ***6.3.2.4 Experimental Error from High-Speed Capturing***

Motion analysis of the experimental work was conducted with the Phantom Miro 120 s high-speed cameras. The lenses used were wide angle Nikon AF-D 28 mm and Nikon AF-D 24 mm. Similar to most lens system, the equipment used were also affected by geometric errors from optical distortion. However, distortion of such prime lenses (fixed focal length) has mostly been corrected through lens design. Therefore, the radial distortion of the lenses is likely to be minimal and investigation work is purely for completeness. Using a grid chart, it was observed that the maximum error was at the near corner of the image, where the radial distance was 1.15 times of the span of view. The error was approximately 1.5% for both the 28 mm and 24 mm lenses.

Using the lens radial distortion model that is commonly used and were mentioned in [116-118], parameters were obtained to compensate for the distortion. Correction of

the 28mm lens reduced the geometric error to 1%. Due to the nature of the uneven distortion across the frame of the 24 mm lens, a piecewise correction equation was required. At a distance of (radius/half span)  $< 0.76$ , no correction was required. Further away towards the corner of the image, correction reduced the error between physical and image position to 1%.

To understand the impact of geometrical error in actual measurement with shuttlecocks, an experiment was set up using the same method. The positions of the shuttlecocks were recorded with two high-speed cameras which were placed side by side at 1 m apart. Each camera had a span of view of 2.45 m. The largest error recorded was 0.023 m and 0.016 m before and after compensating for lens distortion respectively. Even without the distortion correction, it was seen that the error was small ( $\sim 1\%$ ) and may be negligible. Unlike the lab evaluation with a grid, the applied testing with the shuttlecocks also took into account of user error when scaling the image position to the actual physical position. Detailed documentation of investigation work on experimental error is presented in Appendix E.

## 6.4 Result and Discussion

### 6.4.1 Turnover

#### 6.4.1.1 Parameter Identified from Experimental Data

The mean  $\omega_n$  and  $\zeta$  that were identified are listed in Table 26. Physically, a larger  $\omega_n$  means longer period of oscillation, while a larger  $\zeta$  signifies smaller magnitude of oscillation. The mean overshoot refers to the mean amplitude of the first overshoot in oscillation, while the time to complete turnover refers to the time before the completion of the first (and significantly large) oscillation. These were provided for easier relation to the identified parameters.

Table 26 Identified parameters for the turnover process of the shuttlecocks.

	Natural Frequency, $\omega_n$		Damping Factor, $\zeta$		Mean overshoot /degree	Approximate time to complete turnover /s
	Mean	Std. Dev.	Mean	Std. Dev.		
Li-Ning Grandprix	0.0100	0.00047	0.460	0.0187	45	0.05
Li-Ning A+600	0.0102	0.00109	0.390	0.0111	67	0.05
Kason	0.0109	0.00192	0.388	0.0514	61	0.06
Mizuno NS-5	0.0129	0.00156	0.368	0.0649	95	0.06
Max 550	0.0119	0.00053	0.264	0.0056	106	0.055-0.06
Yonex Mavis 350	0.0114	0.00033	0.282	0.0119	114	0.05

The result showed that the feather shuttles had significantly larger  $\zeta$  and marginally smaller  $\omega_n$ . This means that the feather shuttlecocks completed turnover within a shorter time with less overshoot. The mean overshoot and the time to complete turnover agreed with the observation. The mean overshoots observed on the

synthetic shuttles were between  $95^\circ$  to  $114^\circ$ . In contrast, the mean overshoots of the feather shuttlecocks only ranged from  $45^\circ$  to  $67^\circ$ . Interestingly, the time to complete turnover were actually similar among all the shuttles. This trend agrees with the identified  $\omega_n$ . It also agrees with the result that was published in [22], in which the time to complete turnover for various shuttlecocks, including synthetics and feathers, was 0.03 s. The difference in time duration between [22] and the current work is likely due to differing launch conditions. This reinforces the importance of launch consistency for comparable result and it was also mentioned in [94].

Figure 82 and Figure 83 are the chronophotographs of one of the runs of the Li-Ning A600 and the Yonex Mavis 350. In these chronophotographs, it can be seen that the observed straight line flight path supports the assumption of constant flight path angle. However, this is only valid for high speed flight where the large amount of deceleration from drag (11 times of gravity at just 20 m/s) decreases the significance of the gravitational acceleration. For slower flight, such as a net shot, the curved flight path will increase the difficulty in data analysis.

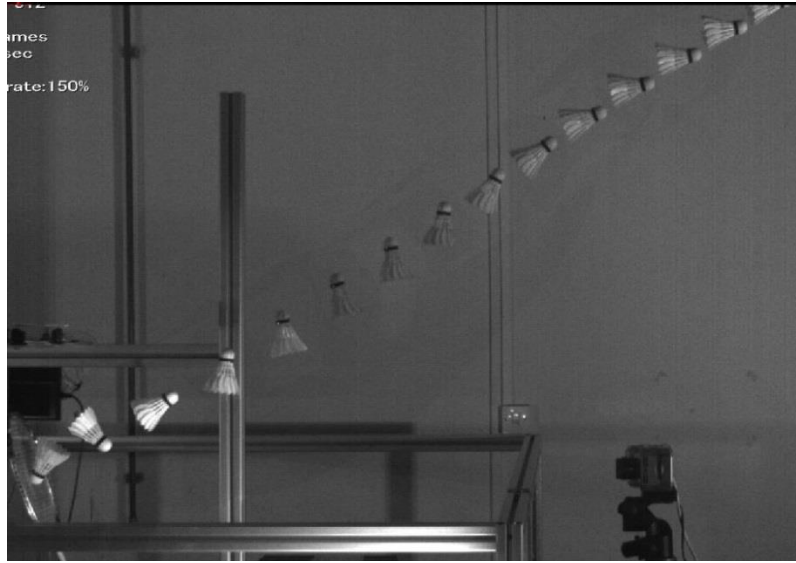


Figure 82 Turnover behaviour observed from one of the runs of the Li-Ning A600 shuttlecock.



Figure 83 Turnover behaviour observed from one of the runs of the Yonex Mavis 350 shuttlecock.

Figure 82 and Figure 83 also demonstrated the difference in angular behaviour that was suggested by the identified  $\omega_n$  and  $\zeta$ . The Mavis 350 showed more overshoot than the A600 but returned to neutral at approximately the same time. It was also observed that the larger overshoot observed on the Mavis 350 resulted in increased amplitude in the subsequent oscillations (time > 0.05 s) when compared to the A600

feather shuttlecock. This was also observed for the other synthetics. This means that the second and subsequent oscillations on the synthetic shuttles will be much more significant to the observer. From the angle of attack plot that is shown in Figure 84, it was seen that this behaviour caused the synthetic shuttles to fly with larger angle of attack in the unsteady flight state.

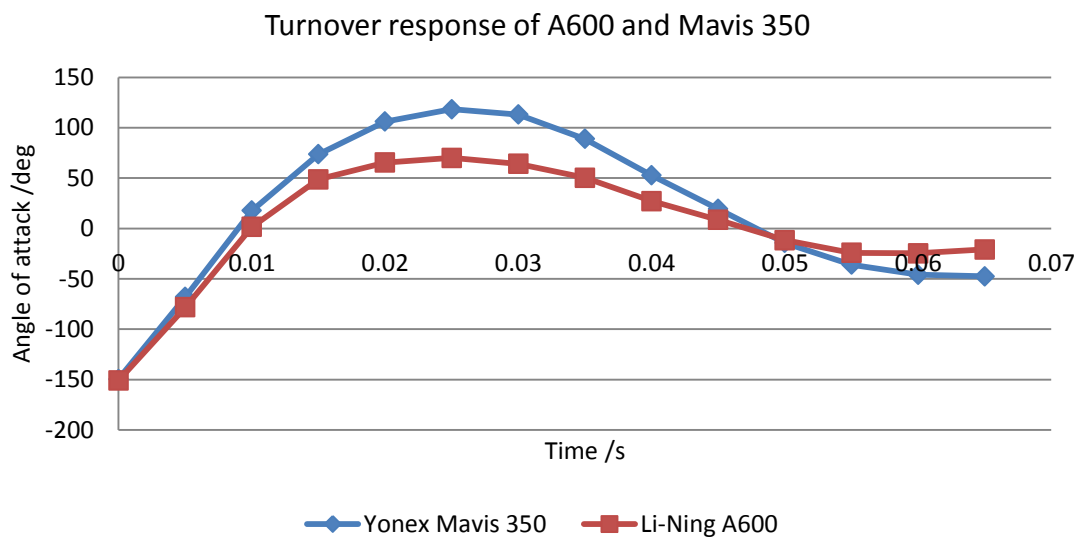


Figure 84 Angular response of runs presented in Figure 82 and Figure 83.

The limited field of view of the camera meant that the subsequent behaviour beyond  $t > 0.065$  s was not captured. However the presented data showed that it is unlikely for the synthetic shuttle to have lower amplitude than the feather shuttles in the subsequent minor oscillations.

While the sample size was limited, the collected data was sufficient to explain the two contrasting observations that were commonly made. Using the time duration of oscillation as the judging criterion—as applied in the literatures—the results obtained in this work would have suggested that the turnover performance of both the feather and the synthetic shuttlecocks were similar. This is also the conclusion

that was reported in the literatures. However, player perception test of the turnover behaviour reports the turnover stability of the synthetic shuttles to be inferior to that of the feather ones. These two contrasting conclusion probably arose because the players use visual cue—which is the oscillation amplitude—to determine the relative angular stability between shuttlecocks. Therefore, the synthetic shuttlecocks which had more overshoot and oscillation amplitude than the feather shuttles would appear to be less stable in the turnover.

#### 6.4.1.2 Response Modelling

The turnover response prediction model was first validated using the experimental result presented in Figure 84. The experimental data and simulated responses are compared in Figure 85 and Figure 86. Good agreement was obtained providing support to the treatment of the turnover using a second order approximation. It also supported the validity of the identified parameters.

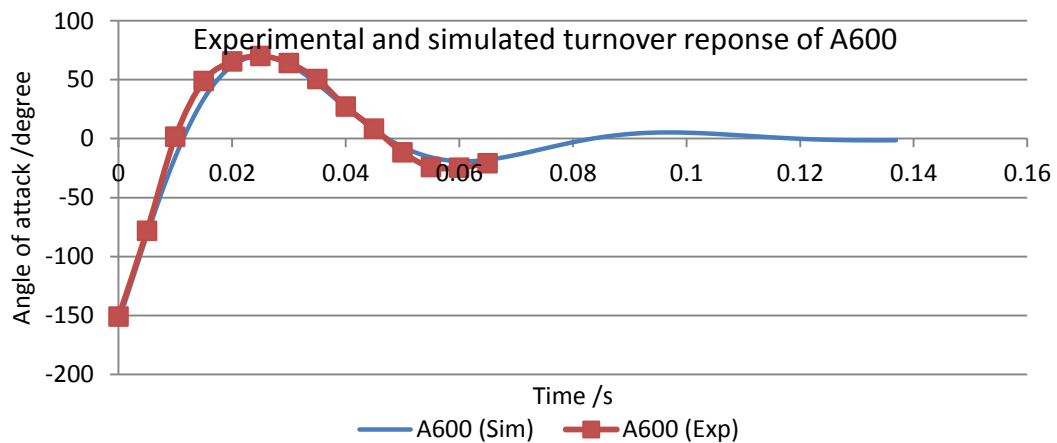


Figure 85 Experimental and simulated turnover responses of the A600.

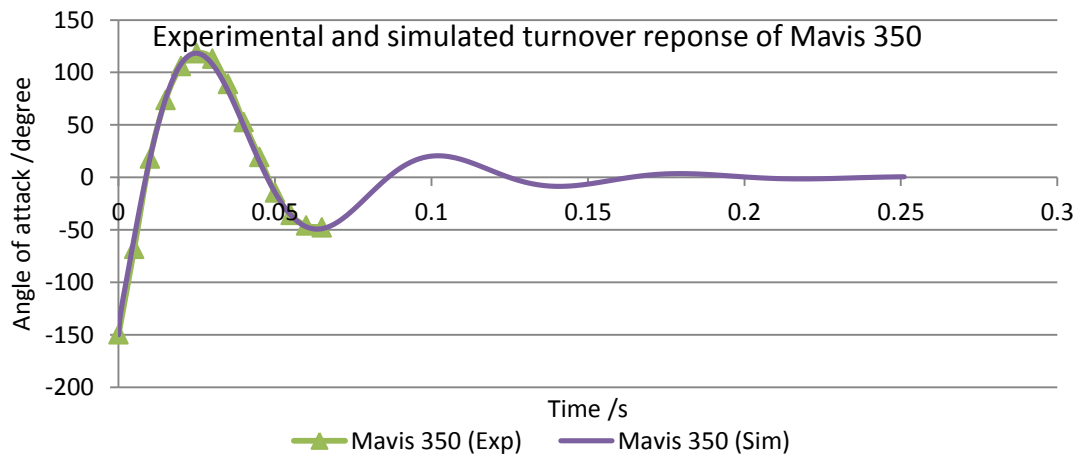


Figure 86 Experimental and simulated turnover responses of Mavis 350.

Using the mean  $\omega_n$  and  $\zeta$  of the tested Mavis 350, Grandprix, and NS-5, the simulated responses were plotted and are shown in Figure 87. The Mavis 350 was chosen because it represented an average synthetic shuttle. The Grandprix was the best performing shuttle for the turnover process, while the NS5 was plotted because of the large  $\omega_n$  observed. The result showed that beyond the first oscillation, the good feather shuttlecock would have almost damped out all the oscillation. On the other hand, the synthetics took much longer to fully damp out the oscillations. The result from the NS5 was very interesting because the combination of a large  $\omega_n$  and a large  $\zeta$  enabled it to smooth out the subsequent oscillations better than the other synthetic shuttlecocks. This was despite having a larger oscillation period than the synthetic Mavis 350. Therefore, it is possible that an undesirably large  $\omega_n$  when coupled with a large  $\zeta$  may produce a better performing shuttlecock than a regular synthetic which has superior (lower)  $\omega_n$ .

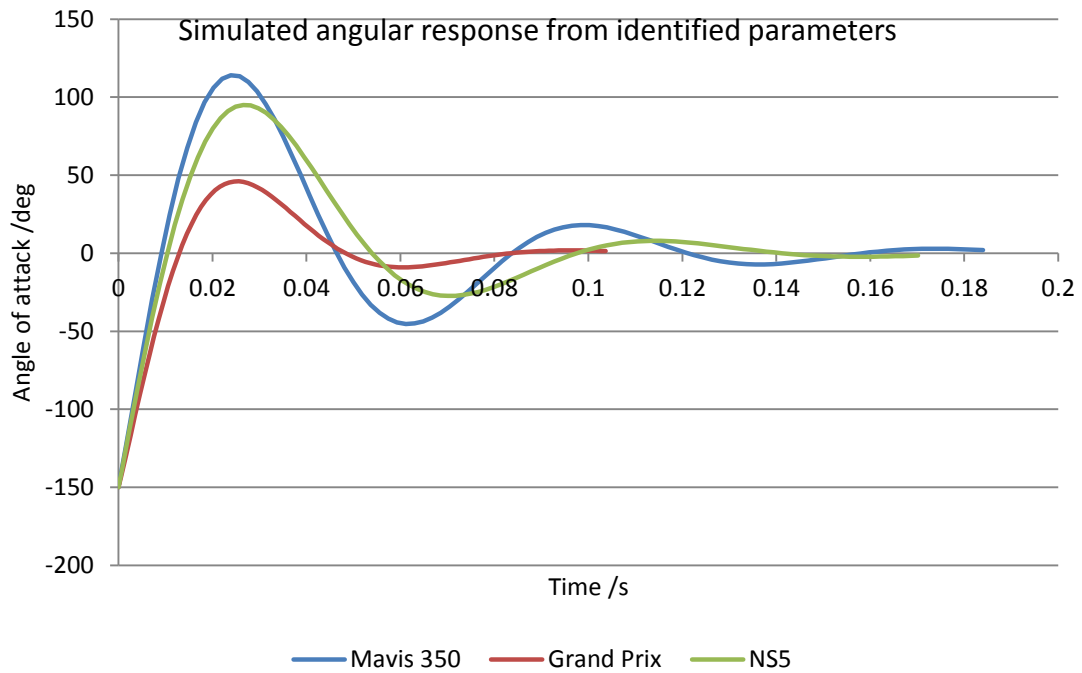


Figure 87 Simulated responses using the averaged parameters from Table 26.

#### 6.4.1.3 Realistic Damping Parameters

Theoretically, the highest possible damping value and lowest possible natural frequency are desired for the best shuttlecock performance. Practically, the underdamped angular response has become a trait of the badminton game where the instability in turnover is used to the attacker's advantage in slicing shots at net play. As observed from the tested shuttlecocks, an  $\omega_n$  of approximately 0.01 and a  $\zeta$  of approximately 0.4 will give a turnover behaviour that is similar to a feather shuttlecock. The desired performance of a good shuttlecock, when under the perturbation condition tested, is represented by the plot for the Grandprix shown in Figure 87. The fundamental parameter impeding turnover performance is not  $\omega_n$ , but  $\zeta$ . Based on the derivation in 4.3.1.3, the lack of damping results in a low  $c$ . The damping can be increased by:

- Increasing the  $I_{yy}$ .

- Increasing the skirt cone width.
- Lengthening the skirt length.
- Moving the C.G. forward.
- Reducing the skirt porosity at region away from the base.

The result also showed that angular performance was more desirable when  $\zeta$  was large, even if the resultant  $\omega_n$  was less than optimal.

## **6.4.2 Flight Trajectory**

### ***6.4.2.1 Shuttlecock Launch Velocity and Range***

The initial launch conditions were processed from the high speed video from camera 1. Due to the high deceleration nature of badminton shuttlecocks, large velocity change was observed early on in flight. Therefore, comparison required all initial velocities to be sampled from the same point in space.

Recognising that error is unavoidable in the digitising process, the values were obtained from multiple point samples before and after the moment of interest. Jittery in the motion was then filtered using the bounce detection algorithm in Tracker. As this function compensated for error by smoothing the spikes, it was suitable for the continuous smooth motion of a shuttlecock. The velocities in Table 27 were then sampled from the processed velocities at 0.002 s after the shuttlecock had passed the most forward point of the launcher frame.

Table 27 Initial launch velocities and velocity ratios of the accepted runs.

Feather	Launch velocity /m/s	$\dot{x}/\dot{z}$	Range /m
Li-Ning A62 XD	24.08	2.28	9.85
Li-Ning Grandprix gold	24.10	2.20	10.50
Li-Ning Grandprix gold	23.88	2.26	9.80
Ashaway Practise	23.63	2.21	9.85
Babolat Tournament	23.78	2.25	9.80
Wilson Club	24.26	2.16	10.00
Yonex Aerosensa 40	23.60	2.27	9.80
Yonex Aerosensa 40	24.39	2.27	10.30
Yonex Aerosensa 2	23.84	2.27	10.00
Average	23.95	2.24	9.99
Synthetic	Launch velocity /m/s	$\dot{x}/\dot{z}$	Range /m
Yonex Mavis 350	24.59	2.18	9.40
Yonex Mavis 2000	23.74	2.16	9.50
Li-Ning X800	23.80	2.21	9.30
Li-Ning X800	23.92	2.20	9.50
Mizuno NS-5	22.88	2.27	10.15
Average	23.79	2.20	9.57

With the exception of the Mizuno NS-5 which had a slower launch velocity, all the shuttlecocks had comparable launch velocities. The  $\dot{x}/\dot{z}$  ratios were also in the range of defined values. Therefore, it is unlikely that any flight differences observed were due to biased launch condition. The average launch velocity of the feather shuttlecocks was 23.95 m/s. This was less than 0.2 m/s more than the average of the synthetic shuttlecocks. The average  $\dot{x}/\dot{z}$  ratio of the feather shuttlecocks and the

synthetic ones were 2.24 and 2.20 respectively. The difference in launch velocity ratios resulted in an average launch angle difference of only 0.35 degree between the feather and synthetic shuttlecocks. Based on the simulated results that were presented in Table 22, this is unlikely to cause bias in the results.

The Mizuno NS-5, an artificial feather shuttlecock, had a significantly lower launch velocity than the rest of the shuttlecocks. However, the launch angle, which is a function of the  $\dot{x}/\dot{z}$  ratio, was similar to the other feather shuttlecocks. The resultant effect from this will be evaluated in the trajectory plots. The flight ranges of the shuttlecocks will be discussed together with the trajectories.

#### ***6.4.2.2 Feather Shuttlecock Trajectories***

The trajectories obtained for the feather shuttlecocks were plotted and are shown in Figure 88. Unexpectedly, the data points fell into two distinct groups of trajectories. The launch point of the shuttlecocks was at the 0 m ground distance point and 1.2 m above the ground. This corresponds to a coordinate point of (0,1.2) on the plot in Figure 88. Since this initial part of the flight was not captured by camera 1, the experimental data from camera 1 started from approximately 1 m after the launch point.

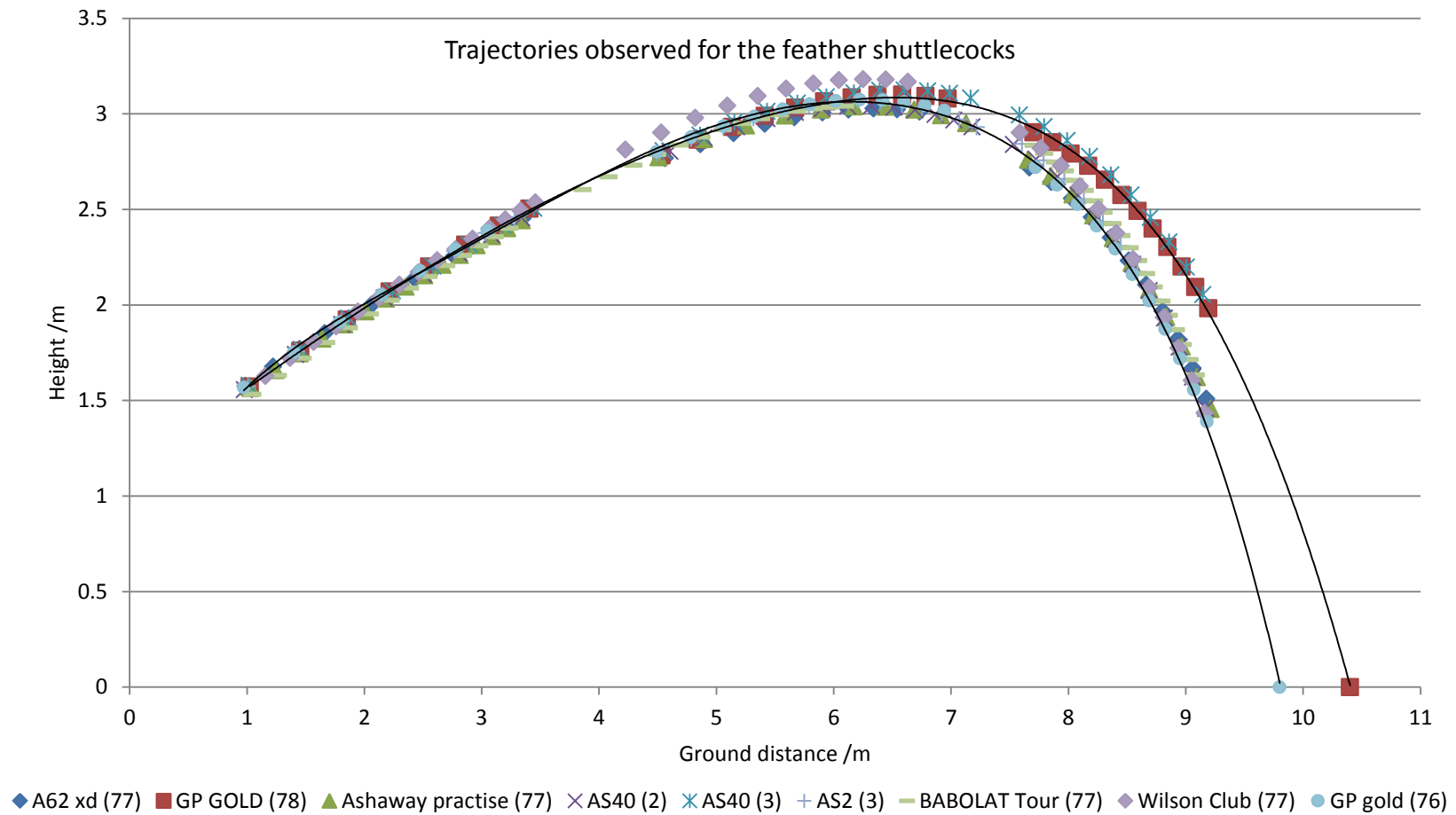


Figure 88 Experimental trajectories observed for the various shuttlecocks.

With exception to the Wilson Club, it was observed that the trajectory data could be represented by two distinct trend lines. The first trend line was that formed by the trajectories of the group of slower grain speed shuttlecocks. The average range of these shuttlecocks was 9.87 m. Vertex height ranged from 3.04 m to 3.07 m. Largest variation between the trajectories of this group of shuttlecocks occurred at approximately 7.7 m after the launch point, where the Babolat Tour had a height of 2.83 m while the A62 xd was only at 2.72 m. This may be due to difference in ground distance at the onset of stall (trajectory vertex), such that the shuttlecock which stalled before the others would have started losing height earlier. On the other hand, the other shuttlecocks which have not stalled would have continued in gaining vertex height. Consequently, the height difference would be the largest at a location after the trajectory vertex. In this situation, it was 7.7 m. It is possible that such a minor difference with a moving shuttlecock cannot be observed by a player. Although observer responsiveness is an area of sports science research, such as in [119], it will not be covered here.

The faster grain speed shuttlecocks, which were the GP Gold (78) and AS40 (3), had much further range of 10.50 m and 10.30 m respectively. Their trajectories formed the second trajectories trend line. As expected, the faster grain speed shuttlecocks flew further and higher. This effect is the same as comparing the path of two objects with different weight, but experiencing the same resistive force. Interestingly, difference in trajectory between the slower and faster shuttlecocks was only obvious beyond the vertex of the trajectory. Samples of speed 78 shuttlecocks were limited because the fundamental purpose of this work was to identify flight behaviour of similar speed rated

shuttlecocks. Nonetheless, the result suggested good differences and it is proposed that more work be done in subsequent grain speed analysis. To aid visualisation, a trend line was plotted for the GP Gold (76), and another trend line was plotted for the GP Gold (78) shuttlecock. These trend lines are also shown in Figure 88. The two shuttlecocks were of the same brand and the same model, but of different grain speed. Therefore, it is unlikely that flight path difference between them was caused by difference in shuttlecock quality.

The observed trajectory of the Wilson Club shuttlecock deviated significantly from the other shuttlecocks. Despite being a speed 77 rated shuttlecock, it had a higher vertex height than all the other shuttlecocks. Flight range was similar to the rest of the shuttlecocks in the group. This may have been attributed by the slight decrease in  $\dot{x}/\dot{z}$  ratio (larger elevation in launch angle) or the higher observed spin rate. The flight observed axial spin will be discussed in the later section of this chapter.

Insignificant difference was observed between the various types of feather shuttlecocks. More deviation between shuttlecocks was expected because the shuttlecocks consisted of various grades that ranged from economical practice grade to BWF approved tournament shuttles. A possible explanation is that the difference between the various grades of shuttlecocks lies in their durability. Fundamentally, the shape and size (physical dimensions) of these shuttlecocks were very similar. Therefore, their “out of box” flight performance is likely to be similar. Since the shuttlecocks were tested in their brand new condition, there may not be much difference in performance. It is possible that difference may be evident upon usage and wear, with the tournament-grade

shuttlecocks exhibiting less performance degradation. At the time of writing, durability of shuttlecock has never been studied in any scientific literature.

#### ***6.4.2.3 Synthetic Shuttlecock Trajectories***

The trajectories obtained for the synthetic nylon skirt shuttles were plotted against that of the Yonex AS40 (BWF approved) and are shown in Figure 89. Similar to the feather shuttlecocks in Figure 88, the flight trajectories of the synthetic nylon shuttlecocks (Yonex Mavis 350, Yonex Mavis 2000, Li-Ning X800) could also be described by one distinct trend line.

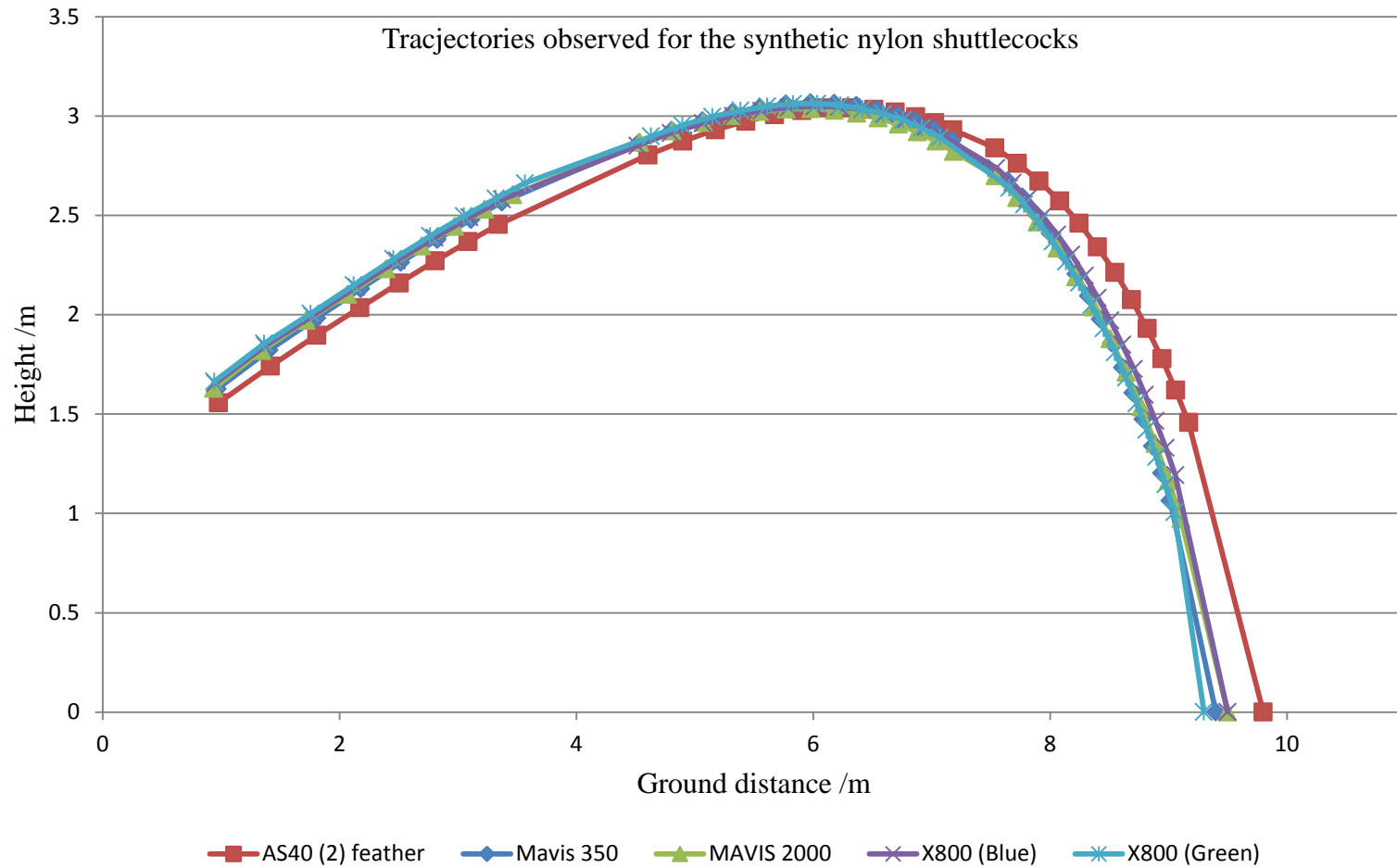


Figure 89 Trajectories observed for the synthetic nylon shuttlecocks as compared to the reference feather shuttlecock (AS40 (2)).

In comparison with the reference feather shuttlecock, it was seen that the synthetics had higher initial height along the data points from the first camera. This difference along the same point on the ground distance was approximately 0.13 m. An example of the height difference observed at camera 1 was plotted for the Yonex AS40 (feather) and the X800 (synthetic) and it is shown in Figure 90. It may be caused by launch point adjustment on the shuttlecock launcher for the synthetics, as was documented in 6.4.2.1. It may also be due to the increased angle of attack during the turnover process that induced lift. This significant portion of turnover response would have occurred in the initial flight segment where ground distance was less than 1m away from the launch point. The segment was not captured in this part of the experiment.

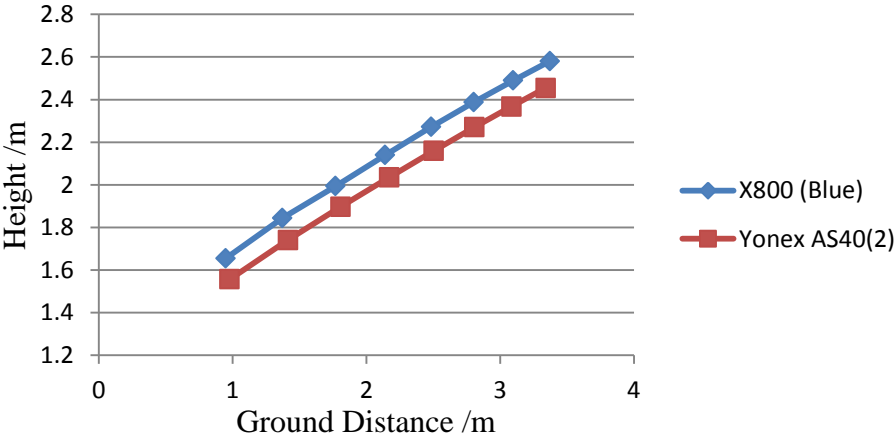


Figure 90 Difference in trajectory height observed at camera 1.

Despite similar initial launch conditions, the discussed synthetic nylon shuttlecocks also had shorter flight range than the feather shuttlecocks of the same grain speed. The average flight range of the tested nylon shuttlecocks was 9.43 m and it was 0.44 m less than the feather shuttlecocks. This agrees well with the flight performance predicted from the wind tunnel test (Figure 70), where the tested synthetics (X800

blue, X800 (green) and Mavis 350) had higher  $\frac{c_d S}{m}$  than the feather shuttlecocks that were tested. Physically, a higher  $\frac{c_d S}{m}$  means a higher drag resistance per unit mass of the shuttlecock. Therefore, the flight performance was not unexpected. The minor difference in flight trajectory between the X800 (Green) and the X800 (Blue) was also predicted by the  $\frac{c_d S}{m}$  measured. This suggests that speed ratings given by the shuttlecock manufacturers may not always be representative of actual performance. This phenomenon which goes against conventional thinking of the synthetic being too fast was also proposed in [120].

Trajectory vertex heights were similar for the synthetic and feather shuttlecocks. However, the vertex of the synthetic shuttlecocks occurred earlier than the feather shuttlecocks. Comparing their trajectories, it was observed that near the vertex of the trajectories, there was a force holding the feather shuttlecock upward, delaying the onset of stall. This phenomenon will be discussed through the velocity and spin rate plot.

The trajectory of the artificial feather shuttlecock (Mizuno NS-5) was plotted against the reference AS40 shuttlecocks in Figure 91. Due to availability issue, only the speed 78 version of the NS-5 was tested. The trajectory observed for the NS-5 was similar to the AS40 (3) which also had a high grain speed of 78. Slight reduction in range observed on the NS-5 may be due to the slower launch velocity.

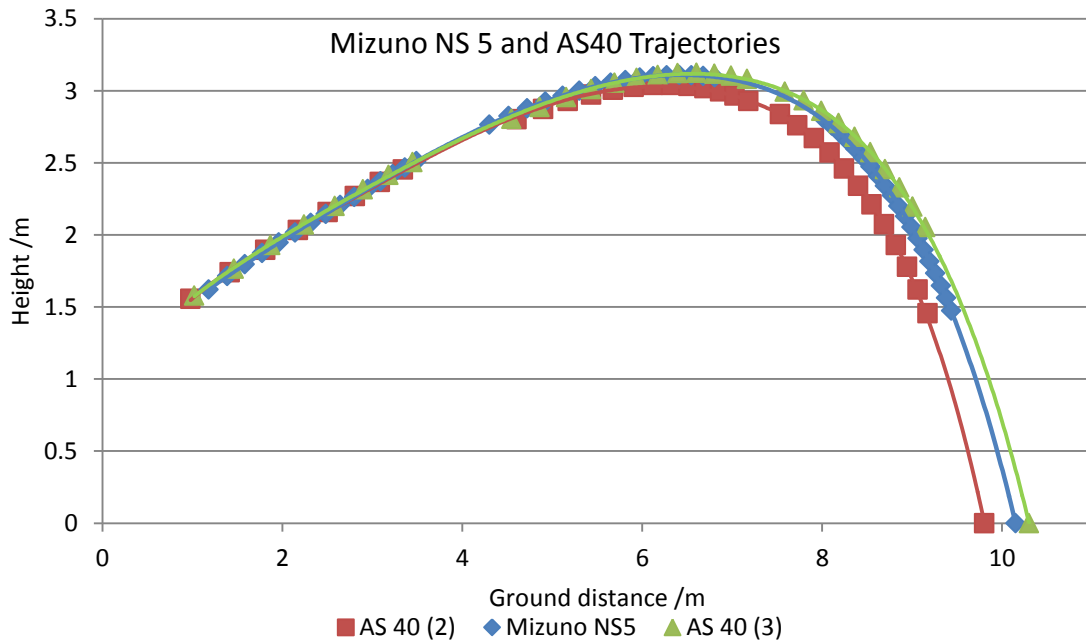


Figure 91 Trajectory plot for the NS-5 artificial feather shuttle against the AS40 tournament-grade feather shuttlecocks.

It was observed that the NS-5 did not exhibit the higher initial height that was observed for the other synthetic shuttles. This may support the proposition that the increase in the initial height was contributed by the launch mechanism. This is because the NS-5 did not require the same launch drop point adjustment that was needed for the other synthetics. Moreover, the turnover performance of the NS-5 was almost as lacking as the other synthetics. Therefore, if the initial height lift was turnover related, it should have been observed on the NS-5 too.

#### 6.4.2.4 Velocity Profile

The velocity profiles of the individual feather and synthetic shuttlecocks are given in Appendix G. Due to the similarity between the obtained results, only the results from the Li-Ning X800(Green) and the Yonex AS40(2) are presented here for discussion. The velocity profiles of the two shuttlecocks were plotted and are shown in Figure 93. Due to the high drag-low weight characteristic, the shuttlecocks decelerated from

24 m/s to approximately 6 m/s within the first 0.5 s of flight. Beyond that, flight velocities of the shuttlecocks were observed to be between 4.9 m/s to 5.4 m/s. No significant difference was observed between the velocity profiles of the various feather and synthetic shuttlecocks. The above means that the tested shuttlecocks had similar drag and deceleration characteristic. This agrees with the wind tunnel drag measurements that were presented in Figure 70.

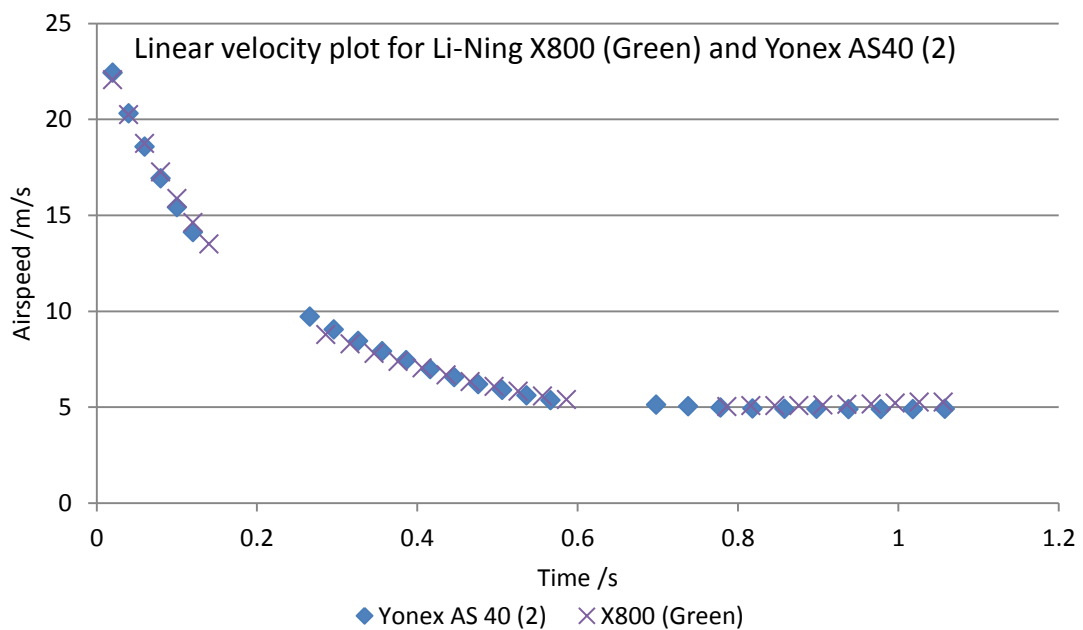


Figure 92 Comparison of velocity profile for the Li-Ning X800 (Green) and Yonex AS40 (2) shows negligible difference.

#### 6.4.2.5 Feather Shuttlecock Spin Rate

The axial spin rates of the individual shuttlecocks were plotted with respect to time in Appendix G. Similar to the velocity and trajectory plots, each cluster of data point symbolised the spin captured from one of the three main cameras. The spin rates were obtained by counting the rotation of the shuttlecock feather shafts which were pre-marked prior to testing. The usage of high speed cameras produced good temporal resolution in spin estimation. Possible errors from limit in temporal

resolution ranged from 6-7% at camera 1 to under 4% at camera 3. This can be further reduced with higher frame rates in capturing. It should be noted that the errors are just theoretical maximum error due to time step limitation. Error in practice is likely to be smaller because of the flexibility in choice of appropriate start and end sample points when manually processing.

The variation in spin rate is demonstrated in Figure 93, where spin data from three of the nine feather shuttlecocks were plotted. All the Li-Ning branded shuttlecocks had less spin and their spin performance can be demonstrated by the Li-Ning Grandprix Gold (76) in Figure 93. The BWF approved Babolat and Yonex shuttlecocks had much higher spin. For instance, the maximum spin rate observed for the Yonex AS40 (2) was 84 rad/s, while the maximum for the Grandprix Gold (76) was only 61 rad/s. Theoretically, faster spin may produce better flight stability from gyroscopic effect. However, there was no appreciable difference between the observed trajectories. The Wilson Club (77) had the highest spin rate. The spin rate of the Wilson Club shuttlecock was already more than 100 rad/s from the first reading outside of the launcher. With reference to the secondary gyroscopic effect discussed in section 4.3.3, the high spin rate may be the reason for the higher trajectory observed for the Wilson Club (77).

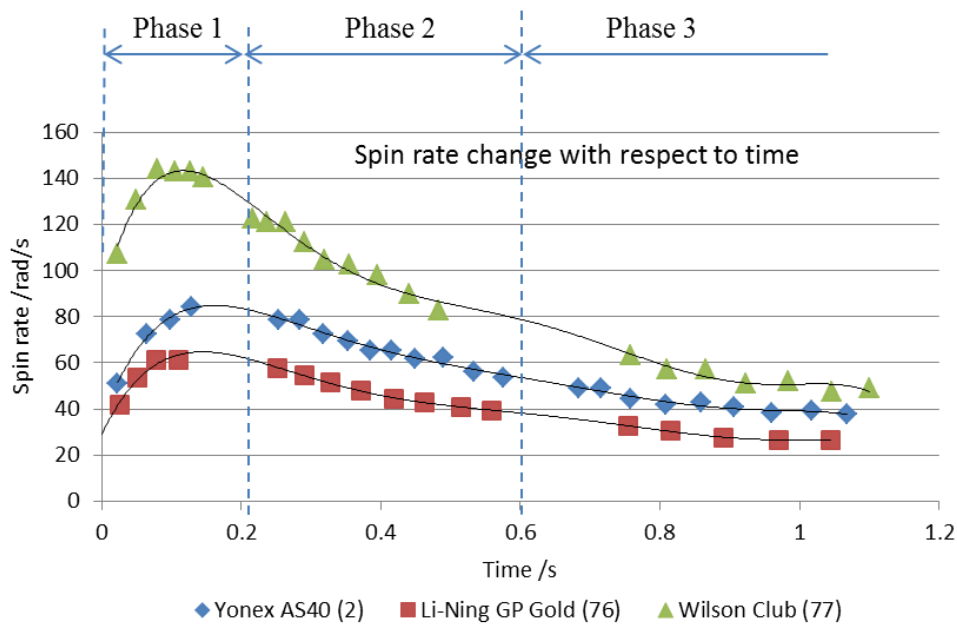


Figure 93 Spin rate profile for the Yonex AS40, Li-Ning Grandprix Gold, and Wilson Club feather shuttlecock.

Despite their difference in spin magnitude, the trends in spin rate change were similar. In general, the spin profiles can be described by:

- Phase 0 (Time ~ 0 s)  
 Coming out of the shuttlecock launcher, the shuttlecock started with a low spin rate.
- Phase 1 (0 s < Time < 0.2 s)  
 Within the frame of the first camera, the spin acceleration took place due to the spin rate being a lot slower than the steady-state spin of the corresponding linear velocity. The maximum spin rate in-flight was attained here.
- Phase 2 (0.2 s < Time < 0.6 s)  
 This segment was observed by camera 2. The large reduction in linear velocity meant that the axial spin is now higher than the corresponding

steady state spin. Therefore spin deceleration occurred in this phase. This is similar to a wind-milling state.

- Phase 3 (Time > 0.6 s)

Camera 3 showed that most of the spin deceleration for a feather shuttlecock occurred within the frame of the second camera. As this phase was beyond the vertex of the trajectory, there was little change in linear velocity. Therefore, change in spin rate was also limited. In the beginning of the frame of camera 3, the residual spin from the previous high-speed segment continued to bleed off before stabilising to a near steady spin rate. This steady spin rate was approximately just half the maximum attained spin rate and was lower than the initial spin rate at near Time ~ 0.

This observed trend, when evaluated against the velocity profile, supports the proposed spin behaviour of the shuttlecock, whereby the shuttlecock does not attain the steady state spin rate of the wind tunnel. This is because of delay in spin response and fast deceleration in linear velocity.

#### ***6.4.2.6 Synthetic Shuttlecock Spin Rate***

The axial spin rates of the synthetic shuttlecocks were also plotted with respect to time and they are also shown in Appendix G. The flight observed spin data for these synthetic nylon shuttlecocks were compiled in Figure 94. Similar to the feather shuttlecocks that were tested, significant variation in magnitude of spin was observed between the shuttlecocks.

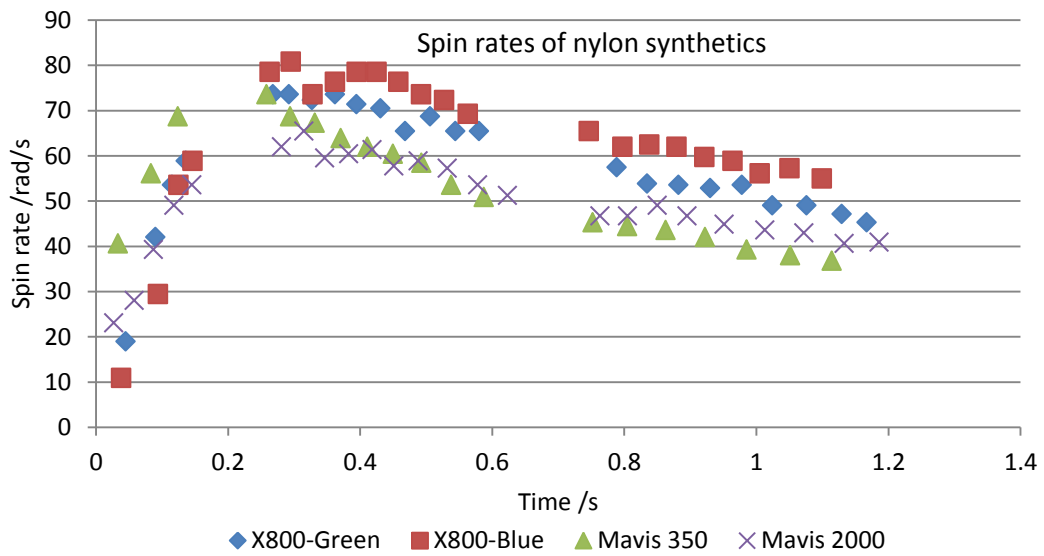


Figure 94 Compiled spin-time data for the synthetic shuttlecocks.

The axial spin profile of the Mavis 2000 and both the X800 were very similar. Taking the spin-time profile of the X800 (Green) as a median representation of the tested synthetics, Figure 95 shows the comparison to the AS40 (2) feather shuttlecock. Since the linear velocity profiles of these two shuttlecocks were found to be similar in Figure 92, it is unlikely for spin difference to be attributed by airspeed.

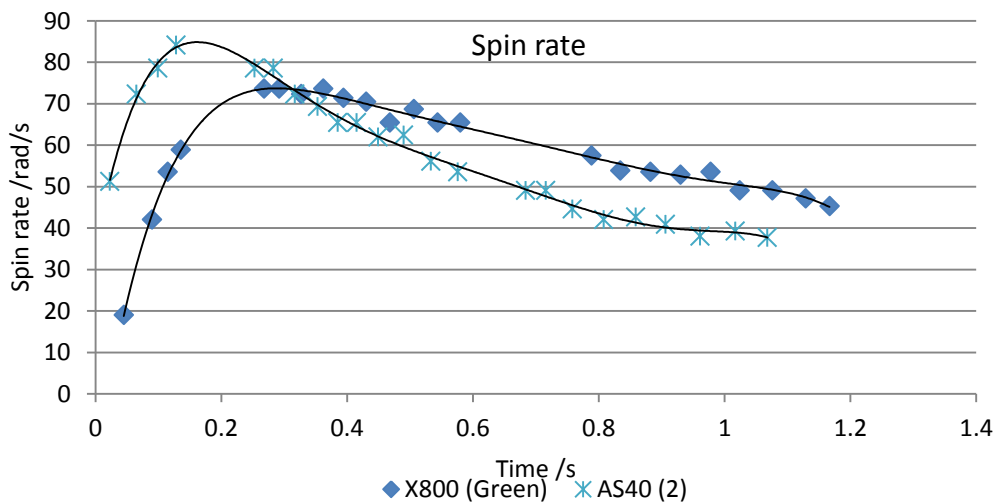


Figure 95 Comparing the X800 (Green) and AS40 (2) spin-time profile showed significant differences between the feather and synthetic shuttlecocks.

In comparison with the AS40 (2) feather shuttlecock, the spin profiles of the X800 (Green) and the other synthetic shuttles showed the following differences:

- Initial spin rate of the synthetic shuttlecock upon coming out of the launcher was much lower than the good feather shuttlecocks. Assuming that all the shuttlecocks started with no spin at impact with racket, then it is possible that spin torque,  $T$ , was much higher on the feather shuttlecocks.
- While peak spin rate for the feather shuttlecock occurred at time  $< 0.2$  s, the synthetic shuttlecocks took longer to attain their peak spin rate. This supports the proposition of insufficient  $T$  and  $Q$  for the synthetics.
- With a later occurring peak spin rate, spin deceleration of the synthetic shuttles were also delayed. It started much nearer to the vertex of the trajectory (time  $\sim 0.45$  s) than the feather shuttlecocks.
- Beyond the peak spin rate of the feather shuttlecock, aggressive spin deceleration was observed. This spin deceleration rate tapered down towards

the end of the flight. On the other hand, spin deceleration of the synthetic shuttlecocks was gentler. The trend line of the X800 (Green) has shown that the spin deceleration is linear with respect to time. This also suggests  $Q$  being smaller on the synthetic.

The above described observations remain valid even when comparing the spin rate of the X800 synthetic shuttlecock with a much slower spinning feather shuttlecock, the GP Gold (76). From the plot that is shown in Figure 96, it was observed that the much slower spinning GP Gold (76) also demonstrated the same difference from the X800 as the AS40. Compared to the X800, the GP Gold had higher initial spin, earlier occurring peak spin, earlier onset of the spin deceleration and a non-linear spin deceleration rate.

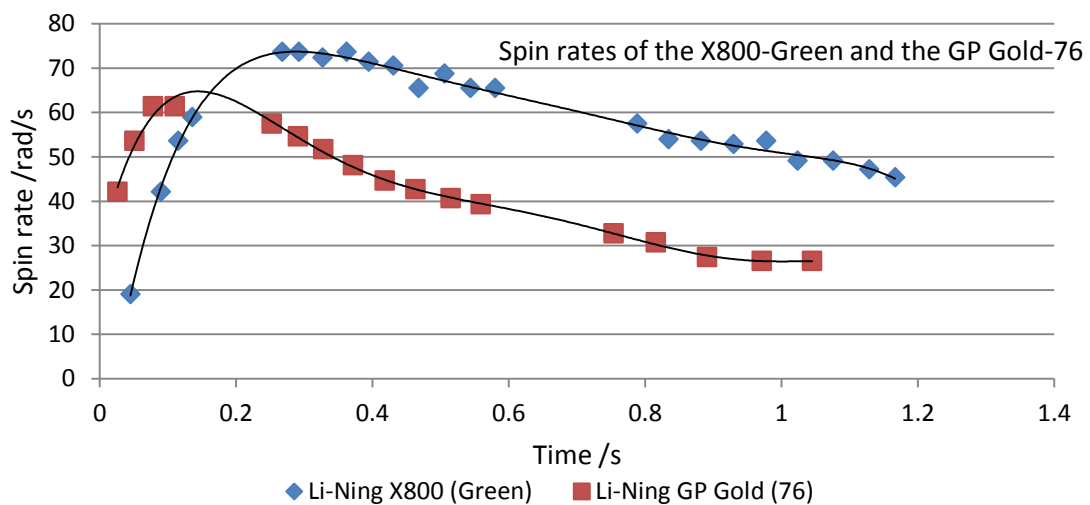


Figure 96 Spin rates of the GP Gold feather shuttlecock and the X800 synthetic shuttlecock.

The combination of a delayed onset of spin deceleration and a reduced rate of spin deceleration means that the synthetics were actually spinning faster at and beyond the trajectory vertex. This means that the spin-induced pitching and yawing are

unlikely to be any less significant on the synthetic shuttlecocks than on the feather ones. Therefore, contrary to suggestions from literatures, the “drop steepness” of the tested synthetics should not be inferior to that of the feather shuttlecocks.

#### ***6.4.2.7 Stall Velocities***

Stall velocity is defined as the velocity of the shuttlecock at maximum trajectory height (vertex). Decomposing the subsequent post stall trajectory behaviour into directional components, it can be deduced that the shuttlecock with the smaller  $\dot{x}$  will travel less in the x-direction and have a steeper drop at the end of the flight. As  $\dot{z} = 0$  at stall, the velocity at stall will be equal to  $\dot{x}$ . Therefore, a shuttlecock with a lower stall velocity will also have a lower  $\dot{x}$  that will result in a more vertical drop which is often associated with good shuttlecocks. Consequently, a lower stall velocity is preferred.

The above assumes that there is negligible difference in lift and spin-induced pitching moment between the tested shuttlecocks. This is likely to be a fair assumption because the post-stall flight conditions of the various shuttles were similar. Therefore, analysis of the post stall velocity may be useful for post-stall behaviour study. The stall velocities of the tested shuttlecocks are tabulated in Table 28.

Table 28 Stall velocities observed for all the tested shuttlecocks.

Feather	Stall Velocity /m/s
Li-Ning A62 XD	6.86
Li-Ning Grandprix gold	6.90
Li-Ning Grandprix gold	6.57
Ashaway Practise	6.64
Babolat Tournament	6.54
Wilson Club	6.61
Yonex Aerosensa 40	6.68
Yonex Aerosensa 40	6.85
Yonex Aerosensa 2	6.55
Synthetic	
Yonex Mavis 350	6.71
Yonex Mavis 2000	6.90
Li-Ning X800	6.78
Li-Ning X800	7.06
Mizuno NS-5	6.93

Interestingly, there was no significant difference between the stall velocities of the shuttlecocks. The various synthetic shuttlecocks had similar stall velocities as the feather shuttlecocks. It implies that the post-stall behaviour of the feather shuttlecocks and the synthetic shuttlecocks may be similar. This is discussed in the next section.

#### ***6.4.2.8 Trajectory Similarities***

Post-stall behaviour is the major criticism of the synthetic shuttlecocks. The synthetics were always thought to be faster with a drop that was never as steep as the feather shuttlecock. The results that were presented disagree with the convention

because flight parameters in the post-stall region were similar for the tested synthetic shuttlecocks and feather shuttlecocks. In the post-stall flight region, the synthetic shuttlecocks also had higher spin rate than some of the feather shuttlecocks. Therefore, it is unlikely for spin-induced pitching moment to be any less significant on the synthetic than on the feather shuttlecocks. This means that the resultant post-stall trajectory should be similar for synthetic and feather shuttlecocks.

The trajectories of the feather and synthetic shuttlecocks were applied to validate this proposition. As seen in Figure 97, the experimental trajectories of the AS40 (2) and Mavis 2000 were plotted and compared. The curve “Mavis 2000 (shifted)” was obtained by translating the original Mavis 2000 trajectory by 0.3 m in the x-axis. Following this translation, it was observed that both shuttlecocks had the same steepness in post-stall drop.

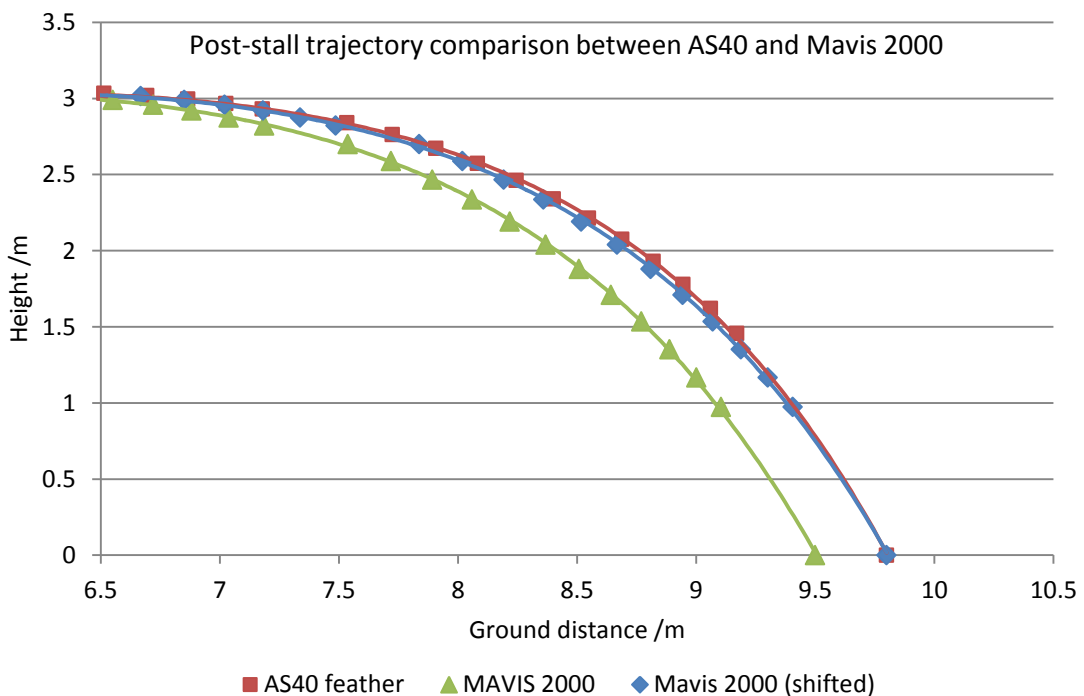


Figure 97 Only translation was required to fit the post-stall trajectory of the Mavis 2000 to that of the AS40.

Therefore, it can be said that if the synthetic and feather shuttlecocks were to start the post-vertex stall at the same point in space, their resultant trajectories would likely show negligible difference.

## **6.5 Summary of Experimental Work**

In this chapter, Phase II of the proposed testing methodology was detailed and applied to study of the shuttlecock flight.

In the quantification of turnover stability, it was observed that the amplitude of oscillation was as important as the time to complete turnover. Parameter identification and response simulation were also demonstrated using the obtained results. Turnover stability of the feather shuttlecocks proved to be superior over the synthetic shuttlecocks. This was because the higher damping factor of the feather shuttlecocks resulted in lesser overshoot. The poorer turnover performance of the synthetic was likely due to the skirt porosity. However, it should be noted that the relative instability of the synthetic shuttles might have given an extra advantage to the attacking player during net play.

The second part of the applied testing in Phase II documented the experimental work to test the trajectory, velocity and spin of the shuttlecock. This was the most important step in shuttlecock testing because the results were representative of behaviour in real usage. Processing the high-speed captured frames, in-flight parameters were obtained and compared. With the reference values (especially those from the BWF approved shuttles), prototypes can also be evaluated using the same method that was described. A clear shot was used because it had the ability to test all the characteristics of a shuttlecock. These included high speed deceleration and slow speed angular behaviour in axial and longitudinal directions. The current experimental setup can also be applied to testing of the other modes of play.

The flight testing results showed that there was little difference between the feather shuttlecocks and the synthetic ones. Beyond the turnover phase, the only noticeable difference between them was the reduced flight range of the synthetic shuttlecocks. The spin measurements demonstrated that it was unlikely for the synthetic shuttlecocks to have inferior post-vertex flight performance because they had even higher spin than the feather ones. There was no noticeable difference between the various grades of feather shuttlecocks that were tested.

## **7. SHUTTLECOCK TESTING: PHASE III (MECHANICAL)**

Methods to analyse the skirt strength and fatigue properties were proposed and are described in this chapter. The durability tests in this section are novel procedures that were developed. To further understand the shuttlecock performance, some of the shuttlecocks were evaluated after application of the developed wear induction methods. This is a very important phase in shuttlecock testing because durability and performance degradation is one of the major performance criteria that is often ignored in new developments.

### **7.1 Introduction**

The surveyed scientific literatures mainly focused on the science behind the badminton flight, in which the shuttlecocks studied were usually assumed to be in a “new” condition. The limited information on durability was only available in test results published in patents, such as [66] and [61]. Even in these articles, durability and skirt stiffness were usually described in pure qualitative forms with little to no description of test criteria.

Therefore, the proposed shuttlecock testing for Phase III of the evaluation framework that are described and demonstrated in this chapter are original methodologies. Phase III of the shuttlecock testing consists of the following evaluation components:

- Shuttlecock skirt stiffness testing
- Durability evaluation

The shuttlecock skirt stiffness refers to the compressive strength of the skirt. This parameter is important because it affects the skirt deformation and the impact response of the shuttlecock.

The durability of the shuttlecock refers to the ability of the shuttlecock to resist damage. Wear induction machines were developed to artificially wear out the shuttlecocks. Subsequently, the machine worn shuttlecocks were evaluated for their flight performance. By comparing the flight performance of the shuttlecocks before and after the wear induction, the durability and damage magnitude can be quantified

## 7.2 Shuttlecock Skirt Compression Tester (SSCT)

Compression testing of shuttlecock skirt can be conducted on any compression (universal) tester with the right load cell rating. Since a suitably rated load cell system was not available to this research and the cost of the proprietary load cell system was prohibitive, a shuttlecock skirt compression tester (SSCT) was developed in this part of the work.

### 7.2.1 SSCT Components

The SSCT is shown in Figure 98.

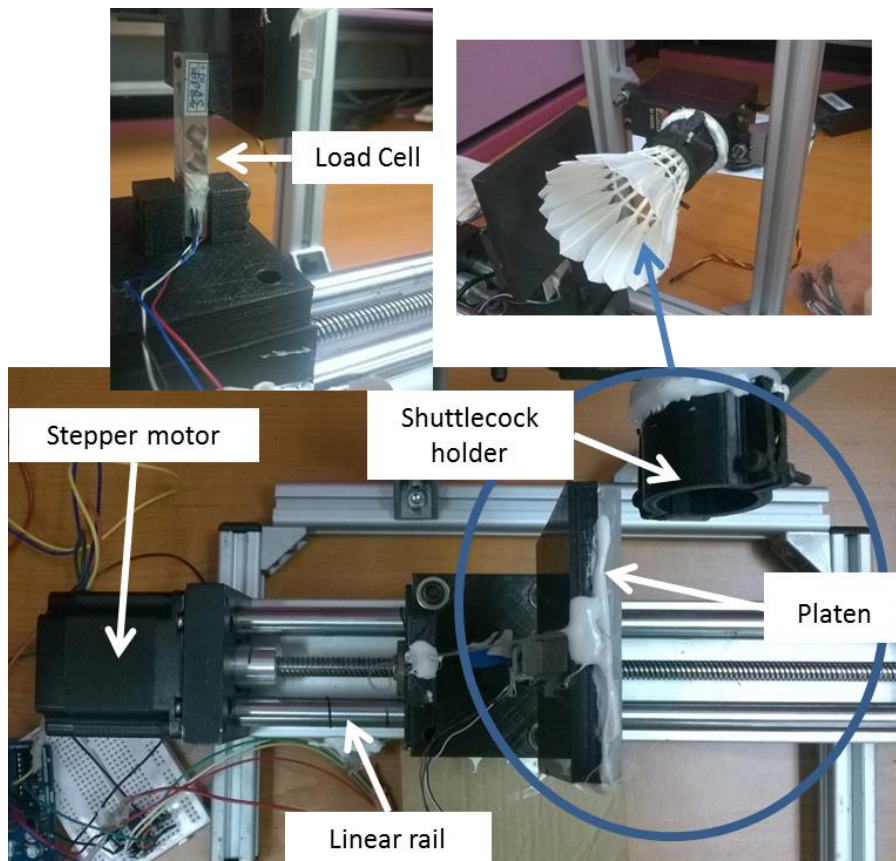


Figure 98 Components of the SSCT.

It comprised of the following components:

- Linear rail with a screw gear
- 24 V stepper motor
- DVR8825 stepper motor driver carrier
- Arduino UNO R3 microcontroller
- 24V 2.5 A power supply
- Seeed Studio 500 g load cell
- Burr-Brown INA125P amplification chip
- Attachment mountings/Platen fabricated with Additive Manufacturing
- 22 mm Aluminium profile frame

The connection between the Arduino, the DVR8825 and the stepper motor followed the example provided by Pololu Corporation, the manufacturer of the DVR8825 driver carrier [121]. The circuitry of the load cell amplification system followed the example provided by Seeed Studio [122].

The load cell system was calibrated using weights. The calibration data was plotted and is shown in Figure 99. A trend line was also plotted and it shows good agreement with the data. Strain reading from the Arduino can be converted to load (N) through the relationship of  $\text{load} = 0.00721 \times \text{strain reading}$ . During the calibration process, it was observed that the system was unable to produce reading when the applied force was less than 0.1 N. This minimum dead load is a common issue with load cell systems.

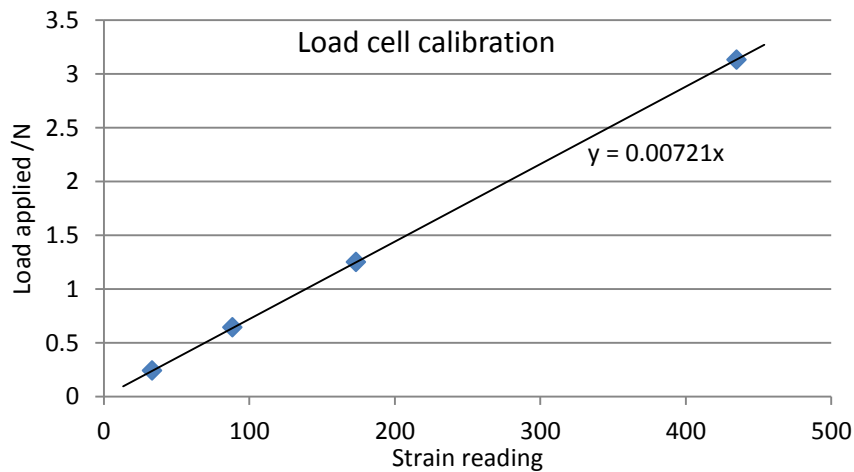


Figure 99 Calibrated load cell system chart.

Compliance and rigidity of the compression tester are important for accurate result. The relatively low testing force (up to 2 N) of the badminton shuttlecock means that even the 22 mm aluminium profile frame that was used is sufficient for obtaining good rigidity. It is likely that bracing of the platform will be required for higher load applications, such as the compression testing of the cork material.

### 7.2.2 SSCT Functioning

The linear actuator was powered by the 24 V stepper motor that was driven through the DRV8825. The usage of a stepper motor eliminated the need of a position encoder because the input to the stepper motor was sent in step. The compressive force was measured through the 500 g load cell. This can be replaced by a 100 g load cell for more precise measurement. The signal from the load cell was amplified through the INA125P chip. The compression mechanism and the load cell system were integrated and controlled by the Arduino Uno.

The test specimen was first mounted on the tester by using the cork clamp which did not touch or constrain the skirt motion. The skirt compression tester was then operated automatically in the pre-programmed algorithm as follows:

- Turning on the tester, the position of the compression platen was calibrated by first moving the platen towards the test specimen. Upon contact with the specimen, the load produced would have triggered a reversal of the platen by 1500 steps (3.83 mm). This motion is illustrated in Figure 100.

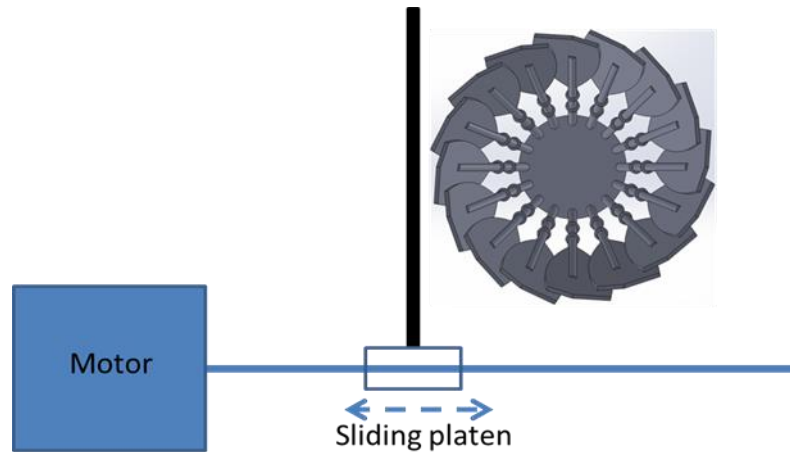


Figure 100 Mechanical motion of the sliding platen on the SSCT.

- Upon the completion of calibration, the stepper crept toward the shuttlecock skirt at a rate of 0.3833 mm/s (150 steps/second). This compression rate was referenced from ASTM D 1667-97, which is a test standard for flexible cellulite material and closed cell foam.
- Each motion step was 0.00256 mm of travel. The force on the load cell was recorded with the step reading at every step interval. Therefore, the sampling frequency of the developed tester was 150 Hz.
- Compression was terminated when the compressive force exceeded a pre-defined value or when platen displacement exceeded 13500 steps, whichever occurred first.

The force-displacement curve was then plotted for the specimen. The full Arduino source code of the tester is given in Appendix H. To eliminate bias from non-homogenous skirt property along the circumference, each shuttlecock was tested three times at 120 degrees interval along the circumference.

### 7.2.3 SSCT Preliminary Trial

In the preliminary trial of the SSCT, a Carlton Club (practice-grade feather shuttlecock) and a Yonex Aerosensa 10 (mid-range feather shuttlecock) were tested. The displacement-force curves were plotted and are shown in Figure 101. A 20 sample moving average trend line was also plotted for each displacement-force curve. Since there was no filtering, noise in data of such nature was unavoidable. However, the fluctuation in the trend lines suggested that the issue with the data was more than that induced by noise. Troubleshooting the tester traced the issue to the surface roughness of the compression platen.

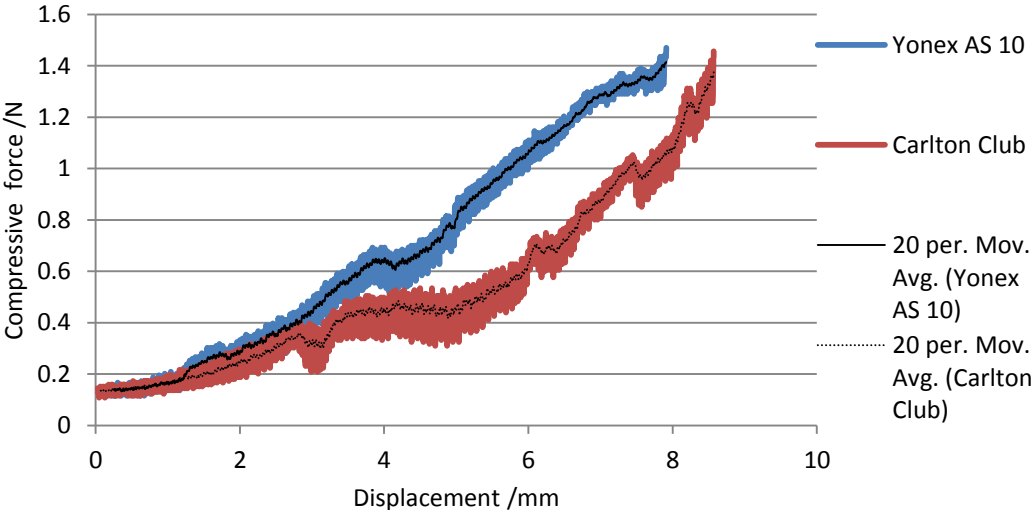


Figure 101 Displacement-Compression force plot for the trial compression test.

The natural grain of the fused deposition modelling (FDM) manufactured compression platen resulted in jerky force read out during the skirt compression.

This was because the tip of the feather shaft was getting caught on the rough surface.

The surface grain of the platen is shown in Figure 102.

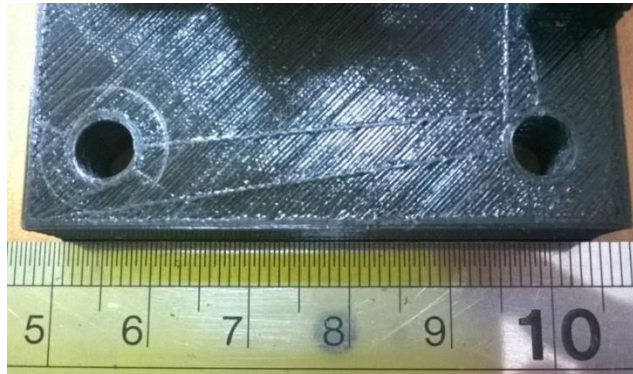


Figure 102 Surface roughness from the grain of FDM process.

A smooth acrylic plate was thus added on the platen surface and the compression test was repeated. The 20 sample moving average trend lines were plotted against the original results and are shown in Figure 103. The result showed that the addition of a smooth acrylic plate greatly reduced the fluctuations. As expected, the practice-grade Carlton feather shuttlecock, which has a softer skirt, showed more deformation under the same load as the Yonex AS10.

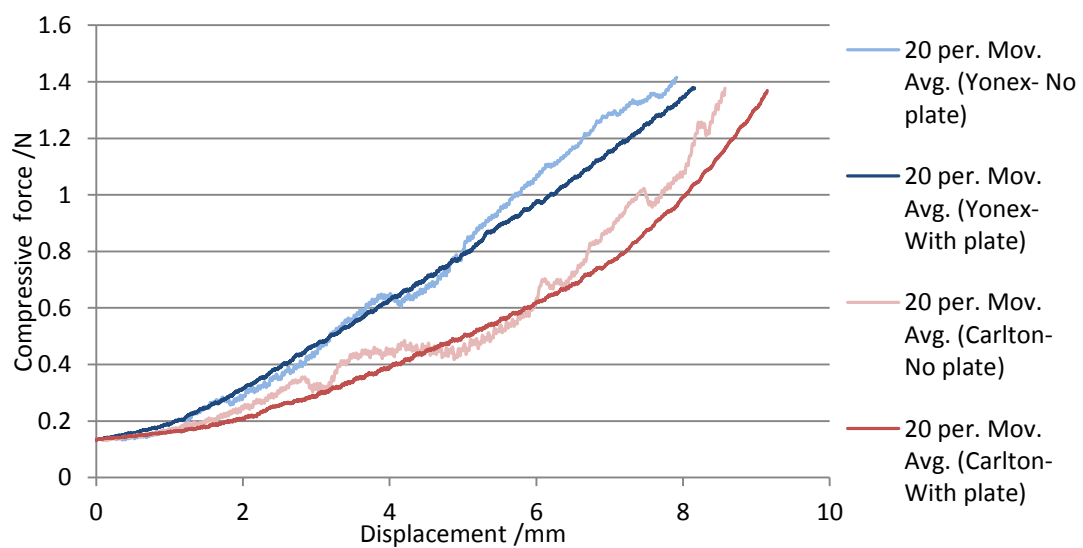


Figure 103 Displacement-force curves for the specimens tested with and without the acrylic plate on the platen.

The minimum dead load problem with the load cell system was also causing inaccuracy in the analysis of softer skirts. This was because the compressive displacement at 0.1 N (minimum dead load) was significantly larger on a softer shuttle. Therefore, the load cell was pre-loaded such that the no compression load on the load cell was larger than 0.1 N. This additional pre-load was subsequently subtracted from the recorded result.

### **7.3 Wear Induction Machines**

As discussed in section 2.2.2, wear and tear of a badminton shuttlecock usually occurs at the feather. The damage can take the form of vane wear (Figure 104) or shaft breakage (Figure 105). The badminton stroke that potentially does the most damage to a shuttlecock is the smash shot. In a smash shot, it is highly possible that the racket string will directly strike the skirt on the shuttlecock, such as when a shuttlecock is smashed while dropping down from a high-clear. This results in the skirt compressing (flattening). In contrast, certain badminton shots, such as a clear shot, will tend to put impact on the cork segment of the shuttlecock, thereby causing the skirt to open up at impact.



Figure 104 (L) Feather vane wear from usage.



Figure 105 (R) Feather shaft breakage from usage.

The damage of a smash stroke is so significant that the shuttlecock approval scheme by the Badminton World Federation (BWF) applies smash resistance as the indicator of shuttlecock durability. In their testing, a shuttlecock is smashed 10 times from a high lift-vertical fall. To qualify as an approved shuttlecock, there must be no feather breakage or decrease in the diameter after the 10 smashes. Such a test comprehensively evaluates the durability of the feathers and the string and the glue holding them together. Anecdotally, it was said that shuttlecocks of the past did not contain the string that surrounds the feather to strengthen them. This caused the shuttlecock skirt to be prone to collapse under a strong smash, reducing the diameter and drag, making a fast smash even faster. The attacking player who was striving for the final game point could then use this property to create an unfair advantage over their competitors.

Despite the above, the smash test as an indicator to durability is insufficient for non-tournament users. This is because the durability evaluation by the BWF only evaluates the smash durability. It does not take into account of the general degradation of the shuttlecock with feather wear from lower intensity usage. This is

probably due to the high intensity of play and high rate of change of shuttlecocks during a sponsored tournament. Therefore, feather vane wear and distortion are unlikely to be of concern. In contrast, a non-tournament user should not focus purely on smash resistance as the sole criterion to durability. Instead, the general performance degradation should be considered. This is because the shuttlecock in the non-tournament usage is likely to be played with lower intensity. Moreover, the shuttlecock, which was paid for by the user, will remain in play until it has degraded beyond the satisfaction of the individual. Therefore, the definition of shuttlecock durability in a non-tournament environment will be different from that of the BWF. Thus, a new measure of durability is required in addition to the current smash test.

For effective evaluation of durability in Phase III, smash durability (high intensity impact) and vane wear resistance (low intensity impact) should be studied. Two wear induction machines were developed in this part of the work for the testing of durability. They are:

- The vane wear induction device (VWID)
  - For testing of the resistance to vane wear
- The smash test machine (STM)
  - For testing of smash durability

### **7.3.1 Vane Wear Induction Device (VWID)**

Upon contact with a racket, a badminton shuttlecock has both linear velocity and axial spin. Two dominant actions result from this collision. Firstly, the initial contact between a spinning shuttlecock and a stationary string bed results in a rubbing motion. Further into the collision, the shuttlecock skirt stops spinning and is

compressed. The amount of compression is dependent on both the strength of impact and the stiffness (deformation resistance) of the shuttlecock. Given the same impact force, a stiffer shuttlecock skirt should deform less. After the impact, the shuttlecock bounces off from the string bed and the elastic skirt returns to the conical shape from the deformed state. A vane wear induction device (VWID) was developed to simulate these modes of wear. This developed VWID focuses on wear induction to the feather, which is the dominant type of damage to shuttlecocks that have been used for longer duration. Unlike the testing by BWF that involves human testers, the VWID reduces variability in lab condition.

#### ***7.3.1.1 VWID Components***

The VWID shown in Figure 106 consists of the following components:

- Two giant size servos (servo 1 and 2) to simulate the motion of a string bed pressing on the shuttlecock.
- Additive manufactured joint parts and press bed (platen). The platen utilises a grid of 1mm radius rods interlocked at 8 mm spacing between the rods. This simulates the racket string bed.
- A 5 N load cell attached to the platen.
- A third servo (servo 3) to hold and rotate (axial spin) the shuttlecock.
- Arduino Uno microcontroller with an INA125p amplifier for system control and force monitoring.

The servos could be connected to any pulse width modulated output channel of the Arduino. In depth detail of the servo library and connection method was referenced

from the Arduino servo library [123]. The load cell circuit followed that used for the SSCT [122].

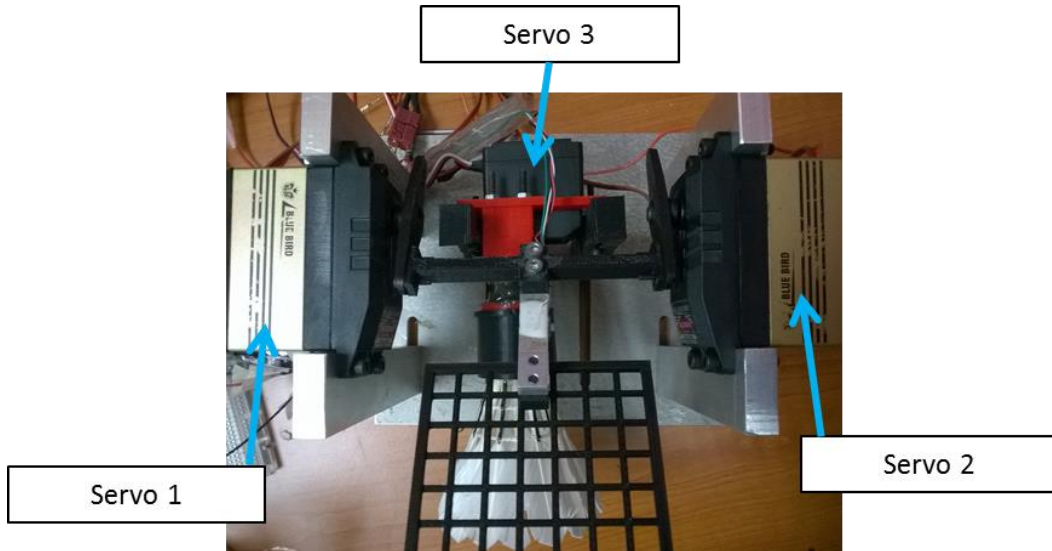


Figure 106 Top view of the VWID, showing the three servos and the shuttlecock being tested.

### 7.3.1.2 VWID Functioning

The functioning of the VWID is illustrated in Figure 107 and Figure 108.

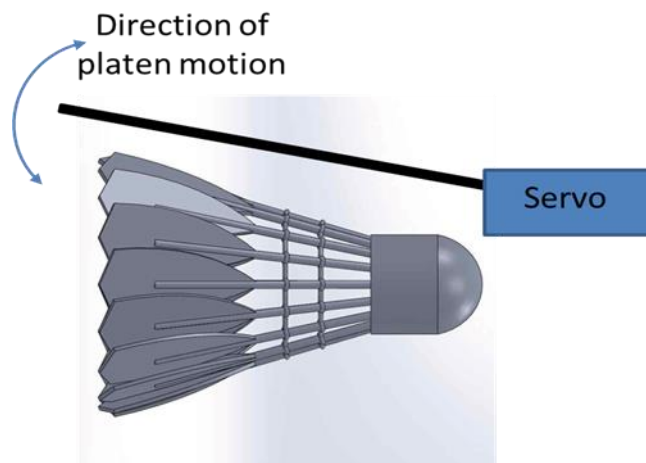


Figure 107 The direction of motion for the compression platen.

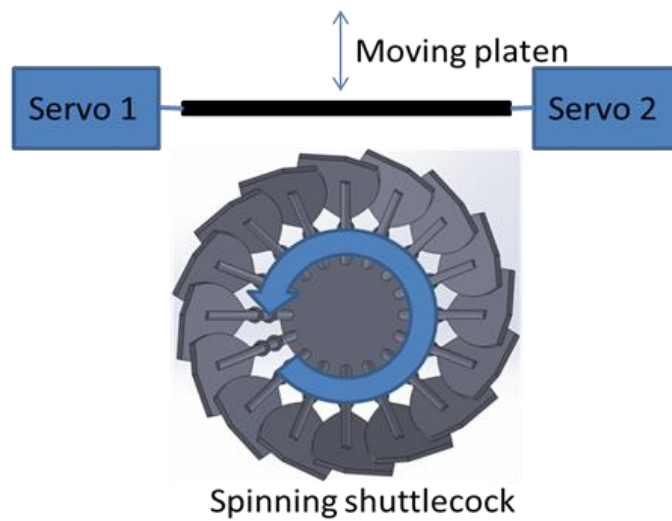


Figure 108 The spin direction of the shuttlecock with respect to the motion of the platen.

The machine works in the following principle:

- The process begins with the shuttlecock being spun by servo 3. There is no contact between the compression platen and the shuttlecock at this point in time.
- The compression platen powered by servo 1 and 2 moves down towards the spinning shuttlecock at a constant rate. The platen then contacts the shuttlecock and exerts force onto the shuttlecock skirt, resulting in skirt deformation. The shuttlecock continues spinning in this stage.
- As the platen moves down, the compressive force on the skirt is increased. This force is measured and recorded through the load-cell. Beyond a pre-defined threshold force,  $f_1$ , spin of the shuttlecock is stopped. The motion of the platen continues.
- As the platen continues to move down, the compressive force continues to increase. Beyond a second pre-defined threshold force,  $f_2$ , the compression

is released. If the force does not exceed  $f_2$  beyond the maximum allowable deformation (displacement), the compression is also released.

- This compression cycle is repeated for the test duration.

### ***7.3.1.3 VWID Preliminary Trial***

In the preliminary trial, a Carlton Club practice-grade feather shuttlecock and a BWF approved Babolat Tour feather shuttlecock were treated on the VWID. The compression rate of 0.6 Hz is equivalent to a shuttlecock being hit six times every 10 s. The first threshold force  $f_1$  was set to 0.5 N, while  $f_2$  was defined as 1.5 N. Each shuttlecock was treated for 15 mins and photos were taken at five mins interval for comparison of the vane damage. These photos of the post VWID treated shuttlecocks are tabulated in Figure 109.

VWID duration	Babolat Tour	Carlton Club (High)	Carlton Club (Low)
5 min			
10 min			
15 min			

Figure 109 Feather vane wear after vane wear induction on Babolat Tour (Tournament-grade) and Carlton Club (Practice-grade).

After the first 5 mins of treatment, the Babolat Tour had negligible damage on the vane with just minor distortion on some of the outer edge feather strands. On the other hand, the Carlton Club was beginning to show some feather vane wear. With longer treatment duration, vane wear on the Carlton Club was observed to be more severe. Distortion of the feather vane shape was also increasing in severity. The tournament-grade Babolat Tour showed good resistance to the VWID. Visually, the distortion on the Babolat Tour was insignificant even after 10 mins on the VWID.

At the end of the 15 mins VWID treatment, the Babolat Tour was able to retain the original feather vane profile. This means that the vanes still had the same coverage as when the shuttlecock was new and there was no change in the skirt porosity. There was also very limited distortion in the feather vane strands when compared to the Carlton Club. The Carlton Club had shown severe distortion of the vane profile after 15 mins of treatment. It was noticed that the feather strands were distorted such that the feathers were no longer able to retain the original surface area of the cone formed by the feather vanes.

Since the wear on the Babolat Tour shuttlecock after 15 mins of treatment was even less severe than the Carlton at the 5 mins interval, it may be possible that the Babolat will be more durable in actual rally play. The damage to the feather vane also appeared to be similar to that of actual play that was shown in Figure 104.

During the VWID treatment, it was noticed that the lower skirt stiffness of the Carlton Club resulted in spin being terminated at larger compressive displacement than with the Babolat Tour. This resulted in extra wear from additional rubbing (shearing) of the feather strands on the press bed. To understand the possible

implications of this to the resultant vane wear, a new Carlton Club was treated with  $f_1$  reduced to 0.3 N. Based on the compression data in Figure 115 and Figure 122, the reduced  $f_1$  stopped the axial spin of the Carlton Club when compressive displacement was 5 mm. This was the same compressive displacement as the Babolat Tour when  $f_1$  was 0.5 N. This meant that spin of both shuttlecocks were terminated at the same compressive displacement.

The result with the reduced  $f_1$  is given in Figure 109 and labelled as Carlton (Low). It is seen that the wear at the 15 mins interval was less severe than Carlton (High). However, it did not change the conclusion that the tournament-grade Babolat shuttlecock had less vane wear.

#### ***7.3.1.4 VWID Limitations***

The preliminary trial demonstrated that the VWID was capable of differentiating feather vane durability between a tournament-grade shuttlecock (Babolat Tour) and a practice-grade one (Carlton Club). However, the VWID did have limitations.

Firstly, the speed of impact and axial spin in real usage was not replicated by the VWID. This was because the servo motors used for the compression motion were unable to attain the actual racket speed which can range from 5-45 m/s depending on the stroke of play. Secondly, the stopping of axial spin in the VWID was signalled by the compressive load. This may have increased abrasion wear when the same  $f_1$  was applied to the softer skirt. A possible improvement that can be implemented in subsequent development is to apply a torque sensor to the axial spin axis. The torque value can then be used as an indicator to the termination of the axial spin. Despite

these limitations, the current VWID provides a consistent method to evaluate durability through vane wear induction.

### 7.3.2 Smash Test Machine (STM)

In the smash test by the BWF, durability is determined through the resistance to feather shaft breakage and the ability of the shuttlecock to retain a consistent diameter across the skirt. This because the impact force exerted on the shuttlecock skirt during a smash is so large that the skirt undergoes severe skirt compression. Figure 110 shows the impact deformation of a shuttlecock under high-speed smash shot by a national level badminton player from the Singapore Badminton Association (SBA). To replicate the impact from smash, a shuttlecock smash test machine (STM) was implemented through modification of the shuttlecock launcher that was developed.

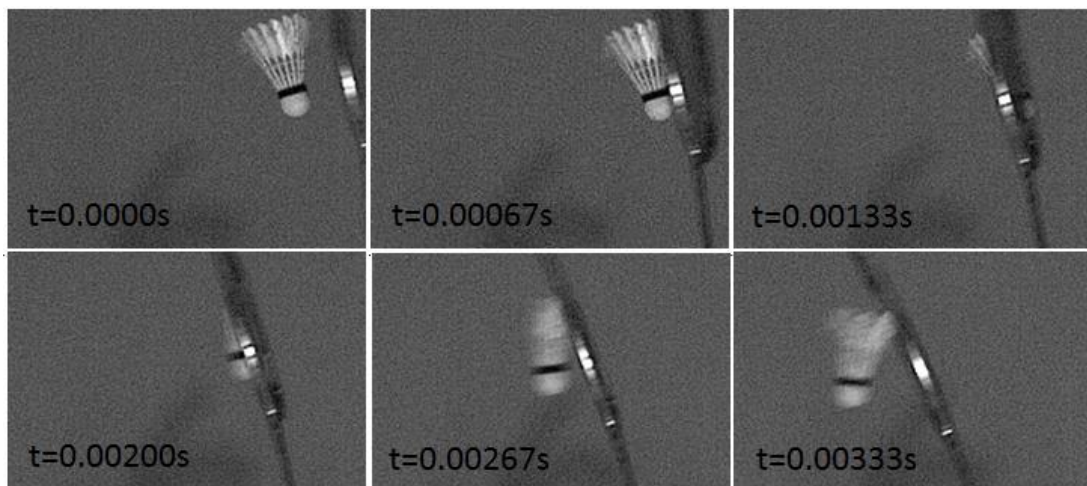


Figure 110 Deformation of the skirt under smash impact from the racket.

#### 7.3.2.1 STM Components

The fundamental components of the STM are identical to the shuttlecock launcher that was developed, with the following exceptions:

- A standard alloy badminton racket which was lengthened to 0.785 m in length.
- A larger racket holder with extra counterweight to compensate for the longer and heavier racket.

The modified racket-holder segment is presented in Figure 111.



Figure 111 The extended badminton racket for attaining the desired smash speed.

### ***7.3.2.2 STM Functioning***

The functioning of the STM was the same as the shuttlecock launcher documented in 6.1.3. However, the following changes had to be made:

- Increase in the racket rotation rate to approximately 57.6 rad/s.
- Change in the drop release mechanism time delay to 125 ms.

The increased rotation rate produced a resultant racket tip speed of 45 m/s. Using a post-impact shuttlecock-racket speed ratio of 1.33, the shuttlecock would be launched with a speed of 60 m/s [124]. The time delay of the drop mechanism was also changed to accommodate the change in racket speed. This ensured that the racket was hit on the racket string bed without touching the racket frame.

The high-speed chronographs of the smash deformation process with the current method are presented in Figure 112. The smash impact resulted in the total collapse of the skirt. This is similar to the actual smash impact that was captured and presented in Figure 110.

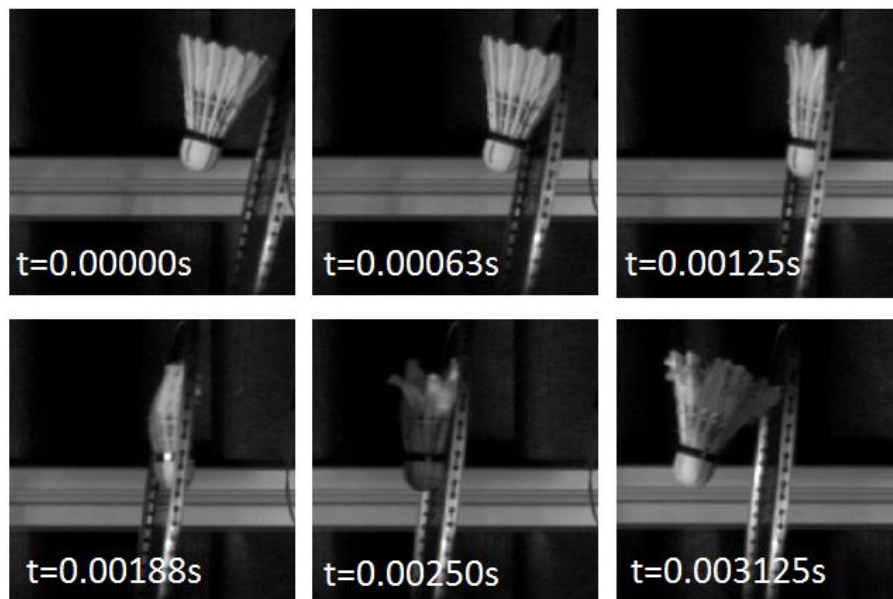


Figure 112 High-speed chronographs of the smash deformation process using the STM.

### ***7.3.2.3 STM Preliminary Trial***

Three types of feather shuttlecocks were tested in the preliminary trial for 10 smashes. These were the Babolat Tour (BWF approved tournament-grade), Li-Ning Grandprix Gold (mid-range) and Ashaway Service (practice-grade). Five readings of

diameter were taken at random position for each shuttlecock prior to the STM treatment. The diameters were recorded again after the fifth smash and the tenth smash. Photos of the shuttlecocks were taken before and after the STM treatment to document changes in vane wear and circularity.

The results from the preliminary trial on the STM are presented in Table 29 and Figure 113. Table 29 shows the skirt diameter measurements, while Figure 113 presents the visual condition of the shuttlecocks before and after the STM damage. Comparing the results, it was observed that the better shuttlecocks were able to resist damage better than the practice-grade Ashaway Practice.

Table 29 Measurements of the skirt diameters when the shuttlecocks were new, after 5 smashes and after 10 smashes. Test was discontinued for the Ashaway after just 2 smashes because the skirt collapsed into an ellipsoid.

Shuttlecock Type	No. of smashes	Diameter readings /mm				
		1	2	3	4	5
Ashaway Practice (77)	0 (new)	64.67	64.52	64.67	65.00	64.58
	2	Ellipsoidal shape of 72.64 (width) x 57.74 (height)				
Li-Ning Grandprix Gold (76)	0 (new)	65.41	65.46	65.23	65.67	65.85
	5	66.85	66.37	66.40	66.08	66.63
	10	67.20	66.64	66.61	67.24	67.00
Babolat Tour (77)	0 (new)	64.29	64.64	64.71	64.22	64.56
	5	66.38	65.36	65.98	65.60	66.50
	10	66.42	66.66	66.69	66.65	66.10

	Before (New)	After (Damaged)
Ashaway Practice (77)		
Li-Ning Grand Prix Gold (76)		
Babolat Tour (77)		

Figure 113 Visual condition of the shuttlecock skirts before (New) and after the STM treatment (Damaged).

Three major observations were made from the results:

- From the values in Table 29, the shuttlecock skirt diameters increased after the STM treatment when compared to the brand new condition. For both the Li-Ning Grandprix Gold and Babolat Tour, it was observed that the diameter increased when measured after five smashes. A further increase was observed after 10 smashes. No measurement was possible for the Ashway Practice because the skirt collapsed into an ellipse after just two smashes.
- The Ashaway Practice showed severe feather wear after the first two smashes. On the other hand, the Li-Ning Grandprix only exhibited some amount of vane wear. The vane wear on the Babolat Tour was negligible. This phenomenon, which can be seen from Figure 113, agrees with the preliminary trial results of the VWID in Figure 109. In both tests, the tournament-grade feather shuttlecocks were able to better resist vane wear than the practice-grade feather shuttlecocks.
- The Li-Ning Grandprix Gold and the Babolat Tour were able to resist permanent deformation from smash impact at the tested speed. However, the Ashaway Practice shuttlecock had collapsed into an ellipse that measured 72.64 mm (width) x 57.74 mm (height) in just two smashes. This means the Ashaway Practice would have failed in the standard BWF smash test criteria.

#### ***7.3.2.4 STM Limitations***

The current method of testing for smash durability is feasible and differences were observed between the shuttlecocks of different grades. However, it is possible that an increase in smash speed may increase test efficiency and make the test a more

stringent one. It is proposed that future test can be conducted with higher racket speed for the STM.

The second limitation is the methodology in diameter measurement. The randomly selected positions for diameter measurements mean that the changes in diameter cannot be tracked for each opposing feather pair on the shuttlecock. To overcome this limitation, diameter measurements will be taken for every opposing feather pair in the subsequent experiment. This approach means that a standard shuttlecock with 16 feathers will have eight diameter readings along the circumference.

In this study, the STM was only conducted for 1 specimen per shuttlecock type because the focus was on the process of inducing a high speed smash. Due to the fact that feather breakage from smash impact may be highly random, it is proposed that more samples be tested for better reliability of the result.

## **7.4 Experimental Methods**

In Phase III, the devices that were developed in section 7.2 and 7.3 were applied to the testing of the shuttlecock specimens for the following properties:

- Skirt stiffness
- Durability
  - Specimen preparation with VWID and STM
  - Flight evaluation

### **7.4.1 Skirt Stiffness**

The shuttlecocks used for the Phase I evaluation (Table 15) were tested for their skirt strength prior to any wear induction. The test was conducted after the applied testing in Phase II. These set the reference values for skirt stiffness of some of the current shuttlecocks. Two additional practice-grade shuttles were included for comparison with the tournament-grade feather ones.

Each shuttlecock was tested three times at 120 degree interval along the circumference of the skirt. The feather shuttlecocks were tested to 1.8 N compression, while the softer synthetic shuttlecocks were tested to 1 N. This was because the synthetic shuttlecocks were already showing large deformation of more than 45% strain at 1 N. The load values and compression platen positions were recorded through the Arduino serial monitor. Similar to the treatment of data in the preliminary trials, a 20 sample moving average was taken from the results and then processed for the curve of compressive force with displacement.

## **7.4.2 Durability**

The durability of the shuttlecocks was evaluated through investigation of the flight degradation caused by wear induced on the shuttlecocks. This was done by first preparing the shuttlecock specimens using the VWID and STM. The shuttlecock specimens were then evaluated with the experimental technique that was presented in Phase II (chapter 6).

### ***7.4.2.1 Shuttlecock Preparation- VWID***

The Li-Ning Grandprix Gold (76) and the Babolat Tour (77) were selected for an extended VWID testing. The comparison of these two shuttlecocks provided insights into the possible differences in durability between a mid-range shuttlecock and a tournament-grade one.

Each shuttlecock was treated on the VWID for 30 mins. The condition of the shuttlecock skirt was photographed before the treatment and at every 10 mins interval. The test specimens were both goose feather shuttlecock which are reputed to have better durability than the duck feather in the Ashaway Practice used in the preliminary trial. Therefore, f1 and f2 for both shuttlecocks were standardised at 0.5 N and 1.5 N respectively. These are the original force threshold values that were used in the preliminary trial. The compression cycle rate was increased to 0.9 Hz for more efficient testing.

### ***7.4.2.2 Shuttlecock Preparation- STM***

Four shuttlecocks were tested for their smash durability using the STM treatment described in section 7.3.2. These were:

- Ashaway Practice (Practice-grade feather shuttlecock)
- Li-Ning A62XD (Practice-grade feather shuttlecock)
- Yonex AS40 (Tournament-grade feather shuttlecock)
- Yonex Mavis 350 (Synthetic nylon shuttlecock)

The specimens selected range from the synthetic nylon to the BWF approved tournament-grade feather shuttlecock. They provided a good sample group for observing smash durability of the various types of shuttlecocks. The racket rotation speed of the STM was kept constant for all the shuttlecocks. A Phantom Miro 120S high-speed camera recording at 1600 fps was used to capture the moment before and after each smash. The smash speeds of the runs were then processed from the video using Tracker™.

A total of 15 smashes were performed on each shuttlecock. The diameters of the shuttlecock specimens were measured before the smash, after five smashes, after ten smashes and after 15 smashes. Eight measurements of diameter were taken for each run. Photos of the shuttlecocks before and after the STM treatment were also taken to document the state of wear of the feather vanes.

#### ***7.4.2.3 Flight Evaluation***

The same experimental set up and test methodology as Phase II (chapter 6) was used to evaluate the flight performance. The exception was slight shift in camera positions. The set-up is shown in Figure 114. The changes in camera positions are described in Table 30. The new positions of the high-speed cameras are highlighted in bold text. The shifts in positions were for reducing the distance between camera 1 and camera 2. The change in distance of camera 3 and the change in height of

camera 2 were due to difficulty in replicating the camera positions to the exact centimetre. Since videos from the cameras are processed with reference to the measured physical coordinates of the cameras, all changes will be accounted for in the processed results. Therefore, it is highly unlikely for this change to affect the final result.



Figure 114 Experimental set up for the post-wear performance evaluation of the shuttlecock specimens.

Table 30 Changes in the camera positions, where the new positions are bolded in the table.

	Camera 1	Camera 2	Camera 3
Distance from launcher /m	2.14 -> <b>2.25</b>	5.84 -> <b>5.75</b>	8.37 -> <b>8.38</b>
Height of camera /m	<b>1.85</b>	2.82 -> <b>2.83</b>	<b>1.97</b>

The obtained flight trajectories were then compared against the flight trajectories that were recorded for the same shuttlecock before the wear induction.

## 7.5 Results and Discussion

### 7.5.1 Skirt Stiffness

The compressive force-displacement curves of the shuttlecocks were plotted and are presented in Figure 115 to Figure 122.

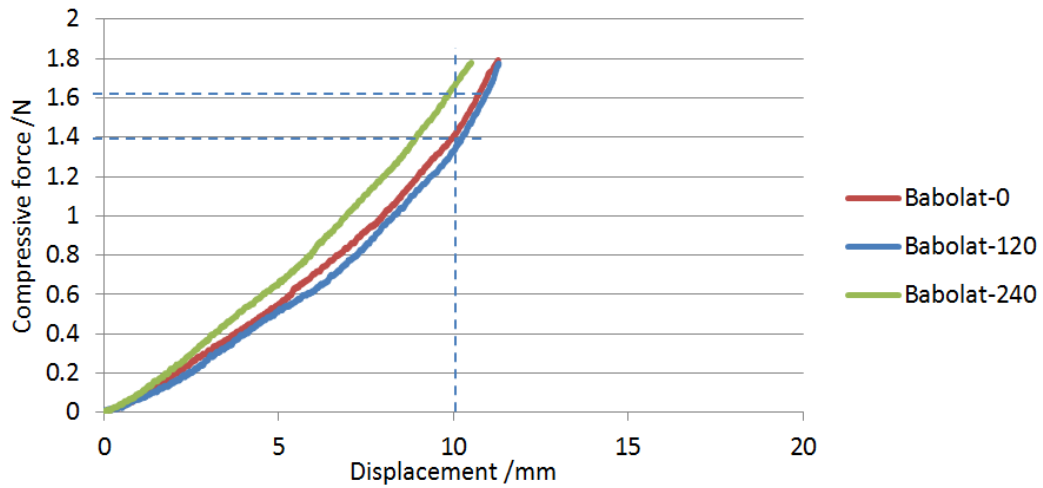


Figure 115 Compressive force-displacement plot of Babolat Tour (77).

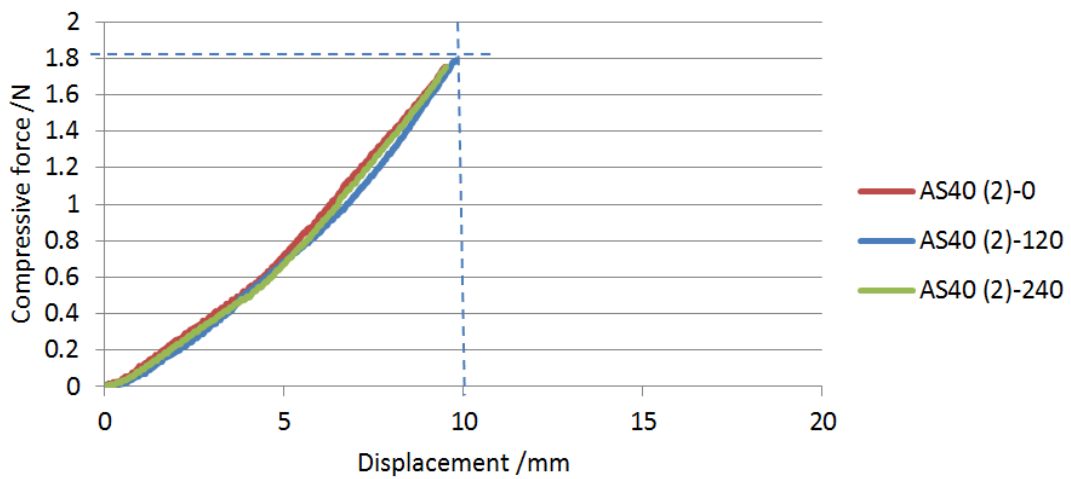


Figure 116 Compressive force-displacement plot of Yonex AS40 (2).

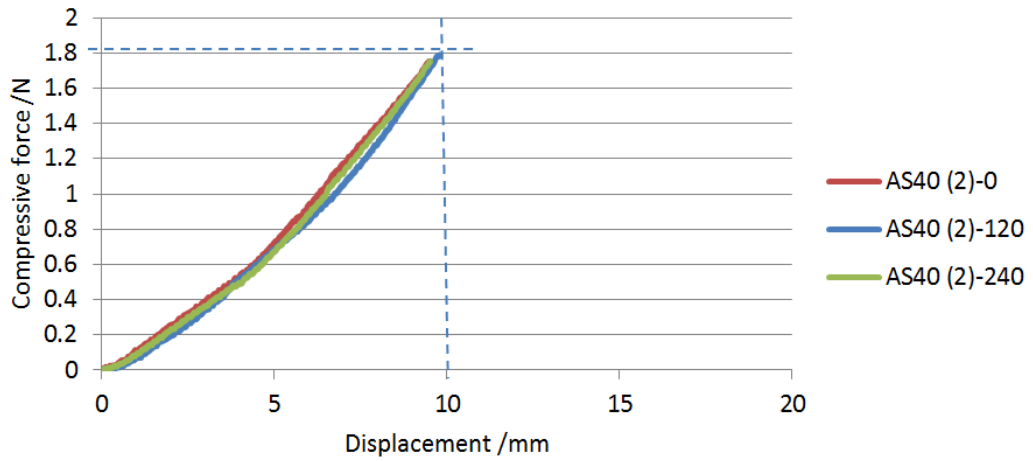


Figure 117 Compressive force-displacement plot of Yonex AS40 (3).

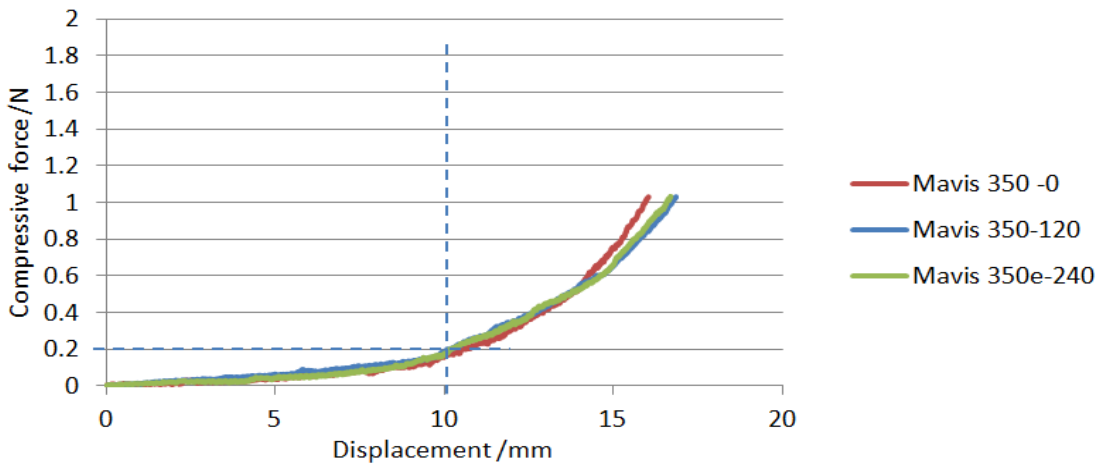


Figure 118 Compressive force-displacement plot of Yonex Mavis 350.

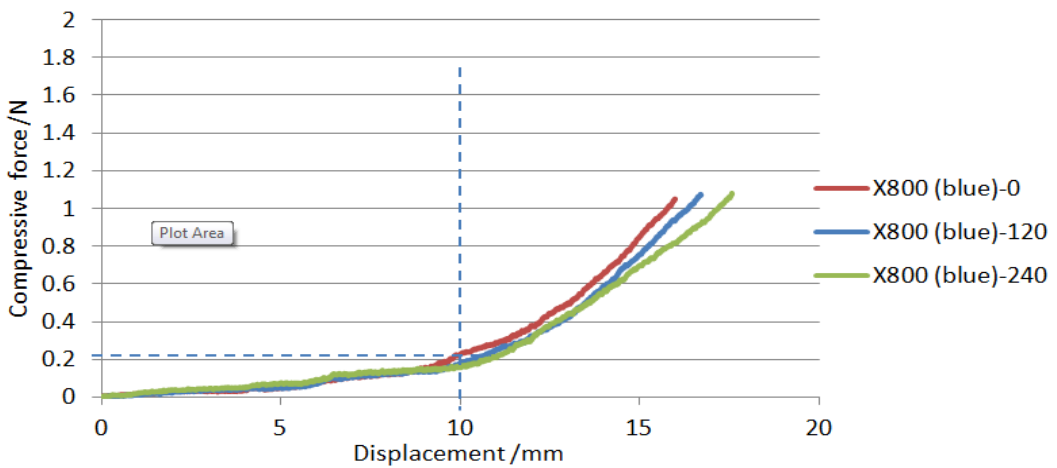


Figure 119 Compressive force-displacement plot of Li-Ning X800 (Blue).

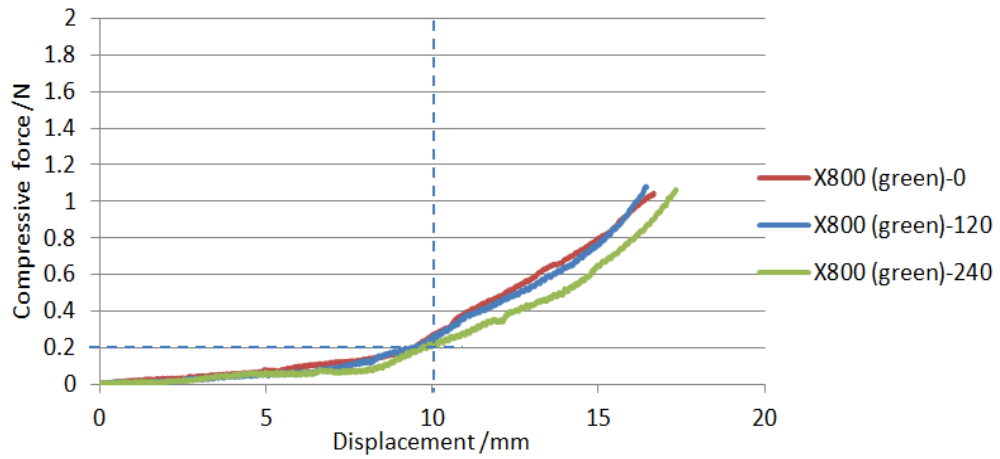


Figure 120 Compressive force-displacement plot of Li-Ning X800 (Green).

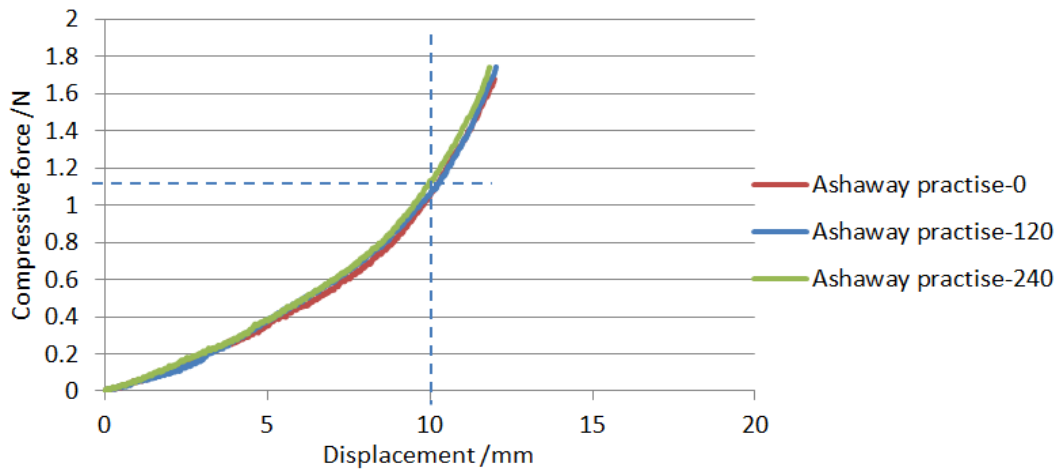


Figure 121 Compressive force-displacement plot of Ashaway Practice.

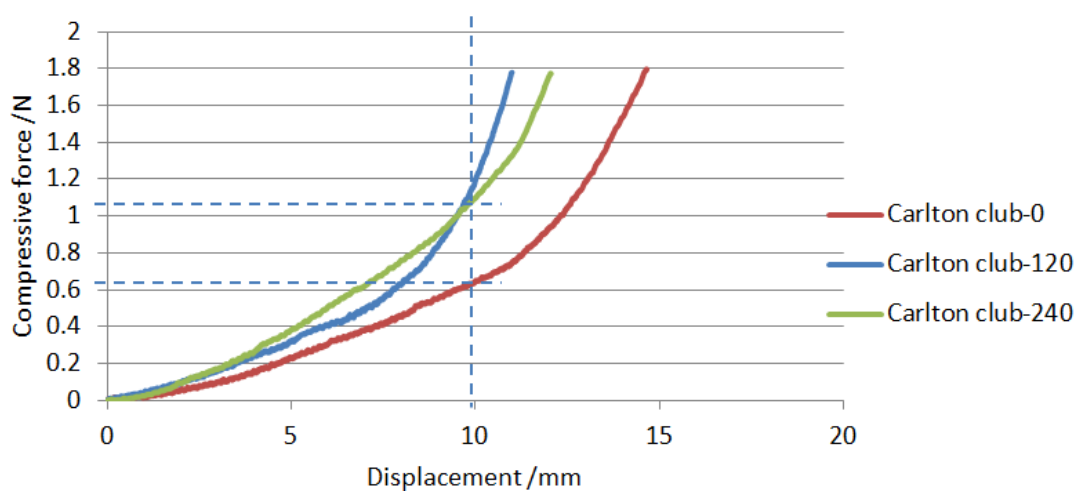


Figure 122 Compressive force-displacement plot of Carlton Club.

The tournament-grade feather shuttlecocks (Figure 115 to Figure 117) showed progressive increase in compressive force as displacement increased. The skirt stiffness, which is the gradient of the curve, showed gradual increase with increasing displacement. The Babolat Tour required 1.4 N of force for 10 mm compressive displacement (30% compressive strain), while both the Yonex AS40 required 1.8 N of force for the same strain. Strain refers to the compressive displacement as a percentage of the initial skirt radius.

It only took approximately 0.2 N to deform the much softer synthetic shuttlecocks (Figure 118 to Figure 120) by the same 30% compressive strain. This result means that the stiffness of the tested synthetic skirt was much lower than the tested feather shuttlecock. Therefore, the synthetic will require less energy than the feather shuttlecock for the same displacement. It is likely that this will result in larger deformation of the synthetic skirt during play, even at low impact force.

Compared to the tested tournament-grade feather shuttlecocks, the tested synthetics showed a low and almost constant stiffness when the displacement was under 8 mm. Going beyond 10 mm compression, all three tested synthetics showed large increase in skirt stiffness. This increase was likely to be the effect of stiffening features along the skirt profiles which were implemented along the mid-chord of the skirt. Therefore, the stiffening effect did not show in the early stage of compression when only the end of the skirt netting was compressed. This also suggests that the synthetic shuttlecock skirts had very little strength, but the stiffening members helped to maintain the structural integrity. In large deformation, it is likely that the stiffening members will aid in the skirt recovery when strain exceeds 30%. At lower

strain, recovery capacity will be impeded by the poor strength of the synthetic skirt netting.

The stiffness plot of the AS40 and the X800 shown in Figure 123 further elaborates this phenomenon. The skirt stiffness of the AS40 was 0.17 N/mm at 5 mm compressive displacement. The skirt stiffness of the X800 at the same 5 mm compression was only 0.02 N/mm. This showed that the skirt stiffness of the AS40 was much higher than that of the X800 during the initial compression. The stiffness of the X800 increased greatly as the compressive displacement increased, at which a stiffness of 0.23 N/mm was recorded at 16.7 mm (50% strain). Same stiffness was observed on the AS40 when displacement was just 7 mm, demonstrating the stiffness of the AS40.

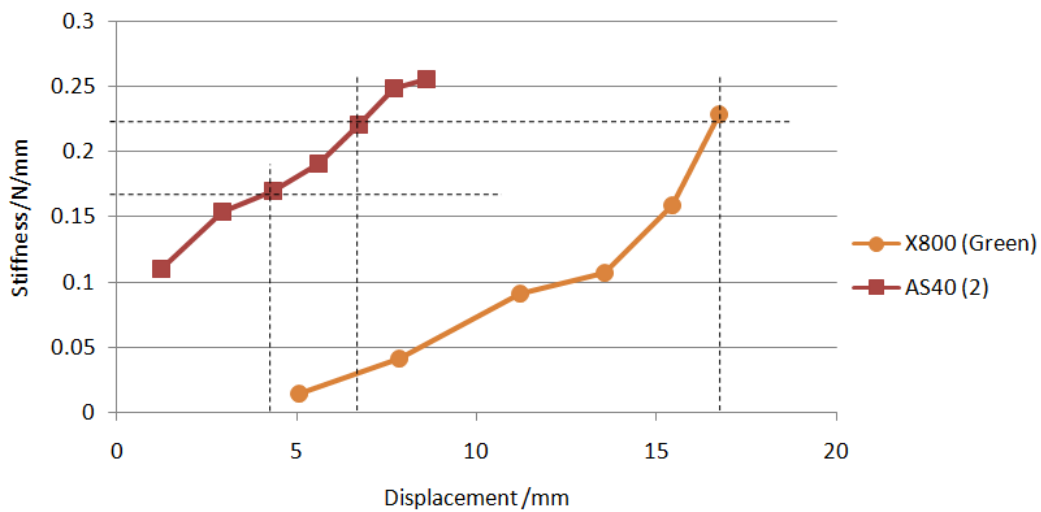


Figure 123 Change in skirt stiffness with compressive displacement of the tournament-grade AS40 feather shuttlecock and the X800 synthetic shuttlecock.

From compressive force-displacement plots in Figure 121 and Figure 122, it was seen that the tested practice-grade feather shuttlecocks have compression behaviour that was between that of the synthetics and tournament-grade feathers. Similar to the

tournament-grade feather shuttlecocks, these lower-tier feather shuttles have more stiffness at the early stage of compression. However, the lower feather stiffness than the tournament-grade shuttles means that the lower-tier feather shuttles also experienced higher compressive strain. The larger compressive strain on the Ashaway Practise and Carlton Club also resulted in the feather compressing and deforming the stiffening string that is applied in all commercial feather shuttlecocks. This resulted in a large increase in skirt stiffness when compressive displacement exceeded 8.7 mm, as seen in Figure 124. The stiffening ring on the Ashaway Practise and Carlton Club had a diameter of approximately 38 mm.

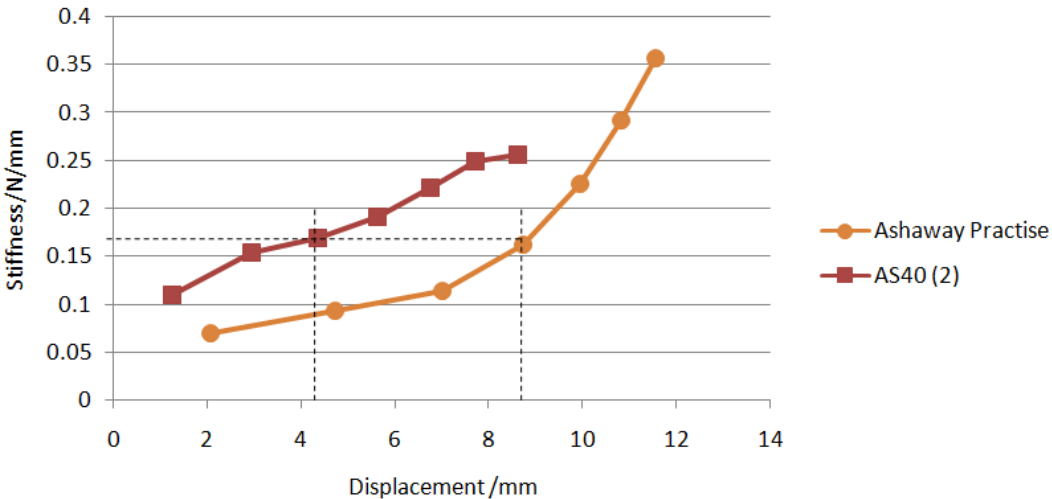


Figure 124 Change in skirt stiffness with compressive displacement of the top-grade AS40 feather shuttlecock and the practice-grade feather shuttlecock.

**7.5.2 VWID Prepared Specimen**

The photographs showing the condition of the feather vanes of the shuttlecocks are presented in Figure 125. Qualitatively, there was little difference between the medium-grade Li-Ning Grandprix Gold and the tournament-grade Babolat Tour at the 10 mins interval. However, the Li-Ning Grandprix started exhibiting much more feather vane distortion than the Babolat Tour at the 20 mins and the 30 mins interval.

By the end of the VWID treatment process, the Babolat Tour still retained the initial shape of the feather vane. On the other hand, the vane distortion on the Grandprix Gold shuttlecock resulted in the micro feather strands protruding out of the shuttlecock skirt. It is highly possible that the flight drag of the shuttlecock will be increased by the non-uniform strands. This will be evaluated in the flight testing.

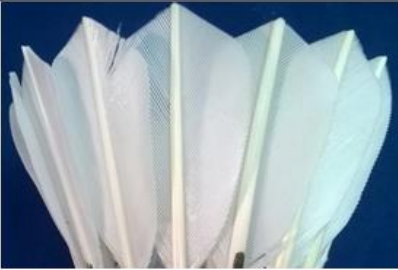
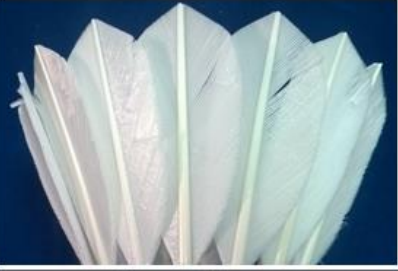
VWID duration	Li-Ning GrandPrix Gold	Babolat Tour
New		
10 min		
20 min		
30 min		

Figure 125 The feather vane condition of the shuttlecock specimens at each interval of the VWID treatment process.

### 7.5.3 STM Prepared Specimen

All the shuttlecocks underwent 15 smashes on the STM, with exception for the Ashaway Practice which had two broken feathers after the seventh smash. Therefore, the testing was terminated for the Ashaway shuttlecock. The smash speeds were obtained through digitizing the high-speed videos and they are presented in Table 31. The boxes that are highlighted in Table 31 are smash attempts where the shuttlecock contacted the racket frame. These are considered as flawed launch and they were not included in the calculation of the means and standard deviations. The mean smash speeds of the shuttlecocks were between 58.7 m/s to 60.1 m/s.

Table 31 Smash speeds recorded for the tested shuttlecocks during the STM treatment. The boxes highlighted in red are smash attempts where part of the shuttlecock contacted the racket frame.

Smash Attempt No.	Shuttlecock smash speed /m/s			
	Ashaway Practice	Li-Ning A62xd	Yonex AS40	Yonex Mavis 350
1	57.0	61.1	58.3	61.6
2	59.8	60.1	48.7	59.7
3	63.1	45.7	59.5	57.4
4	59.2	62.1	61.3	61.3
5	52.3	58.9	60.2	63.6
6	54.2	57.4	61.2	63.9
7	58.9	58.1	62.7	57.3
8		58.2	58.2	57.7
9		62.3	58.4	57.5
10		54.7	59.4	58.7
11		58.6	59.3	58.7
12		57.8	59.0	63.9
13		58.6	58.2	58.8
14		61.0	61.0	58.7
15		60.4	59.5	62.3
Mean	58.7	59.2	59.7	60.1
Std. Dev.	2.7	2.0	1.3	2.4

Using a two-tailed T-test to compare the fastest mean smash speed (Mavis 350) and the slowest mean smash speed (Ashaway Practice), a p-value of 0.164 was obtained. At a 95% confidence interval,  $(p = 0.164) > (\alpha = 0.05)$ . Therefore, it is unlikely for the mean smash speeds to be significantly different.

The diameters measured for the specimens are presented in Figure 126 to Figure 129. These figures represent the shape distortion of the shuttlecocks after the smash impact, where shape distortion refers to the loss in circularity. The Y-axis scale of Figure 127 to Figure 129 have been standardised for easier visualisation. The Y-axis scale for the Ashaway Practice was not standardised because the feather breakages increased the range fluctuation. The two dips in diameter after 7 smashes in Figure 126 were due to the broken feather shafts.

Although the diameters of all the shuttlecocks increased after the smash attempts, the increase was much less than what was observed in the preliminary trials. This was because the shuttlecock specimens used in this part of the study were specimens that were already used for the flight measurement in section Phase II (chapter 6). Therefore, the initial diameters before the STM treatment were already enlarged as compared to the brand new shuttlecocks used in the preliminary study.

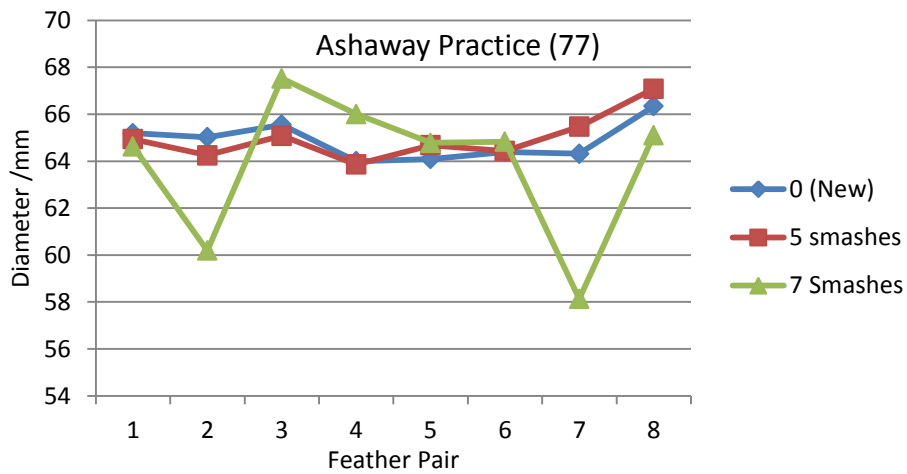


Figure 126 Diameter measurements for the Ashaway Practice feather shuttlecock.

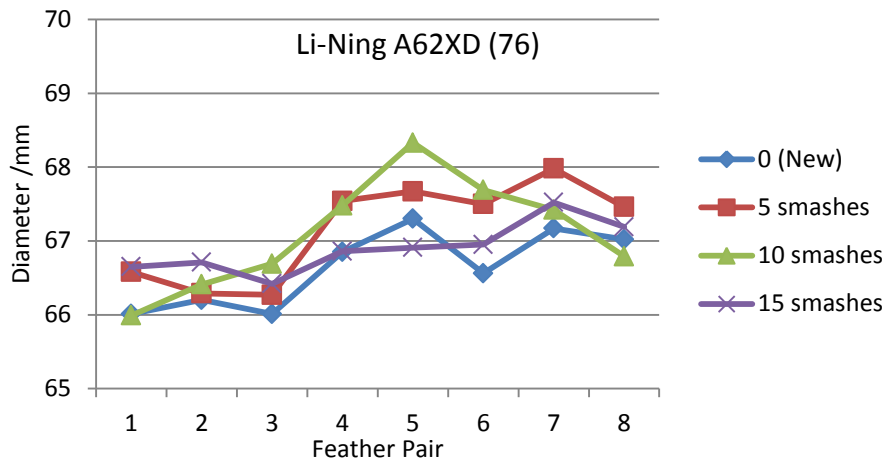


Figure 127 Diameter measurements for the A62XD feather shuttlecock.

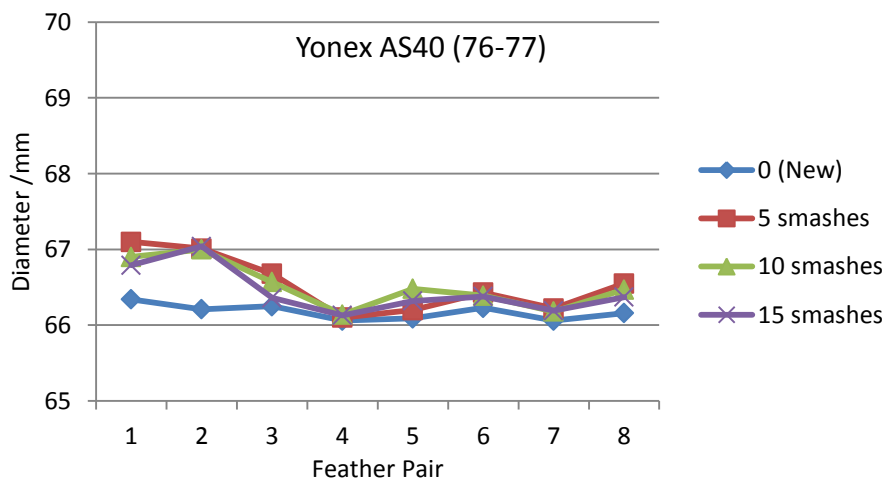


Figure 128 Diameter measurements for the Yonex AS40 feather shuttlecock.

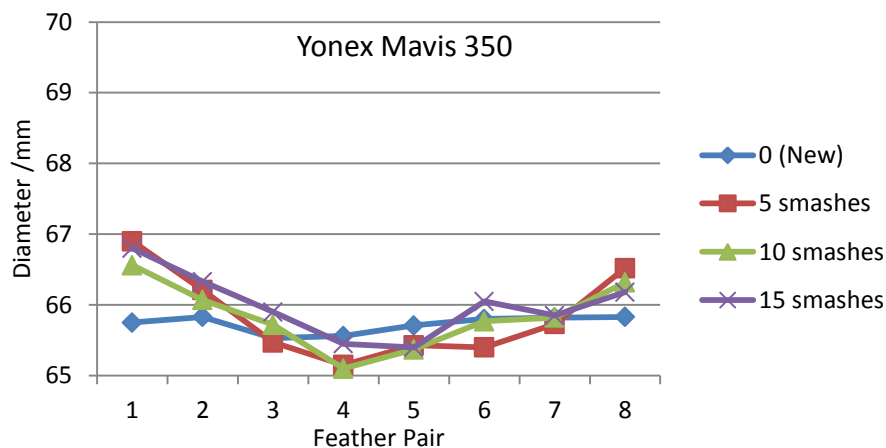


Figure 129 Diameter measurements for the Yonex Mavis 350 synthetic shuttlecock.

Through the results, it was seen that the BWF approved tournament-grade Yonex AS40 was able to resist skirt dimension changes better than the other two tested feather shuttlecocks. The limited change in the diameters of the Yonex Mavis 350 was expected because expansion was constrained by the one-piece moulded skirt design.

The photos of the feather vanes before and after the smash attempts are shown in Figure 130. Comparing the vane visual condition before and after the SMT treatment, it was observed that damage to the vane was more prominent in the two lower-grade feather shuttlecocks. The tournament-grade Yonex AS40 and the synthetic Yonex Mavis 350 showed negligible wear on the vanes after the smash attempts. There was no crack or breakage observed on the nylon netting of the synthetic shuttlecock skirt. The difference in vane condition between the Yonex AS40 and the Li-Ning A62XD after 15 smashes was very significant. This is also shown in Figure 131, where the Yonex AS40 was still almost like new after the 15 smashes. This agrees with the findings from the VWID section where the tournament-grade shuttlecocks were observed to have better vane durability.

	Before (New)	After (Damaged)
Ashaway Practice (77)		
Li-Ning A62XD (76)		
Yonex AS40 (77)		
Yonex Mavis 350		

Figure 130 Visual condition of the shuttlecock specimens before and after the smash attempts.



Figure 131 Feather vane condition of the Yonex AS40 (left) and Li-Ning A62XD (right) after 15 smashes.

## 7.5.4 Flight Evaluation

### 7.5.4.1 Launch Conditions

The initial flight conditions and the total flight range are shown in Table 32. The launch velocities ranged from 23.7 m/s to 24.5 m/s at angles of 65.75° to 66.13°. The launch velocities were similar to those that were observed for the Phase II measurement that were presented in section 6.4.2.1. Therefore, comparison between the pre- and post-wear trajectories is unlikely to be biased by launch conditions. In comparison with the pre-wear baselines, all shuttlecocks experienced reduction in range after the wear induction. This was the most severe with the Ashaway Practice shuttlecock and it was probably because the Ashaway shuttlecock exhibited the most wear damage.

Table 32 The initial launch flight conditions of the shuttlecocks.

Feather	Launch velocity /m/s	$\dot{x}/\dot{z}$	Range /m
Li-Ning Grandprix Gold	24.5	2.26	9.3
Babolat Tournament	23.7	2.22	9.6
Ashaway Practice	23.8	2.24	9
Li-Ning A62 XD	24.5	2.25	9.3
Yonex Aerosensa 40	23.9	2.23	9.5
Yonex Mavis 350	24.2	2.24	9.4

The required racket speed for all the shuttlecocks was the same as the experiment that was described in section 6.4.2.1, with the exception of the Ashaway Practice. The Ashaway shuttlecock required a higher racket speed to achieve the launch criteria. With the original racket speed, the 3 run averaged launch speed of the Ashaway was approximately 21.5 m/s.

#### ***7.5.4.2 Trajectory***

The trajectories of the Babolat Tour and Li-Ning Grandprix Gold before and after the VWID process were plotted and they are shown in Figure 132. The trajectory of the Babolat Tour shuttlecock showed little deviation after vane wear. However, less height and range were observed for the Li-Ning Grandprix Gold. Compared to the baseline which was obtained before the VWID, the Li-Ning Grandprix Gold had a decrease of 0.5 m in range and 0.1 m in vertex height after the wear treatment. Because of the reduced range, the Li-Ning Grandprix Gold after VWID reached the trajectory vertex earlier than the baseline. Since there was no significant difference between the shuttlecocks in the early segment of the pre-vertex trajectory, then it was likely that launch angle and velocity were not a possible source of error. The

flight behaviour of the post-wear Li-Ning Grandprix Gold was that of a shuttlecock with higher drag. Therefore, it is likely that the VWID treatment has increased the drag characteristic. It is also possible that a larger difference will be observed between the baseline and the post-wear result if a lower grade shuttlecock was evaluated.

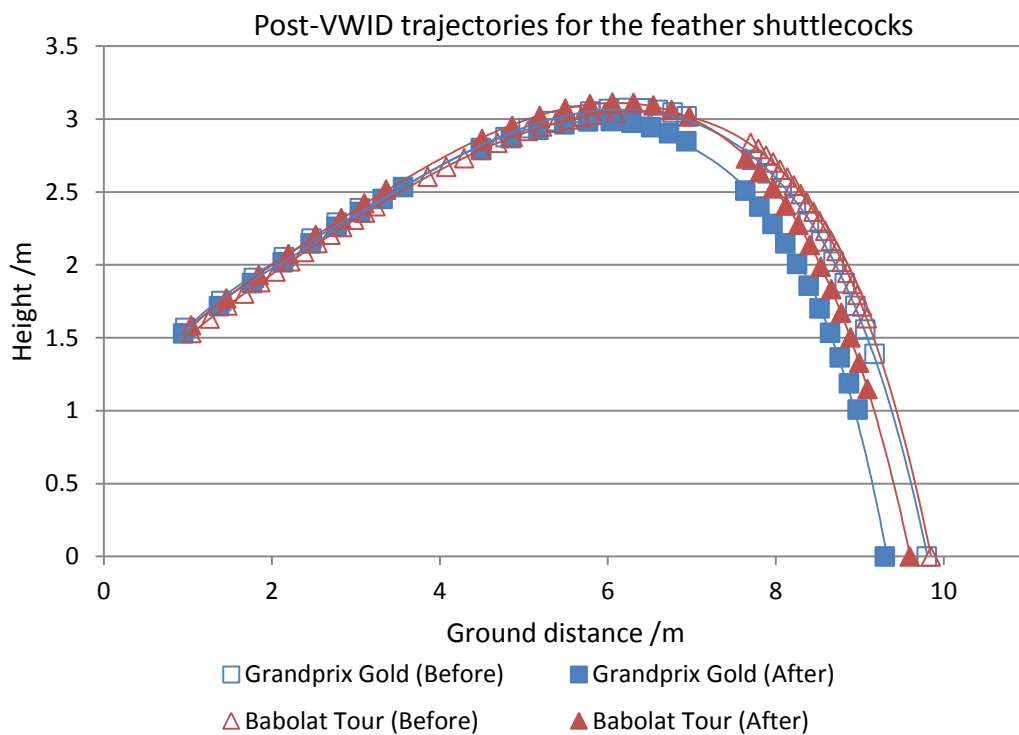


Figure 132 Trajectories of the Babolat and Li-Ning Grandprix Gold shuttlecocks before and after the VWID treatment.

Trajectories for the three feather shuttlecocks treated with the STM were plotted and are shown in Figure 133. Due to a different baseline trajectory (section 6.4.2.3) from the feather shuttlecocks, the trajectories for the Yonex Mavis 350 synthetic shuttlecock were plotted separately from the feather shuttlecock trajectories and these are presented in Figure 134.

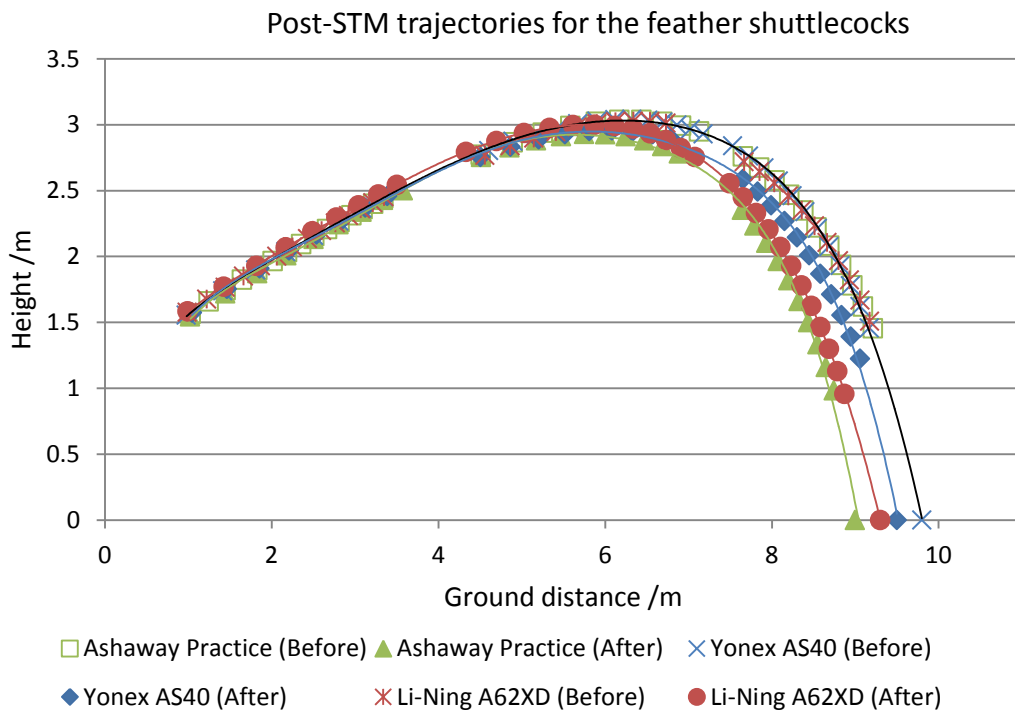


Figure 133 Trajectories observed for the three feather shuttlecocks before and after STM.

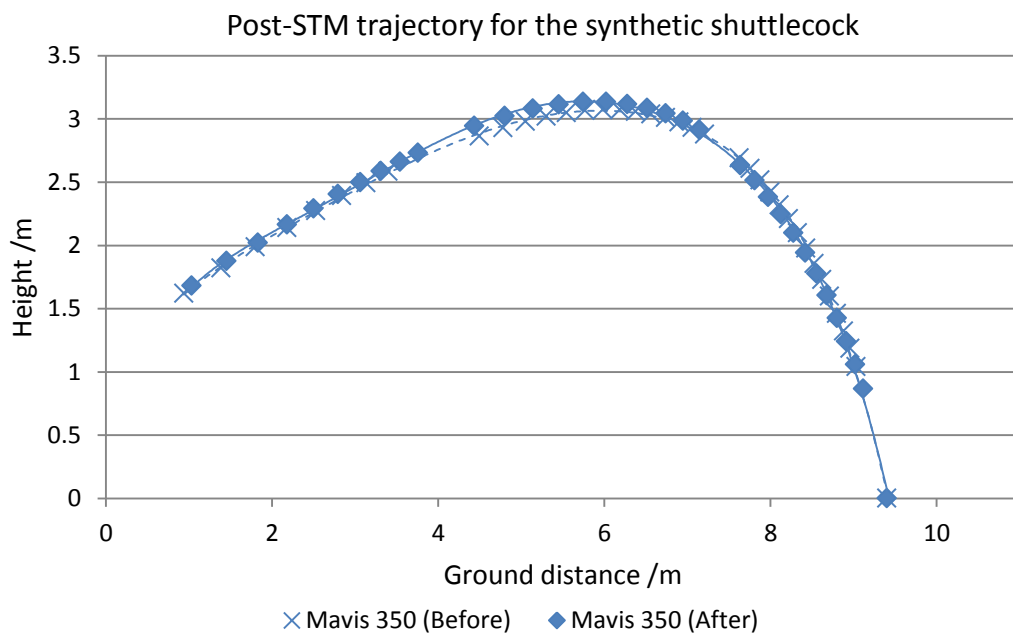


Figure 134 Trajectories observed for the Yonex Mavis 350 shuttlecock before and after STM.

From Figure 133, it was observed that the feather shuttlecock trajectories exhibited deviation from their baselines. All the shuttlecocks showed reduction in range and height after the STM was applied. The deviation magnitude agreed with the damage magnitude that was documented in Figure 130. The Yonex AS40, which had the least visual damage, was able to retain the original flight characteristic better than the other feather shuttlecocks. The Ashaway which had broken feathers showed the largest reduction in range and vertex height. Based on the result that was presented in Figure 88, this 1m reduction in range was almost equivalent to the difference of two grain weight.

Figure 128 shows that there was little difference in trajectory for the Yonex Mavis 350 before and after the smash wear process. This observation agreed with the pre- and post-smash wear condition observed during the specimen preparation, where there was no visible wear and just minor change in dimensions.

#### ***7.5.4.3 Spin***

The axial spin rate profiles of the shuttlecocks were also obtained from the high-speed videos. Using the spin rates that were determined in section 6.4.2.5 and 6.4.2.6 as baseline, the changes in spin profiles from wear and tear were determined. The spin profiles of the VWID treated specimens were plotted and they are shown in Figure 135. The spin profile of the Babolat Tour remained unchanged after the VWID process. Although there was a minor reduction in spin rate for the Grandprix Gold after the VWID process, the difference was too small to be considered significant from the perspective of change in spin-induced yaw deviation.

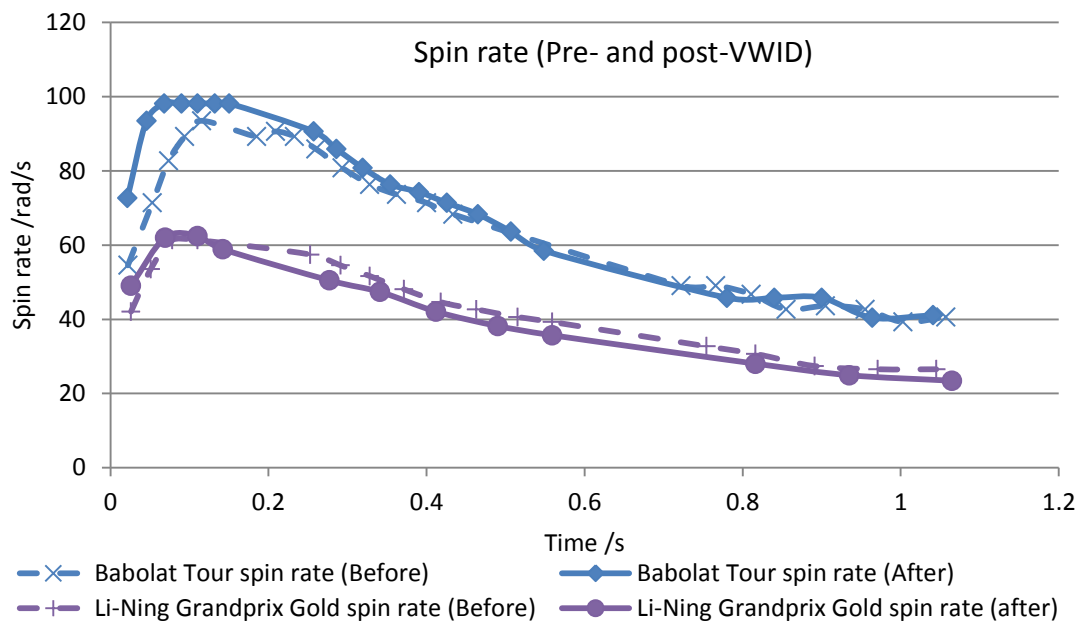


Figure 135 Spin rate of the feather shuttlecocks before and after the VWID process.

The spin profiles of the STM specimens are shown in Figure 136. In comparison to the insignificant change in spin rate with the VIWD prepared specimens, the spin profiles of the feather shuttlecocks after the smash test were very interesting. The differences observed between the spin rates that were measured before and after the STM reflected the state of degradation that was observed. The largest difference was observed on the Ashaway Practice shuttlecock, where the spin rate had significantly increased. The peak spin rate increased by 68.5%, while the spin rate in the post trajectory vertex drop segment also increased by over 30%. This will produce an increase of over 30% in spin-induced yawing moment, which will lead to larger sideway trajectory deviation.

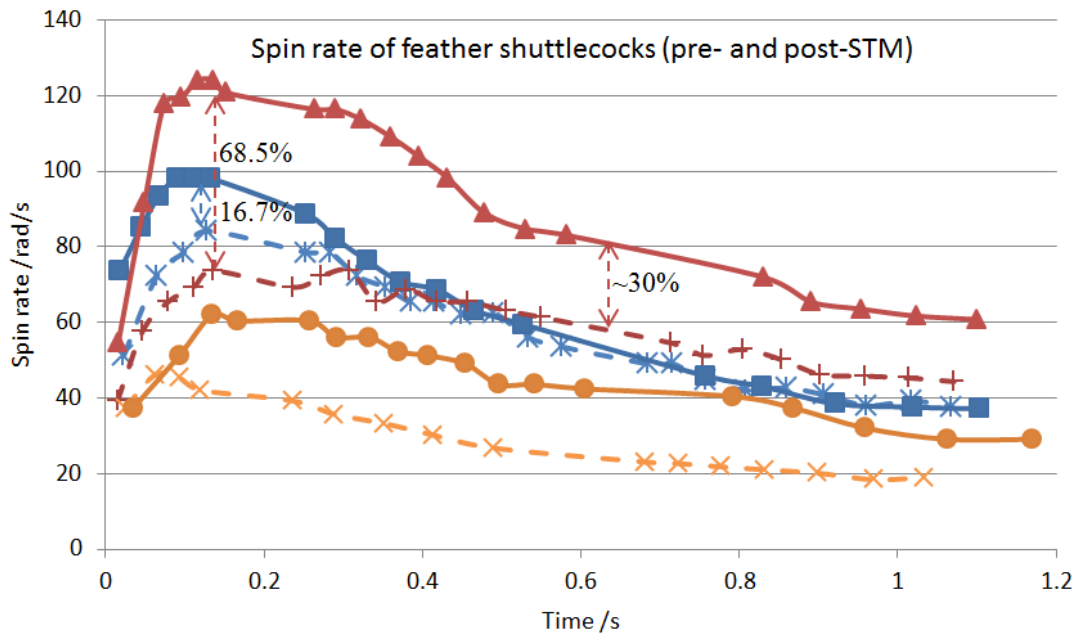


Figure 136 Comparison of the spin rates of the feather shuttlecocks before and after the smash test.

In contrast the peak spin rate of the Yonex AS40 only increased by 16.7% after the STM process. There was no spin rate difference before and after the STM in the post-vertex trajectory flight segment of the AS40. The spin performance of the Yonex Mavis 350 is shown in Figure 137. The spin rate of the Yonex Mavis 350 was lower after the STM process. The peak spin rate decreased by 15.1% as compared to before STM. However, the difference in the post vertex spin rate was of much smaller magnitude than the difference that was observed for the Ashaway Practice and Li-Ning A62XD. The reduction in post vertex spin rate was approximately 7% for the Yonex Mavis 350.

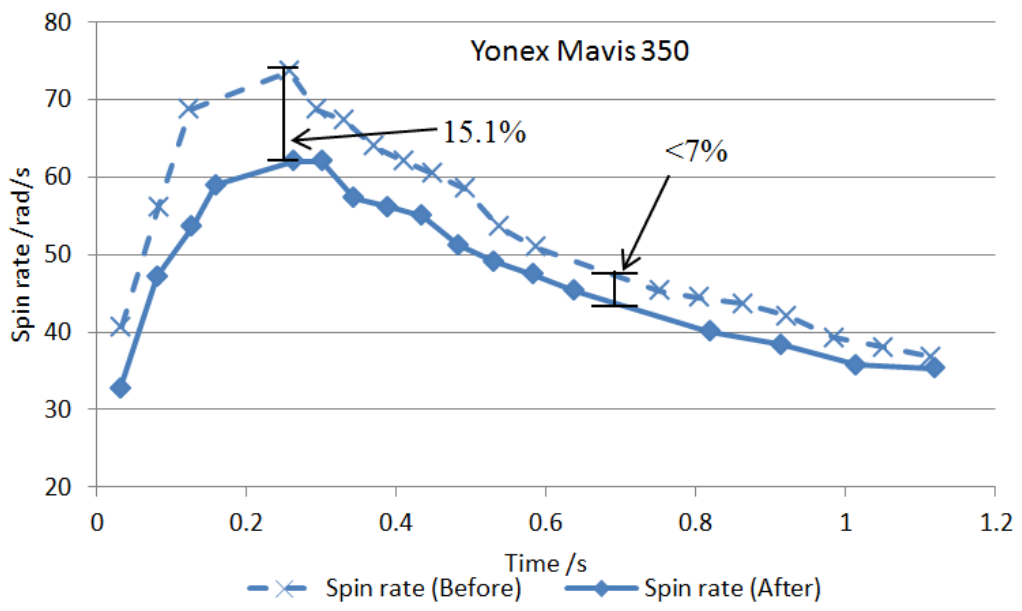


Figure 137 Spin rate profiles of the Yonex Mavis 350 synthetic shuttlecock

## 7.6 Summary

In this chapter, the mechanical strength of the shuttlecock skirt was evaluated. It was discovered that the tournament-grade feather shuttlecocks had very high skirt stiffness. The practice-grade feather shuttlecocks and synthetics had significantly lower skirt stiffness which led to larger skirt compression.

Two methods of wear induction were also developed. The first method was the VWID which induced wear on the feather vane. The second method applied the modified shuttlecock launcher as a smash test machine. Preliminary trials with the two methods demonstrated that the tournament-grade shuttlecocks were able to better resist damage than the lower-grade ones.

The wear induction methods were then applied to the shuttlecock specimens that were evaluated in Phase II of the shuttlecock testing (chapter 6). Flight performance of these specimens was evaluated again after the VWID and STM processes. The flight performance degradation was observed by comparing the flight difference before and after the wear induction processes. The tested tournament-grade shuttlecocks exhibited the least degradation in flight performance. This meant that the tournament-grade shuttlecocks had the best durability.

## 8. SHUTTLECOCK DEVELOPMENT PROCESS

### 8.1 Overview

The shuttlecock development process consists of conceptualisation and development. The conceptualisation process applied for the ISR shuttlecock development projects is presented in Figure 138. This conceptualisation process model is not badminton specific and can be applied to development of other products. The various components of this model are discussed in detail in this chapter. Upon the selection of the most promising or the preferred concept, the concept is developed into prototypes and then the product.



Figure 138 Conceptualisation process model applied for shuttlecock development.

For the shuttlecock development industrial projects supported by work from this thesis, a shuttlecock development process model was developed and it is presented in Figure 139. This development process model consists of a design phase and a testing phase. In the design phase, virtual prototyping techniques were used in place of traditional physical prototyping to speed up the development process. Upon the derivation of a satisfactory model, functional prototyping and testing begins. The three phase shuttlecock evaluation framework was used for obtaining scientific numerical data of the actual prototype. Player perception study of the prototype was then conducted for qualitative feedback. If the test results are acceptable, the design is accepted and manufacturing process will be developed.

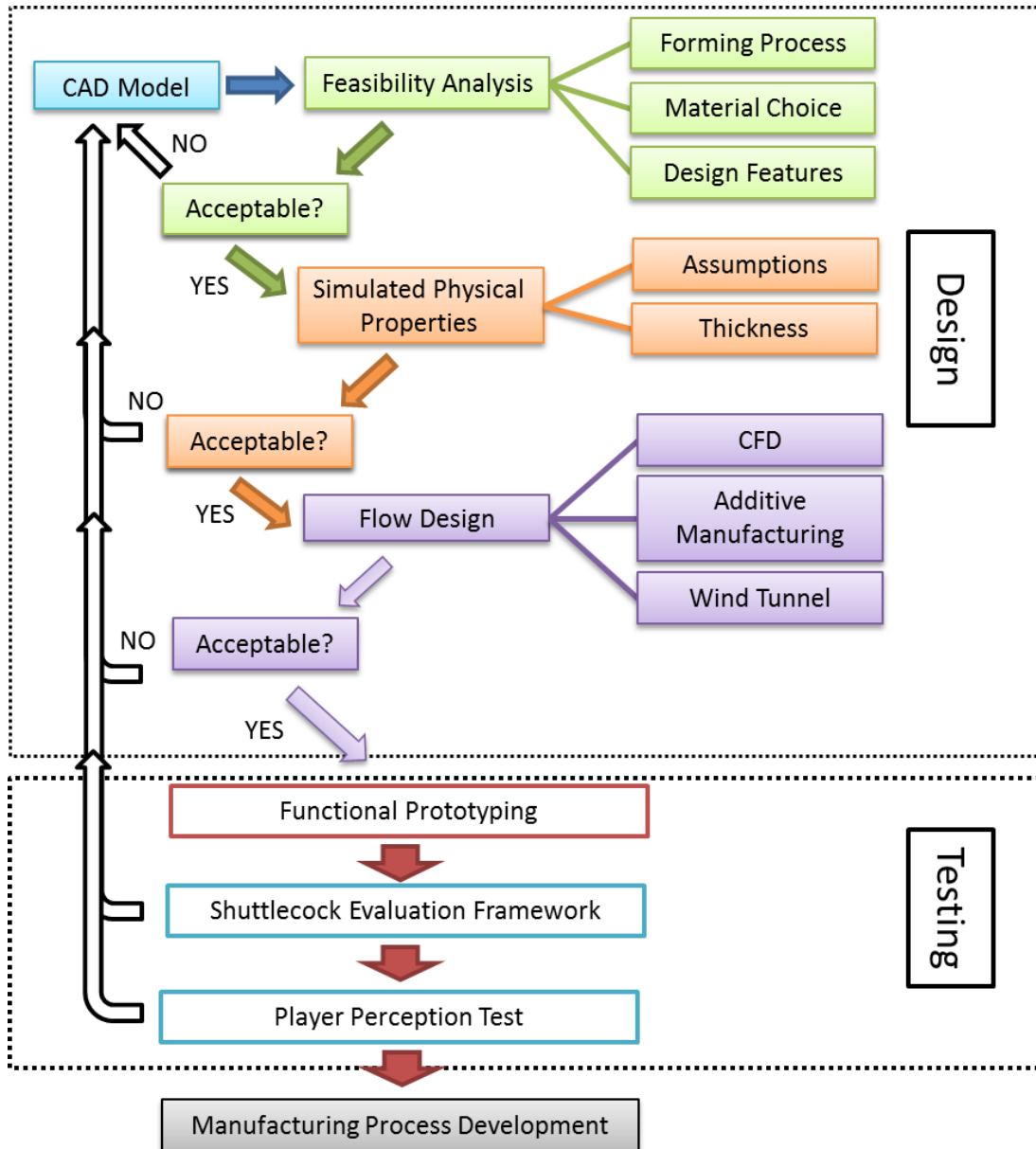


Figure 139 The developed shuttlecock development process model that involves design and testing.

## 8.2 Design Objectives

The key considerations are listed and ranked in the stage of defining the design objectives. These objectives are usually derived from the problem statement in the project. For instance, if the motive behind the development of a synthetic shuttlecock lies in the durability and inconsistent supply of the current feather shuttlecocks, then the objective may be increased durability through an artificial shuttlecock without

sacrificing flight performance. Through the key considerations, tolerable ranges of parameters are defined to form the target project specifications. For the badminton shuttlecocks, these can be the weight,  $\frac{SCd}{m}$  or material usage. An example of the shuttlecock qualitative considerations being translated to quantitative project specifications is shown in Figure 140.

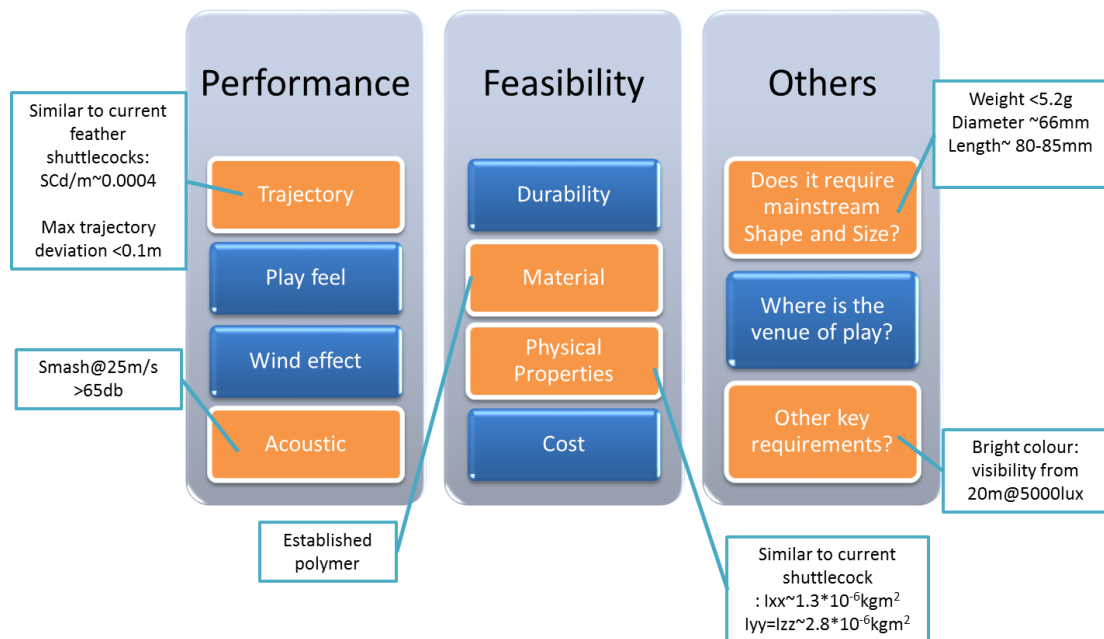


Figure 140 Key considerations (qualitative) translated to target project specifications (quantitative).

### 8.3 Conceptual Design

The concepts generated in the conceptual design phase are early stage ideas that are inspired by the design objectives. These concepts are not based on scientific evidence, nor are they proven to work. In this conceptual design phase, the idea should not be constrained by external factors such as feasibility or cost. Concept generation should involve a team that consists of members from different field. For instance, concept development for badminton shuttlecock can involve a composite engineer or an electronic engineer. This is because members outside of the field are

able to approach the design from different angles and are less constrained by the practicality issues which tend to impede creative development.

The focus in this phase is to justify the concepts based on the developed objectives using instinct. For example, if the objective is shuttlecock weight minimisation, then a thin-walled structure with large proportion of gaps can be justified. If the objective is an increase in spin rate, then the concept may hover around the altering of the skirt folds or even the addition of propeller blades within the skirt. The underlying principle to a revolutionary design is that no proposition is too radical.

Before proceeding to the next phase, the generated concepts should be listed, sorted and filtered. Similar concepts are grouped and integrated. Three to five concepts are then chosen from the list based on the “potentials” of the design. These “potentials” for a shuttlecock design include performance, marketability, technical feasibilities, owned technology and possible infringement on existing intellectual properties (IP).

#### **8.4 Preliminary Concept Exploration**

The objective of the preliminary exploration is to gather information to aid the concept selection process in the next phase. Therefore, this stage of concept exploration can involve hard model prototyping for visual purpose, some brief analysis on functionality and discussions among the stakeholders. An example of the work process used for the preliminary concept exploration in shuttlecock development is shown in Figure 141.

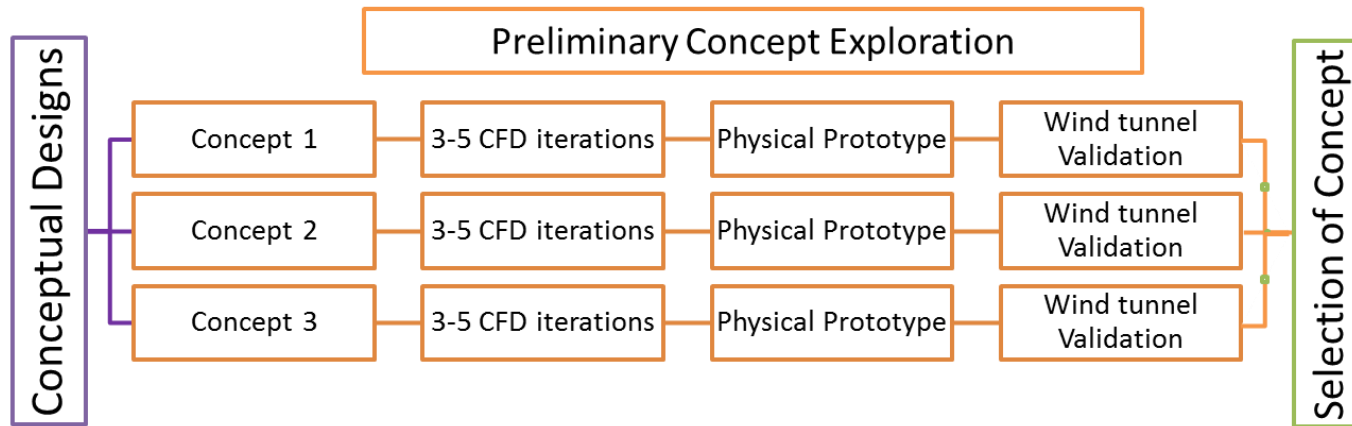


Figure 141 Work process of preliminary concept exploration.

The work process in Figure 141 can be changed according to focus and purpose. In this example, the objective was exploring feasibility of various geometries as a substitute for the conical shape of a shuttlecock. Therefore, the early CFD iteration determined the preliminary dimensions and performance of each concept. Physical prototypes were built using a combination of hand crafting and additive manufacturing. The prototypes were then used to validate the CFD work and to communicate the idea to the client.

### **8.5 Concept Selection**

Concept selection was achieved through usage of evaluative tools such as the Pugh matrix (decision matrix method) or the requirement feature matrix. Table 33 shows an example of the Pugh matrix approach which was applied. The functionality column was translated from the project specifications with the addition of other parameters. These included performance, market acceptability, cost and technical feasibility in fabrication. The decision on concept choice was then made using the net score. However, it should be noted that there are instances where the second or third ranking concept may be selected because of the prominence of form over function.

Table 33 The Pugh Matrix used for preliminary shuttlecock concept development.

Functionality	Feather Shuttlecock (Current)	Concept 1	Concept 2	Concept 3	Concept 4	Concept 5
Drag	0	2	0	2	1	2
Side Force	0	1	1	2	1	0
SCd/SC Ratio	0	1	0	2	1	1
Durability	0	0	2	-1	0	-1
Stability	0	1	-2	-1	0	1
"Hit Zone"	0	1	2	1	1	0
Net		6	3	5	4	3

### 8.6 Concept Development- Design

The selected concept was developed and optimised in the concept development phase, following the process that was outlined in Figure 139. The specification of the design concept can be simulated through the processes that are described in section 8.6.1 to 8.6.3. The feasibility analysis ensures that the design is feasible with existing technology. Through virtual prototyping, simulation of physical properties and flow ensures that CAD design fulfils the requirement physically and aerodynamically.

The end result is a tabulation of the simulated specifications of the design iterations. An example is presented in Table 34. Through this table, improvements with each iteration can be traced. The design shortfalls can also be identified for correction in the subsequent iterations.

Table 34 Sample virtual prototyping specification iteration table.

	Cork /g	Skirt /g	Total /g	C.G. /mm	Ixx /kgm <sup>2</sup> /10 <sup>-6</sup>	Iyy Izz /kgm <sup>2</sup> /10 <sup>-6</sup>	$\frac{SCd}{m}$ /m <sup>2</sup> /kg
Target	2.3	2.7	5	~ 28.5	1.2	2.9	0.000405
V1	2.4	3.1	5.5	30.5	1.3	4.5	0.000391
V2	2.2	2.7	4.9	29.1	1.2	3.1	0.000385
V3	.	.	.	.	.	.	.
.	.	.	.	.	.	.	.
.	.	.	.	.	.	.	.
.	.	.	.	.	.	.	.
.	.	.	.	.	.	.	.

### 8.6.1 Feasibility Analysis

In the first step of the design phase, feasibility analysis is carried out for various considerations in the following order:

- Material selection: The exact material need not be defined, but the material family must be decided. For example, the material can be a low density expanded polymer or a medium density polymer.
- Fabrication process: Based on the selected materials, an appropriate method of fabrication can be decided on.
- Feature size and feasibility: From the fabrication process, feasibility of the geometry will be studied. These may include the reproducibility of micro features and the consideration of ease in moulding and tooling.

- Assembly: Post-fabrication assembly is usually required for shuttlecocks because multiple part designs may reduce fabrication cost. The assembly method should be simple and strong because large impact forces are imparted onto the shuttlecock at play.

The design requires modification when the considerations are not satisfied. This is to ensure that the eventual optimised virtual prototype is a feasible design that can be fabricated as a functional product.

### **8.6.2 Physical Properties Simulation**

The physical properties of the shuttlecock can be simulated through CAD software such as Solidworks<sup>TM</sup>. Although the exact material composition is not defined in this phase, the density is assumed from the material category. For instance, a thin-walled polymer skirt may comprise of a rigid polymer of  $1.2 \text{ g/cm}^3$ , while a flexible foam skirt structure will likely be constructed of expanded polymer with density in the region of  $0.06 \text{ g/cm}^3$ . By applying the densities of the selected material groups, mass properties such as the mass, moments of inertia and centre of gravity can be calculated. Examples of the mass properties in iterations can be seen in Table 34.

In the shuttlecock development, the mass properties were kept as close to the target value as it was possible. This was because these were important parameters that affected the flight performance and the resultant target aerodynamic parameters. However, it was recognised that the mass properties would change accordingly with the changes in skirt features that were made to achieve the desired flight performance. Therefore, unlike the phase of feasibility analysis (8.6.1), the CAD designs which showed some deviations from the project specifications would still

progress on to the flow design (8.6.3) phase. The approach taken was a concurrent analysis of physical properties and aerodynamic performance with minor alteration to the features in each iteration.

### **8.6.3 Flow Design**

This phase of flow design applied CFD simulation in design analysis and additive manufacturing in design validation. For this work, Ansys<sup>TM</sup> CFX<sup>TM</sup> was used for flow simulation to obtain the drag force, the lift and side force, the spin torque and the pitching moment. The general simulation framework followed the methodology that was described in chapter 3, where RANS was applied to an unstructured mesh of tetrahedrals with prism layers. Since mesh (volume) size requirement is highly dependent on the geometry and the feature size, the number of volumes applied in Table 6 can only be applied as an initial guess. For quick design iterations, the shuttlecock model was assumed to have air-speed independent aerodynamic coefficients in the range of operating air speeds. Therefore, the simulation was conducted with only one flow speed in the early phase of simulation. The basis was discussed in section 2.3 and further verified in section 3.3. A more thorough simulation involving various air speeds and angles of attack was conducted when the design was more matured.

After the CAD design performance has been proven through simulation, design validation was done through wind tunnel testing of additive manufactured prototypes, such as the example shown in Figure 142. As shuttlecocks are usually light weight thin-walled structures, the skirt was thickened in the CAD file prior to the fabrication of the prototype. This helped the shuttlecock in resisting skirt

deformation at high flow speed. Additive manufactured shuttlecock prototypes were unlikely to be playable but they provided information on the validity of the simulations.

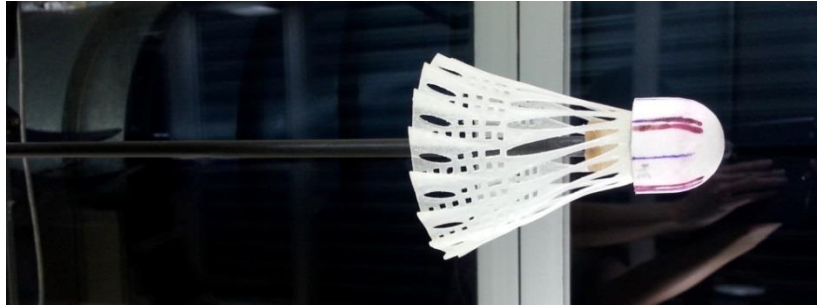


Figure 142 Additive manufactured shuttlecock prototype in the wind tunnel for design validation [125].

### **8.7 Concept Development- Testing**

When the validation work is satisfactory, the concept is developed into a functional prototype. The possible skirt fabrication methods include injection moulding, compression moulding, vacuum forming and autoclave moulding. The motive in this phase is to obtain a prototype that is as anticipated in the design and to identify technical difficulties in fabrication.

The functional prototype was then tested with the shuttlecock evaluation framework that was described in chapter 5 to 0. The system of testing provides a methodology to evaluate the prototype performance through collecting performance indicators that cannot be estimated in the virtual prototyping phase. These are the turnover response, skirt stiffness and the play durability. Through the results, refinements were made to the design. In the last phase of testing, a perception study was conducted with players to evaluate the tactile responses that were not accounted for in the current evaluation framework. This is an important component in the final

evaluation of a badminton shuttlecock because the success of such product was largely driven by fulfilment in the user experience. The perception testing also marked the end of the shuttlecock development process and the start of the manufacturing process development where the result was translated to an actual product.

### **8.8 Advantages**

The major advantage of the described shuttlecock development process is the reduction in time and resources required. The application of virtual prototyping with CAD and CFD greatly reduces the lead time in the design stage. By using additive manufacturing to build prototypes for the validation of the early virtual prototypes, the iterations of the costly moulding process can be delayed and reduced. The launch of a new physical mould for prototyping is only conducted when the design is sufficiently matured. Therefore, wastage in time and money for mould and tooling can be minimised. This approach of a validated virtual prototype also reduces the testing burden.

In the projects supported by this thesis, CFD proved to be an invaluable tool for the stakeholders. The CFD results help the engineers to analyse the issues and aid the industrial designers in understanding the fundamental flow needs. It also provides the clients, who are often not from engineering background, a visualisation tool to understand the work done. This proved to be crucial in building confidence between the engineering firm and the client.

## 8.9 Limitations

The limitation in the described shuttlecock development process is the increased element of unknown prior to the availability of a functional prototype. Although the virtual prototyping process provides more information on the flight performance than an equivalent wind tunnel evaluation, the current methodology does not account for structural or peripheral performance. With the applied process, properties such as skirt stiffness and impact vibration feedback cannot be evaluated till a functional prototype is available. In contrast, functional prototypes are fabricated much earlier in the traditional method of shuttlecock development. This provides insight on tactile properties that are not simulated in the process model described in this thesis.

However, just like the tradition method of development, any deficiency in structural or peripheral performance with the described process is also detected in the first iteration of functional prototyping. Therefore, actual lost due to this limitation is the effort in the virtual prototyping and not in the tooling or moulding.

The cost of the virtual prototyping tools may also be a limitation. Despite advancements in these tools, the virtual prototyping software products are expensive. The cost has become prohibitive to acquire a software license for lower value sport products, unless there are applications across a wide product range. As an example, the yearly commercial license for the Ansys CFX suite is approximately US\$ 56,000- about half the budget for a year-long shuttlecock development project at ISR.

## **8.10 Summary**

In this chapter, the work flow in shuttlecock development was documented with samples of the tools that were used in decision making. The development process started out with identifying the project specifications from the problem statement. Concepts were then conceived and explored to best fulfil the objectives. Based on a decision making tool, such as the Pugh Matrix, one of the concepts was developed into further design. The design stage consisted of three stages: The feasibility analysis, the physical properties simulation and the flow design. Iterations of the design were proposed to be done through the virtual prototyping tools and then validated with additive manufactured prototypes. Upon obtaining a satisfactory performing shuttlecock design, functional prototypes were fabricated for testing with the developed shuttlecock evaluation framework. Finally, perception study was conducted for feedback from players. With positive perception feedback, the design development would transit to development of production method.

## 9. CONCLUSION AND RECOMMENDATIONS FOR FUTURE WORK

### 9.1 Conclusion

The research has fulfilled the objectives that initiated this project: the work was developed into a novel testing framework for badminton shuttlecocks; an original 6 DOF flight model was formulated and was then applied to explain the fundamental flight phenomena of the shuttlecock; and a shuttlecock development process was put together. The main contributions of this research are as follows:

- 1) A three phase shuttlecock evaluation system has been developed. The comprehensiveness of this evaluation system has never been proposed or attempted in the work found in the open literature. In addition to the testing of the shuttlecocks in brand new condition, the test system also took a novel approach in shuttlecock wear analysis by developing two sets of unique wear induction methods. This was a major step forward in comparing shuttlecock durability—a topic that has never been studied in scientific literatures—between the various grades of shuttlecocks. The evaluation framework and the results presented will be very useful for future shuttlecock development work.
- 2) The formulated 6 DOF equation of motion was instrumental in explaining the various flight phenomena associated with the shuttlecock flight. These included the turnover, the axial spin and the gyroscopic effect. The knowledge derived from the understanding of these phenomena was immensely significant and important for designing a good synthetic

shuttlecock. This was because they provided information on the importance of each of the design parameters.

- 3) The successful demonstration of implementing the development process to shuttlecock is a significant contribution to shuttlecock design work. With the inclusion of virtual prototyping tools that were made possible by technological advancement, the presented process achieved significant saving in time and resources required for new prototype development. The systematic process also provided more information to the designer and reduced the number of unknown in the later stage of development.

### **9.1.1 Shuttlecock Evaluation Framework**

A three phase shuttlecock evaluation framework was developed and applied to various shuttlecocks. Phase I and phase II were non-destructive evaluation of the shuttlecock that included the physical properties and flight performance, while Phase III consisted of destructive testing to evaluate the durability of the shuttlecock. The wear induction machines and the subsequent analysis were novel approach to durability in the field of badminton shuttlecocks. Moreover, the results from all the three phases of testing were significant contribution to knowledge of badminton flight.

From the measurements in phase I, it was observed that the tested feather and synthetic shuttlecocks had similar physical properties. A new and original alternative to grain-weight speed rating was proposed and justified. The wind tunnel test suggested that the synthetic shuttlecocks had higher air resistance in flight and this was confirmed by the experimental data in phase II.

In phase II, the turnover performance of feather and synthetic shuttlecocks were experimentally evaluated and then analysed using a 2<sup>nd</sup> order approximation. This is an original approach to the shuttlecock turnover and it is much more useful than the prior judging methods. It was observed that the feather shuttlecocks had higher damping factor which improved the turnover performance. Testing the steady-flight state with various grades of shuttlecocks, including the BWF approved tournament-grade ones, the practice feather shuttlecocks and the synthetics, it was observed that difference in flight trajectory was negligible. The obtained linear velocity profiles and post-vertex trajectories were similar. This research has scientifically shown that post-vertex drop quality of the tested synthetic shuttlecock was not inferior to the feather shuttlecocks. Moreover, the synthetic shuttlecocks had higher spin rate than the feather shuttlecocks in the post-vertex region and this would have increased the gyroscopic aided change in pitch angle. Therefore, from an aerodynamic point of view, the synthetic is not inferior to the feather shuttlecock in flight trajectory.

The novel durability study in phase III showed that the tested tournament-grade shuttles had less performance degradation than the practice-grade feather shuttles. The better shuttlecocks were able to resist the induced smash damage and the vane wear. Flight performance study was used to investigate the post-wear flight performance. Taking the durability advantage into account, the additional cost of tournament-grade feather shuttles may be offset by the increased serviceable life. In addition to better durability, the evaluated tournament-grade feather shuttlecocks also demonstrated significantly higher skirt stiffness. It is thus possible that the feedback from the racket will be different in play.

### **9.1.2 Flight Modelling**

Using segments of the developed 6 DOF flight equation model, the three phenomena associated with the shuttlecock flight were described and modelled. The damped angular motion of the shuttlecock was explained using the experimental data. Through identification and validation with experimental data, the underdamped turnover behaviour was modelled through the 2<sup>nd</sup> order transfer function approach. It was shown that study of axial spin should be conducted through actual flight measurements because spin rates observed in the wind tunnel were unlikely to occur in flight. The delay in spin acceleration and deceleration created very different spin profiles for the different tested shuttlecocks during the Phase II testing. These spin profiles would have never been noticed using the traditional method of wind tunnel steady-state spin measurement. Spin-induced precession was also modelled and simulated with experimental data. It was observed that a reversed precession model was able to predict the motion.

### **9.1.3 Rapid Design iteration**

A shuttlecock development process integrating virtual prototyping tools was presented. The development process started with the conceptualisation and ended with transition to development of manufacturing process. Using the virtual prototyping tools and additive manufacturing, the development time of each iteration is greatly shortened. With application of CAD and CFD, cost and effort in moulding was greatly reduced during the design phase. Applying additive manufacturing to design validation also eliminated the need of a costly mould. This approach meant that moulding was not required till the design have been established and matured.

The testing process applied the developed shuttlecock evaluation framework to evaluate the prototypes, showing the importance and significance of the experimental work in chapters 5 and 6.

## **9.2 Future Work**

### **9.2.1 Improvement to Motion Capture**

In the current work, experimental data for study of the flight phenomenon were obtained through digitising the high-speed videos. The high-speed video method has the advantage of minimal weight addition to the shuttlecock. However, the obtained position coordinates tend to be less reliable than a proper marker tracking system. The effort required in data extraction is also more intense with high-speed videos. Therefore, it is proposed that the subsequent work on flight phenomenon be attempted with reflective marker tracking system, such as that from Vicon<sup>TM</sup> or Cortex<sup>TM</sup>. This can be achieved on a shuttlecock by applying reflective tape along the whole cork surface to utilise the cork as a whole marker. Angular information of the shuttlecock should still be recorded through the high-speed videos. The approach increases the precision in position measurements while reducing the post-processing effort.

### **9.2.2 Perception studies**

The testing framework developed in this thesis is only capable of identifying differences between the various shuttlecocks through the experiments. However, it is possible that the human perception may not be able to accurately identify minor differences between various shuttlecocks. The observable responsiveness effect means that shuttlecocks with some deviations from the reference feather shuttlecocks

may still be acceptable. For instance, a 10% increase in turnover oscillation amplitude, which can be captured by the high-speed cameras, may not be detected by the human players. Therefore, it is proposed that an acceptance level be implemented into the testing framework through player perception studies, thereby increasing the test comprehensiveness and reducing the testing effort.

The effect of perception can also be extended to include the correlation between the intensity of play and feedback perception. While the experimental results in this thesis has shown that the various shuttlecocks have very similar flight performance, it is unclear if this difference will be observed to actual shuttlecock play at the field. This is because the experiments compared the shuttlecocks by launching them with the exact same conditions. In the field usage of the shuttlecocks, it might be possible that change in visual perception, psychological perception or racket vibration feedback will result in varying intensity of play. This will mean that the shuttlecocks may have different performance in field testing because the players are hitting a particular type of shuttlecock harder or softer. This is a real problem and it is highly likely that it can affect players at all levels.

### **9.2.3 Spin Effect on Skirt Deformation**

The wind tunnel experiment showed that the centrifugal force from spin was able to prevent the skirt from shrinking at high flow speeds. It is possible that spin can be applied to resist deformation on skirt with lower stiffness, such as the tested synthetic shuttlecocks. Skirt shrinkage reduces the linear deceleration while skirt expansion increases the linear deceleration. Investigation on the effect of spin on

skirt deformation will be beneficial in defining the required skirt stiffness and spin rate in future shuttlecock designs.

#### **9.2.4 Racket-Shuttlecock Impact Mechanism**

The skirt stiffness measurements have shown that a large variation in strength exists between the various tested shuttlecocks. Considering the amount of skirt deformation that occurs upon impact, it is likely that the impact response of the feather shuttlecocks will be significantly different from the much softer synthetic skirts. It is proposed that the effect of skirt stiffness on the racket vibration, the acoustic feedback and the coefficient of restitution be studied. In the experiment in phase II, it was also observed that the tested synthetics required significant adjustments to the launcher for the same launch velocities. It is possible that this was attributed by the difference in impact mechanism between the different types of shuttlecocks. A better understanding in racket-shuttlecock interaction can aid the synthetic shuttlecocks in emulating the post-launch behaviour of the feather shuttlecocks.

#### **9.2.5 Extension to Shuttlecock Development Process**

In the shuttlecock development process that was outlined in chapter 8, virtual prototyping was applied in the means of CAD design and flow simulation. In this work, flow simulation was mainly used to predict the performance of the steady flight state. For performance estimation of the unsteady flight state (turnover), analysis was conducted through multiple cases of steady state simulation. At the current state of development with commercial flow simulation software package, it is actually possible to simulate the transient angular behaviour of the shuttlecock in

the unsteady flight state. This means that the angular behaviour and the aerodynamic parameters on the whole unsteady flight state can be obtained with a single simulation case. For instance, in the ANSYS™ CFX™ suite, the function that can be used is the rigid body simulation with multiple frames of reference. The technical difficulty at current stage is the staggering amount of computational capacity required over multiple steady state cases. Since the computational capacity of computers is ever increasing, it is expected that this approach of a single transient simulation case will be feasible in the near future.

The purpose of the integration of virtual prototyping tools was to reduce labour intensity required for product development. Through working with industry partners, it was noticed that many matured engineering and product development tools have not been adopted by the industry. This is especially so for the designers of consumer products with lower-value and tighter production planning schedule. Therefore, it is hoped that more tools can be integrated into the development process to reduce the iteration burden.

### **9.3 Publications**

#### **9.3.1 Journal Papers**

Lin, C.S.H., C.K. Chua, and J.H. Yeo, *Design of high performance badminton shuttlecocks; virtual and rapid prototyping approach*. Virtual and Physical Prototyping, 2013. **8**(2): p. 165-171.

Lin, C.S.H., C.K. Chua, and J.H. Yeo, Aerodynamics of badminton shuttlecock: Characterization of flow around a conical skirt with gaps, behind a hemispherical

dome. *Journal of Wind Engineering and Industrial Aerodynamics*, 2014. **127**: p. 29-39.

Lin, C.S.H., C.K. Chua, and J.H. Yeo. *Analysis and simulation of badminton shuttlecock flight through parameter identification of a slow-speed serve shot*. *Proceedings of the Institution of Mechanical Engineers, Part P: Journal of Sports Engineering and Technology*, 2015. (In print)

Lin, C.S.H., C.K. Chua, and J.H. Yeo. *Badminton shuttlecock stability: Modelling and simulating the angular response of the turnover*. *Proceedings of the Institution of Mechanical Engineers, Part P: Journal of Sports Engineering and Technology*, 2015. (Under review)

### **9.3.2 Conference Papers**

Lin, C.S.H., C.K. Chua, and J.H. Yeo, Turnover stability of shuttlecocks- Transient angular response and impact deformation of feather and synthetic shuttlecocks, in 6th Asia-Pacific Conference on Sports Technology. 2013, Elsevier: Hong Kong. p. 106-111.

Lin, C.S.H., C.K. Chua, and J.H. Yeo. *Designing a badminton shuttlecock; validation of virtual design by 3d printed thin-walled functional prototype*. in 1st International Conference on Progress in Additive Manufacturing (Pro-AM 2014) 2014. Singapore. p.370-375.

Lin, C.S.H., C.K. Chua, and J.H. Yeo. Comparative analysis of badminton shuttlecock speed and spin rate through flight measurement with high-speed

cameras. 1<sup>st</sup> International Conference in Sports Science & Technology, 2014.  
Singapore.

## REFERENCES

---

1. Datamonitor, *Sports equipment industry profile: US region, 2003-2012*: New York, USA.
2. Datamonitor, *Sports equipment industry profile: Asia-Pacific, 2003-2012*: Sydney, Australia.
3. Datamonitor, *Sports equipment industry profile: Europe, 2003-2012*: London, United Kingdom.
4. Datamonitor, *Sports equipment industry profile: Global, 2003-2012*: New York, USA.
5. Zeng, Y.B., K.Y. Li, and H.Q. Zeng, *Current situation of individual badminton sports in guangzhou*. Journal of PLA institute of physical education, 2007(4): p. 29-31.
6. Chen, W.F., *Investigation and research on the mass badminton sport in the city proper of nanning*. Sport science and technology, 2007(2): p. 72-74.93.
7. Liu, L.Y. and W. Liu, *Investigation of the consumption situation of entertainment group in badminton in Xi'an*. Journal of Xi'an university of arts and science (Natural science edition), 2010(1): p. 121-125.
8. Yan, Y.N. and S.X. Chen, *Relationship between factos forming urban residents consumption behavior on badminton*. Journal of Beijing sport university, 2009(1): p. 8.

9. Meng, L.C. and D.Y. Kong, *Investigation and analysis of participants in badminton sports in hefei*. Journal of Anhui sports science, 2009(3): p. 18.
10. Lim, P.H. and S.A. Mohd, *The development of badminton as a globalised game and the dominance of Chinese and Korean female badminton players and teams in Uber Cup competitions and the Olympic Games: challenges for ASEAN countries to improve elite badminton training to compete and overcome these leading players and teams*, 2012, University of Malaya.
11. Hakuho, I., *Sports Popular in 14 Asian Countries*, in *Global HABIT2012*, Hakuho Inc.: Japan.
12. Snehartha. *Indian badminton in a state of crisis due to shuttlecock shortage*. 2014 [cited 2014 14th Aug]; Available from: <http://www.sportskeeda.com/badminton/indian-badminton-in-a-state-of-crisis-due-to-shuttlecock-shortage>.
13. Ghosal, S. *Drying ponds make an industry sitting ducks*. 2014 [cited 2014 14th Aug]; Available from: <http://mobileet.timesofindia.com/mobile.aspx?article=yes&pageid=14&sectid=edid=&edlabel=ETKM&mydateHid=28-12-2012&pubname=Economic+Times+-+Kolkata&edname=&articleid=Ar01400&publabel=ET>.
14. KPPU *OECD Competition Assessment Toolkit: Case of Indonesia in Shuttlecock Industry*. 2009.
15. Hunter, T. *Sports desk shorts*. 2006 [cited 2014 14th Aug]; Available from: [http://www.crikey.com.au/2006/08/04/sports-desk-shorts/?wpmp\\_switcher=mobile](http://www.crikey.com.au/2006/08/04/sports-desk-shorts/?wpmp_switcher=mobile).

16. *Bird flu affects badminton*. 2008 [cited 2014 8th Aug]; Available from: [http://newsagency.thecheers.org/Health/news\\_12387\\_Bird-flu-affects-badminton.html](http://newsagency.thecheers.org/Health/news_12387_Bird-flu-affects-badminton.html).
17. Carlton, W.C., Shuttlecock with blade-like stems, 3313543. 1967: England.
18. Cooke, A.J. and J. Mullins, *The flight of the shuttlecock*, in *New Scientist* 1994. p. 40.
19. Le Personnic, J., F. Alam, L. Le Gendre, H. Chowdhury, and A. Subic, *Flight trajectory simulation of badminton shuttlecocks*. *Procedia Engineering*, 2011. **13**: p. 344-349.
20. Alam, F., H. Chowdhury, C. Theppadungporn, H. Moria, and A. Subic, *A comparative study of feather and synthetic badminton shuttlecock aerodynamics*, in *17th Australasian fluid mechanics conference* 2010: Auckland, New Zealand.
21. Gordon, W. *Bird2 shuttlecock*. 2014 [20/5/2014]; Available from: <http://www.birdsports.net>.
22. Cooke, A.J., *The aerodynamics and mechanics of shuttlecocks*, in *Department of Engineering* 1992, University of Cambridge: New hall, Cambridge.
23. Cooke, A., *The aerodynamics of shuttlecocks*, in *10th Australasian fluid mechanics conference* 1989: University of Melbourne, Australia.
24. Frank, M.H., A.J. Cooke, and R.S. Cant. *Computational fluid dynamics of a shuttlecock*. in *3rd Conference Engineering of Sport* 2000. Sydney, Australia: Blackwell Science.

25. Cooke, A.J., *Computer simulation of shuttlecock trajectories*. Sports engineering ( International sports engineering association), 2002. **5**(2): p. 93-105.
26. Cooke, A., *Shuttlecock aerodynamics*. Sports engineering ( International sports engineering association), 1999. **2**: p. 85-96.
27. Cooke, A.J., *Shuttlecock design and development*, in *Sports engineering- Design and development*, 1996, Blackwell Science: Balkeman, Rotterdam. p. 91-95.
28. Alam, F., H. Chowdhury, C. Theppadungporn, and A. Subic. *A study of badminton shuttlecock aerodynamics*. in *International conference on mechanical engineering 2009*. 2009. Dhaka, Bangladesh.
29. Alam, F., H. Chowdhury, C. Theppadungporn, and A. Subic, *Measurements of aerodynamic properties of badminton shuttlecocks*. Procedia Engineering, 2010. **2**(2): p. 2487-2492.
30. Alam, F., H. Chowdhury, C. Theppadungporn, A. Subic, M. Masud, and K. Khan, *Aerodynamic properties of badminton shuttlecock*. International journal of mechanical and materials engineering, 2009. **4**(3): p. 266-272.
31. Hasegawa, H., S. Kitta, M. Murakami, and S. Obayashi, *Flow analysis and aerodynamic characteristics of a badminton shuttlecock with spin at high Reynolds numbers*. Sports Engineering, 2013. **16**(2): p. 91-98.
32. Kitta, S., H. Hasegawa, M. Murakami, and S. Obayashi, *Aerodynamic properties of a shuttlecock with spin at high Reynolds number*. Procedia Engineering, 2011. **13**: p. 271-277.

33. Nakagawa, K., H. Hasegawa, M. Murakami, and S. Obayashi, *Aerodynamic Properties and Flow Behavior for a Badminton Shuttlecock with Spin at High Reynolds Numbers*. Procedia Engineering, 2012. **34**: p. 104-109.
34. Texier, B.D., C. Cohen, D. Quéré, and C. Claneta, *Shuttlecock dynamics*. Procedia Engineering, 2012. **34**: p. 176-181.
35. Cohen, C., B. Darbois-Texier, G. Dupeux, E. Brunel, D. Quere, and C. Clanet, *The aerodynamic wall*. Proceedings of the Royal Society A: Mathematical, Physical and Engineering Sciences, 2013. **470**(2161): p. 20130497.
36. Foong, S.K. and J.C.C. Tan, *Trajectories of feather and plastic shuttlecocks*. The impact of technology on sport II, 2008. **2**: p. 449-454.
37. Foong, S.K., J.C.C. Tan, S. Veluri, and S. Sachdeva, *Testing of badminton shuttles with a prototype launcher*. The impact of technology on sport II, 2008. **2**: p. 443-448.
38. BWF, *BWF equipment approval scheme*. 1988.
39. Studer, W.J., Design for a badminton shuttlecock, USD148732 S. 1948: US.
40. Hart, J.H., S.G. Wood, and N. Hamilton, Shuttlecock, WO2013005044 A1. 2013:
41. Brandes, U.W., Shuttlecock, US20110034277 A1. 2011: US.
42. Brandes, U.W., Shuttlecock, US20060199683. 2006: US.

43. SpeedmintonGmbH. *Speedminton* 2014 [cited 2014 22/4/2014]; Available from: [www.speedminton.com](http://www.speedminton.com).
44. Tsung, L.W., Shuttlecock with luminescent means, US5562290. 1996: US.
45. Peterson, S.T., Racquet sport game and shuttlecock for use therewith, US6709353. 2004: US.
46. Jong, H.R., Shuttlecock, WO2010021497. 2010:
47. York, k.R., Shuttlecock-type game ball and method of manufacturing same US20100255939. 2010: US.
48. Chen, X., J. Liu, and X. Liu, Shuttlecock with replaceable feathers, WO2010075720. 2010:
49. Dai, J., A type of shuttlecock, WO2011020224. 2011:
50. Lee, J.S., Separable and fastenable badminton shuttlecock, WO2011046250. 2011: KR.
51. Kim, S.W., Badminton shuttlecock, WO2010008145. 2010: Korea.
52. Larsen, J.K., An artificial feather for shuttlecocks and method of manufacturing such a feather, WO1986002570. 1986:
53. Li, X.F., Badminton shuttlecock of artificial material, CN2226477 Y. 1996: China.
54. Hu, J.W., Badminton shuttlecock, CN2790531 Y. 2006: China.

55. Zhu, H. and B.J. Zhang, Composite shuttlecock, CN101810929. 2007: China.
56. Babolat, E., Shuttlecock and method of manufacture, WO2008099086. 2008: FR.
57. Eguchi, H., M. Ogawa, Y. Tonomura, and S. Yoshida, Artificial feather for shuttlecock, shuttlecock for badminton and manufacturing method for artificial feather and shuttlecock, WO2012133520. 2012:
58. Yoshida, S., M. Ogawa, and Y. Tonomura, Artificial feather for shuttlecock, badminton shuttle cock, and method for manufacturing the artificial feather and the badminton shuttlecock, WO2011021512 2011: JP.
59. Yoshida, S., M. Ogawa, Y. Tonomura, and T. Takenaka, Badminton shuttlecock, WO2010029914. 2010: JP.
60. Yoshida, S., M. Ogawa, Y. Tonomura, and T. Takenaka, Shuttlecock for badminton and base for shuttlecock, WO2010038657. 2010: JP.
61. Ogawa, M., T. Takenaka, Y. Tonomura, and S. Yoshida, Shuttlecock for badminton, WO2009088011 2009: JP.
62. Yoneyama, W., Artificial feather for shuttlecock, shuttlecock, and method for producing artificial feather for shuttlecock, WO2013027535. 2013: JP.
63. Miyazaki, S., K. Tanaka, and W. Yoneyama, Artificial feather for use in shuttlecock, shuttlecock, and method for producing artificial feather for use in shuttlecock, WO2012011498. 2012: JP.

64. Lin, C.S.H., C.K. Chua, and J.H. Yeo, *Turnover stability of shuttlecocks- Transient angular response and impact deformation of feather and synthetic shuttlecocks*, in *6th Asia-Pacific Conference on Sports Technology* 2013, Elsevier: Hong Kong. p. 106-111.
65. Li, X.P., D.S. Mao, and Z. Yaniv, Nylon based composites, US8,686,082. 2014: US.
66. Sato, M. and Y. Omori, Shuttlecock, WO201000473. 2010: JP.
67. Tanaka, K., Shuttle, WO2009069349. 2009: JP.
68. Gordon, W., Improvements in shuttlecocks, WO2008038040. 2008: GB.
69. Gordon, W., Shuttlecocks, WO96/31260. 1996: GB.
70. Verma, A., A. Desai, and S. Mittal, *Aerodynamics of badminton shuttlecocks*. *Journal of fluids and structures*, 2013. **41**: p. 89-98.
71. Calvert, J.R., *The seperated flow behind axially symmetric bodies*, 1967, Cambridge University: Cambridge, UK.
72. Passmore, M., D. Rogers, S. Tuplin, A. Harland, T. Lucas, and C. Holmes, *The aerodynamic performance of a range of FIFA-approved footballs*. *Proceedings of the Institution of Mechanical Engineers, Part P: Journal of Sports Engineering and Technology*, 2011. **226**(1): p. 61-70.
73. Hart, J., *Simulation and Understanding of the Aerodynamic Characteristics of a Badminton Shuttle*. *Procedia Engineering*, 2014. **72**: p. 768-773.

74. Ansys, I. *2013 ANSYS Hall of Fame Competition - Entry*. 2012 [20th Sep 2012]; Available from: <http://www.ansys.com/Hall+of+Fame>.
75. Chua, C.K. and K.F. Leong, *3D Printing and additive manufacturing: Principles and applications*. 4th ed. 2014, Singapore: World Scientific Publishing.
76. Chua, C.K., S.H. Teh, and R.K.L. Gay, *Rapid prototyping versus virtual prototyping in product design and manufacturing*. *Int J Adv Manuf Technol*, 1995. **15**: p. 597-603.
77. Celik, H.K., D. Karayel, N. Caglayan, A.E.W. Rennie, and I. Akinici, *Rapid prototyping and flow simulation applications in design of agricultural irrigation equipment: Case study for a sample in-line drip emitter*. *Virtual and Physical Prototyping*, 2011. **6**(1): p. 47-56.
78. Vinodh, S., S.R. Devadasan, S. Maheshkumar, M. Aravindakshan, M. Arumugam, and K. Balakrishnan, *Agile product development through CAD and rapid prototyping technologies: an examination in a traditional pump-manufacturing company*. *The International Journal of Advanced Manufacturing Technology*, 2009. **46**(5-8): p. 663-679.
79. Goubergrits, L., U. Kertzsch, B. Schoneberg, E. Wellnhofer, C. Petz, and H.C. Hege, *CFD analysis in an anatomically realistic coronary artery model based on non-invasive 3D imaging: comparison of magnetic resonance imaging with computed tomography*. *Int J Cardiovasc Imaging*, 2008. **24**(4): p. 411-21.

80. Markl, M., R. Schumacher, J. Kuffer, T.A. Bley, and J. Hennig, *Rapid vessel prototyping: vascular modeling using 3t magnetic resonance angiography and rapid prototyping technology*. MAGMA, 2005. **18**(6): p. 288-92.
81. Yang, T., R.A. Buswell, and M.J. Cook. *Exploring rapid prototyping techniques for validating numerical models of naturally ventilated buildings*. in *12th Conference of International Building Performance Simulation Association*. 2011. Sydney.
82. Goubergrits, L., S. Weber, C. Petz, H.-C. Hege, A. Spuler, J. Poethke, A. Berthe, and U. Kertzsch, *Wall-PIV as a near wall flow validation tool for CFD*. Journal of Visualization, 2009. **12**(3): p. 241-250.
83. Hu, L.H., X.Y. Zhao, W. Zhu, and F. Tang, *An experimental investigation and characterization on flame bifurcation and leaning transition behavior of a pool fire in near wake of a square cylinder*. International Journal of Heat and Mass Transfer, 2012. **55**(23-24): p. 7024-7035.
84. Chok, C., S. Parameswaran, R. Sun, and M. Gleason, *Numerical investigation of the effects of base slant on the wake pattery and drag of three-dimensional bluff bodies with a rear blunt end*. Journal of wind engineering and industrial aerodynamics, 1994. **51**: p. 269-285.
85. Murakami, S. and A. Mochida, *3-D Numerical simulation of airflow around a cubic model by means of the k-e model*. Journal of wind engineering and industrial aerodynamics, 1988. **31**: p. 283-303.

86. Stathopoulos, T. and Y.S. Zhou, *Numerical simulation of wind-induced pressures on buildings of various geometries*. Journal of wind engineering and industrial aerodynamics, 1993. **46 & 47**: p. 419-430.
87. Peastrel, M., R. Lynch, and J. Angelo Armenti, *Terminal velocity of a shuttlecock in vertical fall*. American journal of physics, 1979. **48**(7): p. 511-513.
88. McCreary, K.M., *A study of the motion of a free falling shuttlecock*, 2005, Physics department, The college of Wooster: Wooster, Ohio.
89. Shibata, M., P. Amornpatchara, and S. Sereeyothin, *Deceleration of a shuttlecock*. ISB Journal of physics, 2010. **4**(2).
90. Chen, L.M., Y.H. Pan, and Y.J. Chen, *A study of shuttlecock's trajectory in badminton*. Journal of sports science and medicine, 2009(8): p. 657-662.
91. Chan, C.M. and J.S. Rossmann, *Badminton shuttlecock aerodynamics: synthesizing experiment and theory*. Sports Engineering, 2012. **15**(2): p. 61-71.
92. Subramaniyan, R., *Effect of local conditions on the flight trajectory of an indoor badminton shuttlecock*, 2008: Bangalore, India.
93. Wang, M. *Shuttlecock speed*. Badminton alley's shuttlecock.com 2002 2nd Jan 2013]; Available from: [http://www.shuttlecock.com/Resources/Shuttlecock/speed\\_info.php](http://www.shuttlecock.com/Resources/Shuttlecock/speed_info.php).
94. Morgan, J.E. *The design and development of a shuttlecock hitting machine for training badminton players at all levels of the game*. in *First international*

*conference on the Engineering of Sport*. 1996. Balkema, Rotterdam: Taylor and Francis.

95. Cao, X., J. Qiu, X. Zhang, and J. Shi, *Rotation Properties of Feather Shuttlecocks in Motion*. *Procedia Engineering*, 2014. **72**: p. 732-737.

96. Lin, C.S.H., C.K. Chua, and J.H. Yeo, *Aerodynamics of badminton shuttlecock: Characterization of flow around a conical skirt with gaps, behind a hemispherical dome*. *Journal of Wind Engineering and Industrial Aerodynamics*, 2014. **127**: p. 29-39.

97. Lin, C.S.H., C.K. Chua, and J.H. Yeo, *Design of high performance badminton shuttlecocks; virtual and rapid prototyping approach*. *Journal Virtual and Physical Prototyping*, 2013. **8**(2): p. 165-171.

98. Ansys, I., *ANSYS CFX-SOLVER modeling guide*, 2010: Canonsburg, PA.

99. Ansys, I., *ANSYS CFX-Solver theory guide*, 2010: Canonsburg, PA.

100. Gomes, M.G., A. Moret Rodrigues, and P. Mendes, *Experimental and numerical study of wind pressures on irregular-plan shapes*. *Journal of wind engineering and industrial aerodynamics*, 2005. **93**(10): p. 741-756.

101. Nelson, R.C., *Flight stability and automatic control*. Second ed. *Aerospace science and technology series*. 1998: McGraw Hill.

102. Barber, S., S.B. Chin, and M.J. Carre, *Sports ball aerodynamics: A numerical study of the erratic motion of soccer balls*. *Computers & Fluids*, 2009. **38**(6): p. 1091-1100.

103. Alaways, L.W., *Aerodynamics of the curve-ball: An investigation of the effects of angular velocity on baseball trajectories*, 1998, University of California Davis.
104. Nathan, A.M., *Determining the 3D spin axis from TrackMan data*, 2012, University of Illinois: Urbana, IL.
105. Brandon, P. *The magnus effect*. 2010 [15th Nov 2012]; Available from: [http://ffden-2.phys.uaf.edu/211\\_fall2010.web.dir/Patrick\\_Brandon/what\\_is\\_the\\_magnus\\_effect.html](http://ffden-2.phys.uaf.edu/211_fall2010.web.dir/Patrick_Brandon/what_is_the_magnus_effect.html).
106. McGhee, R.b., E.R. Bachmann, and M.J. Zyda, *Rigid body dynamics, inertial reference frames, and graphics coordinate systems: A resolution of conflicting conventions and terminology*, 2000, Naval Postgraduate School: Monterey, CA.
107. Bertin, J.J. and R.M. Cummings, *Aerodynamics for engineers*. 5th ed. 2009, Upper saddle river, NJ: Pearson Prentice-Hall.
108. Johnson, G.L., *Wind energy systems*, 2004: Manhattan, KS.
109. Spakovszky, Z.S. *Thermodynamics and propulsion*. 2009 [16th Nov 2012]; Available from: <http://web.mit.edu/16.unified/www/SPRING/propulsion/notes/node86.html>.
110. Kwan, M., M.S. Andersen, C.-L. Cheng, W.-T. Tang, and J. Rasmussen, *Investigation of high-speed badminton racket kinematics by motion capture*. Sports Engineering, 2010. **13**(2): p. 57-63.

111. Liu, X., W. Kim, and J. Tan, *An analysis of the biomechanics of arm movement during a badminton smash*, 2002, Nanyang technological university: Singapore, Singapore. p. 102-103.
112. Kwan, M. and J. Rasmussen, *The importance of being elastic: deflection of a badminton racket during a stroke*. *Journal of sports sciences*, 2010. **28**(5): p. 505-11.
113. Kwan, M., C.-L. Cheng, W.-T. Tang, and J. Rasmussen, *Measurement of badminton racket deflection during a stroke*. *Sports Engineering*, 2010. **12**(3): p. 143-153.
114. Kwan, M., M.S. Andersen, and M.d. Zee, *Dynamic model of a badminton stroke*, in *The engineering of sport 7*, 2008, Springer: Paris, France. p. 563-571.
115. 韓洪敏, 馮勝杰, and 劉于詮, *不同球線和拍擊位置對羽球拍拍擊力量之影響*. *屏東教大體育*, 2010(13).
116. Hugemann, W., *Correcting lens distortions in digital photographs*, 2010, European Association for Accident Research and Analysis.
117. Hartley, R.I. and S.B. Kang, *Parameter-free Radial Distortion Correction with Centre of Distortion Estimation*, N.D., Australian National University & Microsoft Research.
118. L. Ma, Y.Q.C., K.L. Moore, *Rational Radial Distortion Models of Camera Lenses with Analytical Solution for Distortion Correction*. *International Journal of Information Acquisition*, 2004. **1**(2): p. 135-147.

119. Rushton, S.K. and P.A. Duke, *Observers cannot accurately estimate the speed of an approaching object in flight*. Vision research, 2009. **49**(15): p. 1919-1928.
120. Gordon, W. *Bird2: The solution-Blog*. 2014 [cited 2014 18th Aug]; Available from: <http://www.birdsports.net/bird2-the-solution---blog>.
121. Pololu, C. *DRV8825 Stepper Motor Driver Carrier, High Current* [cited 29/11/2014]; Available from: <https://www.pololu.com/product/2133>.
122. Seeed, S. *Weight Sensor (Load Cell)0-500g*. 2012 [cited 2014 28/11/2014]; Available from: [http://www.seeedstudio.com/wiki/Weight\\_Sensor\\_\(Load\\_Cell\)0-500g](http://www.seeedstudio.com/wiki/Weight_Sensor_(Load_Cell)0-500g).
123. Arduino. *Servo library*. 1/6/2012]; Available from: <http://www.arduino.cc/en/Reference/Servo>.
124. Ongvises, A. and X. Xu, *Shuttlecock velocity of a badminton drop shot*. ISB Journal of science, 2013. **7**(1).
125. Lin, C.S.H., C.K. Chua, and J.H. Yeo. *Designing a badminton shuttlecock; validation of virtual design by 3d printed thin-walled functional prototype*. in *1st International Conference on Progress in Additive Manufacturing (Pro-AM 2014)* 2014. Singapore.
126. YONEX. *Report on shuttlecock experiments- Comparing Yonex and the other makers of shuttlecocks*. 2012 [cited 18th Oct 2012]; Available from: [http://www.yonex.com/shuttle\\_news/performance/index.html#h3-03](http://www.yonex.com/shuttle_news/performance/index.html#h3-03).



## Appendix A

### Translation

The following series of coordinate transformations apply to a right handed coordinate system [101]. Taking three rotations about the axes system,

1. Rotation about the z-axis through the yaw angle,  $\psi$ . The rotation matrix is given by:

$$R(\psi) = \begin{bmatrix} \cos\psi & \sin\psi & 0 \\ -\sin\psi & \cos\psi & 0 \\ 0 & 0 & 1 \end{bmatrix} \quad (65)$$

2. Rotation about the y-axis through the pitch angle,  $\theta$ . The rotation matrix is given by:

$$R(\theta) = \begin{bmatrix} \cos\theta & 0 & -\sin\theta \\ 0 & 1 & 0 \\ \sin\theta & 0 & \cos\theta \end{bmatrix} \quad (66)$$

3. Rotation about the x-axis through the roll angle,  $\phi$ . The rotation matrix is given by:

$$R(\phi) = \begin{bmatrix} 1 & 0 & 0 \\ 0 & \cos\phi & \sin\phi \\ 0 & -\sin\phi & \cos\phi \end{bmatrix} \quad (67)$$

The complete rotation matrix is then given by:

$$[R] = R(\phi)R(\theta)R(\psi) \quad (68)$$

Therefore, mapping of earth coordinates into the body frame axes is as:

$$\begin{bmatrix} \dot{x} \\ \dot{y} \\ \dot{z} \end{bmatrix}_{body} = [R] \begin{bmatrix} \dot{x} \\ \dot{y} \\ \dot{z} \end{bmatrix}_{earth} \quad (69)$$

Taking the inverse of [R] on both side,

$$\begin{bmatrix} \dot{x} \\ \dot{y} \\ \dot{z} \end{bmatrix}_{earth} = [R]^{-1} \begin{bmatrix} \dot{x} \\ \dot{y} \\ \dot{z} \end{bmatrix}_{body} \quad (70)$$

Since  $[R]^{-1} = [R]^T$ , therefore,

$$\begin{bmatrix} \dot{x} \\ \dot{y} \\ \dot{z} \end{bmatrix}_{earth} = [R]^T \begin{bmatrix} \dot{x} \\ \dot{y} \\ \dot{z} \end{bmatrix}_{body} \quad (71)$$

where,

$$[R]^T = \begin{bmatrix} \cos\psi\cos\theta & \cos\psi\sin\theta\sin\phi - \sin\psi\cos\phi & \cos\psi\sin\theta\cos\phi + \sin\psi\sin\phi \\ \sin\psi\cos\theta & \sin\psi\sin\theta\sin\phi + \cos\psi\cos\phi & \sin\psi\sin\theta\cos\phi - \sin\phi\cos\psi \\ -\sin\theta & \cos\theta\sin\phi & \cos\theta\cos\phi \end{bmatrix} \quad (72)$$

### Rotation

The angular rate in body frame (p, q, r) can be transformed into the Euler angular rate ( $\dot{\theta}, \dot{\phi}, \dot{\psi}$ ) through the transformation matrix,  $[R_T]$ .

$$[R_T] = \begin{bmatrix} 1 & 0 & -\sin\theta \\ 0 & \cos\phi & \sin\phi\cos\theta \\ 0 & -\sin\phi & \cos\phi\cos\theta \end{bmatrix} \quad (73)$$

$$\begin{bmatrix} p \\ q \\ r \end{bmatrix} = \begin{bmatrix} 1 & 0 & -\sin\theta \\ 0 & \cos\phi & \sin\phi\cos\theta \\ 0 & -\sin\phi & \cos\phi\cos\theta \end{bmatrix} \begin{bmatrix} \dot{\phi} \\ \dot{\theta} \\ \dot{\psi} \end{bmatrix} \quad (74)$$

Taking the first time derivative on both sides, the angular acceleration in body frame is given as,

$$\dot{p} = \ddot{\psi} \cos\theta - \dot{\psi} \dot{\theta} \sin\theta + \ddot{\theta} \quad (75)$$

$$\dot{q} = \ddot{\psi} \sin\theta \sin\phi + \dot{\psi} \dot{\theta} \cos\theta \sin\phi + \ddot{\phi} \dot{\psi} \sin\theta \cos\phi + \ddot{\theta} \cos\phi - \dot{\theta} \dot{\phi} \sin\phi \quad (76)$$

$$\dot{r} = \ddot{\psi} \sin\theta \cos\phi + \dot{\psi} \dot{\theta} \cos\theta \cos\phi - \ddot{\phi} \dot{\psi} \sin\theta \sin\phi + \ddot{\theta} \sin\phi - \dot{\theta} \dot{\phi} \cos\phi \quad (77)$$

## Flight Path Frame

For a shuttlecock flying at  $\alpha$  and  $\beta$ , the rotation matrix for transformation from the flight path reference frame to the body frame is given as,

$$[R_{FP}] = R(\beta)R(\alpha) \quad (78)$$

where

$$R(\alpha) = \begin{bmatrix} \cos\alpha & 0 & \sin\alpha \\ 0 & 1 & 0 \\ -\sin\alpha & 0 & \cos\alpha \end{bmatrix} \quad (79)$$

$$R(\beta) = \begin{bmatrix} \cos\beta & \sin\beta & 0 \\ -\sin\beta & \cos\beta & 0 \\ 0 & 0 & 1 \end{bmatrix} \quad (80)$$

Transformation of flight path axis to the body axis is then given by,

$$\begin{bmatrix} \dot{x} \\ \dot{y} \\ \dot{z} \end{bmatrix}_{body} = [R_{FP}]^T \begin{bmatrix} \dot{x} \\ \dot{y} \\ \dot{z} \end{bmatrix}_{FP} \quad (81)$$

Substitution of (9) into (81), the earth fixed frame and the flight path fixed frame can then be related through,

$$\begin{bmatrix} \dot{x} \\ \dot{y} \\ \dot{z} \end{bmatrix}_{earth} = [R]^T [R_{FP}]^T \begin{bmatrix} \dot{x} \\ \dot{y} \\ \dot{z} \end{bmatrix}_{FP} \quad (82)$$

## Appendix B

### Experimental Setup

The experimental setup consisted of three high speed cameras positioned along the flight path of the shuttlecock. These cameras were aligned square to the horizon and their position, setting and various other details are presented in Table B1.

	Camera 1	Camera 2	Camera 3
Distance from launcher	2.3 m	9.3 m	10.2-10.5 m
Height of camera	2.1 m	2.4 m	1.5 m
Camera type	Photron Fastcam	Phantom Miro	Phantom Miro
Lens focal length	60 mm	50 mm	35 mm
Illumination	1x Unomat LZ601GS	1x Unomat LZ601GS	2x Unomat LX901GZ
Shutter speed	1/9000 s	1/8000 s	1/8000 s
Frame rate	1000 fps	1000 fps	500 fps

Table B1 Detail of the experimental rig.

The lenses were selected based on camera positions and availability. Camera 1 was positioned near the launcher to capture data for initial flight conditions post-launch. That meant smaller variability in flight trajectory between launches was observed at camera 1. Therefore, a 60 mm (in 35 mm format) lens was used. Camera 2 being placed just after the stall point (where maximum height is reached and the shuttlecock starts to turn nose down towards the ground) had a 50 mm lens due to increased flight variability over the location of camera 1.

Camera 3 was positioned approximately 1.5 m above the ground to capture the speed that will be observed by a player who is receiving the shot. Since the different

shuttlecock types will have significantly different range, the ground position of camera 3 was adjusted accordingly. This increased the probability of capturing the shuttlecock within the frame. Adjustment of camera was achieved by test shots of the same type of shuttlecocks prior to the actual experiment. In view of the large variability observed from shot to shot, a wide angle lens would have been ideal. This is because the larger angle of view which was provided by a wide angle lens allows for capturing more of the scene without the need for increased subject to camera distance. However, taking into account of optical distortion and resolution limitation, a 35 mm was selected as a compromise. All camera settings were attained through calibration shots prior to the test. Placement of the experimental setup is depicted in Figure B1.

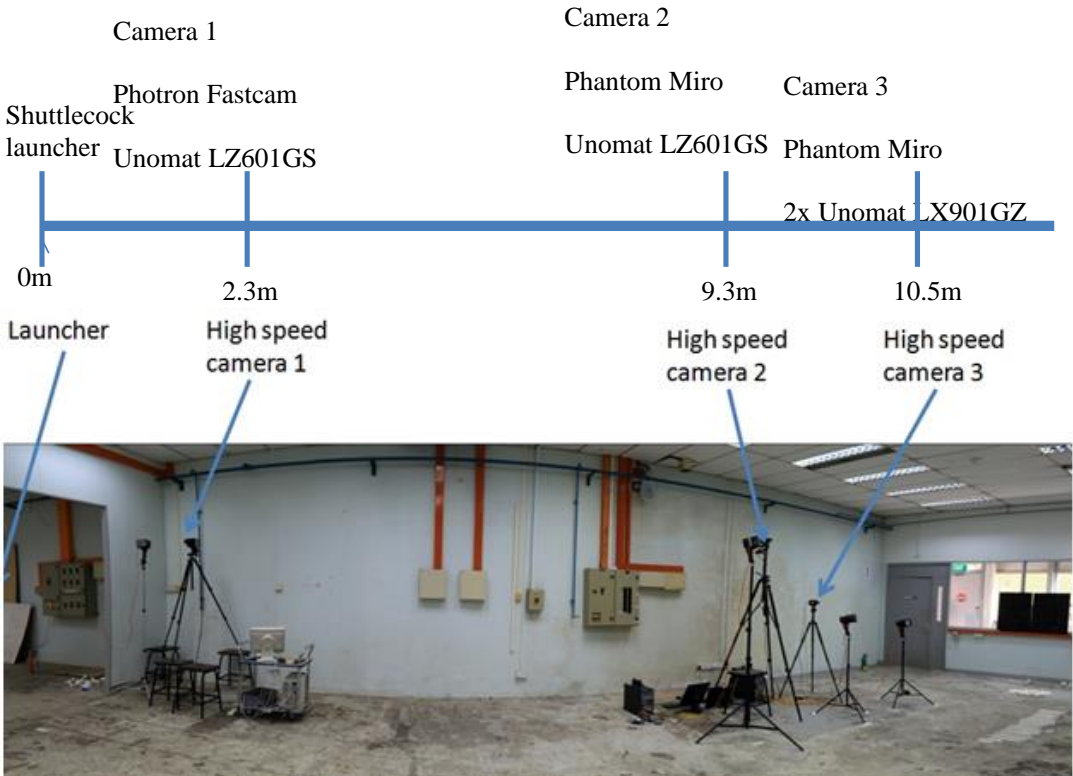


Figure B1 Experimental setup consisting of launcher (not in frame) and three high speed cameras.

The shuttlecock launcher used in the experiment is compressed air-driven, courtesy of Li-Ning, Singapore office. Launcher pressure was kept to a constant 3.5 MPa for every shot. The launcher is shown in Figure B2.



Figure B2 Compressed air driven badminton shuttlecock launcher used for the experiment.

Test environment was in a climate controlled air-conditioned laboratory. Six types of shuttlecocks were evaluated. They were the Ashaway official (76), Li-Ning A+90 (76), Li-Ning A+90 (77), Li-Ning Grandprix (76), Yonex Aerosensa 5 (76) and Yonex Aerosensa 10 (76). A tube (12 pieces) was tested for each shuttlecock type. The shuttlecocks in each tube were labelled 1 to 12 before testing. Two runs of the experiment were conducted. After the 1<sup>st</sup> run of experiment, the 8 median performing shuttles from each tube of Ashaway official, Li-Ning A+90 (76), Li-

Ning A+90 (77) and Yonex Aerosensa 5 were selected for a 2<sup>nd</sup> run to check for consistency in launch method and degradation of shuttlecocks.

## Results

Results are presented in the following pages. First column is the label of the 8 median shuttlecocks selected from the first run. Boxes with N.A. symbolize that no value was captured as the shuttlecock was out of the camera frame. Mean results for each run have been tabulated in Table 9.

Yonex AS-5(76)-Run1

Yonex AS-5	Cam1		Cam2		Cam3		
Run1	Airspeed /m/s	Spin rate /rad/s	Airspeed /m/s	Spin rate /rad/s	Airspeed /m/s	Spin rate /rad/s	Distance /m
AS5-9	24.90	65.46	5.37	49.09	5.31	41.34	10.50
AS5-7	26.19	112.21	5.49	56.11	N.A.	N.A.	10.70
AS5-8	27.23	65.46	5.04	47.13	5.14	36.17	10.80
AS5-2	26.33	65.46	5.26	56.11	N.A.	N.A.	10.90
AS5-3	28.32	130.92	N.A.	N.A.	5.59	42.45	11.10
AS5-10	27.57	117.83	5.10	53.56	5.24	45.67	11.10
AS5-12	28.97	78.55	5.76	49.09	6.23	36.07	11.20
AS5-4	24.87	56.11	5.04	52.37	N.A.	N.A.	11.40
Mean	26.80	86.50	5.29	51.92	5.50	40.34	10.96
Var.	2.24	847.21	0.07	12.81	0.19	17.37	

Yonex AS-5(76)-Run2

Yonex As-5	Cam1		Cam2		Cam3		
Run2	Airspeed /m/s	Spin rate /rad/s	Airspeed /m/s	Spin rate /rad/s	Airspeed /m/s	Spin rate /rad/s	Distance /m
AS5-9	29.43	0.00	5.73	56.11	5.09	39.28	11.30
AS5-7	26.12	98.19	5.03	53.56	5.11	45.32	10.70
AS5-8	25.85	87.28	N.A.	N.A.	5.09	29.46	11.20
AS5-2	N.A.	N.A.	5.19	50.68	5.04	39.28	10.70
AS5-3	26.63	98.19	5.44	58.19	4.97	49.09	10.70
AS5-10	27.13	71.41	N.A.	N.A.	5.02	49.09	10.40
AS5-12	26.60	0.00	5.26	42.08	5.09	31.42	10.50
AS5-4	24.24	98.19	N.A.	N.A.	N.A.	N.A.	9.70
Mean	26.57	64.75	5.33	52.12	5.06	40.42	10.65
Var.	2.44	2048.53	0.07	39.41	0.00	63.05	

Ashaway Official Run1

Ashaway	Cam1		Cam2		Cam3		
Run1	Airspeed /m/s	Spin rate /rad/s	Airspeed /m/s	Spin rate /rad/s	Airspeed /m/s	Spin rate /rad/s	Distance /m
ash1	24.58	60.42	5.71	37.40	N.A.	N.A.	10.30
ash3	24.66	98.19	5.40	49.09	5.41	39.27	10.30
ash6	28.99	90.63	5.05	52.37	5.13	42.08	10.40
ash11	28.75	71.41	N.A.	N.A.	5.11	43.64	10.40
ash4	27.04	117.83	5.02	39.28	5.31	32.73	10.50
ash8	27.63	84.16	5.58	69.31	5.10	53.56	10.50
ash7	28.99	65.46	5.12	53.56	5.74	49.09	10.60
ash5	27.69	90.63	5.22	65.46	5.47	49.09	10.70
ash9	29.33	142.82	5.32	58.19	5.09	46.21	10.80
Mean	27.52	91.28	5.30	53.08	5.29	44.46	10.50
Var.	2.91	684.23	0.06	127.94	0.05	42.80	

Ashaway Official Run2

Ashaway	Cam1		Cam2		Cam3		
Run2	Airspeed /m/s	Spin rate /rad/s	Airspeed /m/s	Spin rate /rad/s	Airspeed /m/s	Spin rate /rad/s	Distance /m
ash1	28.06	78.55	5.44	49.09	5.02	45.32	10.60
ash3	28.06	147.28	5.26	58.19	5.42	41.34	10.60
ash6	25.80	157.10	5.55	50.68	5.01	49.09	9.90
ash11	N.A.	N.A.	N.A.	N.A.	N.A.	N.A.	N.A.
ash4	27.47	130.92	N.A.	N.A.	N.A.	N.A.	10.50
ash8	27.26	43.64	5.27	47.13	5.15	41.34	10.60
ash7	28.33	43.64	5.30	49.09	5.04	39.27	10.60
ash5	28.94	112.21	5.21	65.46	5.09	53.56	10.50
ash9	28.61	147.28	5.21	68.30	5.12	52.37	10.40
Mean	27.82	107.58	5.32	55.42	5.12	46.04	10.46
Var.	0.96	2170.05	0.02	74.28	0.02	32.71	

Li-Ning A+90(76) Run2

A90-76	Cam1		Cam2		Cam3		
Run1	Airspeed /m/s	Spin rate /rad/s	Airspeed /m/s	Spin rate /rad/s	Airspeed /m/s	Spin rate /rad/s	Distance /m
A90-1	26.83	87.28	5.49	58.19	N.A.	N.A.	10.80
A90-3	26.32	65.46	5.19	36.82	5.00	29.75	10.80
A90-6	27.45	147.28	5.31	51.23	4.86	41.66	10.80
A90-11	N.A.	N.A.	5.05	33.66	5.10	34.15	10.80
A90-4	27.63	117.83	5.31	52.37	5.34	41.78	11.00
A90-9	26.31	87.28	5.45	40.63	5.71	36.17	11.00
A90-10	27.73	130.92	N.A.	N.A.	5.36	45.32	11.10
A90-12	27.37	65.46	5.40	43.64	5.30	32.73	11.10
Mean	27.09	100.21	5.32	45.22	5.24	37.37	10.93
Var.	0.31	888.39	0.02	80.49	0.08	32.05	

Li-Ning A+90(76) Run2

A90-76	Cam1		Cam2		Cam3		
Run2	Airspeed /m/s	Spin rate /rad/s	Airspeed /m/s	Spin rate /rad/s	Airspeed /m/s	Spin rate /rad/s	Distance /m
A90-1	25.71	65.46	5.21	44.89	5.22	39.28	10.70
A90-3	25.61	117.83	4.90	51.23	N.A.	N.A.	10.40
A90-6	25.52	84.16	4.80	46.21	5.13	42.08	10.30
A90-11	29.78	0.00	5.62	42.46	5.08	35.70	11.10
A90-4	28.62	78.55	N.A.	N.A.	5.31	35.70	11.10
A90-9	27.47	147.28	4.89	40.63	5.00	36.82	10.50
A90-10	28.04	0.00	5.17	39.28	5.03	26.78	11.00
A90-12	26.02	43.64	5.14	36.82	5.22	31.01	10.50
Mean	27.10	67.11	5.10	43.07	5.14	35.34	10.70
Var.	2.61	2711.7	0.08	23.25	0.01	25.91	

Li-Ning A+90(77) Run1

A90-77	Cam1		Cam2		Cam3		
Run1	Airspeed /m/s	Spin rate /rad/s	Airspeed /m/s	Spin rate /rad/s	Airspeed /m/s	Spin rate /rad/s	Distance /m
a90-77-11	26.23	98.19	5.91	41.34	5.21	41.34	10.80
a90-77-6	N.A.	N.A.	N.A.	N.A.	5.41	56.10	11
a90-77-10	27.32	98.19	5.93	58.91	5.36	53.56	11.00
a90-77-2	26.71	56.11	5.36	43.64	4.97	45.32	11.10
A90-77-1	28.59	87.28	5.74	41.34	5.22	36.82	11.10
a90-77-8	27.58	0.00	5.82	43.64	4.90	49.09	11.10
a90-77-9	28.99	0.00	5.84	43.64	5.26	30.21	11.10
a90-77-12	28.57	112.21	5.48	47.13	5.28	35.70	11.20
Mean	27.72	64.57	5.73	45.66	5.20	43.52	11.05
Var.	1.08	2242.6 8	0.05	37.89	0.03	83.04	

Li-Ning A+90(77) Run2

A90-77	Cam1		Cam2		Cam3		
Run2	Airspeed /m/s	Spin rate /rad/s	Airspeed /m/s	Spin rate /rad/s	Airspeed /m/s	Spin rate /rad/s	Distance /m
a90-77-11	29.51	78.55	5.23	47.13	5.31	39.28	10.60
a90-77-6	27.5	0	5.52	39.27	5.43	30.21	11
a90-77-10	25.88	107.11	5.52	54.17	5.31	49.09	10.90
a90-77-2	28.04	39.28	5.25	49.09	5.40	39.28	10.70
A90-77-1	27.78	130.92	5.23	39.28	5.10	34.15	10.90
a90-77-8	28.62	98.19	5.44	46.21	5.31	43.64	10.90
a90-77-9	N.A.	N.A.	N.A.	N.A.	N.A.	N.A.	N.A.
a90-77-12	29.20	78.55	5.34	49.09	5.13	39.28	10.80
Mean	28.08	76.08	5.36	46.32	5.29	39.27	10.83
Var.	1.27	1659.1 2	0.02	29.50	0.02	37.31	

Yonex Aerosensa 10 Single run

Yonex AS-10	Cam1		Cam2		Cam3		
Run1	Airspeed /m/s	Spin rate /rad/s	Airspeed /m/s	Spin rate /rad/s	Airspeed /m/s	Spin rate /rad/s	Distance /m
as10-9	27.41	0.00	5.40	43.64	5.13	43.64	10.50
as10-8	26.35	0.00	5.27	34.65	5.02	45.32	10.60
as10-10	24.79	49.09	5.01	28.74	5.33	26.78	10.70
as10-1	29.22	0.00	5.45	44.89	4.96	37.40	10.80
as10-7	28.91	0.00	N.A.	N.A.	N.A.	N.A.	10.80
as10-5	26.46	49.09	5.31	52.37	5.21	45.32	10.90
as10-3	25.71	35.70	5.15	32.73	5.13	24.55	11.00
as10-2	29.10	87.28	N.A.	N.A.	5.00	45.32	11.10
Mean	27.24	27.65	5.26	39.50	5.11	38.33	10.80
Variance	2.84	1085.4 4	0.03	79.37	0.02	83.15	

### Li-Ning Grandprix(76) Single run

Grand Prix-76	Cam1		Cam2		Cam3		
Run1	Airspeed /m/s	Spin rate /rad/s	Airspeed /m/s	Spin rate /rad/s	Airspeed /m/s	Spin rate /rad/s	Distance /m
gp2	27.50	65.46	5.19	41.34	5.17	34.15	10.60
gp5	25.74	39.28	5.18	43.64	5.03	30.21	10.60
gp8	27.80	112.2 1	4.86	53.07	5.06	45.32	10.60
gp10	25.76	39.28	5.12	39.28	5.09	28.05	10.70
gp7	26.50	60.42	N.A.	N.A.	5.41	49.09	10.80
gp4	28.33	28.05	5.25	42.08	5.43	37.40	10.90
gp12	27.24	0	5.28	41.34	5.26	18.4	10.90
gp3	27.79	0	4.97	43.64	5.11	7.55	11.00
gp9	27.77	107.1 1	5.13	54.17	5.67	58.91	11.00
Mean	27.16	50.20	5.12	44.82	5.25	34.35	10.79
Var.	0.89	1648. 94	0.02	31.55	0.22	219.9 4	

### Range and Velocity

Based on the mean distance travelled in Table 9, all shuttlecocks showed decrease in range in the second run. This suggests increased drag from damaged feathers. With an average of 11.05 m and 10.83 m in run 1 and 2 respectively, the Li-Ning A+90 speed 77 shuttlecock exhibited the longest range. This was expected as it had a higher speed rating of 77 as compared to the others which were speed 76. However, range variation within each shuttlecock group was significantly larger than the difference between their average ranges. This variation could have been attributed by the launch method. Based on the result, it is difficult to conclude if the effect was from the feather damage or due to inherent variation in shuttlecock consistency. Yet, there is no correlation for the same shuttlecock in different runs. That is, a

shuttlecock that previously flew further than the average could have a longer or shorter range than the average in the 2nd run.

In the open literature, there is no work to investigate the consistency between shuttlecocks of the same model. This means it is difficult to validate the variation that was observed in the flight range. While not an academic publication, just recently (late 2012) YONEX did publish experimental result of spread in landing distance for shuttlecocks of the same type in their shuttlecock promotion material [126]. In that study, three types of shuttlecocks, each of sample size 24 were launched through a racket simulator. The spread in landing distance was observed to be 0.5 m, 0.7 m and 1.2 m respectively.

In the second run, all four types of shuttlecocks (Yonex AS-5, Ashaway Official and Li-Ning A+90 speed 76 and 77) exhibited range reduction. As such, it is possible that damage on shuttlecocks was affecting the result. The distance travelled for the Ashaway shuttlecock was consistently shorter than the rest of the shuttlecocks. This is evident from the range of the individual shuttlecocks and the mean range of the Ashaway shuttlecock. Such a difference was equivalent to a speed rating difference of more than 1. Analysis of the airspeed at camera 1 showed that the Ashaway actually had a faster mean speed at camera 1 than all the other speed 76 rated shuttlecocks. Therefore, it is unlikely that difference in range is the consequence of biased launch condition.

Airspeed was estimated using the captured footages of the shuttlecocks. Distance travelled on-screen for a short segment of flight—approximately 0.01 s for high speed and 0.05 s for slower flight—was first measured. Variation in time duration was due

to difference in time the shuttlecock remained in the camera's field of view at different flight speed. The measured distance was then multiplied by the ratio between the actual distances to on-screen distance. This ratio was obtained by comparing the actual dimensions of the shuttlecock with on-screen size. Flight speed was then estimated by dividing the flight distance over duration. Since measurement at the corners of the captured frame could have suffer from parallax error, measurements were taken at the centre of the frame whenever possible.

Based on the airspeed recorded by camera 2 and 3, one can conclude that most of the deceleration in flight occurred before the post-stall phase of the flight. Airspeed at position of camera 1 (2.3 m) ranged from 24-29 m/s. At position of camera 2 (9.3 m), airspeed had reduced to below 5.5 m/s in most instances. It is proposed that another camera be added between camera 1 and camera 2 to observe the deceleration in airspeed.

In the later phase of flight, terminal velocity, which was relatively low for a low weight-high drag shuttlecock, prevented significant speed change from camera 2 to camera 3. Therefore, airspeed estimated through data from camera 3 was also mostly below 5.5 m/s. Small magnitude of the variance shows that data estimated from camera 3 had very small difference across samples of the same shuttlecock model. However, it does not mean that there was no error. Optical errors from parallax error and lens optics could have been a possible source of error. Such errors are usually systematic errors which only affects the accuracy but not precision. Therefore, the effect will not be observed in a study of the variance. It is suggested that a calibration chart be used to reduce effect of lens optics errors in future studies.

## **Spin Rate**

Various markings were made along the feather stems of the shuttlecocks prior to the experiment. Based on the position of the feather shaft with respect to time, spin rate was estimated from the recorded video footages of the three cameras. This was done by first observing the time required for the shuttlecock to rotate through a certain number ( $n$ ) of feathers. “ $n$ ” was not a fixed number because of the large variation in spin rate between shuttlecocks and difference in camera field of view at different camera positions. For a typical feather shuttlecock with 16 feathers, the angle of rotation would have been  $n/16 \times 360$  degree. The observed angle of rotation was then divided by the time taken. The difficulty was in choosing the start or end video frames for the time duration such that the shuttlecock had completed the exact full rotation of  $n$ -number of feathers.

Error was minimized by doing proper selection of starting and ending duration (frame) with the video playing back at 1 fps. Moreover, the high speed cameras allowed for high capturing rate which aid the resolution of playback. Resolution here refers to being able to find a frame with the feathers in the exact position that is desired. As an example, if a camera was capturing at 50 fps for a fast spinning shuttlecock, one may only have a video that captured a frames of the shuttlecock before it reaches the desired rotational angle and then a second frame after it has passed. That means, 3 video frames after  $2/50$  s. However, if the capture rate were 10 times as fast, at 500 fps, there would have been 21 frames captured within the same time span of  $2/50$  s. In another words, the gap between the 3 video frames that were captured at 50 fps would be filled by an additional 18 frames if it was shot at 500 fps. Therefore, more frames captured within the same time interval would

produce data with better temporal resolution. This would increase the probability of being able to choose a start frame or end frame with the shuttlecock feather at the desired position. Finer temporal resolution also reduces error when the wrong frame is chosen. This is because  $\pm 1$  frame at 50 fps is equivalent to an error of  $\pm 1/50$  s, while  $\pm 1$  frame at 500 fps is only an error of  $\pm 1/500$  s.

Theoretically, spin rate captured by camera 1 should be the highest, while spin rate captured by camera 2 and 3 should be similar. This is because the steady state shuttlecock spin rate, as observed from literature review, increases with airspeed. This was observed by both Cooke [22] and Kitta et al. [32] who did measurement of steady state spin rate in the wind tunnel. No data of actual in-flight spin rate was available in the open literature. Since the shuttlecock had much higher airspeed at position of camera 1, it made sense for the observation of correspondingly high spin rate. From the experimental result, spin rate observed at camera 1 was indeed much higher than camera 2 and 3, except for some outlier cases. With the exception of the Ashaway Official shuttlecock, all shuttlecock types had one or more experimental runs with no spin rate being observed at position of camera 1.

The above suggests that there was residual effect at work in the spin rate. This means that the actual observed in-flight spin rate will be significantly different from the steady state spin rate typically measured in wind tunnel testing. This is possible when one considers that a shuttlecock starts its flight path with little to no spin. Thus, time is required before a shuttle can reach its full steady state spin of that corresponding airspeed. However, since a shuttlecock experiences very high initial deceleration (of airspeed), there might be insufficient time for angular acceleration to

take place. Therefore, a shuttlecock at a distance away from the launch point could either be spinning slower than or equal to the steady state spin rate. This might explain the large variation in spin rate observed at camera 1 despite similar launch velocity. It is important to note that the above is in contrast to what was proposed by Cooke [22] who observed insignificant time delay in wind tunnel.

Similar effect can also be said about deceleration in spin rate. Since there was very little variation in airspeed estimated through camera 2 and camera 3, the corresponding spin rate that should have been observed must be similar. However, the spin rate at camera 3 was observed to be lower in almost all instances. This is also observed in the comparison of mean spin rate of various types of shuttlecocks in Table 9. This suggests that shuttlecock spin deceleration takes time.

It is proposed that the higher airspeed in the early part of flight (before and after position of camera 1) induced a much higher spin rate in the shuttlecock. Along the flight path, spin kinetic energy may have dissipated at a slower rate than airspeed was lost. Therefore, there was residual spin rate being measured at camera 2, which meant that steady state spin rate corresponding to that airspeed would be lower. As spin deceleration continued along the path of camera 2-3, the spin recorded at camera 3 will be lower. This can be supported by the experimental result showing large differences in spin rate, despite the small difference in airspeed between the positions of camera 2 and camera 3. A possible way to validate the proposed is to investigate the steady spin rate of the various shuttlecocks in a terminal velocity free-fall. The observed steady state spin rate can then be evaluated against the spin rate estimated. For the proposed explanation to hold true, the steady state spin rate

must be significantly slower than that observed from camera 2. In addition, it should also be equal to or slower than the spin rate captured by camera 3. However, since no reliable terminal velocity drop test was conducted, it is impossible to validate the above. More work is planned.

Interestingly, shuttles that started out with low/no spin rate at camera position 1 had similar spin as the others at camera position 2 and 3. Examples include the experimental result of the Li-Ning A90-77-8 and gp12 and Yonex AS10-1 in their first run. These shuttlecocks were not spinning in the earlier part of flight. However, the spin rates towards the end of flight were actually close to the mean spin rate of their respective group. It is again proposed that another camera be included between camera 1 and 2 in future study to observe the angular acceleration/deceleration, in addition to the change in airspeed discussed earlier.

In consideration of the shuttlecock damage and way of launching the shuttlecock, it is not clear if the observed was attributed by shuttlecock design, feather profile, launch method or simply damage to feathers.

Spin of a shuttlecock stabilizes the flight trajectory, much like rifling of a bullet or spin of an arrow. Spin may also affect aerodynamic drag coefficient of a shuttlecock, as it was observed by Kitta et al. [32]. Spin reduced the skirt deformation at high airspeed. This allows the shuttlecock to maintain its cross-sectional area. Consequently, there is less change in the resultant drag force.

In this experiment, it was observed that the acceleration and deceleration of spin rate is equally important as the spin rate itself. In addition, it will be interesting to study how the shuttlecock spin rate and its time derivative, varies with wear and tear when

launched with a launcher that does not induce premature wear and tear on the feather. Such could be part of a future durability analysis.

### **Shuttlecock Damage**

Due to the launch mechanism of the current launcher, damage in feathers was observed in all shuttlecocks within the first run. Close-up photography of an example is provided in Figure B3. Attempts to restore them back to shape resulted in better feather condition. However, it was observed that feathers are like polymers, where properties are severely affected upon deformation into plastic state. Reshaped feathers exhibited tendency to return to deformed condition with slight touch. An example is given Figure B4.



Figure B3 Typical damage of 3-5 feathers in one launch using a launcher, in contrast to a perfect condition shuttlecock.

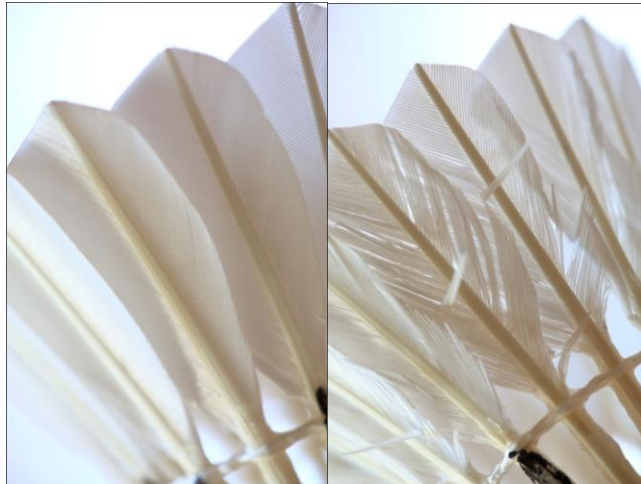


Figure B4 Left: Feather in perfect condition before launch.

Right: Distorted feather after 1 launch, "smoothed".

Ideally, durability of a shuttlecock can be measured by the amount of feather deformation in a launch. After all, damage to shuttlecock in play due to strokes like a strong smash is inevitable. As such, this could be a good representation of the durability. Yet, quantifying such damage is difficult and inaccurate. Moreover, such observation is meaningless when one considers that wear and tear bares little influence to the general market. It is the degradation in shuttlecock performance though wear and tear that is of vital concern. It means that even if the feathers appear worn, a shuttlecock is still perfectly playable so long as there is no appreciable performance difference in flight or feel. Shuttlecock durability for the general market should be measured by the performance degradation, rather than appearance.

Despite damage to the shuttlecocks in the preliminary studies, it is safe to conclude that high speed imaging method for testing shuttlecock performance is feasible. A new method of launch is required to test both feather and synthetic shuttlecocks effectively. The subsequent analysis will also be conducted using Tracker.

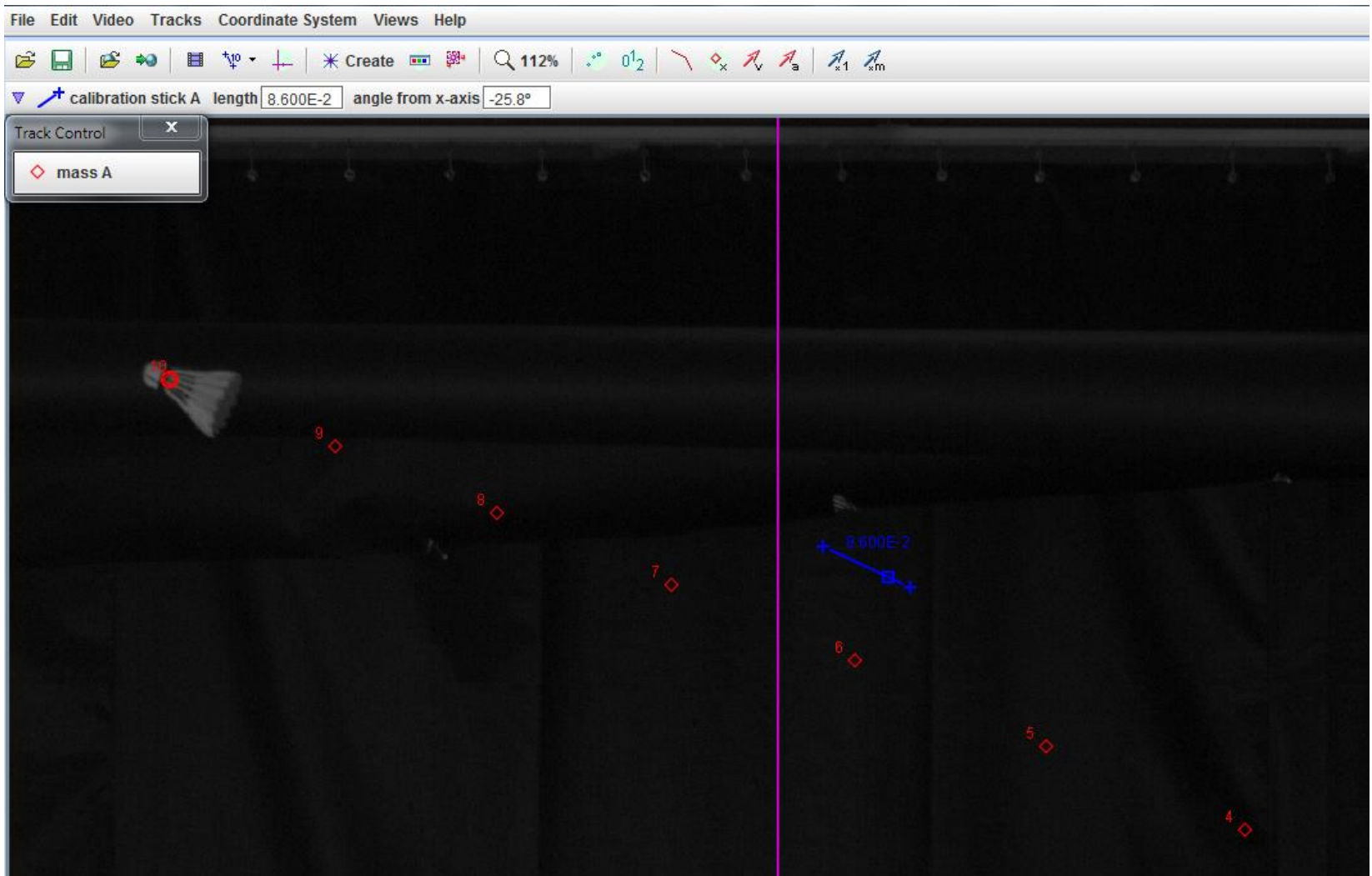


Figure B5 Analysis using Tracker software.

## Appendix C

Specimen	Mass /g						
	Yonex AS40 (BWF)	Yonex AS40 (BWF)	Babolat Tour	Yonex Mavis 350	Yonex Mavis 2000	Li-Ning X800	Li-Ning X800
1	5.3778	5.2151	4.9297	5.1565	5.3407	5.4481	5.2915
2	5.1701	5.2576	5.0265	5.2189	5.3488	5.4117	5.2546
3	5.1874	5.3051	5.2029	5.1248	5.4915	5.4287	5.2381
4	5.185	5.3383	5.1791	5.1485	5.3407	5.4537	5.293
5	5.3628	5.2984	5.038	5.2083	5.4158	5.4486	5.2914
6	5.3609	5.287	4.8553	5.1291	-	5.4087	5.272
7	5.3073	5.2514	5.1691				
8	5.0551	5.2964	5.0276				
9	5.3329	5.3947	5.0465				
10	5.2158	5.2698	4.7855				
11	5.3512	5.2319	5.0791				
12	5.3615	5.2432	5.0373				
Speed rating	2 (76)	3 (77)	77	Blue (76)	Blue (76)	Blue (77-78)	Green (75-76)
Average	5.272	5.282	5.031	5.164	5.388	5.433	5.273
Std Dev	0.105	0.050	0.126	0.040	0.066	0.020	0.023
Min	5.055	5.215	4.786	5.125	5.341	5.409	5.238
Max	5.378	5.395	5.203	5.219	5.492	5.454	5.293

Table C1-Shuttlecock mass data

Babolat	Reading /mm						Chord Length, C/mm
	1	2	3	4	5	Average	
1	64.70	64.30	65.10	64.80	64.95	64.77	85.93
2	64.00	65.00	65.60	65.00	64.20	64.76	84.87
3	65.05	65.00	65.10	64.95	64.95	65.01	85.22
4	65.05	63.80	64.40	64.75	64.65	64.53	85.58
5	65.10	65.45	64.85	65.30	64.70	65.08	85.18
6	65.20	64.20	64.60	65.30	65.30	64.92	84.92
7	66.30	65.70	66.30	66.00	65.75	66.01	84.74
8	65.30	64.80	65.25	65.45	65.80	65.32	85.58
9	65.40	64.60	64.95	65.25	65.85	65.21	85.84
10	64.45	65.25	65.20	66.00	65.05	65.19	86.26
11	65.25	65.00	64.50	65.10	64.45	64.86	85.33
12	65.05	65.50	65.40	65.60	65.00	65.31	85.12
Li-Ning X800 (Green)	66.00	65.05	65.70	65.55	66.00	65.66	79.84
Li-Ning X800 (Blue)	65.91	65.94	65.79	65.50	65.72	65.79	79.03
Yonex Maxis 350 (Blue)	66.00	65.80	65.45	65.40	66.30	65.77	79.79
Li-Ning GP Gold 76	65.75	66.15	65.70	66.00	65.75	65.87	85.19
Yonex AS40 (3)	66.00	66.00	66.10	66.05	66.00	66.03	85.38
Yonex AS40 (2)	66.00	65.80	65.90	65.85	65.70	65.85	85.53

Table C2-Shuttlecock diameter and length measurements

## Appendix D

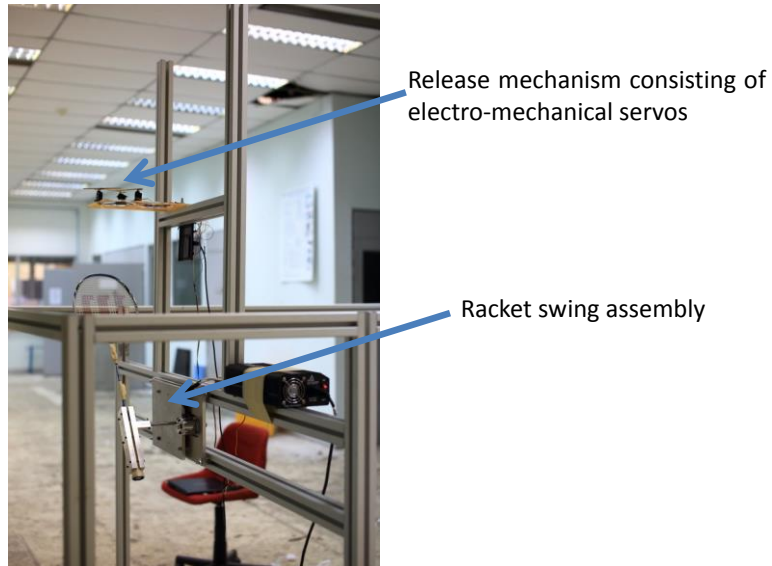


Figure D1 Shuttlecock launcher employing the principle of a rotating racket.

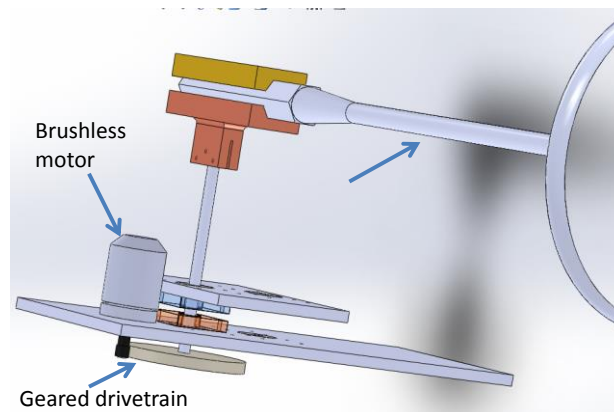


Figure D2 CAD model of the various parts in the drivetrain of the launcher.



Figure D3 L-R Arduino circuit board with the prototyping breadboard. Flex resistor to determine the racket position.

## Appendix E

### Calibrating for Lens Radial Distortion

The experimental setup is shown in Figure E1, where the camera plane and grid plane were aligned to be parallel. Calibration shots of the grid chart were taken with both the 24mm and 28mm lenses. Presence of image distortion from lens optics could be observed from the curved lines in the calibration shots, such those presented in Figure E2 and Figure E3. The grid was formed by squares of 3 cm by 3 cm. Through these calibrated shots, the influence of radial distortion and the effectiveness of proposed correction technique were evaluated.

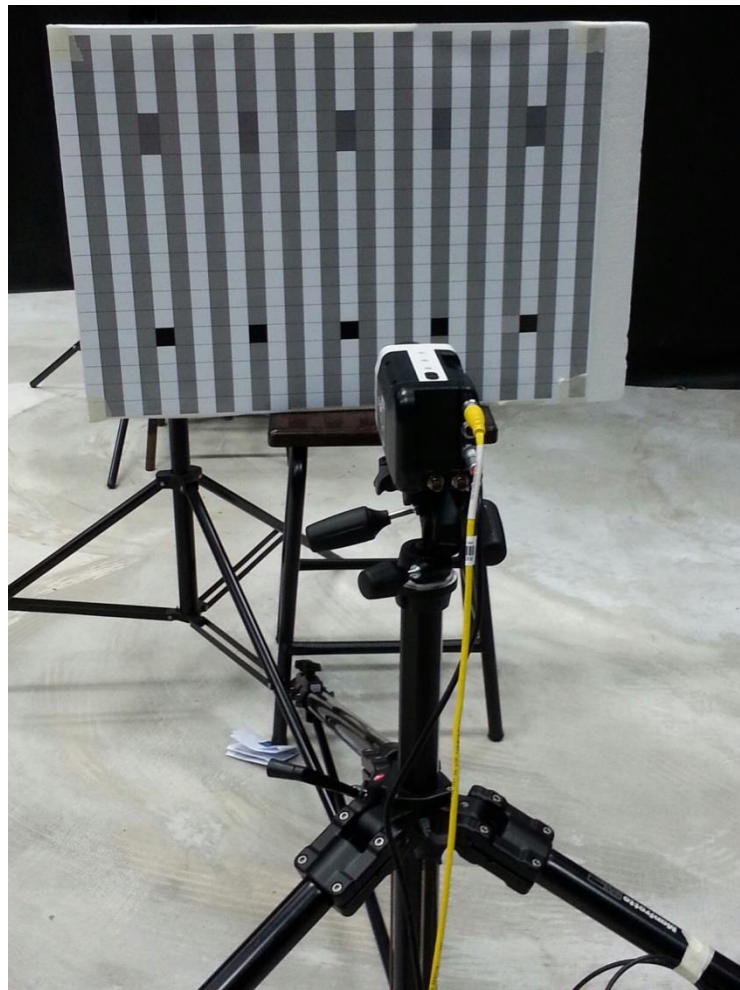


Figure E1 Experimental setup for data collection of lens distortion.

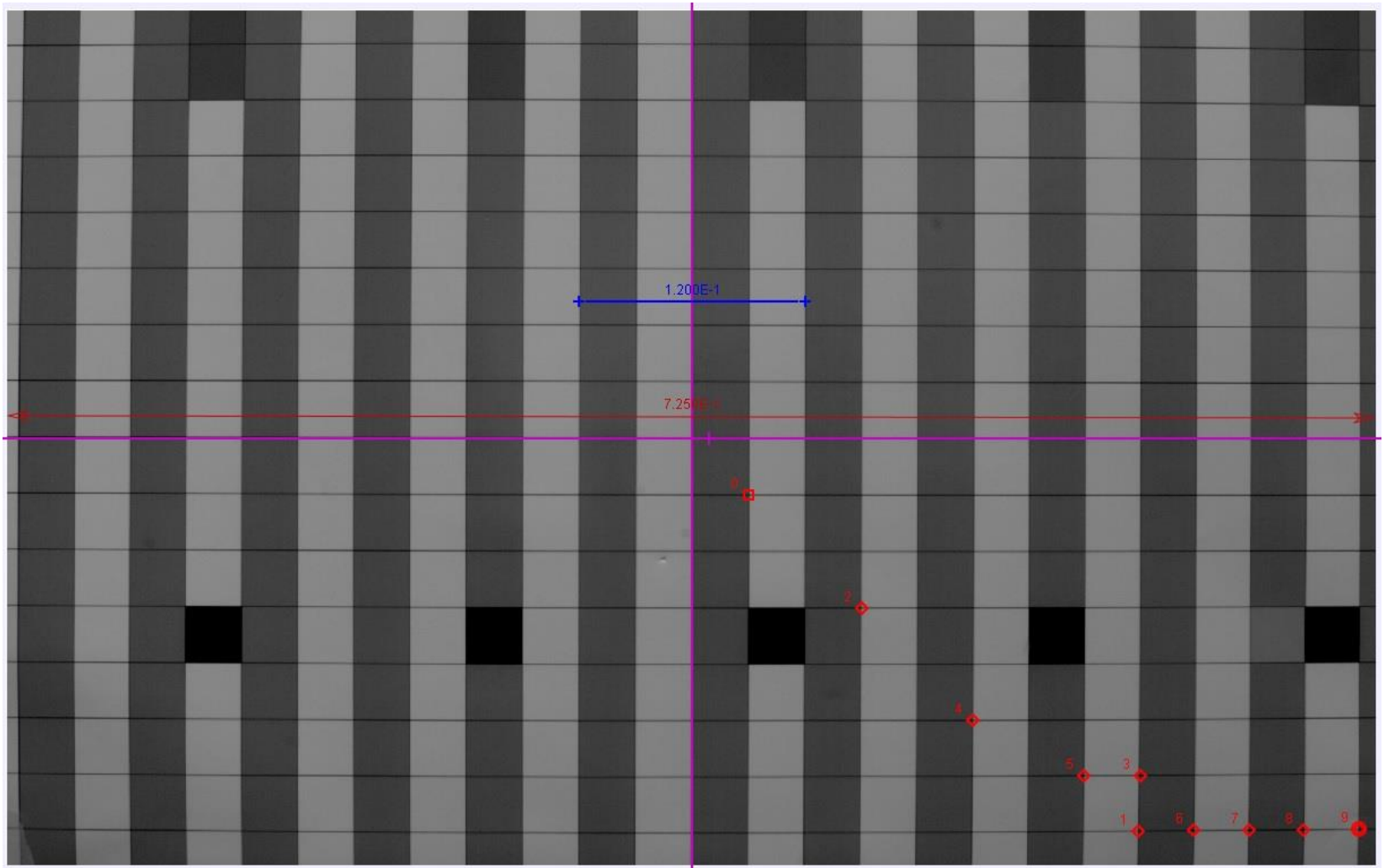


Figure E2 Calibration of lens distortion by grid chart for the Nikon AF-D 28mm/2.8

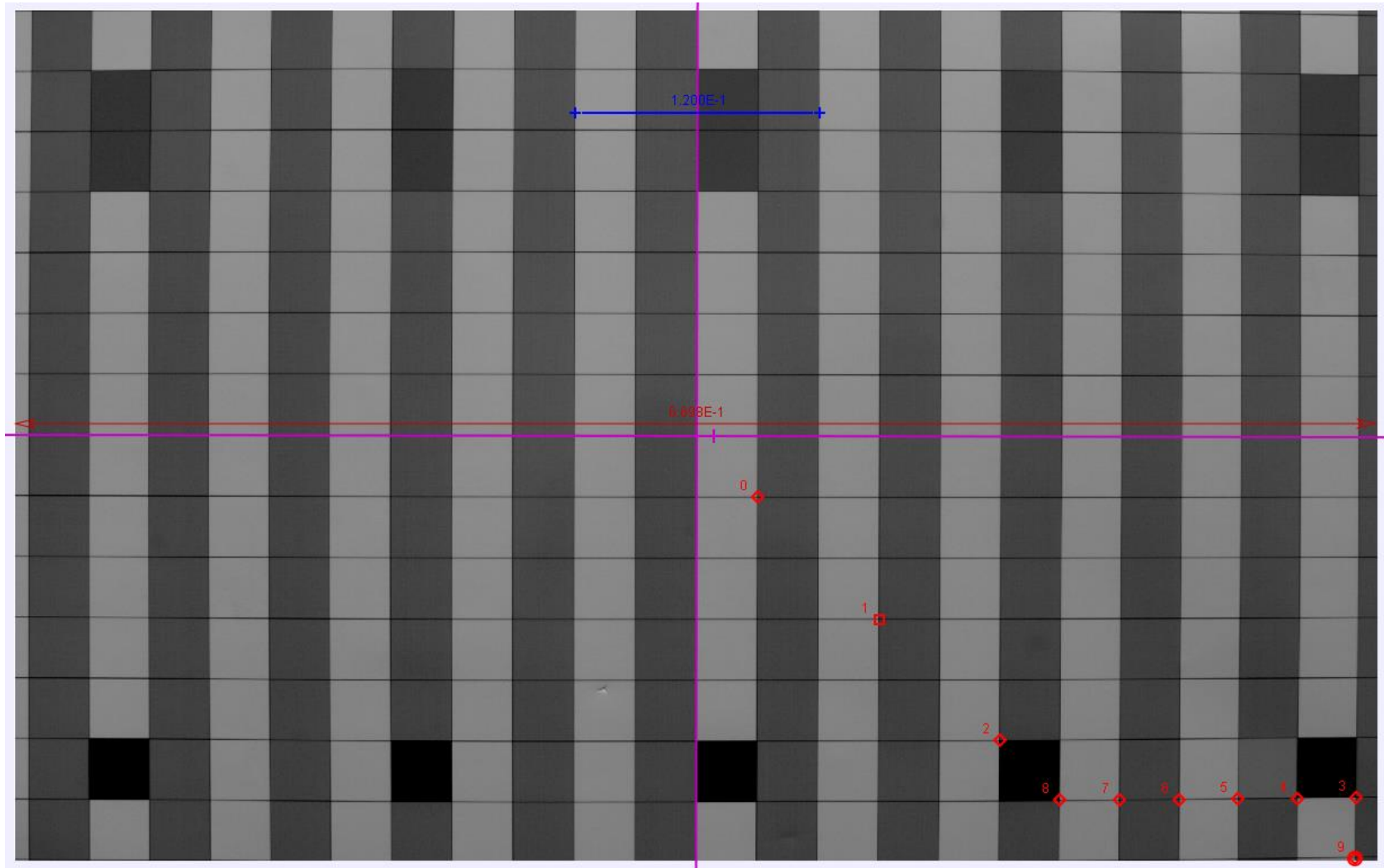


Figure E3 Calibration for distortion for the Nikon AF-D 24mm/2.8.

The images were processed for the positions of the various points. These obtained image positions were then tabulated together with their actual physical position and they are shown in Table E1 and Table E2. The symbols x and y refer to the position coordinate in the image, and r is the radius from centre of the image frame. The position coordinate and radius in actual physical space are represented by X, Y and R. The formula  $r/R$  gives the proportionate error of image radius over the physical radius. Span refers to the span width of the image. To demonstrate the error, the  $r/R$  ratios were plotted and these are presented in Figure E4.

x	y	r	X	Y	R	r/R	% Span	R-r
0.030	0.030	0.043	0.030	0.030	0.042	1.009	11.7	-3.7E-04
0.090	0.090	0.128	0.090	0.090	0.127	1.004	35.1	-4.9E-04
0.149	0.150	0.212	0.150	0.150	0.212	0.999	58.5	2.3E-04
0.208	0.180	0.275	0.210	0.180	0.277	0.995	76.3	1.4E-03
0.238	0.179	0.298	0.240	0.180	0.300	0.994	82.8	1.8E-03
0.238	0.209	0.316	0.240	0.210	0.319	0.992	88.0	2.4E-03
0.267	0.209	0.339	0.270	0.210	0.342	0.990	94.4	3.4E-03
0.296	0.209	0.362	0.300	0.210	0.366	0.989	101	3.9E-03
0.325	0.208	0.386	0.330	0.210	0.391	0.987	108	4.9E-03
0.354	0.208	0.411	0.360	0.210	0.417	0.986	115	6.0E-03

Table E1 Grid calibration data for Nikon AF-D/2.8 28mm.

x	y	r	X	Y	R	r/R	% Span	R-r
0.030	0.030	0.043	0.030	0.030	0.042	1.006	12.7	-2.7E-04
0.090	0.090	0.128	0.090	0.090	0.127	1.002	38.0	-2.5E-04
0.150	0.150	0.212	0.150	0.150	0.212	0.998	63.3	3.2E-04
0.179	0.179	0.253	0.180	0.180	0.255	0.995	76.0	1.2E-03
0.208	0.179	0.275	0.210	0.180	0.277	0.994	82.6	1.6E-03
0.278	0.179	0.298	0.240	0.180	0.300	0.992	89.6	2.5E-03
0.267	0.178	0.321	0.270	0.180	0.324	0.989	96.9	3.5E-03
0.296	0.178	0.345	0.300	0.180	0.350	0.987	104	4.4E-03
0.325	0.178	0.370	0.330	0.180	0.376	0.985	112	5.7E-03
0.325	0.207	0.385	0.330	0.210	0.391	0.985	117	5.8E-03

Table E2 Grid calibration data for Nikon AF-D/2.8 24mm.

From the tabulated results, error for  $R/\text{Span} < 0.76$  was observed to be insignificant.

At points far away from the centre of the frame, significant deviation from optical distortion was observed.

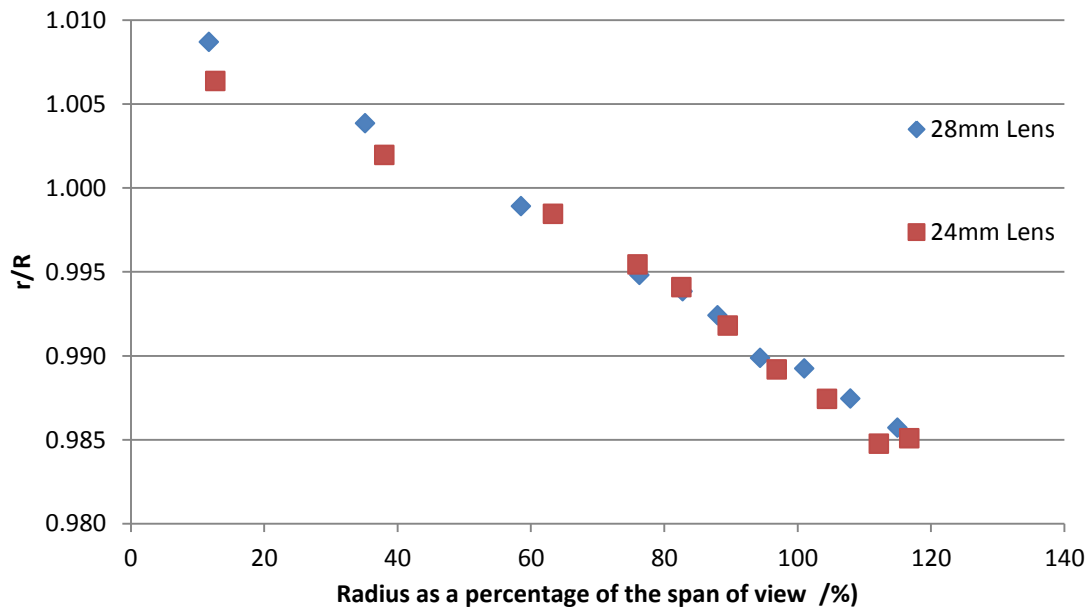


Figure E4 Plot of ratio of  $r/R$  vs. the radius as a function of span.

Radial distortion on the lens was modelled as:

$$\hat{R} = f(r) \times r + r = (a_1r^2 + a_2r^4 + a_3r^6 + a_4r^8) \times r + r \quad (1)$$

where  $\hat{R}$  is the physical radial distance from the centre of the frame, while  $r$  is the image radius.

Taking square of both side and then substituting the relationship between the radius and coordinate values, where,

$$\hat{R}^2 = (X^2 + Y^2)$$

$$r^2 = (x^2 + y^2)$$

Then equation (1) can be expressed as:

$$\hat{R} = f(r) \times r + r$$

$$\hat{R} = (f(r) + 1) \times r$$

$$\hat{R}^2 = (f(r) + 1)^2 \times r^2$$

$$(X^2 + Y^2) = (f(r) + 1)^2 \times (x^2 + y^2)$$

$$(X^2 + Y^2) = (f(r) + 1)^2 x^2 + (f(r) + 1)^2 y^2$$

Taking the individual vector component and then square root, then the mapping of radial distortion can be expressed as:

$$\begin{bmatrix} X \\ Y \end{bmatrix} = (f(r) + 1) \begin{bmatrix} x \\ y \end{bmatrix} \quad (2)$$

Ideally the mapping should be done with a grid size that covers the same physical space as the experimental setup used for capturing shuttlecocks. However, production of a grid chart that is the same size as the capture area (> 2.5 m in span) was not feasible. Therefore, a dimensionless variable of  $r/\text{span}$  was used for mapping

the correction of the distortion. This has the advantage of the same correction factors being independent of the physical span of view. The idea is represented in Figure E5.

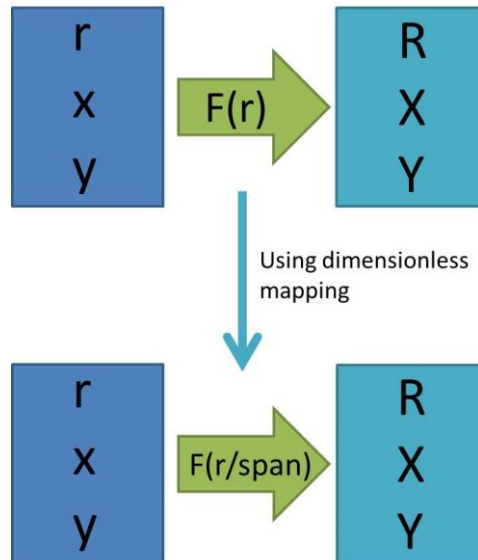


Figure E5 Using mapping of a dimensionless constant.

Therefore, equation (2) can be expressed as,

$$\begin{bmatrix} X \\ Y \end{bmatrix} = (f(r/span) + 1) \begin{bmatrix} x \\ y \end{bmatrix}$$

Using the radial distortion relationship and the obtained experimental data of image radius and physical radius, the parameters of correction,  $a_1$ ,  $a_2$ ,  $a_3$  and  $a_4$  were obtained. These are presented in Table E2. Fields marked with “Narrow” refer to correction parameters that were obtained from data of  $R/span < 0.76$ . Fields marked with “Wide” refer to parameters obtained from the data of the full field of view.

	$a_1$	$a_2$	$a_3$	$a_4$
24mm Narrow (76% of horizontal span)	-0.46685	5.00162	-14.841	13.196
24mm Wide (115% of horizontal span)	-0.41886	1.847507	-2.34268	0.916488
28mm Narrow (76% of horizontal span)	-0.628607	6.455936	-18.0514	14.64537
28mm Wide (115% of horizontal span)	-0.56554	2.34375	-2.6718	0.9094

Table E2 Parameters identified from the experimental data.

Applying the wide field correction data of the 24mm lens showed little improvement in accuracy over the raw uncorrected data. This was plotted and is presented in Figure E6. Deviation was still observed for data far away from the centre of the frame.

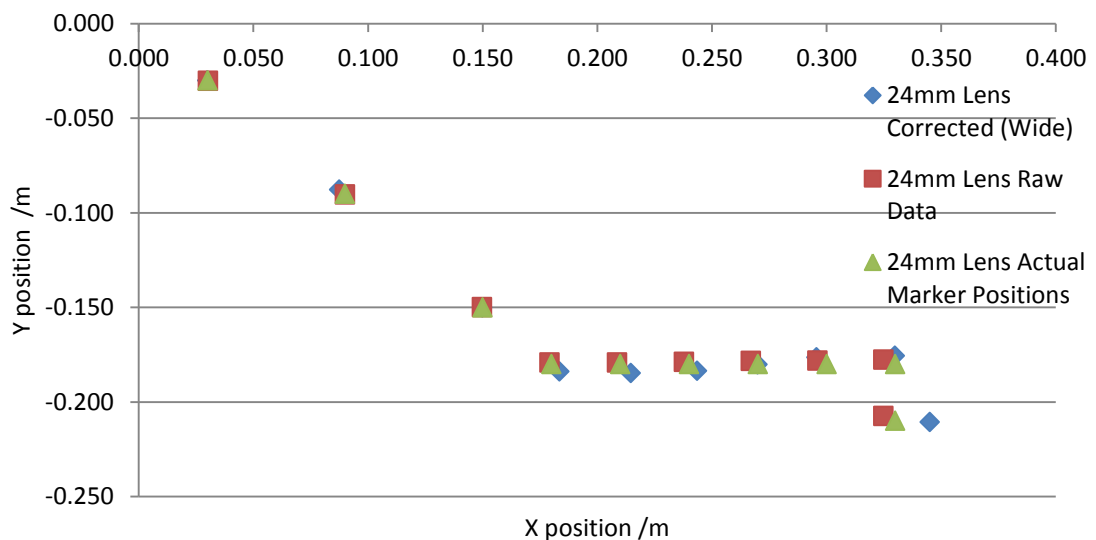


Figure E6 Comparison of data for the 24mm lens. The corrected position coordinates shows little improvement over the raw data.

Therefore, a more effective and simplified method of distortion correction was developed. This involved a piecewise radial distortion correction. Since the uncorrected data at  $R/\text{span} < 0.76$  showed good agreement with the actual physical coordinates, correction was only applied to points outside this area. The last term in  $f(r/\text{span})$  was also dropped to give the following equation.

$$f(r/\text{span}) = (a_1 r^2 + a_2 r^4 + a_3 r^6)$$

Using the data of  $R/\text{span} > 0.76$ , parameters were identified. These are presented in Table E3. The calibration results were plotted against the raw data and these are presented in Figure E7 and Figure E8.

	$a_1$	$a_2$	$a_3$
24mm Lens	0.004096	-0.00233	0.010938
28mm Lens	0.002871	-0.00151	0.008492

Table E3 Identified parameters with data of  $R/\text{span} > 0.76$ .

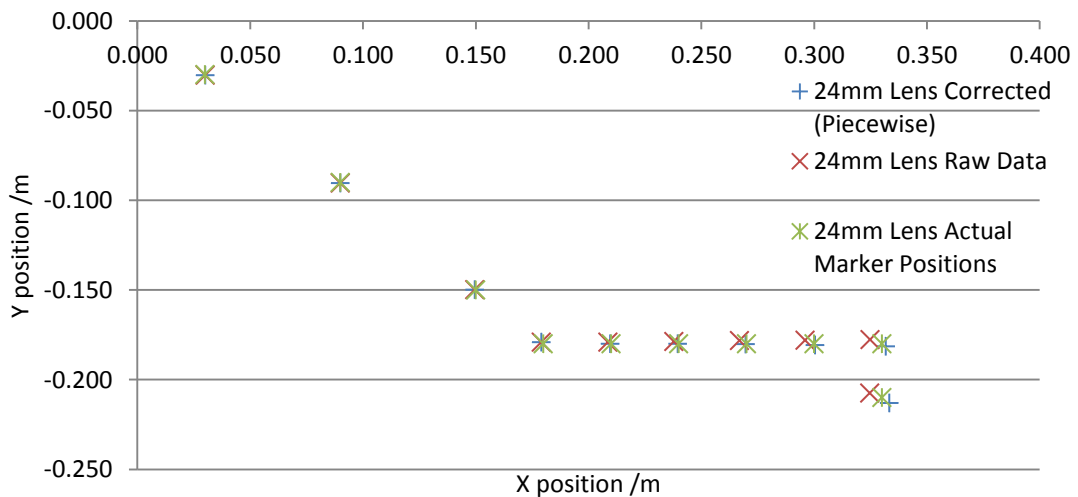


Figure E7 Corrected data by the piecewise approach for the 24mm lens.

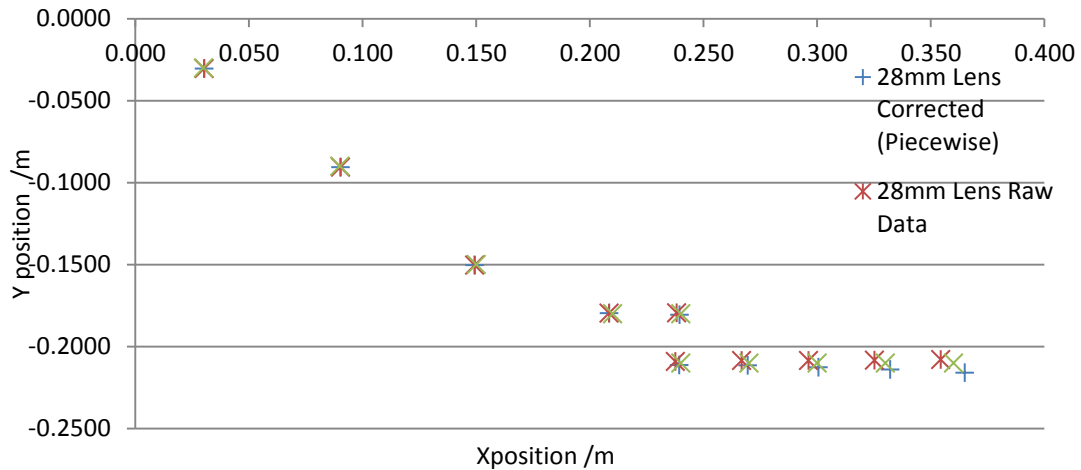


Figure E8 Corrected data by the piecewise approach for the 28mm lens.

### Applied Error (Planar)

The measurement error in applied condition was studied by setting up two high speed cameras side by side at 1 m apart. The span of view of each camera was 2.45m. The image frames of these cameras were aligned parallel to each other and badminton shuttlecocks were placed in various locations within the frame. The experimental setup is illustrated in Figure E9. Four points on the image were sampled. These four points were:

- (1.005, 1.955)
- (0.500, 1.955)
- (0.500, 1.490)
- (1.005, 1.210)

The origin was defined as the location on the ground in the centre between the two cameras.

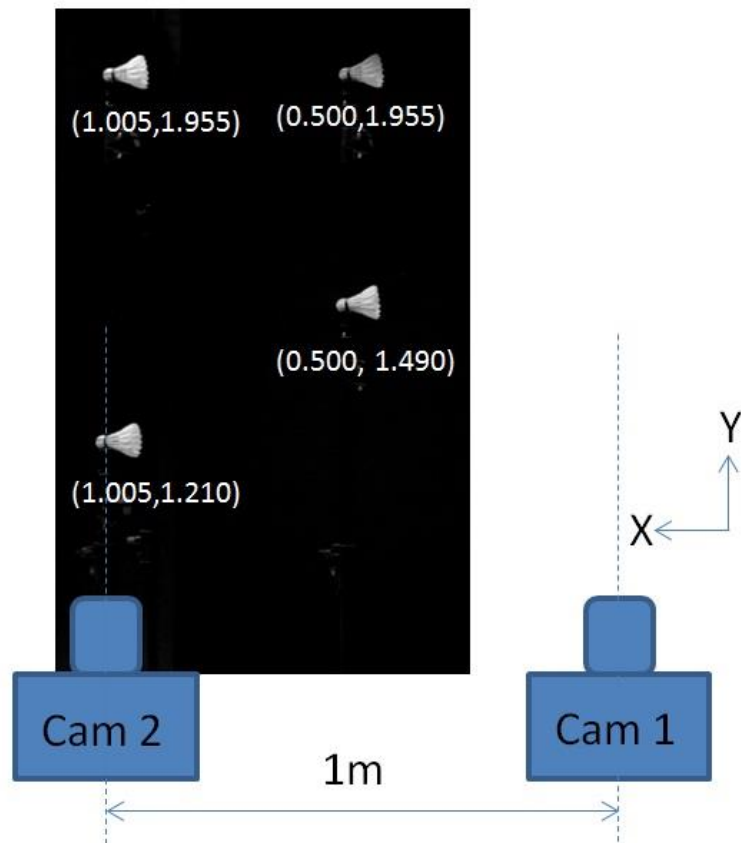


Figure E9 Experimental setup for observation of parallax error.

The shuttlecock positions were captured using both cameras. The results were then compared with the actual physical positions that were measured. Since the shuttlecocks were positioned on the far edge of Cam 1, lens correction was applied to the data from Cam 1. The raw data from Cam 1 and Cam 2, the physical data and the corrected data from Cam 1 were plotted and these are presented in Figure E10. The numerical position data are presented in Table E4.

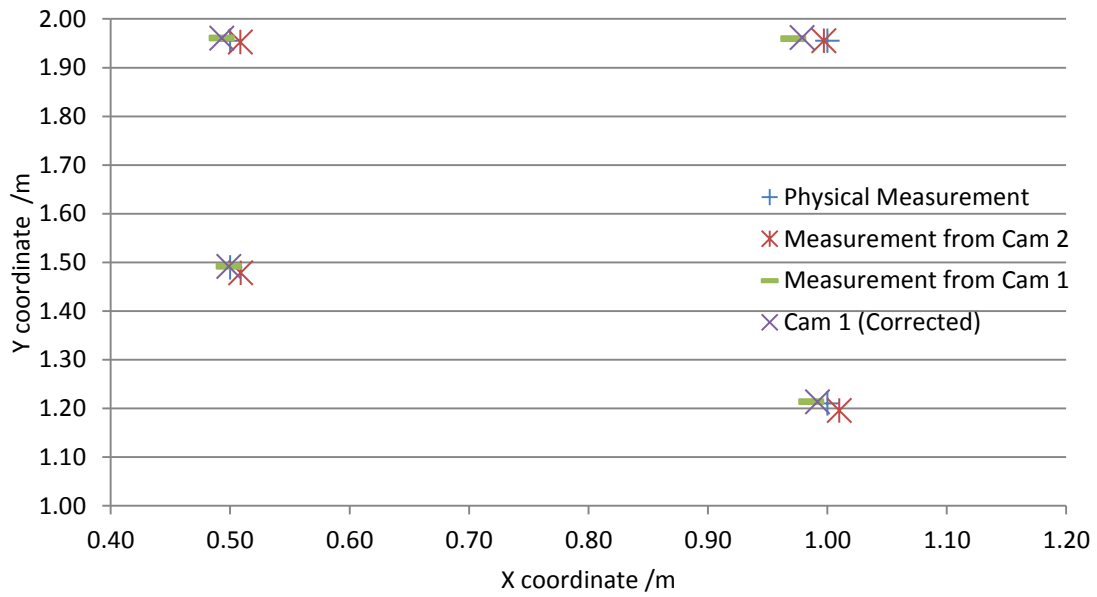


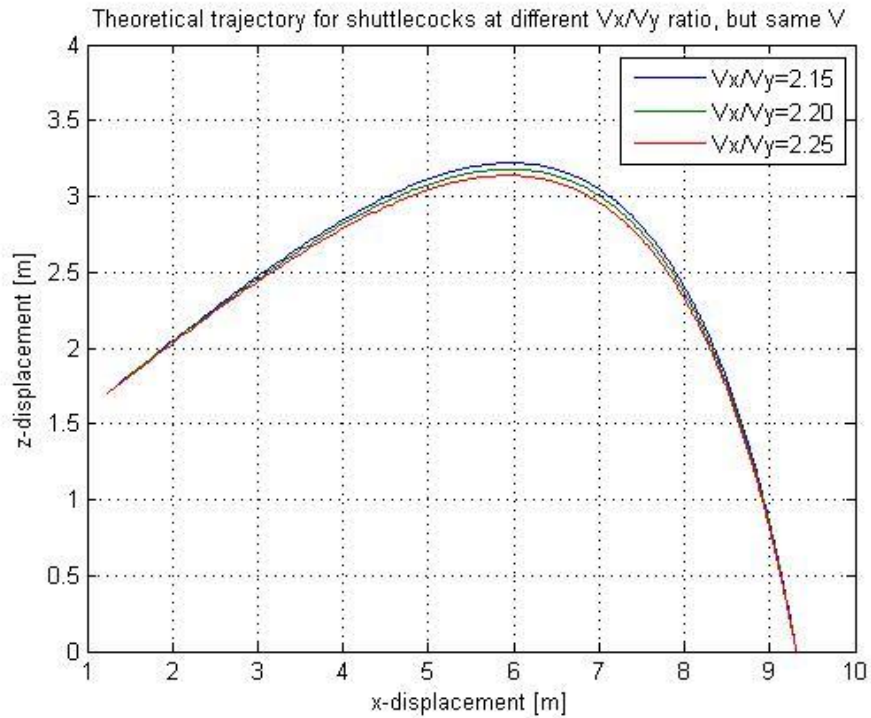
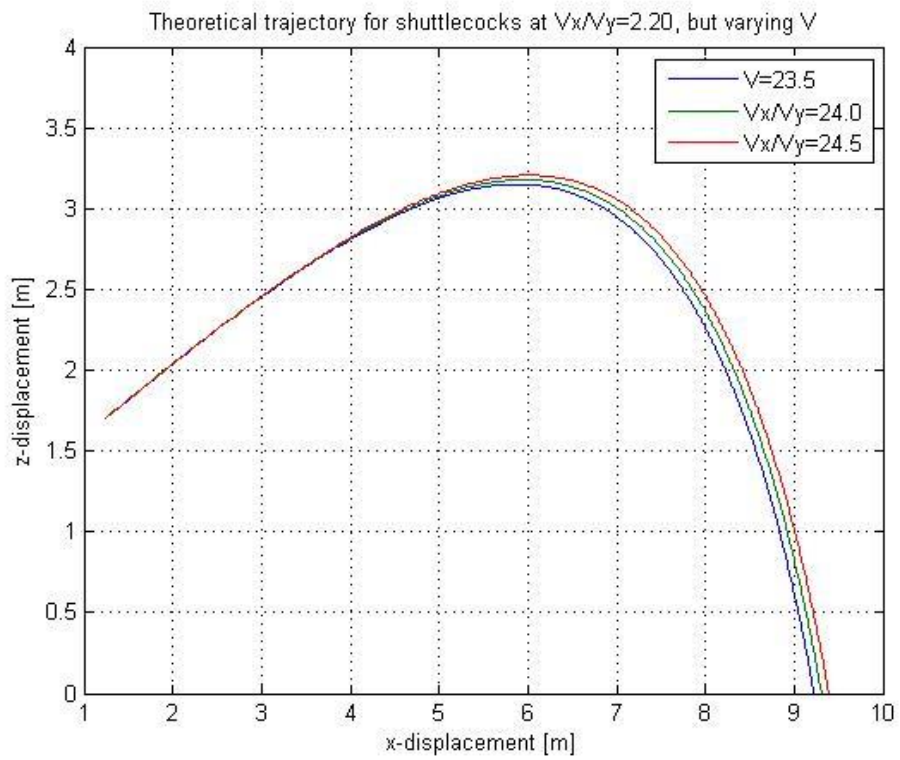
Figure E10 Comparison of shuttlecock positions observed for the various methods of measurement.

Cam 1		Cam 2		Physical		Cam 1 (Corrected)	
X	Y	X	Y	X	Y	X_corrected	Y_corrected
0.99	1.21	1.01	1.20	1.00	1.21	0.99	1.21
0.97	1.96	1.00	1.96	1.00	1.96	0.98	1.96
0.50	1.49	0.51	1.48	0.50	1.49	0.50	1.49
0.49	1.96	0.51	1.95	0.50	1.96	0.49	1.96

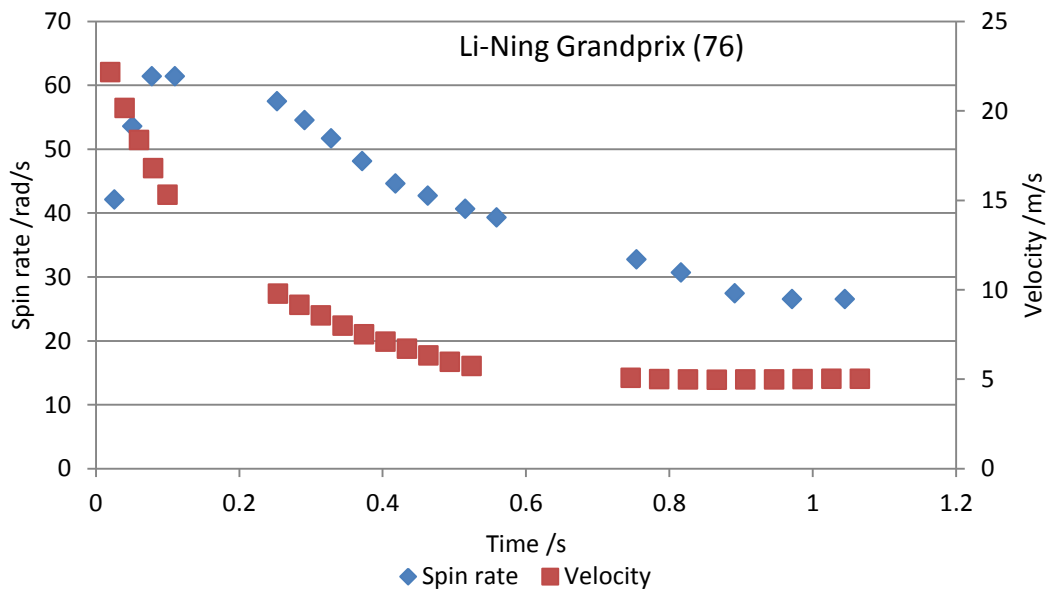
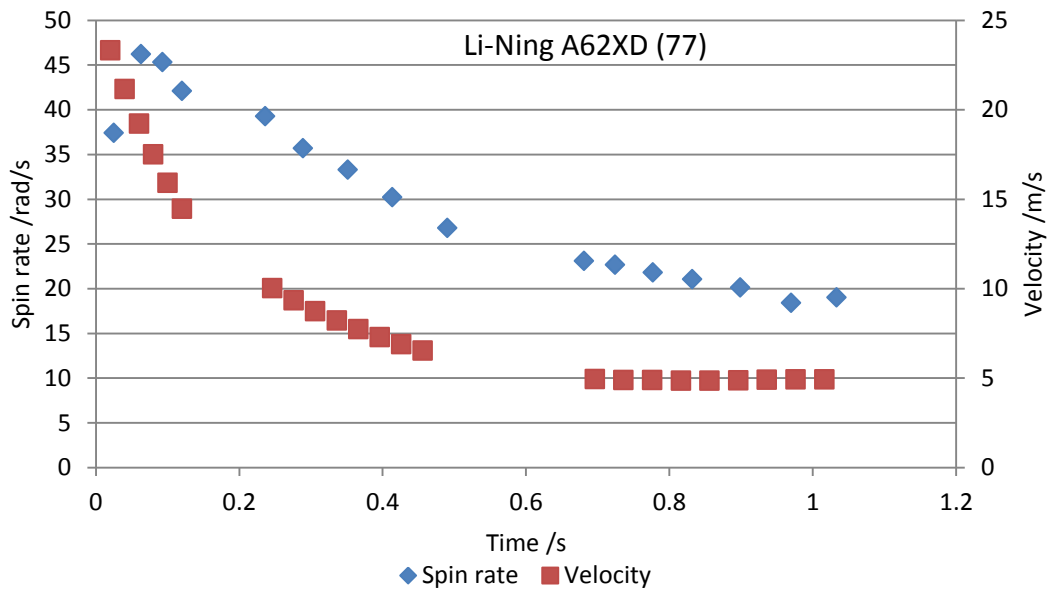
Table E4 Position coordinates that were obtained in the testing for applied error.

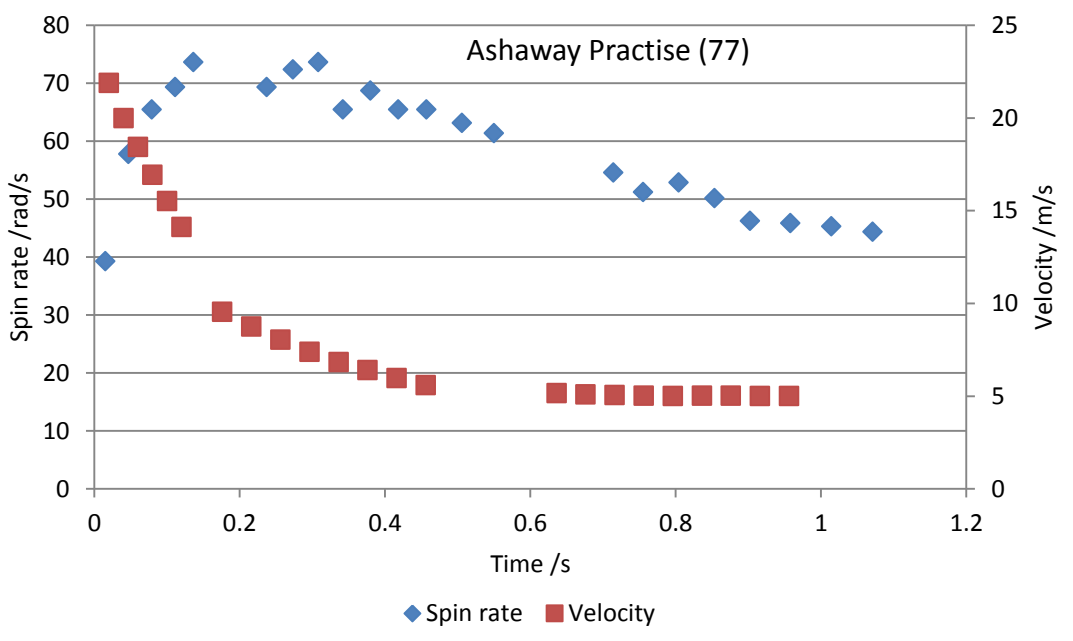
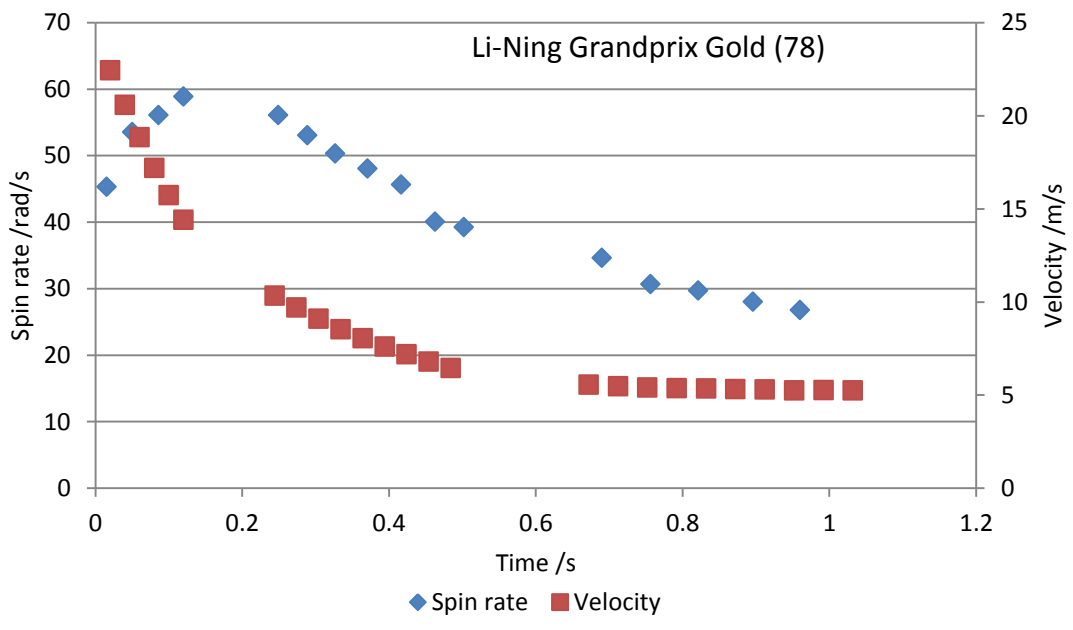
The largest error was observed for Cam 1 and it occurred at the point of (1.00, 1.96). The errors in radial distance before and after correction were 0.023m and 0.016m respectively. Since this is less than 1% of the span of view of one camera, it is unlikely to be significant for trajectory and velocity tracking. This error may be significant for higher derivatives of the linear components, such as the accelerations and aerodynamic force estimations.

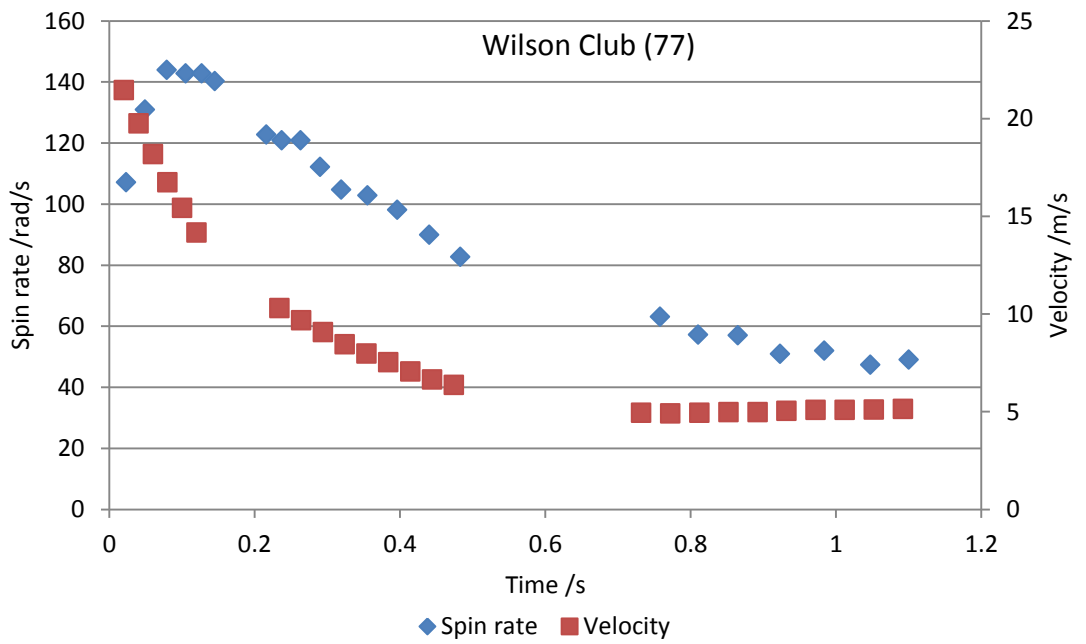
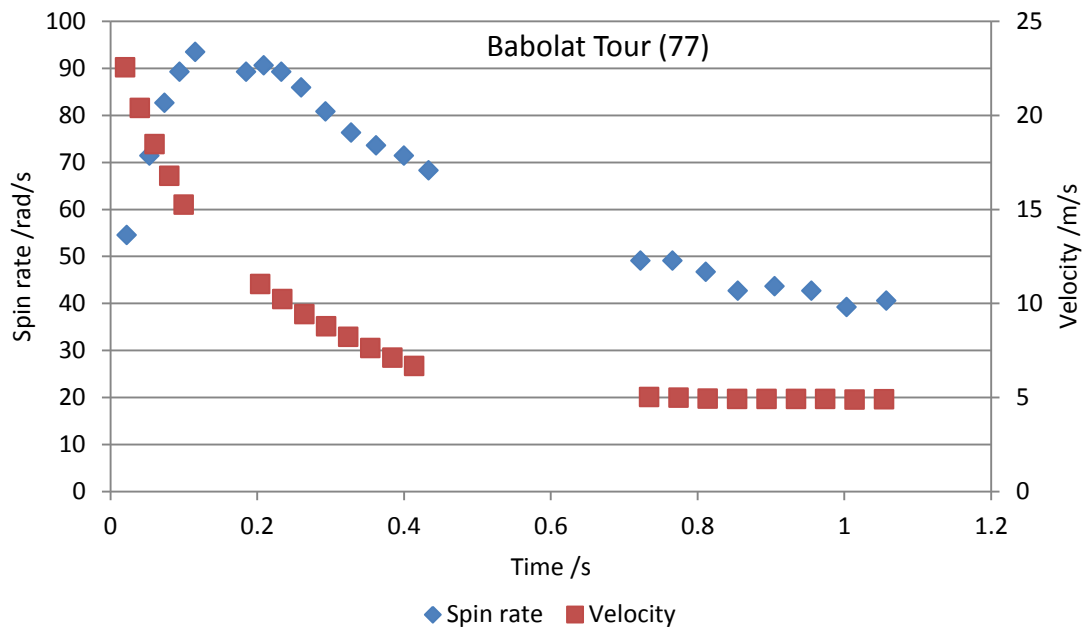
## Appendix F

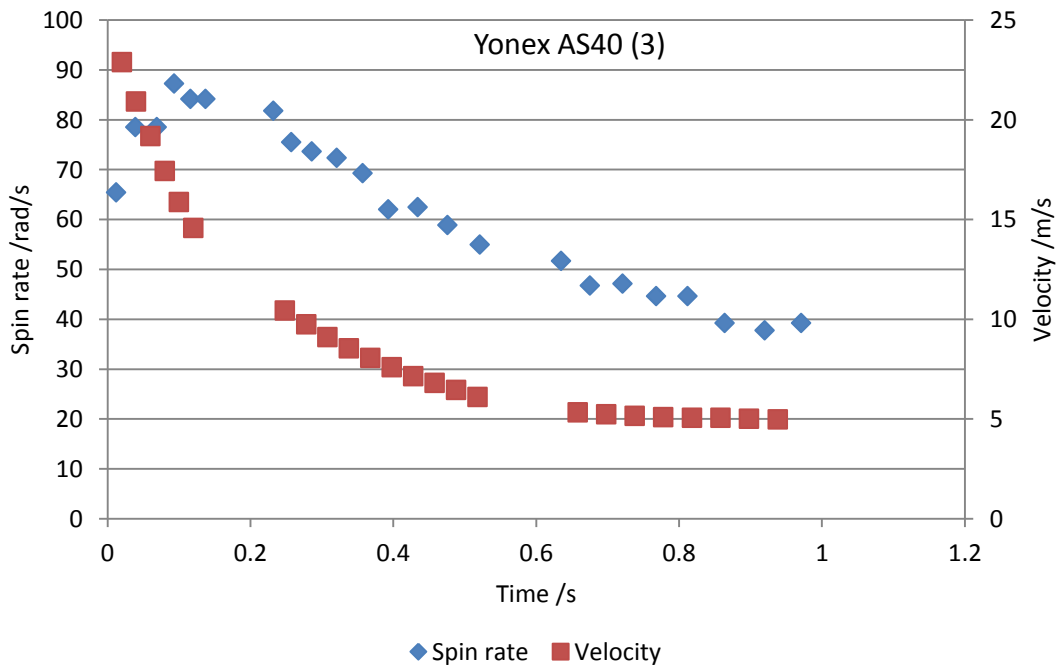
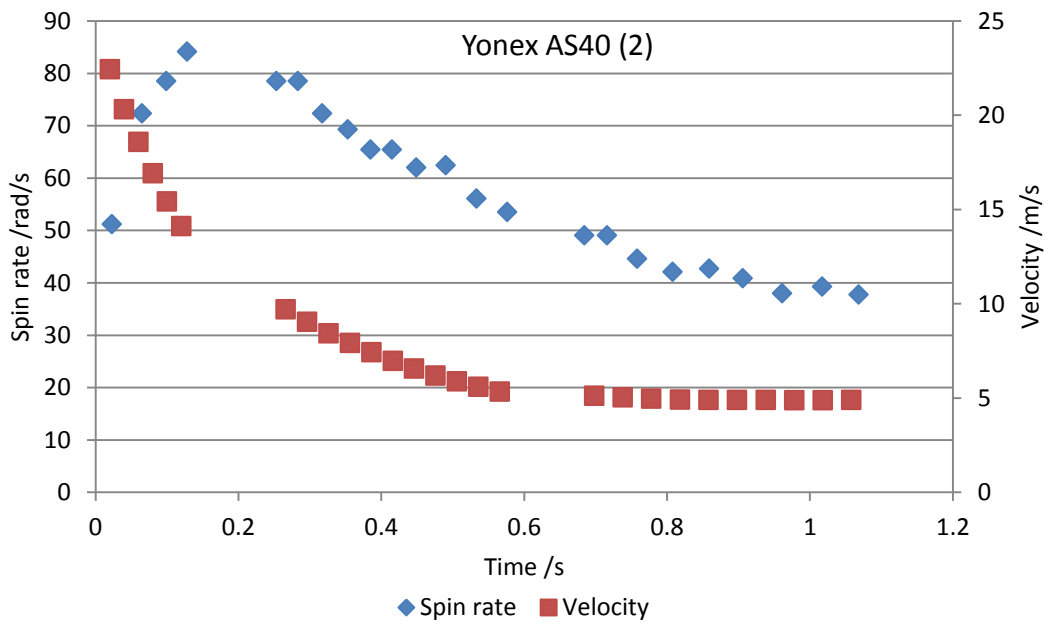


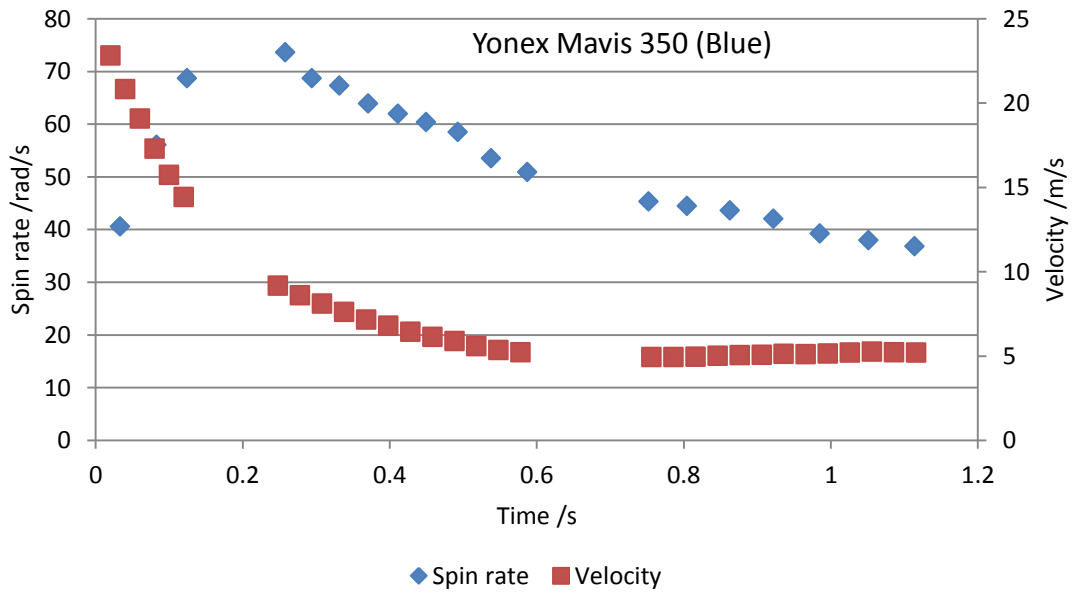
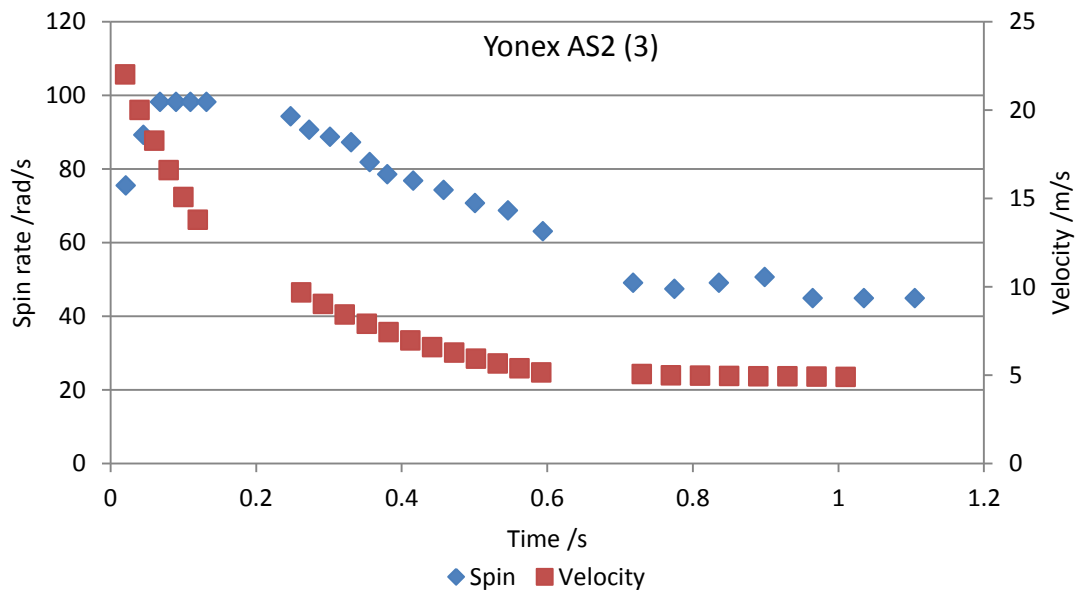
## Appendix G

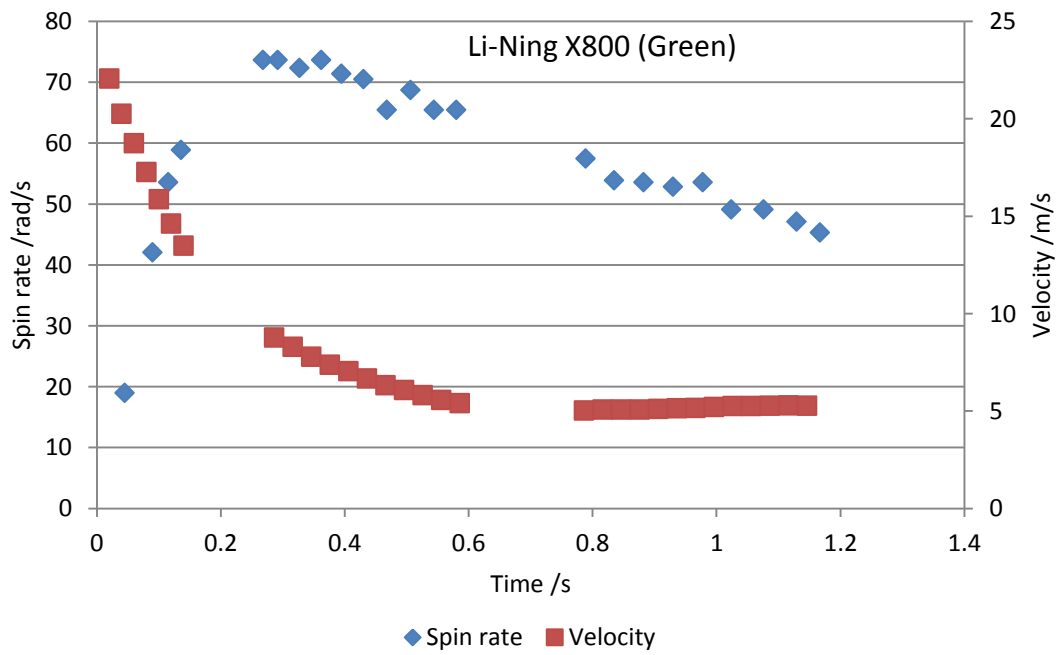
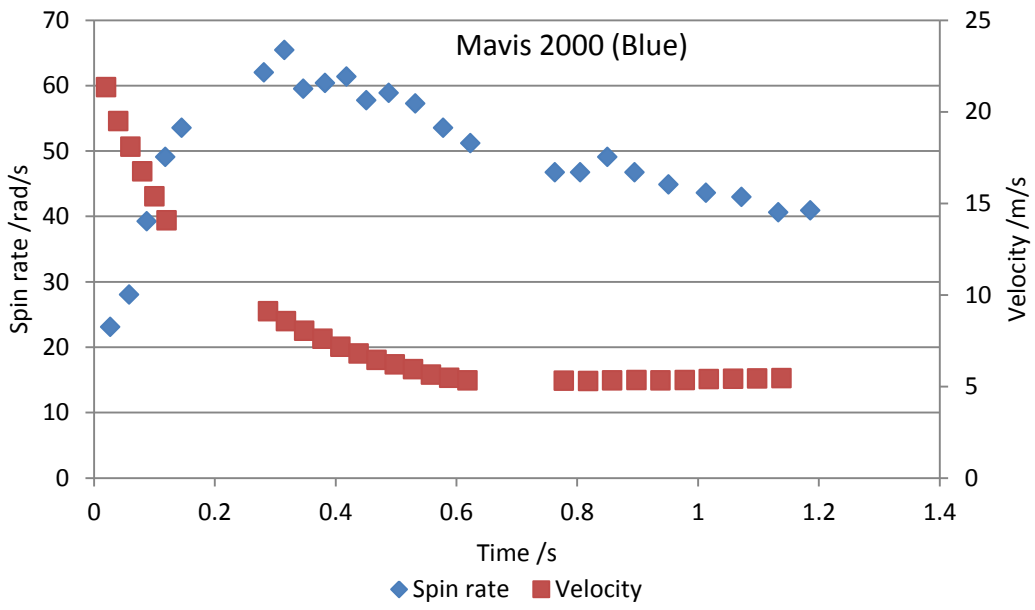


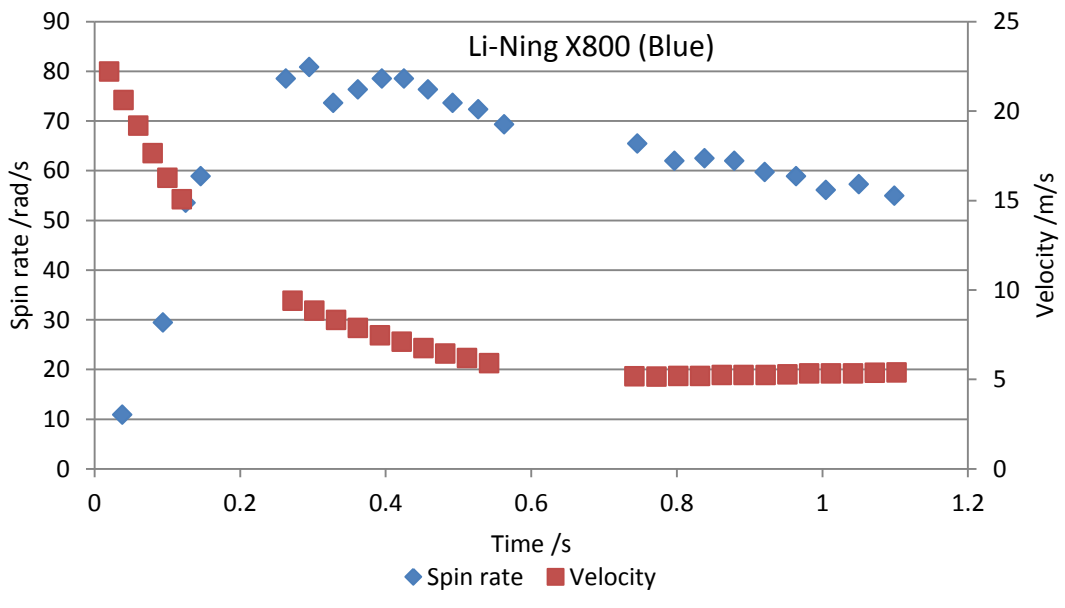












## Appendix H

```
int Distance = 0;           //initialise the variables
int lightpin=0;
int lightreading;
int load;
int load_zero;
int reverse=0;

void setup()               //initialise the pinMode for the controllers
{
  Serial.begin(115200);

  pinMode (10, OUTPUT);
  pinMode (9, OUTPUT);
  digitalWrite (10, LOW);
  digitalWrite (9, LOW);
  digitalWrite (10, HIGH);
  lightreading= analogRead (lightpin);

  while (lightreading >650) //Zero the platen to the travel limit
  {
    digitalWrite (9, HIGH);
    delayMicroseconds(300);
    digitalWrite(9, LOW);
    delayMicroseconds(200);
    lightreading= analogRead (lightpin);
    Serial.println(lightreading);
  }

  delay(5000);

  load_zero=analogRead(1)+12;
  load=analogRead(1);
  digitalWrite (10, LOW);

  while (load<load_zero)   //Moving the platen forward to contact
  {
    digitalWrite (9, HIGH);
    delayMicroseconds(100);
    digitalWrite(9, LOW);
    delayMicroseconds(500);
    load=analogRead(1);
    Serial.println(load);
  }

  while (reverse<1200)    //Reverse platen 1200 steps
  {
    digitalWrite (10, HIGH);
    digitalWrite (9, HIGH);
    delayMicroseconds(300);
    digitalWrite(9, LOW);
    delayMicroseconds(500);
```

```

        reverse=reverse+1;
    }

    delay(5000);
    digitalWrite (10, LOW);

}

void loop ()          //start of compression process
{

    load = analogRead(1);
    Serial.print(load);
    Serial.print(" ");
    Serial.println(Distance);

    digitalWrite(9, HIGH);
    delayMicroseconds(1);
    digitalWrite(9, LOW);
    delayMicroseconds(5000);
    Distance=Distance+1;
    delay(1);

    if (load>200)      //stop compression when load >200
    {
        if (digitalRead (10)==HIGH)
        {
            digitalWrite(10, LOW);
            delay(500);
        }
        else
        {
            digitalWrite(10,HIGH);

            for (Distance=7500; Distance>10;Distance--)
            {
                digitalWrite(10,HIGH);
                digitalWrite(9, HIGH);
                delayMicroseconds(100);
                digitalWrite(9, LOW);
                delayMicroseconds(500);
            }
            delay(500000);
        }
        Distance =0;
        delay(300);
    }

    if (Distance>13500) //stop compression if displacement >13500
    {
        if (digitalRead (10)==HIGH)
        {
            digitalWrite(10, LOW);
            delay(500);
        }
    }
}

```

```
}
else
{
    for (Distance=7500; Distance>10;Distance--)
    {
        digitalWrite(10,HIGH);
        digitalWrite(9, HIGH);
        delayMicroseconds(100);
        digitalWrite(9, LOW);
        delayMicroseconds(500);
    }
    delay(500000);
}
Distance =0;
delay(300);
}
}
```